

UNIVERSITY OF OKLAHOMA

GRADUATE COLLEGE

MICROSEISMIC MAPPING OF FLUID INDUCED HYDRAULIC
FRACTURES AND ANALYSIS OF LOCATION UNCERTAINTIES

A THESIS

SUBMITTED TO THE GRADUATE COLLEGE

in partial fulfillment of the requirements for the

Degree of

MASTER OF SCIENCE

By

CAMILO MORENO
Norman, Oklahoma
2011

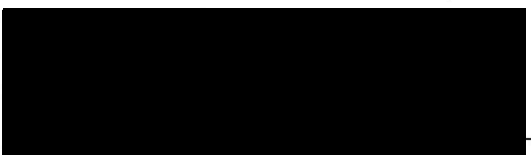
MICROSEISMIC MAPPING OF FLUID INDUCED HYDRAULIC
FRACTURES AND ANALYSIS OF LOCATION UNCERTAINTIES

A THESIS APPROVED FOR THE
MEWBOURNE SCHOOL OF PETROLEUM AND GEOLOGICAL
ENGINEERING

BY


Dr. Carl H. Sondergeld, Chair


Dr. Chandra S. Rai


Dr. G. Randy Keller

© Copyright by CAMILO MORENO 2011
All Rights Reserved.

ACKNOWLEDGMENTS

To my parents Luis and Patricia, and my sister Monica for their love and continuous support.

I would like to thank the members of my committee Dr. Cristina R. Roca and Dr. Holly Keller for their valuable thoughts during this work.

A special thanks to Gary Moore, Bruce Epstein, and Mike Crow for their help at the Integrated Core Characterization Center and to all of my colleagues: Alvaro Qui, Yanyuan Cheng, Ellen Collins and the rest of people who helped me during this process.

I am grateful to Deena for having my research work.

I would like to thank my parents Pablo Ortega, Justo Diego Roca and Gloria Garcia for their unconditional love and support during these years. This journey was made possible by a Fulbright-Humanism Grant. I have really enjoyed this experience and I am very grateful to the IAC and the rest of people who supported me during this time. I want to thank you all.

I am especially grateful to my family, but the biggest thank you goes to my advisor, Dr. Cristina R. Roca, for her support and guidance throughout these years.

ACKNOWLEDGEMENTS

First, I want to express my gratitude to my advisor Dr. Carl H. Sondergeld for giving me the opportunity to work under his supervision. I thank him for his continuous advice and support since the very beginning. I will always admire his passion for teaching and researching.

I want to thank the members of my committee Dr. Chandra S. Rai and Dr. G. Randy Keller for their valuable thoughts during this work.

Also, special thanks to Gary Stowe, Bruce Spears and Mike Shaw for their help at the Integrated Core Characterization Center and to rest of my colleagues: Alvaro Ortiz, Yashwanth Chitralla, Elijah Odusina and the rest of people who helped me during this process.

I am infinitely grateful to Devon for funding my research work

I would like to thank my friends Pablo Barajas, Juan Diego Pinilla and David Galvis for their unconditional friendship during these years. You have been the closest thing to a family in Norman. Camila, I have really enjoyed the time I have spent with you, you very special to me. Also the rest of people that have come into my life, I want to thank you all.

I am especially thankful to my family; from the distance they have given me the love, support, advice and motivation throughout these years.

TABLE OF CONTENTS

<i>TABLE OF CONTENTS</i>	<i>v</i>
<i>LIST OF TABLES</i>	<i>vii</i>
<i>LIST OF FIGURES</i>	<i>xiii</i>
<i>ABSTRACT</i>	<i>xli</i>
1. INTRODUCTION	1
2. LITERATURE REVIEW	7
2.1 Hydraulic fracturing overview.....	7
2.1.1 History and development of HF	8
2.1.2 Current status of hydraulic fracturing technology.....	11
2.2 Microseismicity	13
2.2.1 Microseismicity development.....	15
2.2.2 Microseismicity tools.....	17
2.3 Hydraulic fracturing experiments at laboratory scale	20
2.4 Microseismic event location	28
2.5 Considering anisotropy	32
2.6 Formation permeability from microseismic data.....	37
2.6.1 r-t technique for permeability estimation	37
2.6.2 Inversion approach to permeability estimation.....	39
3. STATEMENT OF THE PROBLEM	42
4. RESULTS AND ANALYSIS	52
4.1 Calibration results	52

4.1.1	Indiana limestone.....	52
4.1.2	Lyons sandstone.....	54
4.1.3	Pyrophyllite	58
4.2	Microseismic event location.....	62
4.2.1	Indiana limestone.....	62
4.2.2	Lyons sandstone.....	77
4.2.3	Pyrophyllite	117
4.3	Effect of surface sensors	149
4.3.1	Indiana limestone.....	149
4.3.2	Lyons sandstone.....	155
4.3.3	Pyrophyllite	160
4.4	Microscopic observations.....	167
4.4.1	Indiana limestone.....	168
4.4.2	Lyons sandstone.....	171
4.4.3	Pyrophyllite	174
4.5	Permeability estimation using microseismicity	179
4.5.1	Lyons sandstone.....	179
4.5.2	Pyrophyllite	185
5.	CONCLUSIONS.....	191
	REFERENCES.....	195
	APPENDIX A: TRANSVERSE ISOTROPY.....	210

LIST OF TABLES

Table 2.1 – Frequency ranges for different seismic techniques.....	14
Table 2.2 - Summary of hydraulic fracturing laboratory experiments indicating the authors, sample, properties of the samples and variables tested.....	26
Table 3.1 - Velocity measurements of P-wave and S-wave on pyrophyllite plugs taken parallel, perpendicular and at an angle of 45° to the bedding orientation	43
Table 3.2 - Anisotropic parameters (Thomsen, 1986) calculated from the velocity values obtained from the 3-plug technique for pyrophyllite samples at 3000 psi confining pressure.....	44
Table 3.3 - Average P-wave velocity values obtained from CVA measurements for Indiana limestone samples used in the study.....	44
Table 3.4 - Average P-wave velocity values obtained from CVA measurements for Lyons sandstone samples used in the study.....	44
Table 3.5 - Values of stress applied to Indiana limestone samples using flat jacks during hydraulic fracturing experiments.	49
Table 3.6 - Values of stress applied to Lyons Sandstone samples using flat jacks during hydraulic fracturing experiments.	50

Table 3.7 - Values of stress applied to pyrophyllite samples using flat jacks during hydraulic fracturing experiments respect to the orientation of the bedding planes.	50
Table 4.1 - Average absolute error values for pencil breaks experiments in Indiana Limestone samples.	53
Table 4.2 - Average absolute error values for pencil breaks experiments in Lyons sandstone samples.	56
Table 4.3 - Average absolute error values for pencil breaks experiments in pyrophyllite samples.	60
Table 4.4 - Breakdown pressures recorded during the hydraulic fracturing experiments in Indiana limestone samples. Note that all breakdown pressure values have similar magnitude. Also, breakdown pressures are calculated using the value of the tensile strength of Indiana limestone obtained by performing a Brazilian test on a sample representative of this lithology.	64
Table 4.5 - Average uncertainty values for each coordinate in all three Indiana limestone samples.	74
Table 4.6 - Root mean square error for each Indiana limestone sample.	77
Table 4.7 - Breakdown pressures recorded during the hydraulic fracturing experiments in Lyons sandstone samples. The breakdowns seem to depend on the horizontal applied stress; highest breakdown	

pressures were recorded when the lowest horizontal applied stress was applied (samples S8 and S9) whereas the lowest breakdown pressures were recorded for sample with the highest applied stress (S4, S6 and S7). Breakdown pressures were calculated for each sample using the tensile strength of Lyons sandstone obtained by performing a Brazilian test on a sample representative of this lithology. 80

Table 4.8 - Average uncertainty values for each coordinate in all Lyons sandstone samples. 114

Table 4.9 - Root mean square error for locations in Lyons sandstone samples. 116

Table 4.10 – Recorded breakdown pressures compared to the calculated values. Pressure were calculated using tensile strength of the pyrophyllite obtained from a Brazilian test performed on a representative sample of pyrophyllite. 121

Table 4.11 - Average uncertainty values for each coordinate in all pyrophyllite samples. 145

Table 4.12 - Root mean square error for locations in pyrophyllite samples. 146

Table 4.13 - Average uncertainty values for X, Y and Z coordinates in sample C15. 152

Table 4.14 - Average uncertainty values for samples C15 and C16 with and without sensors placed on the upper surface of the sample. Error increased in the Z-direction when no surface sensors were used on the upper surface of the samples.....	153
Table 4.15 - Increase (percentage) of error in spatial coordinates for Indiana limestone samples C15 and C16 when no sensors are attached to the upper surface of the sample.....	154
Table 4.16 - rms error for Indiana limestone C15 and C16 when surface sensors are used and when they are not used.	154
Table 4.17 - Average uncertainty values for X, Y and Z coordinates in sample S4.....	157
Table 4.18 - Average uncertainty values for Lyons sandstone samples with and without sensors placed on the upper surface of the sample. Error increased in the Z-direction when no surface sensors were used on the upper surface of the samples.....	158
Table 4.19 - Increase (percentage) of error in spatial coordinates for Lyons sandstone samples when no sensors are attached to the upper surface of the sample.	159
Table 4.20 - rms error for Lyons sandstone samples when surface sensors are used and when they are not used.....	160
Table 4.21 - values for X, Y and Z coordinates in sample P11.	163

Table 4.22 - Average uncertainty values for pyrophyllite samples with and without sensors placed on the upper surface of the sample. Error increased in the Z-direction when no surface sensors were used on the upper surface of the samples.....	164
Table 4.23 - Increase (percentage) of error in spatial coordinates for pyrophyllite samples when no sensors are attached to the upper surface of the sample.	165
Table 4.24 - rms error for pyrophyllite samples when surface sensors are used and when they are not used.....	165
Table 4.25 - Values of process zone length, width and height with or without sensors attached to the upper surface of the sample. The area of the process zone (length*width) is exhibited along with the SRV (Stimulated Reservoir Volume).....	166
Table 4.26 - Values of fracture height, pressure difference between injection pressure and far-field reservoir pressure, viscosity and compressibility of the reservoir fluid, porosity, apparent diffusivity and formation permeability for Lyons sandstone samples experiments.	181
Table 4.27 - Parameters used by the inversion approach for permeability for each Lyons sandstone sample.	183

Table 4.28 - Formation permeability values for Lyons sandstone samples obtained using the inversion approach, r-t method and measured using the AP608.	184
Table 4.29 - Values of fracture height, pressure difference between injection pressure and far-field reservoir pressure, viscosity and compressibility of the reservoir fluid, porosity, apparent diffusivity and formation permeability for pyrophyllite samples.	186
Table 4.30 - Parameters used by the inversion approach for permeability samples.	188
Table 4.31 - Formation permeability values for pyrophyllite samples obtained using the inversion approach, r-t method and experimentally using ultra low permeameters (ULP) (Tinni, 2011).	188
Table 4.32 - Formation permeability values for Lyons sandstone and pyrophyllite samples obtained using the inversion approach and r-t method.	189

LIST OF FIGURES

- Fig. 1.1 – U.S. energy consumption by fuel showing the importance of natural gas in the energy window. Natural gas share was 25% in 2009 and it is expected to be 24% in 2035 (EIA Annual Energy Outlook 2011) 1
- Fig. 1.2 – Distribution of shale basins in United States (Ground Water Protection Council, 2009)..... 2
- Fig. 1.3 – U.S. natural gas distribution by source. Projection shows that over two thirds of the natural gas in U.S. will come from exploitation of shale gas and tight gas (EIA Annual Energy Outlook 2011). Note the growth in shale gas by 2035. 3
- Fig. 2.1 - Schematics of a geophone (Barzilai et al. 1998)..... 17
- Fig. 2.2 – Geometry showing a borehole in a transversely isotropic medium where the X-axis is aligned with the direction of the bedding and the Y-axis is perpendicular to the bedding (Aadnoy, 1987). σ_x , σ_y , σ_z are the three principal stresses. σ_x and σ_y are aligned with the X' and Y'-axis, respectively. Θ is the angle from the X-axis and φ is the angle measured from the bedding orientation to the horizontal axis. 35
- Fig. 3.1 – Top) CVA response of sample C14 (limestone) showing a velocity anisotropy of 6% where the red lines represent the standard deviation with a value of ± 0.061 km/s. Bottom) CVA response of

sample S4 (sandstone) showing a velocity anisotropy of 4% and the red lines represent the standard deviation with a value of ± 0.044 km/s. 45

Fig. 3.2 – CVA response for pyrophyllite. Azimuthal measurements of P-wave velocity indicate 25% velocity anisotropy. Position of the peaks also indicates the orientation of the bedding in the sample. 46

Fig. 3.3 – Sketch of a sample completion. Red lines show the counter bore and the wellbore which is filled with epoxy to seal the high pressure stainless steel tubing which acts as our wellbore (Chitrala et. al, 2010). A perforation or hole is drilled in the tubing (not in the sample). 47

Fig. 3.4 – Piezoelectric sensors attached to a limestone sample. A vertical array of sensors is used to simulate an observation well. Two flat jacks are used to apply a horizontal stress (Chitrala et. al, 2010). 48

Fig. 3.5 – Magnified waveforms recorded by 16 piezoelectric sensors attached to Lyons sandstone, S4, during a hydraulic fracturing experiment. The X-axis is represents the time in microseconds and ranges from 90 μ s to 150 μ s and the Y-axis is the amplitude in volts and ranges from -1 to 1 Volts. 49

Fig. 3.6 – Hsu-Nielson source for the testing and calibration of acoustic emission systems. They recommend a lead diameter of 0.5 or 0.3 mm and 2H hardness (source: <http://www.ndt.net/ndtaz/ndtaz.php>). 51

Fig. 4.1 - Pencil break calibrations for different Indiana limestone samples C14 (upper left), C15 (upper right) and C16 (bottom). 53

Fig. 4.2 - Pencil breaks calibration for different Indiana Limestone samples C14 (upper left), C15 (upper right) and C16 (bottom), showing the error in the X- and Y-axis with error ellipses (red lines) 54

Fig. 4.3 - Pencil breaks calibration for different Lyons sandstone samples; green dots represent the located events, the black dots are the real locations of the pencil breaks and the blue squares represent the sensors attached to the sample 56

Fig. 4.4 - Pencil break calibrations for Lyons Sandstone samples S4, S6, S7, S8, S9, S11, S13 and S14 showing the error in the X- and Y-axis with error ellipses (red lines) 58

Fig. 4.5 - Pencil break calibrations for different pyrophyllite samples; green dots represent the located events, the black dots are the real locations of the pencil breaks and the blue squares represent the sensors attached to the sample. The dashed lines represent the fabric direction in the sample. 59

Fig. 4.6 - Pencil break calibrations for pyrophyllite samples P5, P6, P9, P12 and P16 showing the error in the X- and Y-axis with error ellipses (red lines)..... 61

Fig. 4.7- Pump pressure (black) and cumulative AE (red) as a function of time. Note that in all experiments that the majority of AE activity occurs prior to the actual breakdown pressure. 63

Fig. 4.8 - Plan view of sample C14 (Indiana limestone) showing the spatial and temporal evolution of the hydraulic fracture. The green dots represent the early time events, while the orange and purple represent the intermediate and late time events, respectively. The cyan squares represent sensors attached to the sample. The red arrows represent the direction of the stress applied with a magnitude of 833 psi. The two circles in the center of the plot represent the counter borehole and the borehole. 77 MS events were locatable within the sample. 64

Fig. 4.9 - Lateral view of sample C14 perpendicular to the fracture plane. The red triangle represents the location of the perforations in the tubing..... 65

Fig. 4.10 - Lateral view of sample C14 parallel to the fracture. This view allows observing the development of a narrow fracture in the direction of the applied stress..... 66

- Fig. 4.11 - Surface of sample C14 showing a fracture enclosed by the dark blue lines in the direction of the stress applied (red arrows) 67
- Fig. 4.12 - Plan view of sample C15 showing the spatial and temporal evolution of the hydraulic fracture. The green dots represent the early time events, while the orange and purple represent the intermediate and late time events, respectively. The cyan squares represent sensors attached to the sample. The red arrows represent the direction of the stress applied with a magnitude of 840 psi. The two circles in the center of the plot represent the counter borehole and the borehole. 124 MS events were locatable within the sample. 68
- Fig. 4.13 - Lateral view of sample C15 perpendicular to the fracture plane. The red triangle represents the location of the perforations in the tubing 69
- Fig. 4.14 - Lateral view of sample C15 parallel to the fracture. This view allows observing the development of a narrow fracture in the direction of the applied stress..... 69
- Fig. 4.15 - Surface view of sample C15 showing a fracture growing in the direction of the stress applied (red arrows). The fracture is enclosed by the dark blue lines. 70
- Fig. 4.16 - Plan view of sample C16 (Indiana limestone) showing the spatial and temporal evolution of the hydraulic fracture. The green

dots represent the early time events, while the orange and purple represent the intermediate and late time events, respectively. The cyan squares represent sensors attached to the sample. The red arrows represent the direction of the stress applied with a magnitude of 809 psi. The two circles in the center of the plot represent the counter borehole and the borehole. 118 MS events were locatable within the sample. 71

Fig. 4.17 - Lateral view of sample C16 perpendicular to the fracture plane.

The red triangle represents the location of the perforations in the tubing. 72

Fig. 4.18 - Lateral view of sample C16 parallel to the fracture. This view

allows observing the development of a narrow fracture in the direction of the stress applied. 72

Fig. 4.19 - Surface view of sample C16 showing a fracture development in

the direction of the stress applied (red arrows). The fracture is enclosed by the dark blue lines. 73

Fig. 4.20 – Plan view of sample C14 showing the uncertainties of the MS

events as error ellipses; it can be observed the highest uncertainties in the X-Y plane are in the X-direction where there are no sensors attached to the sample. 75

Fig. 4.21 – Lateral view perpendicular to the fracture plane for sample C14 showing uncertainties of MS events in the X-Z plane; higher uncertainties are in the Z-direction. No surface sensors are used in this sample..... 75

Fig. 4.22 - Average uncertainties of hypocenter locations in each coordinate indicating values for early, intermediate and late time events for samples C14, C15 and C16 76

Fig. 4.23 - Pumping pressure (black) and cumulative AE (red) as a function of time. The majority of acoustic emissions are recorded before reaching the breakdown pressure. A secondary activity is noticeable in all samples once the pump is shut off..... 79

Fig. 4.24 - Plan view of sample S4 (Lyons sandstone) showing the spatial and temporal evolution of the hydraulic fracture. The green dots represent the early time events, while the orange and purple represent the intermediate and late time events, respectively. The cyan squares represent sensors attached to the sample. The red arrows represent the direction of the stress applied with a magnitude of 1040 psi. The two circles in the center of the plot represent the counter borehole and the borehole. 765 MS events were locatable within the sample. 81

Fig. 4.25 - Lateral view of sample S4 perpendicular to the fracture plane.

The red triangle represents the location of the perforations in the tubing..... 82

Fig. 4.26 - Lateral view of sample S4 parallel to the fracture. This view

shows the development of a fracture in the direction of the stress applied with some events out of plane. Later events, purple, are more concentrated about the hydraulic fracture plane. 82

Fig. 4.27 - Surface view of sample S4 indicating the fracture growing in the

direction of stress applied (red arrows). The fracture is enclosed by the dark blue lines..... 84

Fig. 4.28 - Plan view of sample S6 (Lyons sandstone) showing the spatial

and temporal evolution of the hydraulic fracture. The green dots represent the early time events, while the orange and purple represent the intermediate and late time events, respectively. The cyan squares represent sensors attached to the sample. The red arrows represent the direction of the stress applied with a magnitude of 1080 psi. The two circles in the center of the plot represent the counter borehole and the borehole. 861 MS events were located within the sample. Note narrower purple distribution. 85

Fig. 4.29 - Lateral view of sample S6 perpendicular to the fracture plane.

The red triangle represents the location of the perforations in tubing.

..... 86

Fig. 4.30 - Lateral view of sample S6 parallel to the fracture plane. The red triangle represents the location of the perforations in tubing. Note

narrowly focused late time events (purple). 86

Fig. 4.31 - Surface view of sample S6 indicating the fracture growing in the direction of stress applied (red arrows). The fracture is enclosed by

the dark blue lines..... 88

Fig. 4.32 - Plan view of sample S7 (Lyons sandstone) showing the spatial and temporal evolution of the hydraulic fracture. The green dots

represent the early time events, while the orange and purple

represent the intermediate and late time events, respectively. The

cyan squares represent sensors attached to the sample. The red

arrows represent the direction of the stress applied with a magnitude

of 1160 psi. The two circles in the center of the plot represent the

counter borehole and the borehole. 531 events were located within

the sample. 89

Fig. 4.33 - Lateral view of sample S7 perpendicular to the fracture plane.

The red triangle represents the location of the perforations in tubing.

..... 90

- Fig. 4.34 - Lateral view of sample S7 parallel to the fracture plane. The red triangle represents the location of the perforations in tubing. Notice the narrower distribution of purple events. 90
- Fig. 4.35 – Left) Surface view of sample S7 indicating the fracture growing in the direction of stress applied (red arrows). The fracture is enclosed by the dark blue lines. Right) One inch diameter plug taken at the borehole position (Y-Z view) showing the induced fracture enclosed by the black lines. 92
- Fig. 4.36 - Plan view of sample S8 (Lyons sandstone) showing the spatial and temporal evolution of the hydraulic fracture. The green dots represent the early time events, while the orange and purple represent the intermediate and late time events, respectively. The cyan squares represent sensors attached to the sample. The red arrows represent the direction of the stress applied with a magnitude of 150 psi. The two circles in the center of the plot represent the counter borehole and the borehole. Note the orientation of the fracture is at an angle to the applied stress. 93
- Fig. 4.37 - Lateral view of sample S8 perpendicular to the applied stress direction. The red triangle represents the location of the perforations in tubing. 94

Fig. 4.38 - Lateral view of sample S8 parallel to the applied stress direction. The red triangle represents the location of the perforations in tubing. An apparent wider zone is evident due the out of plane growth of the fracture..... 94

Fig. 4.39 - Lateral view of sample S8 parallel to the fracture plane which is 10° off from the direction of the applied stress. This view shows a much thinner width of the microseismic cloud compared to the apparent width observed in the view parallel to the applied stress. It also shows a growth of a fracture that is inclined with respect to the vertical axis..... 95

Fig. 4.40 - Surface view of sample S8 indicating the fracture growing in the direction of stress applied (red arrows). The fracture is enclosed by the dark blue lines..... 96

Fig. 4.41 - Plan view of sample S9 (Lyons sandstone) showing the spatial and temporal evolution of the hydraulic fracture. The green dots represent the early time events, while the orange and purple represent the intermediate and late time events, respectively. The cyan squares represent sensors attached to the sample. The red arrows represent the direction of the stress applied with a magnitude of 150 psi. The two circles in the center of the plot represent the

counter borehole and the borehole. Asymmetrical wing development and note right wing is not parallel to the applied stress direction. 97

Fig. 4.42 - Lateral view of sample S9 perpendicular to the applied stress.

The red triangle represents the location of the perforations in the tubing. It is evident that the left wing of the hydraulic fracture is underdeveloped in comparison to the right wing..... 98

Fig. 4.43 - Lateral view of sample S9 parallel to the applied stress. The red triangle represents the location of the perforations in the tubing. Out of plane growth of the sample give this apparent wider process zone. 98

Fig. 4.44 - Lateral view of sample S9 parallel to the fracture plane which is 45° off from the direction of the applied stress. This view shows a much thinner width of the process zone compared to the apparent width observed in the view parallel to the applied stress. However, the width of the process zone is biased since the left wing is not aligned with the right wing which leads to observation of a wider zone..... 99

Fig. 4.45 - Surface view of sample S9 indicating the fracture growing in the direction of stress applied (red arrows). The fracture is enclosed by the dark blue lines..... 100

Fig. 4.46 - Plan view of sample S11 (Lyons sandstone) showing the spatial and temporal evolution of the hydraulic fracture. The green

dots represent the early time events, while the orange and purple represent the intermediate and late time events, respectively. The cyan squares represent sensors attached to the sample. The red arrows represent the direction of the stress applied with a magnitude of 580 psi. The two circles in the center of the plot represent the counter borehole and the borehole. 101

Fig. 4.47 - Lateral view of sample S11 perpendicular to the fracture plane.

The red triangle represents the location of the perforations in tubing. 102

Fig. 4.48 - Lateral view of sample S11 parallel to the fracture plane. The red triangle represents the location of the perforations in the tubing.

Note the downward growth. 102

Fig. 4.49 - Lateral view of sample S11 showing the induced hydraulic fracture enclosed by the two black lines. Good agreement with physical fracture and microseisms locations. 104

Fig. 4.50 - Plan view of sample S13 (Lyons sandstone) showing the spatial and temporal evolution of the hydraulic fracture. The green dots represent the early time events, while the orange and purple represent the intermediate and late time events, respectively. The cyan squares represent sensors attached to the sample. The red arrows represent the direction of the stress applied with a magnitude

of 580 psi. The two circles in the center of the plot represent the counter borehole and the borehole. Note the departure of the fracture direction from the applied stress and the asymmetric wing development. 105

Fig. 4.51 - Lateral view of sample S13 perpendicular to the fracture plane. The red triangle represents the location of the perforations in the tubing. 106

Fig. 4.52 - Lateral view of sample S13 parallel to the fracture plane. The red triangle represents the location of the perforations in the tubing. Note the downward growth and because of the projection a false width of the fractured zone is observed. 106

Fig. 4.53 - Lateral view of sample S13 parallel to the fracture plane. The red triangle represents the location of the perforations in the tubing. Note the downward growth and because of the projection a false width of the fractured zone is observed. 108

Fig. 4.54 - Lateral view (Y-Z plane) of sample S13 showing an inclined and concave fracture. Microseisms locations agree with the observed visual fracture orientation and location. 109

Fig. 4.55 - Plan view of sample S14 (Lyons sandstone) showing the spatial and temporal evolution of the hydraulic fracture. The green dots represent the early time events, while the orange and purple

represent the intermediate and late time events, respectively. The cyan squares represent sensors attached to the sample. The red arrows represent the direction of the stress applied with a magnitude of 550 psi. The two circles in the center of the plot represent the counter borehole and the borehole. Again, asymmetric wing development and deviation of fracture direction from the applied stress direction is observed. 110

Fig. 4.56 - Lateral view of sample S14 perpendicular to the applied stress. The red triangle represents the location of the perforations in the tubing..... 111

Fig. 4.57 - Lateral view of sample S14 parallel to the applied stress. The red triangle represents the location of the perforations in the tubing. Out of plane projection gives a false representation of process zone. 111

Fig. 4.58 - Lateral view of sample S14 parallel to the applied stress. The red triangle represents the location of the perforations. Out of plane projection gives a false representation of process zone. 113

Fig. 4.59 - Left) Lateral view of sample S14 (Y-Z plane) showing a fracture that is not aligned with the direction of the stress applied but it is deviated 45 degrees. Right) One inch diameter plug taken out of the

sample at 45 degrees from the direction of the stress applied
 indicating the existence of a fracture (enclosed by black lines) 114

Fig. 4.60 - Average uncertainties of hypocenter locations in each
 coordinate for early, intermediate and late time events for Lyons
 sandstone samples..... 116

Fig. 4.61 - Pumping pressure (black) and cumulative AE (red) as a
 function of time for pyrophyllite samples. The majority of acoustic
 emissions are recorded before reaching the breakdown pressure. 120

Fig. 4.62 - Plan view of sample P5 showing the spatial and temporal
 evolution of the hydraulic fracture. The green dots represent the early
 time events, while the orange and purple represent the intermediate
 and late time events, respectively. The cyan squares represent
 sensors attached to the sample. The red arrows represent the
 direction of the stress applied with a magnitude of 970 psi. The two
 circles in the center of the plot represent the counter borehole and the
 borehole. The dotted lines represent the bedding planes. Note the
 paucity of activity. If representative, the asymmetry wing
 development. 122

Fig. 4.63 - Lateral view of sample P5 perpendicular to the fracture plane.
 The red triangle represents the location of the perforations in the
 tubing..... 123

Fig. 4.64 - Lateral view of sample P5 parallel to the fracture plane. The red triangle represents the location of the perforations in the tubing..... 123

Fig. 4.65 – Analytical solution for hoop stress concentration around wellbore wall (Aadnoy, 1987) when a horizontal stress (red lines) with a magnitude of 1000 psi is applied parallel to the direction of the bedding planes (0° - 180°). The red circle indicates the zone of tensile state in the wellbore wall. The green dashed line is the predicted orientation the fracture should follow. The fracture shows a deviation of 20° from the orientation of the applied stress..... 125

Fig. 4.66 - Plan view of sample P6 showing the spatial and temporal evolution of the hydraulic fracture. The green dots represent the early time events, while the orange and purple represent the intermediate and late time events, respectively. The cyan squares represent sensors attached to the sample. The red arrows represent the direction of the stress applied with a magnitude of 990 psi. The two circles in the center of the plot represent the counter borehole and the borehole. The dotted lines represent the fabric planes. 126

Fig. 4.67 - Lateral view of sample P6 parallel to the fracture plane. The red triangle represents the location of the perforations in tubing. 127

Fig. 4.68 - Lateral view of sample P6 perpendicular to the fracture plane.
The red triangle represents the location of the perforations in tubing.

..... 127

Fig. 4.69 - Surface of sample P6 showing the direction of the applied stress (red arrows) which is perpendicular to the orientation of the fabric. The dark red lines enclose the induced hydraulic fracture and do not show a clear deviation of the fracture from the applied stress.

..... 128

Fig. 4.70 – Analytical solution for hoop stress concentration around wellbore wall (Aadnoy, 1987) when a horizontal stress (red lines) with a magnitude of 1000 psi is applied perpendicular to the direction of the bedding planes (0° - 180°). The reddish circle indicates the zone of tensile state in the wellbore wall. The green dashed line is the predicted orientation the fracture should follow. The fracture shows a deviation of 20° from the orientation of the applied stress. 129

Fig. 4.71 - Plan view of sample P9 showing the spatial and temporal evolution of the hydraulic fracture. The green dots represent the early time events, while the orange and purple represent the intermediate and late time events, respectively. The cyan squares represent sensors attached to the sample. The red arrows represent the direction of the stress applied with a magnitude of 980 psi. The two

circles in the center of the plot represent the counter borehole and the borehole. The dotted lines represent the foliation planes. 130

Fig. 4.72 - Lateral view of sample P9 perpendicular to the fracture plane.

The red triangle represents the location of the perforations in the tubing..... 131

Fig. 4.73 - Lateral view of sample P9 parallel to the fracture plane. The red triangle represents the location of the perforations in the tubing..... 131

Fig. 4.74 - Plan view of sample P9 showing a fracture deviated 20 degrees from the direction of the stress applied (red arrows)..... 133

Fig. 4.75 - Plan view of sample P10 showing the spatial and temporal evolution of the hydraulic fracture. The green dots represent the early time events, while the orange and purple represent the intermediate and late time events, respectively. The cyan squares are sensors attached to the sample. The red arrows represent the direction of the stress applied with a magnitude of 960 psi. The two circles in the center of the plot represent the counter borehole and the borehole. The dotted lines represent the foliation planes. 134

Fig. 4.76 - Lateral view of sample P10 parallel to the fracture plane. The red triangle represents the location of the perforations in the tubing. 135

- Fig. 4.77 - Lateral view of sample P10 perpendicular to the fracture plane. The red triangle represents the location of the perforations in the tubing..... 135
- Fig. 4.78 - Plan view of sample P11 showing the spatial and temporal evolution of the hydraulic fracture. The green dots represent the early time events, while the orange and purple represent the intermediate and late time events, respectively. The cyan squares represent sensors attached to the sample. The red arrows represent the direction of the stress applied with a magnitude of 950 psi. The two circles in the center of the plot represent the counter borehole and the borehole. The dotted lines represent the foliation planes. 136
- Fig. 4.79 - Lateral view of sample P11 perpendicular to the fracture plane. The red triangle represents the location of the perforations in the tubing..... 137
- Fig. 4.80 - Lateral view of sample P11 parallel to the fracture plane. The red triangle represents the location of the perforations in the tubing. 137
- Fig. 4.81 - Surface view of sample P11 showing a fracture enclosed by the red lines in the direction of the stress applied..... 138
- Fig. 4.82 - Plan view of sample P12 showing the spatial and temporal evolution of the hydraulic fracture. The green dots represent the early

time events, while the orange and purple represent the intermediate and late time events, respectively. The cyan squares represent sensors attached to the sample. The red arrows represent the direction of the stress applied with a magnitude of 1020 psi. The two circles in the center of the plot represent the counter borehole and the borehole. The dotted lines represent the foliation planes. 139

Fig. 4.83 - Lateral view of sample P12 parallel to the fracture plane. The red triangle represents the location of the perforations in the tubing. 140

Fig. 4.84 - Lateral view of sample P12 perpendicular to the fracture plane. The red triangle represents the location of the perforations in the tubing. 140

Fig. 4.85 - Surface view of sample P12 showing a fracture (enclosed by red lines) that is not completely aligned with the direction of stress applied (red arrows). The fracture deviates 10° to the East. 141

Fig. 4.86 - Plan view of sample P16 showing the spatial and temporal evolution of the hydraulic fracture. The green dots represent the early time events, while the orange and purple represent the intermediate and late time events, respectively. The cyan squares represent sensors attached to the sample. The red arrows represent the direction of the stress applied with a magnitude of 520 psi. The two

circles in the center of the plot represent the counter borehole and the borehole. The dotted lines represent the foliation planes. 142

Fig. 4.87 - Lateral view of sample P16 parallel to direction of the stress applied. The red triangle represents the location of the perforations in the tubing..... 143

Fig. 4.88 - Lateral view of sample P16 perpendicular to direction of the stress applied. The red triangle represents the location of the perforations in the tubing. 143

Fig. 4.89 - Surface view of sample P16 showing a fracture (enclosed by red lines) that deviates 55° to the west from the direction of stress applied (red arrows). The induced fracture seems to be more oriented towards the direction of the foliation. 145

Fig. 4.90 – Plan and lateral views of pyrophyllite samples showing location of MS events using Berryman’s equations for strong anisotropy (Berryman, 2008) (green dots) and a constant velocity model (black triangles). Hypocenters located using a constant velocity model form a cluster around the borehole in most cases. 148

Fig. 4.91 - Plan view of sample C15 showing the different spatial distribution between MS events located using information recorded by the surface sensors (green dots) and the MS events located neglecting the information recorded by the surface sensors (orange

open circles). The red arrows represent the orientation of the stress applied with a magnitude of 1000 psi..... 150

Fig. 4.92 - Lateral view of sample C15 perpendicular to the fracture plane showing the different spatial distribution between MS events located using information recorded by the surface sensors (green dots) and the MS events located neglecting the information recorded by the surface sensors (orange open circles). The purple lines represent the displacement in the Z-axis of each event located ignoring the information recorded by the surface sensors compared to the location of the same event when all sensors are used. The red triangle represents the perforation point in the tubing. Note some events are located outside the sample when surface sensors are not taken into account. 151

Fig. 4.93 - Lateral view of sample C15 parallel to the fracture plane showing the different spatial distribution between MS events located using information recorded by the surface sensors (green dots) and the MS events located neglecting the information recorded by the surface sensors (orange open circles). The red triangle represents the perforation point in the tubing. 152

Fig. 4.94 - Plan view of sample S4 showing the different spatial distribution between MS events located using information recorded by the surface

sensors (green dots) and the MS events located neglecting the information recorded by the surface sensors (orange open circles).

The red arrows represent the orientation of the applied stress with a magnitude of 1040 psi. 155

Fig. 4.95 - Lateral view of sample S4 perpendicular to the fracture plane showing the different spatial distribution between MS events located using information recorded by the surface sensors (green dots) and the MS events located neglecting the information recorded by the surface sensors (orange dots). The red triangle represents the perforation point in the tubing. 156

Fig. 4.96 - Lateral view of sample S4 parallel to the fracture plane showing the different spatial distribution between MS events located using information recorded by the surface sensors (green dots) and the MS events located neglecting the information recorded by the surface sensors (orange dots). The red triangle represents the perforation point in the tubing. 156

Fig. 4.97 - Plan view of sample P11 showing the different spatial distribution between MS events located using information recorded by the surface sensors (green dots) and the MS events located neglecting the information recorded by the surface sensors (orange dots) . The red arrows represent the orientation of the stress applied

with a magnitude of 950 psi. The dashed lines represent the bedding planes. 161

Fig. 4.98 - Lateral view of sample P11 perpendicular to the direction of stress applied showing the different spatial distribution between MS events located using information recorded by the surface sensors (green dots) and the MS events located neglecting the information recorded by the surface sensors (orange dots). The red triangle represents the perforation point in the tubing. 162

Fig. 4.99 - Lateral view of sample P11 parallel to the direction of stress applied showing the different spatial distribution between MS events located using information recorded by the surface sensors (green dots) and the MS events located neglecting the information recorded by the surface sensors (orange dots). The red triangle represents the perforation point in the tubing. 162

Fig. 4.100 – Two plugs are taken out from the sample along the direction of the fracture after it is fractured. The red and blue cylinders are the 1” diameter by 2” long plugs and the red line represents the fracture on the upper surface of the sample. 168

Fig. 4.101 – The right plug (Fig. 4.99) is cut into 10 slices where slice 1 is the farthest from the injection source whereas slice 10 is the closes to the perforation point. Each slice is 2 mm width and 50 mm long. The

figure in the far right shows the eight pictures that were taken along the fracture in slice 2..... 168

Fig. 4.102 – Fracture morphology observation of slice 1 of sample C16 (Indiana limestone). Pictures were taken starting at the top of the slice moving downwards (From a to h). The induced fracture is observed in the different pictures showing that it is not a planar feature. Bifurcation is observed in some cases (b, c and f). 170

Fig. 4.103 – Fracture morphology observation of slice 1 and 10 of sample S4 (Lyons sandstone). Pictures were taken starting at the top of the slices moving downwards (From a to e). Slice 1 is farthest from the injection source than slice 10. It is clear that the fracture observed in the slice closer to the injection point (slice 10) is wider than the fracture in slice 1..... 173

Fig. 4.104 – The left plug (Fig. 4.99) is cut into 7 discs where disc 1 is at the top of the plug whereas disc 7 is at the bottom. Each disc has a height of 5 mm and a diameter of 25 mm. 175

Fig. 4.105 – Fracture morphology observation of disc 4 of sample P18 (pyrophyllite). Pictures of the fracture were taken starting at the closest point from the injection point of the disc moving outwards (From a to e). The figures on the right are magnified images. 177

- Fig. 4.106 – Fracture morphology observation of disc 4 of sample P18 (pyrophyllite) at higher magnification than Fig. 4.104. Evidence of shear failure and zigzagging is observed. Small widths of the induced fracture are observed (600 nm- 3 μ m). 179
- Fig. 4.107 - r-t plots for each Lyons sandstone showing the radial distance of each MS event to the perforation point as a function of time since the start of the injection. The blue diamonds represent the MS events and the red line is the triggering front of microseismicity which is defined by the diffusivity, D. 180
- Fig. 4.108 - Plan view of Lyons sandstone samples showing the distribution of the microseismic clouds which are enclosed by green ellipses. The aspect ratio of the microseismicity cloud is determined by the dimension of each ellipse (short axis to long axis) 183
- Fig. 4.109 - r-t plots for each pyrophyllite sample showing the radial distance of each MS event to the perforation point as a function of time since the start of the injection. The blue diamonds represent the MS events and the red line is the triggering front of microseismicity which is defined by the diffusivity, D 186
- Fig. 4.110 - Plan view of pyrophyllite samples showing the distribution of the microseismic clouds which are enclosed by green ellipses. The

aspect ratio of the microseismicity cloud is determined by the
dimension of each ellipse (short axis to long axis)..... 187

ABSTRACT

Microseismic monitoring of hydraulic fractures is done to yield spatial and temporal plots of hypocenters. There are rendered without any estimates of uncertainty leading the engineer to believe the hypocenter locations are absolute. The hypocenter location problem becomes more complex in anisotropic shale reservoirs. Hypocenter locations are determined from the arrival times of P-wave and/ S-waves and a known velocity model. The difference in the velocity structure and complex fracture networks make accurate fracture mapping difficult. I report on a series of laboratory microseismic studies during controlled hydraulic fracturing of limestone, sandstone and a strongly foliated metamorphic rock, pyrophyllite. Uncertainties in each spatial coordinate and rms error for each sample are presented. The importance of surface sensors in reducing the uncertainty of the microseismic event locations is demonstrated however, reduced uncertainty does not show any considerable effect on the interpreted stimulated reservoir volumes. Fracture alignment is controlled as predicted by applied stresses in isotropic materials. However, when applied horizontal stress is low there is little to no control on the fracture orientation. The stimulated reservoir volume (SRV) appears to decrease with high applied horizontal stress. Hydraulic fracture propagation in anisotropic materials is altered by the magnitude of anisotropy but is

predictable when the anisotropic elastic constants are included in calculations. Microscopic observations show that fractures are not planar features as assumed by most models, instead they deviate, are discontinuous and bifurcate. These observations also show the existence of both shear and tensile failure. Permeability can be predicted from the distribution of microseismic events. Reasonable values are determined for low permeability rocks.

1. INTRODUCTION

United States energy consumption by year in 2009 was dominated by oil with a 37%, followed by natural gas with a 25% share (Fig. 1.1). This shows the important role that natural gas plays in the country's energy future.

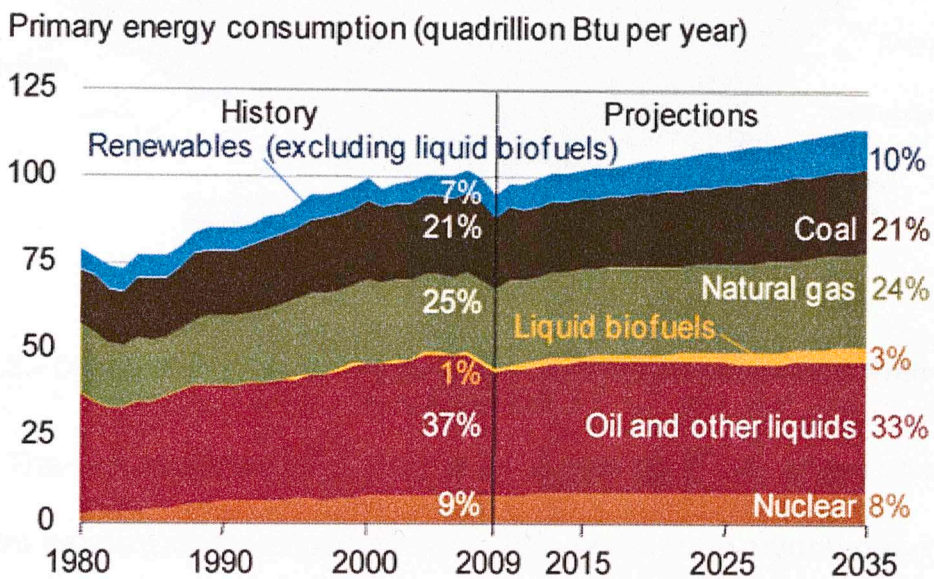


Fig. 1.1 – U.S. energy consumption by fuel showing the importance of natural gas in the energy window. Natural gas share was 25% in 2009 and it is expected to be 24% in 2035 (EIA Annual Energy Outlook 2011)

The United States possesses 2552 trillion cubic feet (Tcf) of potential natural gas resources, and out of that amount, natural gas from shale resources accounts for 827 Tcf (32.4%) (EIA Annual Energy Outlook 2011). Those resources are spread around the country in different basins (Fig. 1.2).

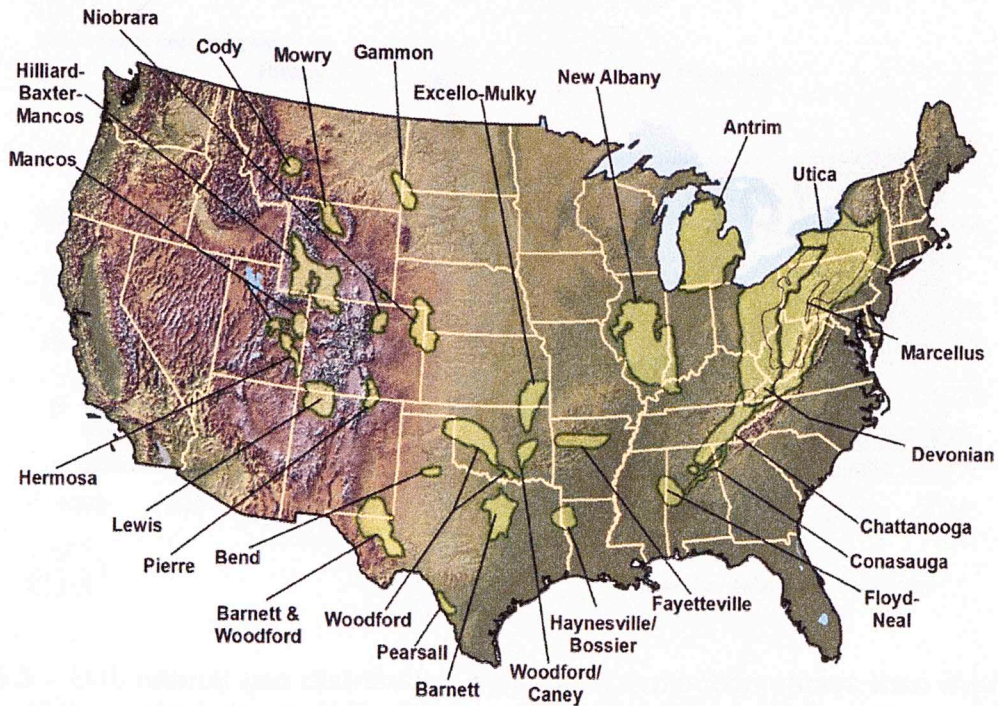


Fig. 1.2 – Distribution of shale basins in United States (Ground Water Protection Council, 2009).

The U.S. natural gas supply in 2009 was 23.7 Tcf, where shale gas and tight sands gas made up 14% and 28% of the total natural gas supply, respectively. It is expected that shale gas to constitute 45% of U.S. total natural gas supply by 2035 while tight gas sands will account for 22% (Fig. 1.3).

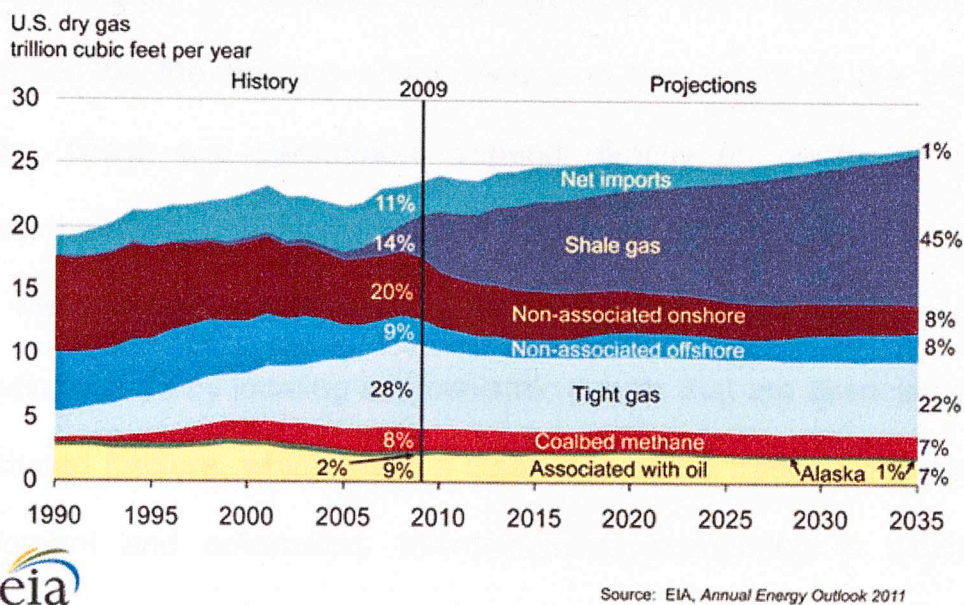


Fig. 1.3 – U.S. natural gas distribution by source. Projection shows that over two thirds of the natural gas in U.S. will come from exploitation of shale gas and tight gas (EIA Annual Energy Outlook 2011). Note the growth in shale gas by 2035.

Projection from Fig. 1.3 shows that shale gas and tight gas will account for more than two thirds of U.S. natural gas. However, shale gas and tight gas are found in formations which have very low permeability, thus the exploitation of this resource is not economically feasible unless some sort of procedure is applied to enhance the natural permeability of the rock. Here is where hydraulic fracturing comes into play; hydraulic fracturing is the process of inducing cracks in the rocks with the objective of creating more conductive paths between the reservoir and the wellbore. Since the first hydraulic fracturing treatment in 1947 this technique has been extensively used to overcome damage and increase production in conventional and unconventional reservoirs.

Evaluation of success of a hydraulic fracturing treatment is determined by the fracture conductivity and the extent of the induced fracture. These two parameters depend directly on geometry of the fracture; therefore, estimating its dimensions is of great importance.

Microseismic monitoring is a technique that allows mapping of the hydraulic fracture by locating microseismic events that are associated with the induced fracture, which gives a clear idea of the fracture dimensions, containment and orientation. Microseismicity monitoring is similar to earthquake location; waveforms emitted during the process are recorded by sensors that are located downhole in an observation well or on the surface. Arrival times are picked from those recorded waveforms, and, along with a correct velocity model, microseismic event hypocenters are calculated. Most engineers and geophysicist do not report on uncertainties in hypocenter location, thus a true estimation of fracture dimensions is not achieved.

This thesis contains a study of a set of laboratory scale hydraulic fracturing experiments performed in different lithologies: Indiana limestone, Lyons sandstone and pyrophyllite. Circumferential Velocity Analysis (CVA) studies were performed on every sample to determine the appropriate velocity model; it was found that Indiana limestone and Lyons sandstone samples have an azimuthal velocity variation less than 4%,

hence they were treated as isotropic, whereas, pyrophyllite presents a velocity anisotropy of 25%, enough to be treated as anisotropic.

14 piezoelectric sensors were attached around the sample to get good azimuthal coverage and a pair of sensors was placed on the upper surface of the sample for better constrain of hypocenter depths. Different horizontal stresses, varying from 150 to 1000 psi, were applied to the samples to control the fracture direction. The injection fluid used during the experiments was oil with a viscosity of 50 cp, while the pumping rates used were 5 cc/min (pyrophyllite), 10 cc/min (Lyons sandstone) and 15 cc/min (Indiana limestone). Arrival times were automatically picked from the recorded waveforms and were used with appropriate velocity models for hypocenter locations. A calibration technique (Hsu and Brekenridge, 1981) showed that the lowest average absolute error is ± 3.03 mm in Indiana limestone, ± 3.60 mm in Lyons sandstone and ± 5.23 mm in pyrophyllite. The average root mean square (rms) error in the location of acoustic emissions is 0.54 mm for Indiana limestone samples, 1.69 mm for Lyons sandstone samples and 0.91 for pyrophyllite samples. Locations of microseismic events agree with visual observation of the hydraulic fracture. The importance of the surface sensors was also examined; microseismic event hypocenters were calculated with and without information recorded by sensors attached to the upper surface of the

samples. It was found that when surface sensors were not used the average rms error increased 43% for Indiana limestone samples, 56% for Lyons sandstone samples and 35% for pyrophyllite.

This study is divided into four parts. Chapter 2 includes a review of hydraulic fracturing, explains the development of microseismicity over the years and its importance as a hydraulic fracturing monitoring technique. Also, it includes the theory of velocity anisotropy and the distributions of stress around the wellbore wall in a transversely isotropic formation. Finally, it explains two different techniques to estimate in-situ formation permeability from microseismic data. Chapter 3 includes a description of the problem and the approach used during this project. Chapter 4 contains the results obtained and Chapter 5 includes a summary and conclusions.

2. LITERATURE REVIEW

2.1 Hydraulic fracturing overview

Hydraulic fracturing is the process of inducing a highly conductive path from the reservoir to the wellbore, thus increasing the productivity of the wells (Heydarabadi et al., 2010). Also, hydraulic fracturing was established as a technique for bypassing damage in moderate but high- permeability reservoirs (Parker et al., 1994). Hydraulic fracturing consists of blending special chemicals to make the appropriate fracturing fluid and then pumping the blended fluid into the pay zone at high enough rates and pressures to wedge and extend a fracture hydraulically. First, a neat fluid, called a “pad” is pumped to initiate the fracture and to establish propagation. This is followed by a slurry of fluid mixed with a propping agent which continues to extend the fracture and carry the proppant deeply into the fracture. After the materials are pumped, the fluid chemically “breaks back” to a lower viscosity and flows back out of the well, leaving a highly conductive propped fracture for oil and/or gas to flow easily from the extremities of the formation into the well (Gidley et al., 1989).

2.1.1 History and development of HF

The first commercial hydraulic fracturing treatment aimed to enhance production was conducted in the Hugoton Gas Field in 1947 on Kelper Well 1. As a fracturing fluid a gasoline-based napalm-gel was used. However, these unpropped treatments did not increase production leading to the belief that hydraulic fracturing did not represent any improvement in well performance (Gidley et al., 1989).

In 1949, 11 out of 23 wells where hydraulic fracturing treatments had been applied reported significant increase in productivity in fields located in Wyoming, Colorado, Oklahoma and Texas (Clark, 1949).

In 1952, the use of refined and crude oils as fracturing fluid gained popularity due the lower cost; the lower cost permitted greater volumes per job. Nevertheless, a gradual change began in 1953 when aqueous-base fluids began being used, and by the end of 1963 up to 60 per cent of the fracturing jobs used this type of fluid (Hassebroek and Waters, 1964).

In 1953, hydraulic fracturing treatments started in the Caddo-Pine Island field, located in Caddo Parish, Louisiana, and Marion County, Texas. The first treatment used 8,000 lb of sand and 450 to 650 barrels of oil. The injection rate varied from 5 to 6 bbl/min at an average pump pressure of 2500 psig. The average cost of a hydraulic fracturing treatment ranged from \$2,500 to \$3,500 per well. Wells that were

hydraulically fractured showed better performance than those where acid treatments were performed (Paterson, 1957).

In 1957, mathematical relations between fracturing efficiency, injection rate, pumping time and fracture width were developed to predict fracture extent. This explained why some fluids were more efficient than others and why some pumping rates yielded better results. From this time forward, fracturing treatments changed from an experimental basis to technically based perspective (Hassenbroek and Waters, 1964).

In the 1970's new hydraulic massive fracturing (MHF) treatments employing great volumes of water began to be used. In these treatments up to 1 million gallons of water and 3 million pounds of proppant were used. At the time, MHF was the only method to economically develop tight reservoirs (Veatch, 1983).

The first commercial vertical Barnett Shale well was the C.W. Slay No. 1 drilled and stimulated in 1981 by Mitchell Energy. The first fracturing attempts consisted of titanium and zirconium based crosslinkers with hydroxypropyl guar (HPG) and carboxymethyl hydroxypropyl guar (CMHPG). Usually, those treatments employed about 600,000 gallons of crosslinked fluid and over 1 million pounds of 20/40 mesh northern white sand (Matthews et al., 2007).

As of 1983 more than 800,000 hydraulic fracturing treatments had been performed and about 35-40% of all wells drilled at that time were fractured hydraulically. Treatments varied greatly; from 650-750 gallons of fracturing fluid to 1 million of gallons and up to 3 million pounds of propping agent. 25-30% of the total U.S. oil reserves at that time had been economically producible by application of this technique (Veatch, 1983).

Hydraulic fracturing was well known as a technique to improve productivity in low-permeability reservoirs and overcome damage in moderate- and high-permeability reservoirs. Hydraulic fracturing provides improved fines control in unconsolidated formations; the pressure drop due to production will be distributed over the surface area of the created surface instead of the surface area of the wellbore or gravel pack radius. This distribution of pressure leads to a decrease in flow rate per unit area which reduces flow velocity. A reduction in flow velocity minimizes formation fines movement (Parker et al., 1994).

In 1995, Union Pacific Resources (UPR) performed the first "waterfrac" in the Cotton Valley formation. A waterfrac is achieved by pumping large volumes of water with a small amount of chemicals such as surfactants and friction reducers. Usually 20/40 Ottawa sand is mixed at 0.5 ppg. Preliminary results showed a similar production to that obtained by previous fracturing techniques for 30-70% less fracturing costs. In

1997, using this technique represented about \$4.5 million in savings (Walker et al., 1998).

After successful use of waterfracs in the Cotton Valley formation Mitchel Energy began experimenting in 1997 with waterfracs in the Barnett Shale. It was thought that same success would be obtained using this type of treatment and subsequently different versions of the treatment were used until a working design was reached. A current average fracturing job in the Barnett shale consists of 750,000 gallons of slickwater and 80,000 pounds of proppant pumped at 60 bpm with proppants concentrations from 0.1 to 0.5 ppg (Fisher et al., 2002).

2.1.2 Current status of hydraulic fracturing technology

Hydraulic fracturing was first established as a technique to overcome damage and increase production in conventional and tight gas reservoirs. However, development of unconventional reservoirs has pushed hydraulic fracturing to new technology limits.

The potential benefits of refracturing have caught the attention of oil and gas operators for more than 50 years. If an original treatment is inadequate or the existing proppant deteriorates over the time, refracturing the well reestablishes linear flow into the wellbore (Dozier et al., 2003). Wells with effective initial treatment can be re-stimulated by

creating a new fracture that propagates along a different azimuth than the original fracture which exposes more net pay to the wellbore (Dozier et al., 2003).

The accelerated development of shale gas reservoirs is being fueled by continued improvements in completion and stimulation technologies for horizontal wells. Horizontal wells are playing an important role in the production economics in unconventional gas reservoirs (Cipolla et al., 2009). The key to a successful development of an unconventional gas reservoir is to create complex fracture networks that contact a large reservoir volume (Mayerhofer et al., 2006). However the nature and degree of the fracture complexity must be understood in order to select the best stimulation strategy (Cipolla et al., 2010).

Enhanced hydraulic fracturing techniques attempt to make the stimulation process more effective. One of those is hydraulic fracturing using carbon dioxide (CO₂). Verdon et al. (2010) studied a hydraulic fracturing field case where water and supercritical CO₂ were injected at similar conditions. Microseismicity was used to monitor performance differences. The microseismic event locations show similar patterns in both cases, but in the case of water injection the fracture appeared to extend further laterally. When CO₂ was injected microseismic events were located far above the injection point suggesting that its greater buoyancy

enabled CO₂ to migrate vertically. The magnitude of the events induced in both cases is similar. They concluded that despite the difference in compressibility, density and viscosity, both fluids have similar patterns of induced seismicity.

2.2 Microseismicity

Microseismic theory is analogous to that used in earthquakes; when fluid is injected into the formation causing changes in pore pressure, those changes affect the stability of planes of weakness, such as natural fractures and bedding planes. Shear slippages are produced in planes of weakness leading to failure and events known as microseisms. Microseisms produce elastic waves of high frequencies compared to those emitted by earthquakes. The difference between earthquakes and microseisms is the size of the source; microseisms in field applications have moment magnitudes, which are a measure of the strength of the source, from -3.5 to -2.5 whereas earthquakes usually need to have a Moment Magnitude of +3 to be felt at the surface (Warpinski, 2009). These are received by an array of sensors located either on surface or downhole in an observation well (Warpinski, 1998). Microseismicity has special characteristics that differentiate it from other seismic techniques such as

sonic logs, cross-well seismic and VSP (See **Table 2.1**). The frequency range for microseismic events is 100-3000 Hz (Warpinski, 1998).

Table 2.1 – Frequency ranges for different seismic techniques

Technique	Frequency, Hz
Sonic logs	50-20000
Cross-well seismic	80-2000
VSP	10-150

Analysis is performed to locate each microseism and map the hydraulic fracture, its geometry and orientation. There are two approaches to analyze the recorded data: the first uses the information of the arrival times of the s- and p-wave at different receivers located in different observation wells along with the formation velocities. The location of the microseisms is then triangulated until the calculated location matches the observed arrival times. However, availability of multiple observation wells is difficult unless a complete field study is undertaken. The second approach consists of using a single observation well with a multilevel array of receivers. Nevertheless, this technique requires higher-level technology receivers since more information is required; besides the arrival times from the s- and p- waves, the particle motion of the p-wave is required to estimate the azimuth of the microseism with respect to the position of the receiver (Warpinski, 1998).

2.2.1 Microseismicity development

Microseismicity has its origins in the 1930's when L. Obert and W.I. Duval discovered that a stressed rock pillar emitted microlevel sounds at deep hard rock mine (Obert, 1975). From this point several authors have performed laboratory and field experiments to develop this technique; Obert and Duvall (1942, 1945-a, 1945-b) performed several experiments at laboratory and field scale where they showed that different types of rock under compressive load generate acoustic emissions. Acoustic emission (AE) rate increased as the load was increased. Kaiser reported in 1950 results of laboratory experiments on metals where he noticed the effect of sample stress history on the production of acoustic emissions (Holcomb, 1993). Goodman (1963) also observed the relationship of stress state and acoustic emission rate during cyclic loading experiments that were performed on sandstone and quartz diorite samples. Other authors (Barron (1969, 1970); Mogi (1962); Suzuki et al. (1964); Mae and Nakao (1968); Scholz (1968a, 1968b)) performed experiments under uniaxial and triaxial compressive stresses and found that the acoustic emission rate increases significantly as the compressive failure stress is reached.

During the 1970's, acoustic emission studies were underway on several geotechnical related areas. Some of those investigations were carried out by Barron (1970), where he used a device to detect

microseismic activity in specimens under triaxial load conditions; Anon. (1978), who reported the use of acoustic emissions during the hydrofracturing of a geothermal energy project; Haimson and Kim (1977) and Khair (1977) performed cycling uniaxial and triaxial compressive experiments where AE were used to study fatigue mechanisms; Byerlee and Lockner (1977b) carried out hydraulic fracturing experiments where AE (acoustic emissions) were used to map the fracture; Lockner and Byerlee (1977a) also used AE to map fractures created during deformation of rocks under confining stress. During the 1980's and 1990's several authors also performed laboratory experiments at laboratory scale where different materials were hydraulically fractured and AE were used to map the created fracture and study the fracture mechanisms (Majer and Doe (1986); Matsunaga et al. (1993); van Dam et al. (1998); Groenenboom et al. (1999); Kranz et al. (1990)). At field scale, AE have been used during hydraulic fracturing experiments to estimate fracture geometry (Vinegar et al. (1992); Albright and Pearson (1982); Rutledge and Phillips (2001); Warpinski et al. (1997)), to calculate source parameters of the microseismic events which are related to event strength, stress release and slip dimension (Wyss and Brune (1968); Urbancic and Maxwell (2002); Talebi and Boone (1998)), and to identify the failure mechanisms in the process (Walter and Brune (1993);

Sondergeld and Estey (1982); Lockner (1993)). Also, microseismic data has been used recently to estimate formation permeability as reported by Shapiro et al. (2006), Dinske et al. (2010) and Grechka et al. (2010).

2.2.2 Microseismicity tools

Transducers used in microseismic applications are devices consisting on a coil around a mass hanging on a spring surrounding fixed magnets (See **Fig. 2.1**). When the case (housing) moves the coil moves respect to the fixed magnet. Then the relative velocity is transformed into an electromagnetic field. This magnetic field produces an electrical voltage that can be measured.

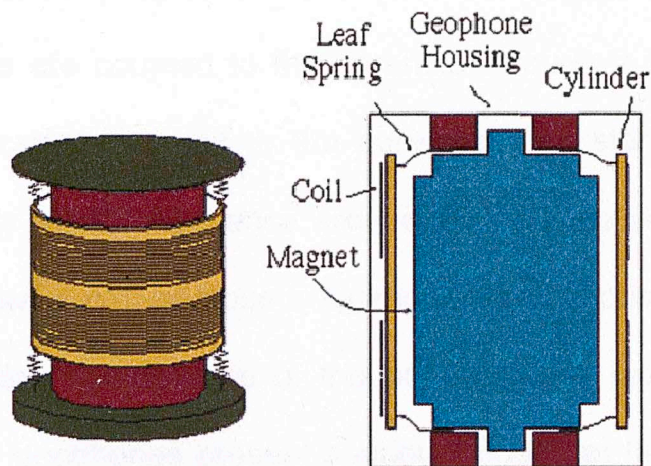


Fig. 2.4 - Schematics of a geophone (Barzilai et al. 1998)

Three-component receivers, where each axis is perpendicular to the other two, are employed to record the polarization information from the

p- and s-waves. Before actual recording is carried out calibration of the receivers is performed in order to know the orientation and polarity response of the transducers; calibration is performed by creating a source at a known location (perforation shot). Usually two of the axes are set in horizontal position while the third is aligned with the vertical direction. Orientation of the receiver is achieved by using the location of the “artificial” source and the signals recorded by the two horizontal channels and the corresponding hodogram, which is a plot of the polarization of the signal (Sleefe et al., 1995).

For microseismic applications accelerometers are a better choice than geophones due the various limitations of the latter; geophones can offer inadequate coupling to the borehole over a wide frequency band. The geophones are coupled to the borehole through a locking arm that extends and clamps the unit to the borehole. The standard swing-arm clamp generally has a resonance around 200-400 Hz (Warpinski et al., 1998) which means that at those frequencies the motions of the clamping unit do not follow the motions of the borehole wall leading to a weak coupling. Also, geophones present spurious modes at frequencies about 25 times higher than the natural frequency of the geophone. This is caused when the spring reaches a resonant frequency in the direction perpendicular to the axis of the geophone (Faber and Maxwell, 1996)

which leads again to a poor coupling of the instrument. Accelerometers, on the other hand, are designed to have resonances above 2000 Hz, they do not present spurious resonances. Accelerometers are more sensitive than geophones at higher seismic frequencies due to their lower electric noise (Sleefe et al., 1995).

Another important characteristic in picking the right tool is the noise specification; the signal-to-noise ratio (SNR) should be as large as possible in order to pick up weaker signals. Since the strength of the event cannot be modified, the noise must be minimized to reach an acceptable SNR. According to Warpinski et al. (1998) there are two types of noise: cultural and electrical. Cultural noise, such as that caused by gas bubbling through perforations from a zone below the receivers, the truck and pumping activity, is difficult to minimize but remedial action can be performed to mitigate it. Electrical noises, in the other hand, are due the transducers, electronic components, noise in the supply power, and pickup over unshielded components and wires (Warpinski et al., 1998).

The electrical-noise floor of the accelerometers is superior to geophones at frequencies encountered in microseismic applications. This means that electrical noise of accelerometers is much lower than that of the geophones at high frequencies (above 1000 Hz) allowing

accelerometers to detect weak signals even at those frequencies (Sleefe et al., 1995).

2.3 Hydraulic fracturing experiments at laboratory scale

Several authors over the years have carried out hydraulic fracturing experiments at laboratory scale. Haimson and Fairhurst (1969) used hydrostone samples loaded polyaxially to simulate the three tectonic stresses encountered in the subsurface. They observed the type of fracture, its inclination and orientation and correlated those to the stress of state in each sample. They also recorded pressures at which the fracture initiated at different pressurization rates and different borehole sizes and compared those values to values obtained from theoretical criteria.

Solberg et al. (1977) performed hydraulic fracture experiments on triaxially stressed samples of oil shale and Westerly Granite. They found that samples with differential stress greater than 29000 psi failed by shear where as samples with differential stress lower than 29000 psi failed in tension.

Lockner and Byerlee (1977a) conducted several hydraulic fracturing experiments in Weber sandstone samples where they used acoustic emissions to locate the microseismic events. The samples were subjected to different differential stresses and fluid injection rates. They

show how failure mode is related to differential stress and fluid injection rate.

Zoback et al. (1977) investigated the effect of fluid injection on breakdown pressure and the effect of pre-existing fractures on the orientation of the resultant fractures. The experiments were carried out using Ruhr sandstone, Weber sandstone and South African gabbro. They proved the dependence of breakdown pressure upon fluid injection rate, whereas the pressure at which hydraulic fracture initiates is independent when the effect of fluid permeation is negligible.

Medlin and Masse (1979) used four different types of limestone quarry rocks (Carthage, Indiana, Lueders and Austin) in hydraulic fracturing experiments at laboratory scale with the purpose of estimate fracture initiation pressure and orientation. Both cylindrical and spherical cavities were tested. Fracture initiation pressure was estimated for each rock type using different injection fluids (non-penetrating grease and penetrating vacuum pump oil) at different conditions (hydrostatic stress and ambient) to observe the effect of each parameter. Results of fracture initiation pressure were compared to those predicted by poroelasticity theory. Fracture initiation pressures obtained from laboratory experiments are consistent with the poroelasticity theory over some range of hydrostatic stress which is variable depending on the rock properties.

Medlin and Masse (1984) used Mesaverde sandstone and Carthage and Lueders limestone in laboratory hydraulic fracturing experiments. They fractured the rock samples using different injection fluids, injection rates and confining stress state to measure different parameters, such as fracture width, fracture length and propagation pressure to evaluate crack propagation theories. Experiments yielded results that contradict equations proposed by Perkins and Kern (1961) and the theory derived from them by Nordgren (1972).

Majer and Doe (1986) hydraulically fractured 300*300*450 mm salt blocks triaxially loaded to investigate the effect of confining pressure on breakdown pressure and the time dependency of breakdown pressure. Also, they used acoustic emissions (AE) to locate the microseismic events and to study the behavior of the hydrofracture process.

Cheung and Haimson (1989) carried out laboratory hydraulic fracturing experiments on fractured Niagara dolomite under triaxial conditions. They studied the conditions that control whether new hydraulic fractures are induced or whether preexisting fractures are reopened when fluid is injected into the sample, and compared the results to values obtained theoretically. The results showed that creation of new fractures or the reopening of preexisting ones can be predicted in most cases,

especially when the penetration of the injection fluid into the rock is taken into account.

Haimson and Zhao (1991) performed several experiments attempting to address the effect of borehole size and injection rate on hydraulic fracturing breakdown pressure using granite and limestone samples. They found that borehole size and rate affect breakdown pressure at the laboratory scale, whereas those effects appear to be negligible at field scale.

Matsunaga et al. (1993) conducted laboratory hydraulic fracturing experiments in acrylic resin blocks, Inada granite, Komatsu andesite and Akiyoshi marble samples using both water and oil as fracturing fluids. AE monitoring was employed to analyze the fracturing mechanism during the fracturing process and the effect of fluid used. From focal mechanism analysis, it was found that events in all three rock samples were caused by shear failure whereas fracture in the acrylic was caused by tensile failure.

Masuda et al. (1993) conducted laboratory experiments on Inada granite samples where they monitored the acoustic emissions generated when fluid was injected into the samples. They proposed two different experiments: one where the sample was dry and subjected to hydrostatic stress and the other where the sample was saturated and subjected to a

differential stress. In the first experiment no acoustic emissions were detected, whereas in the second experiment, as soon as the water pressure was increased for the first time, microfracturing was induced.

van Dam et al. (1998) performed hydraulic fracturing experiments on 30 mm (1 inch) cubic blocks of different materials. They used plaster, cement paste and diatomite. Each block was triaxially loaded to simulate in-situ stresses. Acoustic emissions were used to estimate the fracture radius and the size of the non-penetrated zone. They found that the variation of fracture radius after shut-in influences the leak-off volume.

Song et al. (2001) carried on hydraulic fracturing experiments on Tablerock sandstone. They attempted to establish whether this type of procedure (hydraulic fracturing) was useful to estimate in-situ stresses in highly permeable rocks. After testing several samples varying experimental parameters they found a relationship between breakdown pressure and far-field stress.

Song and Haimson (2001) investigated the effect of pressurization rate and pore pressure on the breakdown pressure using Tablerock sandstone, and from those experiments tried to establish a correlation between breakdown pressure and the far-field stresses. Results yielded, for the case of variable pressurization rate, good agreement between experimental results and theoretical prediction of breakdown pressure

(Detournay and Cheng, 1992). However, for the case when the pore pressure was varied from test to test, the same theoretical approach needed some modification.

Lhomme et al. (2002) conducted hydraulic fracturing experiments at laboratory scale on Colton sandstone samples. Different fluid viscosities and injections rates were used to study the fracture propagation and fracture response. They found that the initiation pressure and breakdown pressure do not depend on rate of pressurization or fluid viscosity which does not agree with previous studies. However, when they used high viscosity fluid and low injection rates they observed a monotonic pressure decrease after breakdown, whereas when low viscosity fluid was used injected at high rates several fluid pressure rises were observed after the first pressure maximum.

de Pater and Dong (2007) performed different laboratory experiments to analyze the effect of confining stress and fluid rheology on hydraulic fracturing treatments using loose sand samples. The injection fluids used in the experiments were a highly viscous Newtonian fluid (500 Poise), Bentonite slurry, a cross-linked gel and the same cross-linked gel with fine quartz particles. Also, different confining stresses, ranging from 29 to 29000 psi, were applied. Only when cross-linked gel with quartz

particles was used as injection fluid was a hydraulic fracture developed at any confining stress applied and any pumping rate.

Surdi et al. (2010) carried out hydraulic fracturing experiments on two identical quartz-rich, Carbon Tan sandstone, where the acoustic activity was monitored. To facilitate fracture initiate two diametrically opposite slits ¼-inch in length were cut. The authors also modeled the distribution of stress concentration in the sample during well pressurization and tried to correlate the stress concentration state during loading and fracturing with the localization of acoustic emissions in space and time.

It is clear that several authors have tried to better understand the hydraulic fracturing process through controlled experimental results. **Table 2.2** summarizes of experimental work on hydraulic fracturing over the years.

Table 2.2 - Summary of hydraulic fracturing laboratory experiments indicating the authors, sample, properties of the samples and variables tested

Author	Sample	Dimensions	Porosity, %	Permeability, md	Variables tested
Haimson and Fairhurst, 1969	Hydrostone	Cubes 5"*5"*5.5" Cylinders 5"*6"	24.9, 25.9, 27	8, 11, 17	Pressurization rate Borehole size
Solberg et al., 1977	Oil shale Westerly granite	Cylinders 1"*2.5"	NA	NA @ambient 3.5*10 ⁻⁵ @14500 psi	Differential stress
Lockner and Byerlee, 1977	Webber sandstone	Cylinders 7.5"*3" Cylinders 1"*2.5	5.5	- -	Differential stress Fluid injection rate

Zoback et al., 1977	Ruhr sandstone Webber sandstone South African gabbro	Cylinders 2.4"*1.2" Cubes 4.7"	-	0.1 - 1.0 -	Pressurization rate Load Porosity Permeability
Medlin and Masse, 1979	Carthage limestone Indiana limestone Lueders limestone Austin limestone	Cylinders 1"*5"	3 14 19 33	0.04 2 1 1.5	Injection fluid Stress conditions
Medlin and Masse, 1984	Mesaverde sandstone Carthage limestone Lueders limestone	Blocks 3"*4"*12"	8 3 19	0.04 1	Injection fluids Injection rate Confining stress
Majer and Doe, 1986	Salt	Blocks 11.8"*11.8"*17.7"	-	-	Confining pressure
Cheung and Haimson, 1989	Niagara dolomite	Blocks 4.9"*4.9"*6.7"	-	-	Orientation of preexisting fracs Stress state
Matsunaga et al., 1993.	Acrylic resin Inada granite Komatsu andesite Akiyoshi marble	Cubes 7.9"	-	-	Injection fluid
Matsuda et al., 1993	Inada granite	Cylinders 2"*4"	1	3×10^{-6}	Saturation Stress state
van Dam et al., 1998	Plaster Cement paste Diatomite Soft plaster	Cubes 11.8"	42 20 70 42	50 1×10^{-3} 0.2 50	Material
Song et al., 2001	Tablerock sandstone	Cylinder 4"*5.1"	26	120	Stress state
Song and Haimson, 2001	Tablerock sandstone	Cylinder 4"*5.1"	26	120	Pressurization rate Pore pressure
Lhomme et al., 2002	Colton sandstone	Cubes 11.8"	17	0.15	Injection fluid viscosity Injection rate
de Pater and Dong, 2007	Sand	Cylinders 16"*20" Cylinders 5.9"*8.7"	-	3000-5000 @72.5 psi	Confining stress Fluid rheology

2.4 Microseismic event location

Microseismic (MS) events generate acoustic waves that travel throughout the earth. The same phenomenon is observed in earthquakes, which makes seismology techniques applicable to microseismicity. The location of a microseismic event is referred to as an inverse problem where the data are the arrival times recorded by different sensors and the unknowns are the spatial coordinates (x, y, z) and the origin time, t_0 , of the MS event (Stein and Wyssession, 2003).

To explain how the inverse problem technique is used, let us assume a MS event with unknown position $x = (x, y, z)$ and unknown origin time t_0 . The arrival times, d_i , are recorded at n sensors whose locations are $s_i = (x_i, y_i, z_i)$. Those arrival times depend on the origin time and the travel time between the source and the sensor,

$$d_i = t_0 + t_i \quad (2.1)$$

Where t_i is the travel time which can be expressed as a function of the spatial coordinates of the source and the sensor,

$$t_i = \sqrt{\frac{(x_i-x)^2 + (y_i-y)^2 + (z_i-z)^2}{v}} \quad (2.2)$$

Where v is the “known” velocity. The simplest case is a constant velocity. The arrival time can be written as,

$$d_i = t_o + \sqrt{\frac{(x_i-x)^2+(y_i-y)^2+(z_i-z)^2}{v}} \quad (2.3)$$

The problem can be stated as data vector d which is the result of a function, A , acting on a vector m which describes the model parameters, or unknowns.

$$d = A(m) \quad (2.4)$$

Simply, the inverse problem can be seen as given observed arrival times, a model must be found that fits the observations. The process starts with an initial guess of the model (spatial coordinates and origin time), m^o . This initial guess allows calculating data, or arrival times, which we compare to the real observed data, m . Usually the starting model leads to erroneous results; therefore, changes in the starting model are necessary to reach a better solution.

$$m_j^1 = m_j^o + \Delta m_j \quad (2.5)$$

here Δm_j is the variation of the j th model parameter adjustment that produces a better fit of the observed data.

The data do not depend linearly on the model parameters; therefore, a linearization of the problem is necessary. This is obtained by expanding the data in a Taylor series about the starting model m^o and keeping only the linear term.

$$d_i \approx d_i^o + \sum_j \frac{\partial d_i}{\partial m_j} \Delta m_j \quad (2.6)$$

Where d_i^o is the vector containing the arrival times calculated using the initial guess of the model. If eqn. 2.6 is expressed in terms of the difference between the observed data (arrival times) and those predicted by the model,

$$\Delta d_i^o \approx \sum_j \frac{\partial d_i}{\partial m_j} \Delta m_j \quad (2.7)$$

The term $\frac{\partial d_i}{\partial m_j}$ is defined as the partial derivative matrix, G_{ij} ; therefore, the difference between the observed and calculated arrival time for a given model m is:

$$\Delta d_i \approx \sum_j G_{ij} \Delta m_j \quad (2.8)$$

The model vector has four unknowns: origin time and the three spatial coordinates; therefore, j ranges from 1 to 4. On the other hand, i varies from 1 to n , where n is the number of arrival times recorded by n sensors, which is usually greater than 4. Since the number of rows and the number of columns in G are not equal, the matrix is not square, so it cannot be inverted. To overcome this problem eqn. 2.8 has to be multiplied by G^T , or the transposed of the partial derivative matrix, leading to,

$$G^T \Delta d = G^T G \Delta m \quad (2.9)$$

And solving for the change in the model, m :

$$\Delta m = (G^T G)^{-1} G^T \Delta d \quad (2.10)$$

This is the least square solution for the change in the model that is required so the spatial coordinates and the origin time approach the observed data. We start with an initial model m^o , which is made up by an initial guess of the spatial coordinates and the origin time. The newly predicted arrival times are calculated and compared to the observed ones. The total squared misfit is then calculated as,

$$\sum (\Delta d_i^o)^2 = \sum (d_i - d_i^o)^2 \quad (2.11)$$

The first model usually does not give a good fit to the observed data; therefore, a change of the initial model needs to be found to improve the solution. The partial derivative matrix around the starting model is estimated,

$$G_{ij} = \left. \frac{\partial d_i}{\partial m_j} \right|_{m^o} \quad (2.12)$$

Once the partial derivative matrix is calculated the change in the model Δm^o and a new model can be estimated to repeat the process.

$$m^1 = m^o + \Delta m^o \quad (2.13)$$

The process is repeated until the total squared misfit is acceptably small.

Some signals have low signal-to-noise ratio due to the noisy environment. This brings the necessity of a solution where each sensor is given certain importance according to its quality. This solution is known as the *weighted least squares* and is expressed as,

$$\Delta m = (G^T W_d G)^{-1} G^T W_d \Delta d \quad (2.14)$$

Where W_d is the data weighting matrix and is obtained by inverting the variance-covariance matrix of the data, or vector d .

2.5 Considering anisotropy

Isotropic, linear elastic materials are completely characterized by two independent constants, usually Young's modulus and Poisson's ratio. Therefore, calculation of both P-wave and S-wave velocities becomes independent of the direction of wave propagation (Mavko et al., 2003). However, for anisotropic rocks, elastic characterization is not as simple as the isotropic case; up to 21 elastic constants are needed to describe the elastic behavior of anisotropic rocks. We often encounter two types of anisotropy: transverse isotropy and azimuthal anisotropy. The former has a hexagonal symmetry with five independent elastic constants, where the

symmetry axis is normally perpendicular to the bedding. The latter is caused by stress anisotropy. Azimuthally anisotropic rocks may have 5, 9 or 13 independent elastic constants, depending on stress orientation and the intrinsic properties of the rock (Wang, 2002).

Most crustal rocks are found experimentally to be transversely isotropic as a result of preferred orientation of anisotropic mineral grains, preferred orientation of the shapes of isotropic minerals, preferred orientation of cracks or thin bedding of isotropic or anisotropic layers (Thomsen, 1986). Ignoring the effect of anisotropy can lead to the drilling of dry holes (Margesson and Sondergeld, 1998) and also to large errors in the location of microseisms when microseismic mapping is performed (Warpinski et al., 2009; Isaac and Lawton, 1999; Vestrum et al., 1999).

Thomsen (1986) points out that in most cases of interest to geophysicists the anisotropy is weak (<10 percent). He suggests that a weak transverse isotropic formation can be characterized by three anisotropic parameters (ϵ , δ and γ) and two velocities (**Appendix A**). The equations of phase velocity variation as a function of the angle are given as,

$$V_p(\theta) = \alpha_0(1 + \delta \sin^2\theta \cos^2\theta + \epsilon \sin^4\theta) \quad (2.15)$$

$$V_{sv}(\theta) = \beta_0 \left(1 + \frac{\alpha_0^2}{\beta_0^2} (\epsilon - \delta) \sin^2\theta \cos^2\theta \right) \quad (2.16)$$

$$V_{sh}(\theta) = \beta_0(1 + \gamma \sin^2 \theta) \quad (2.17)$$

The phase angle, Θ , is the angle between the wavefront normal and the symmetry axis. α_0 and β_0 are the P-wave and S-wave velocities measured parallel to the symmetry axis, respectively.

The magnitude of anisotropy in shale is greater than that estimated by Thomsen (Sondergeld and Rai, 2011); Sondergeld and Rai (1992) measured anisotropies as high as 42% in shear velocity and Hornby et al. (1999) estimated P-wave anisotropy of 38%. Berryman (2008) proposed the following equations for strong anisotropy,

$$V_p(\theta) = \alpha_0 \left(1 + \varepsilon \sin^2 \theta - (\varepsilon - \delta) \frac{2 \sin^2 \theta_m \sin^2 \theta \cos^2 \theta}{1 - \cos 2\theta_m \cos 2\theta} \right) \quad (2.18)$$

$$V_{sv}(\theta) = \beta_0 \left(1 + \frac{V_p^2(0)}{V_s^2(0)} (\varepsilon - \delta) \frac{2 \sin^2 \theta_m \sin^2 \theta \cos^2 \theta}{1 - \cos 2\theta_m \cos 2\theta} \right) \quad (2.19)$$

where Θ_m is the incidence angle near which the extreme SV-wave behavior occurs (Berryman, 2008) and is given as:

$$\tan^2 \theta_m = \frac{C_{33} - C_{44}}{C_{11} - C_{44}} \quad (2.20)$$

When a borehole is drilled in a transversely isotropic formation the stresses around the wall of the borehole are not as simple as if the formation was isotropic. Aadnoy (1987) presented equations to calculate the hoop stress around the borehole wall when the well is drilled in a transversely isotropic formation (**Fig.2.2**). The hoop stress calculation is broken down into the components that contribute to the total hoop stress.

$$\sigma_{\theta\theta} = \sigma_{\theta\theta 1} + \sigma_{\theta\theta 2} + \sigma_{\theta\theta 3} \quad (2.21)$$

Where, $\sigma_{\theta\theta}$ is the total hoop stress at the borehole wall, $\sigma_{\theta\theta 1}$ is the contribution due the borehole pressure, $\sigma_{\theta\theta 2}$ is the contribution of normal stresses and $\sigma_{\theta\theta 3}$ is the shear stress contribution.

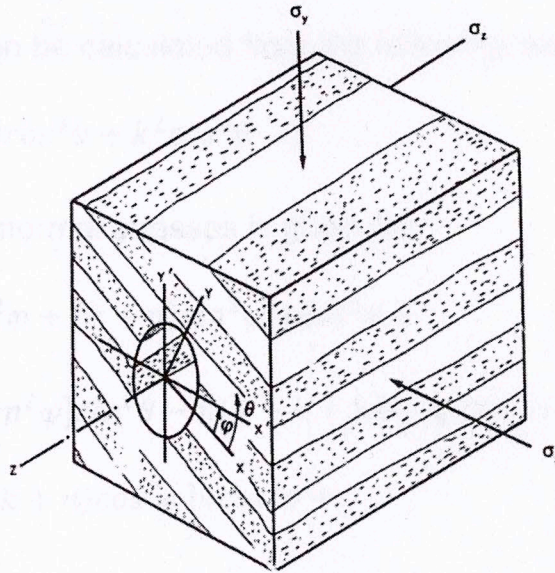


Fig. 2.2 – Geometry showing a borehole in a transversely isotropic medium where the X-axis is aligned with the direction of the bedding and the Y-axis is perpendicular to the bedding (Aadnoy, 1987). σ_x , σ_y , σ_z are the three principal stresses. σ_x and σ_y are aligned with the X'- and Y'-axis, respectively. θ is the angle from the X-axis and ϕ is the angle measured from the bedding orientation to the horizontal axis.

The contribution of the borehole pressure is given as:

$$\sigma_{\theta\theta 1} = P_w \frac{E_\theta}{E_x} [k - n(\sin^2\theta + k\cos^2\theta) + (1 - k^2)\sin^2\theta\cos^2\theta] \quad (2.22)$$

where P_w is the hydrostatic pressure in the borehole, θ is the angle from the X-axis (from the axis of isotropy), E_θ is Young's modulus in the direction tangent to a position at a given angle, θ , from the direction of the

bedding, E_x is the Young's modulus along the X-axis (parallel to bedding).

k , n are given as:

$$k = \left(\frac{E_x}{E_y}\right)^{\frac{1}{2}} \quad (2.23)$$

$$n^2 = 2 + 2k \quad (2.24)$$

The value E_θ / E_x can be calculated from the following expression:

$$\frac{E_x}{E_\theta} = \sin^4\theta + 2\sin^2\theta\cos^2\theta + k^2\cos^4\theta \quad (2.25)$$

The contribution of normal stresses is given as:

$$\begin{aligned} \sigma_{\theta\theta 2} = & \sigma_x \frac{E_\theta}{E_x} \{[-\cos^2\varphi + (k+n)\sin^2\varphi]k\cos^2\theta + \\ & [(1+n)\cos^2\varphi - k\sin^2\varphi]\sin^2\theta - n(1+k+n)\sin\varphi\cos\varphi\sin\theta\cos\theta\} \\ & + \sigma_y \frac{E_\theta}{E_x} \{[-\sin^2\varphi + (k+n)\cos^2\varphi]k\cos^2\theta + \\ & + \sigma_y \frac{E_\theta}{E_x} \{[-\sin^2\varphi + (k+n)\cos^2\varphi]k\cos^2\theta + \\ & [(1+n)\sin^2\varphi - k\cos^2\varphi]\sin^2\theta + n(1+k+n)\sin\varphi\cos\varphi\sin\theta\cos\theta\} \end{aligned} \quad (2.26)$$

σ_x and σ_y are the principal stresses in the horizontal and vertical axis, respectively.

The angle φ is the angle measured from the bedding orientation to the horizontal axis (**Fig. 2.2**).

The shear stress contribution is given by the expression below.

$$\sigma_{\theta\theta 3} = \tau_{xy} \frac{E_\theta}{2E_x} (1+k+n) \left\{ -n\cos 2\varphi + [(1+k)\cos 2\theta + k - 1] \frac{\sin 2\varphi}{\sin 2\theta} \right\} \quad (2.27)$$

Where,

$$\tau_{xy} = 0.5(\sigma_y - \sigma_x)\sin 2\theta \quad (2.28)$$

2.6 Formation permeability from microseismic data

The state of the art technology has allowed using microseismic data not only for mapping hydraulic fractures but also for the estimation of in-situ formation permeability. For this purposes two different techniques are utilized: the r-t method and the inversion approach (Grechka et al., 2010).

2.6.1 r-t technique for permeability estimation

This technique is based on the analysis of spatio-temporal dynamics of induced microseismic clouds. The volume of the injected fluid must be equal to a sum of the fluid volume stored in the fracture and the fluid volume which goes into the formation. A straight planar height-fixed fracture is considered. Under these conditions the half length, L , of the hydraulic fracture is given as a function of the injection time as (Economides and Nolte, 2003):

$$L(t) = \frac{Q_i t}{4h_f C_L \sqrt{2t} + 2h_f w} \quad (2.29)$$

where Q_i is the average injection rate of the treatment fluid, h_f is the average fracture height and w is the average fracture width, t is the injection time and C_L is the fluid-loss coefficient.

In the case of hydraulic fracturing of low permeability formation, such as tight gas sandstones, the fracture body represents the main permeable channel in the formation (Shapiro et al., 2006). The induced fracture changes the stress state in its vicinity leading to the occurrence of microseismic events at a distance very close to the hydraulic fracture (Warpinski, 2000). Therefore, eqn. 2.30 can be considered as a one dimensional approximation for the triggering front of microseismicity in the case a penetrating hydraulic fracture (Shapiro et al., 2006).

$$L = \sqrt{4\pi Dt} \quad (2.30)$$

Where D is the apparent diffusivity and t is the injection time.

During most of the time in hydraulic fracturing treatments the fracture growth is controlled by the fluid loss effects. Basically, this means that the cumulative volume of the lost fluid is significantly larger than the volume of the hydraulic fracture. The fluid loss effects are controlled by the fluid-loss coefficient, C_L , which is characterized by the apparent diffusivity, D, (Shapiro et al., 2006):

$$C_L = \frac{Q_i}{8h_f\sqrt{2\pi D}} \quad (2.31)$$

Also, the fluid loss coefficient can be interpreted neglecting the near-surface effects (e.g., filter cake) from the pressure difference between the fracture and the far field reservoir, ΔP . Economides and Nolte

(2003) approximated the fluid-loss coefficient based on these assumptions as,

$$C_L = \sqrt{\frac{k_r \phi c_r}{\pi \eta_r}} \Delta P \quad (2.32)$$

where k_r is the in-situ reservoir pressure, ϕ is the formation porosity, c_r and η_r are the compressibility and viscosity of the reservoir fluid and ΔP is the difference between the average injection pressure and the far-field reservoir pressure (Shapiro et al., 2006). Substituting eqn. 2.31 into eqn. 2.32 and solving for the formation permeability,

$$k_{r-t} = \frac{\eta_r}{128 \phi c_r D} \left(\frac{Q_i}{h_f \Delta P} \right)^2 \quad (2.33)$$

Eqn. 2.33 is the in-situ formation permeability calculated using the r-t technique. The r-t plots show the distance from the perforation point to the event location as a function of time. Eqn. 2.30 represents the parabolic envelope that better describes the upper bound of the majority of microseismic events, which is dependent on the apparent diffusivity value.

2.6.2 Inversion approach to permeability estimation

The method is based on inverting the diffusion equation under the assumption of 1D flow of the injected fluids from the faces of a hydraulic fracture. From Darcy's law for steady-state 1D:

$$u(x) = - \frac{K_r(x)}{\eta_r} \frac{dp(x)}{dx} \quad (2.34)$$

Here, x is the coordinate in the flow direction, u is the macroscopic velocity, η_r is the viscosity of the fluid, K_r is the in-situ formation permeability and p is the pressure. To obtain the in-situ permeability eqn. 2.34 is integrated over the interval x_1 - x_2 where flow is examined under the boundary conditions $u_1=u_1(x)$, $p_1 = p(x_1)$ and $p_2 = p(x_2)$ (Grechka et al., 2010). The absence of fluid source at $[x_1, x_2]$ and the steady-state flow regime imply a constant filtration velocity $u(x) = u_1$. After integration we obtain,

$$u_1(x_2 - x_1) = -\frac{K_r}{\eta_r}(p_2 - p_1) \quad (2.35)$$

Solving for the in-situ formation permeability,

$$K_r = \eta_r u_1 \frac{x_2 - x_1}{p_2 - p_1} \quad (2.36)$$

The term $(x_2 - x_1)$ can be replaced by $(w_r - w_f)/2$, where w_r is the width of the zone around the fracture where the reservoir pressure has been altered, and w_f is the fracture width. w_r can be approximated by the width of the induced microseismic cloud, $w_{\mu s}$. The width of the microseismic cloud can be expressed in terms of the aspect ratio as (Grechka et al., 2010),

$$w_{\mu s} = 2\alpha_{\mu s} r_{\mu s} \quad (2.37)$$

where $\alpha_{\mu s}$ and $r_{\mu s}$ are the aspect ratio and the radius of the microseismic cloud, respectively. Since $w_{\mu s} \gg w_f$, the latter can be ignored, and eqn. 28 could be re-written as (Grechka et al., 2010),

$$K_r = \eta_r \alpha_{\mu s} \frac{r_{\mu s} u_1}{\Delta P} \quad (2.38)$$

The average leak-off velocity, u_1 , can be obtained by noticing that the fluid volume, V , lost into the formation over a short time interval, Δt , is:

$$V = 4h_f r_{\mu s} u_1 \Delta t \quad (2.39)$$

This volume is equal to the volume injected during the same time interval,

$$V = Q_i \Delta t \quad (2.40)$$

Under the assumption that the fluid is incompressible and only its negligible volume is contained in the fracture itself. Combining eqns. 2.39 and 2.40 and then substituting in eqn. 2.38 (Grechka et al., 2010).

$$K_{inv} = \frac{\eta_r \alpha_{\mu s} Q_i}{4h_f \Delta P} \quad (2.41)$$

Eqn. 2.41 is the in-situ formation permeability according to the inversion approach.

Note that in either fluid solution we are not recovering the intrinsic permeability but an “effective” permeability which may locally reflect the natural fracture density.

3. STATEMENT OF THE PROBLEM

Microseismic monitoring of hydraulic fractures typically produces spatial and temporal plots of hypocenters without any estimates of uncertainty leading the engineer to believe the hypocenter locations are absolute (Chitralla et al., 2010; Castano, 2010). However there is uncertainty in the location of the hypocenters which is associated with the arrival times errors, sensor placement and the acquisition system itself. Hypocenter locations are determined from the arrival times of P-wave, S-wave and a known velocity model, which is based on the measured properties of each sample.

Hydraulic fracturing treatments have been reproduced at the laboratory scale using three different lithologies: Indiana limestone, Lyons sandstone and pyrophyllite. Prior to stimulation treatments, each sample is petrophysically characterized and a Circumferential Velocity Analysis (CVA) is performed, where velocity measurements are made across the diameter of the sample at different azimuths to establish the velocity model. Isotropic materials produce a constant velocity response as a function of azimuth, while anisotropic materials display sinusoidal responses. CVA results show that the limestone and sandstone samples have azimuthal velocity variation less than 4% (**Fig. 3.1**); these samples

are treated as homogeneous and isotropic. However, pyrophyllite samples showed an azimuthal p-wave velocity variation of 25%. CVA responses for anisotropic materials are also useful for the determination of foliations and fracture planes; the peaks indicate the direction parallel to the fabric while the valleys represent the direction perpendicular to the fabric as seen in **Fig. 3.2**. Also, velocity measurements using the three plug technique indicate that pyrophyllite samples are transverse isotropic (Karastathis, 2007). **Table 3.1** shows velocity values obtained for plugs taken parallel, perpendicular and at an angle of 45° to the fabric orientation.

Table 3.1 - Velocity measurements of P-wave and S-wave on pyrophyllite plugs taken parallel, perpendicular and at an angle of 45° to the bedding orientation

Confining Pressure (psi)	Parallel to bedding			Perpendicular to bedding			45°		
	Velocity (km/s)			Velocity (km/s)			Velocity (km/s)		
	P	S1	S2	P	S1	S2	P	S1	S2
250	4.918	-	-	7.044	-	-	4.734	3.086	2.927
500	4.974	-	0	3.809	2.799	2.711	4.741	3.097	2.927
750	4.959	2.848	3.06	3.843	2.81	2.722	4.741	3.104	2.936
1000	5.001	2.839	3.082	3.848	2.821	2.73	4.757	3.115	2.946
1500	5.015	2.848	3.087	3.884	2.839	2.73	4.757	3.122	2.946
2000	4.987	2.871	3.103	3.893	2.857	2.741	4.749	3.137	2.956
3000	5.073	2.885	3.131	3.992	2.878	2.761	4.774	3.14	2.965

From the average of the values in **Table 3.1**, the anisotropic parameters (Appendix A) are calculated (**Table 3.2**).

Table 3.2 - Anisotropic parameters (Thomsen, 1986) calculated from the velocity values obtained from the 3-plug technique for pyrophyllite samples at 3000 psi confining pressure.

ϵ	δ	γ
0.31	0.04	0.10

Table 3.3 and **Table 3.4** show the different average P-wave velocities values obtained from CVA experiments for the limestone, represented by the letter C, and sandstone samples, represented by the letter S, that were used during this study, respectively.

Table 3.3 - Average P-wave velocity values obtained from CVA measurements for Indiana limestone samples used in the study.

Limestone	P-wave velocity (km/s)	Standard deviation, km/s
C14	4.034	± 0.0608
C15	4.010	± 0.0371
C16	4.002	$\pm 0.035.2$

Table 3.4 - Average P-wave velocity values obtained from CVA measurements for Lyons sandstone samples used in the study.

Sandstone	P-wave velocity (km/s)	Standard deviation, km/s
S4	4.335	± 0.0439
S6	4.332	± 0.0531
S7	4.269	± 0.0460
S8	4.336	± 0.0405
S9	4.305	± 0.0636
S11	4.381	± 0.0749
S13	4.468	± 0.0523
S14	4.482	± 0.0469

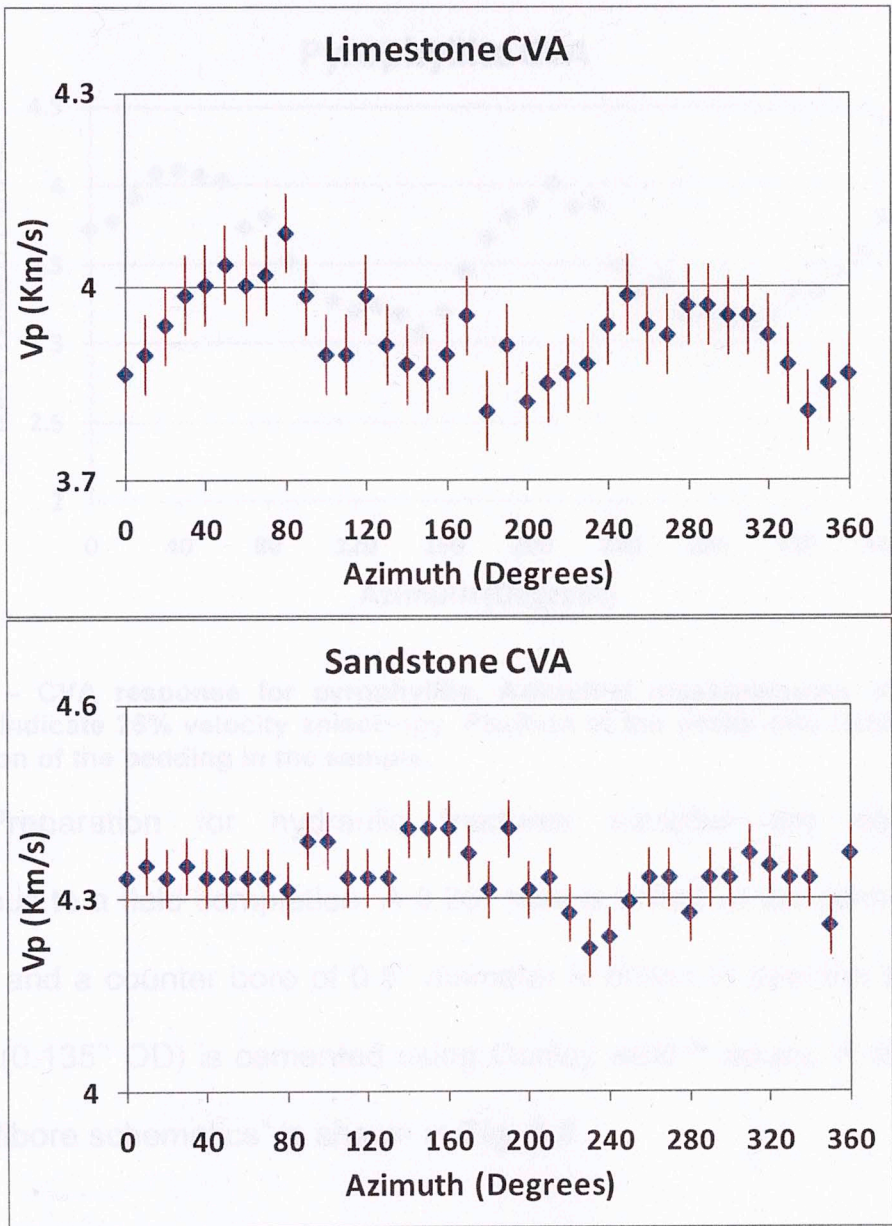


Fig. 3.1 – Top) CVA response of sample C14 (limestone) showing a velocity anisotropy of 6% where the red lines represent the standard deviation with a value of ± 0.061 km/s. Bottom) CVA response of sample S4 (sandstone) showing a velocity anisotropy of 4% and the red lines represent the standard deviation with a value of ± 0.044 km/s.

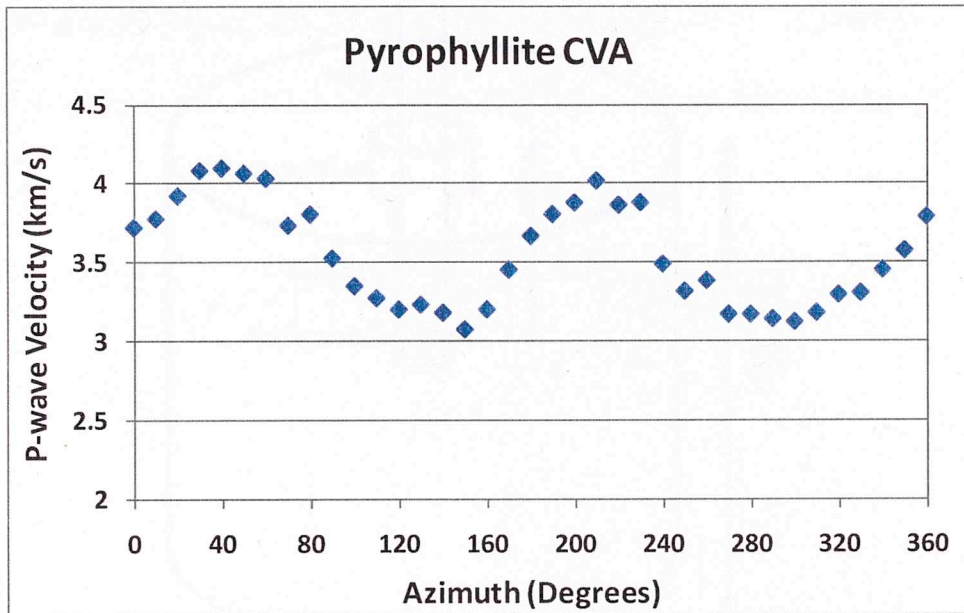


Fig. 3.2 – CVA response for pyrophyllite. Azimuthal measurements of P-wave velocity indicate 25% velocity anisotropy. Position of the peaks also indicates the orientation of the bedding in the sample.

Preparation for hydraulic fractures samples are completed analogous to a field completion. A 0.25" hole is drilled at the center of the sample and a counter bore of 0.5" diameter is drilled to seal the annulus. Tubing (0.135" OD) is cemented using Conley weld™ epoxy. A sketch of the "wellbore schematics" is shown in **Fig. 3.3**.

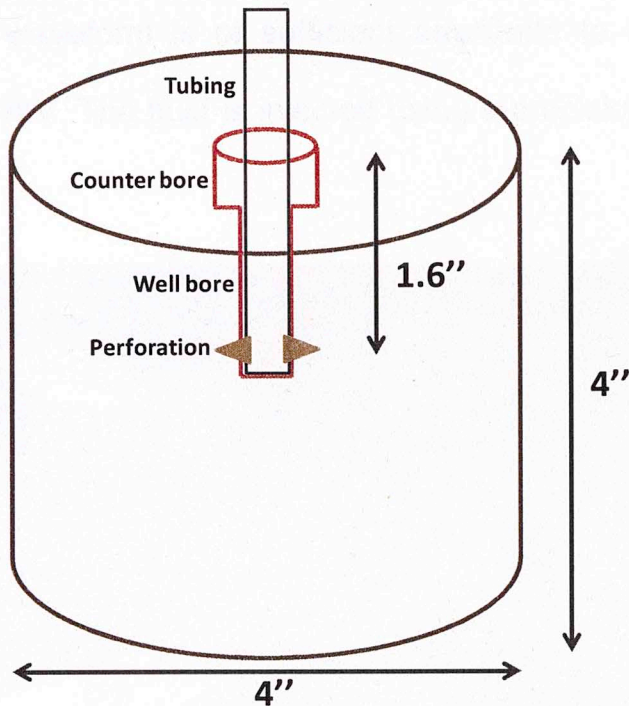


Fig. 3.3 – Sketch of a sample completion. Red lines show the counter bore and the wellbore which is filled with epoxy to seal the high pressure stainless steel tubing which acts as our wellbore (Chitrala et. al, 2010). A perforation or hole is drilled in the tubing (not in the sample).

16 piezoelectric sensors are attached to the sample using Crystal bond™ to provide a good azimuthal coverage (**Fig. 3.4**). The piezoelectric sensors have a frequency response range of 50 KHz to 2 MHz. Each sensor is connected to a 5660B Panametrics-NDT™ wide band preamplifier. The preamplifiers have a frequency pass band of 500 Hz to 40 MHz and two gain settings of 40 and 60 dB. Each captured waveform consists of 1024 samples with 512 pre-trigger samples. The digitizing rate is 5 MHz (0.2 μ sec/point) which makes each recorded signal 204.8 μ s long. The signal trigger gains are set so that the early arriving portion of

the AE signal waveform is of sufficient amplitude to constitute a valid trigger of ± 100 mV. The fluid is injected using a precision Quizix™ -6000 pump.

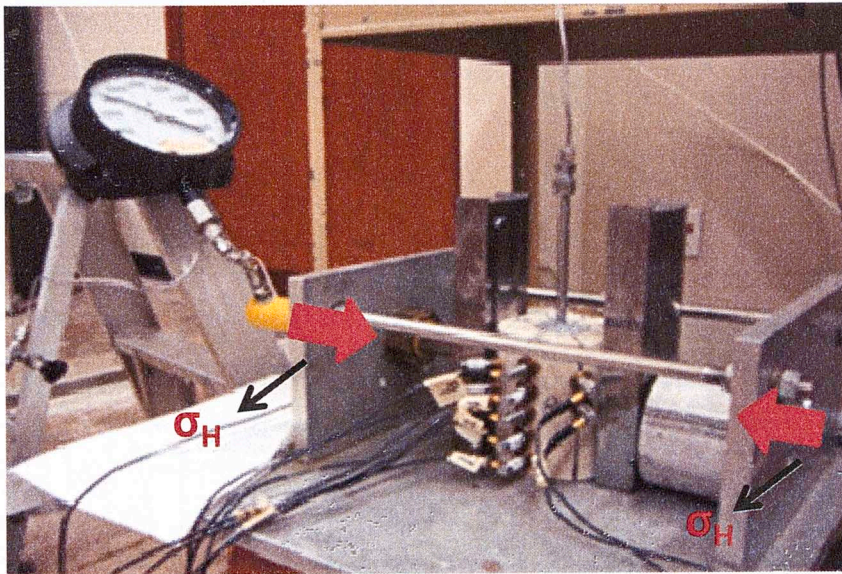


Fig. 3.4 – Piezoelectric sensors attached to a limestone sample. A vertical array of sensors is used to simulate an observation well. Two flat jacks are used to apply a horizontal stress (Chitralla et. al, 2010).

Each waveform generated by the microseismic event is recorded by the 16 piezoelectric sensors attached to the sample (**Fig. 3.5**).

In order to control the fracture direction, a horizontal stress is applied to each sample as shown in **Fig. 3.4**. For anisotropic samples two different experiments are carried out; the first, with the stress applied parallel to the bedding planes, and the second, with the stress applied perpendicular to the bedding planes. **Table 3.5** and **Table 3.6** show the magnitude of stress applied to the Indiana limestone and Lyons sandstone, respectively.

Table 3.7 shows the magnitude of stress applied to pyrophyllite samples along with the orientation with respect to the orientation of the fabric.

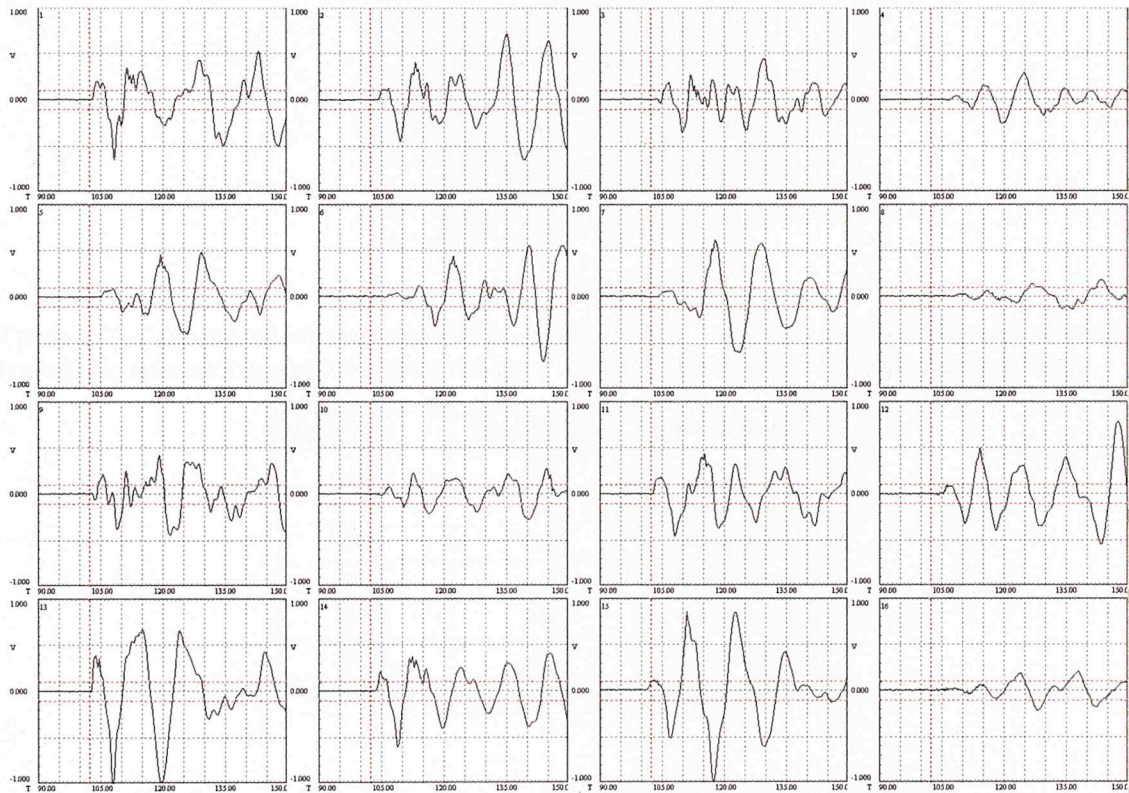


Fig. 3.5 – Magnified waveforms recorded by 16 piezoelectric sensors attached to Lyons sandstone, S4, during a hydraulic fracturing experiment. The X-axis is represents the time in microseconds and ranges from 90 μ s to 150 μ s and the Y-axis is the amplitude in volts and ranges from -1 to 1 Volts.

Table 3.5 - Values of stress applied to Indiana limestone samples using flat jacks during hydraulic fracturing experiments.

Sample	Stress (psi)
C14	833
C15	840
C16	809

Table 3.6 - Values of stress applied to Lyons Sandstone samples using flat jacks during hydraulic fracturing experiments.

Sample	Stress (psi)
S4	1040
S6	1080
S7	1160
S8	150
S9	150
S11	580
S13	580
S14	550

Table 3.7 - Values of stress applied to pyrophyllite samples using flat jacks during hydraulic fracturing experiments respect to the orientation of the bedding planes.

Sample	Stress (psi)	Orientation
P5	970	Parallel
P6	990	Perpendicular
P9	980	Parallel
P10	960	Perpendicular
P11	950	Parallel
P12	1020	Perpendicular
P16	520	Perpendicular

We calibrated the AE recording system using the Hsu and Brekenridge (1981) pencil breaks; eight breaks are carried out on the surface of the sample at known locations. The recorded waveforms, along with a previously determined velocity model, are used to locate each break source and compare it to the known location. This is done to calibrate the velocity model and to check that the sensors are effectively coupled to the sample. **Fig. 3.6** illustrates the principle of this technique.

4. RESULTS AND ANALYSIS

4.1 Calibration results

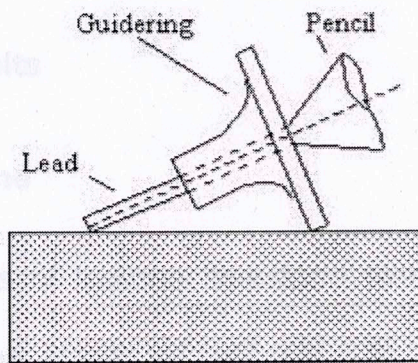
4.1.1 Indiana limestone

Three different samples

and 0.15. Fig. 4.1 shows

figures show a pair of

represent the sensors attached to the sample. The grain dots are the



Lead: 2H
Diameter: 0.5mm (0.3mm)
Length: 3.0 ± 0.5 mm

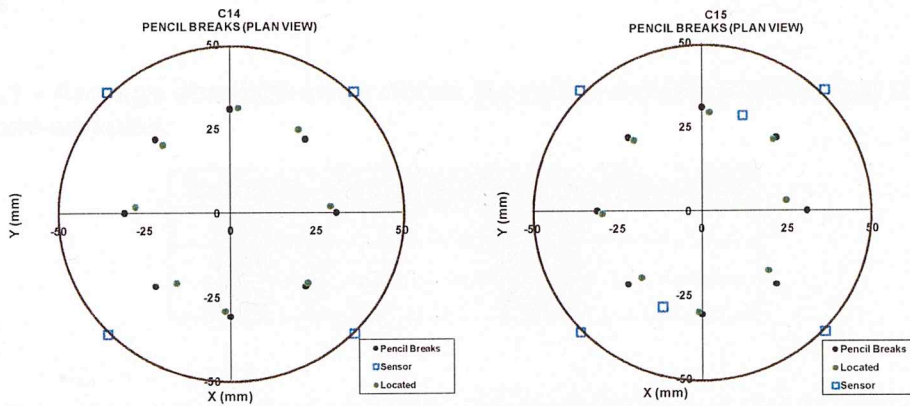
Fig. 3.6 – Hsu-Nielson source for the testing and calibration of acoustic emission systems. They recommend a lead diameter of 0.5 or 0.3 mm and 2H hardness (source: <http://www.ndt.net/ndtaz/ndtaz.php>).

4. RESULTS AND ANALYSIS

4.1 Calibration results

4.1.1 Indiana limestone

Three different samples of Indiana limestone were analyzed; C14, C15 and C16. **Fig. 4.1** shows results of calibration for all three samples. The figures show a plan view of the samples where the cyan squares represent the sensors attached to the sample, the green dots are the located events and the black dots are the actual locations of the pencil breaks.



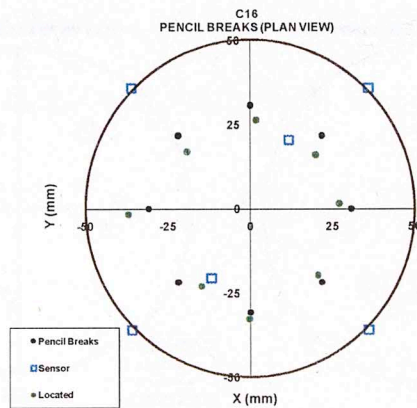


Fig. 4.1 - Pencil break calibrations for different Indiana limestone samples C14 (upper left), C15 (upper right) and C16 (bottom).

With the calculated locations of the sources is possible to compute the error, the rms difference between the real location and calculated location. **Table 4.1** shows the average absolute error for each limestone sample.

Table 4.1 - Average absolute error values for pencil breaks experiments in Indiana Limestone samples.

Sample	Average absolute error, mm
C14	± 3.06
C15	± 3.03
C16	± 4.70

The absolute error is just the distance between the located source and the real location. The error in the X and Y coordinate are represented by error ellipses as shown in **Fig. 4.2**.

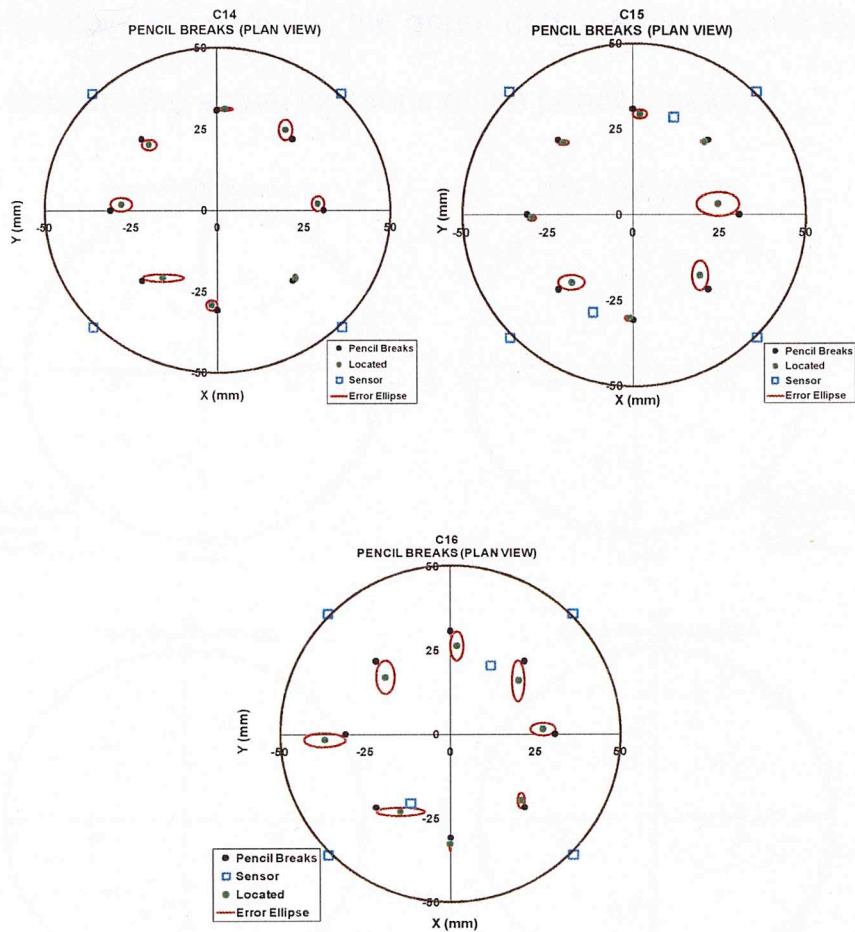
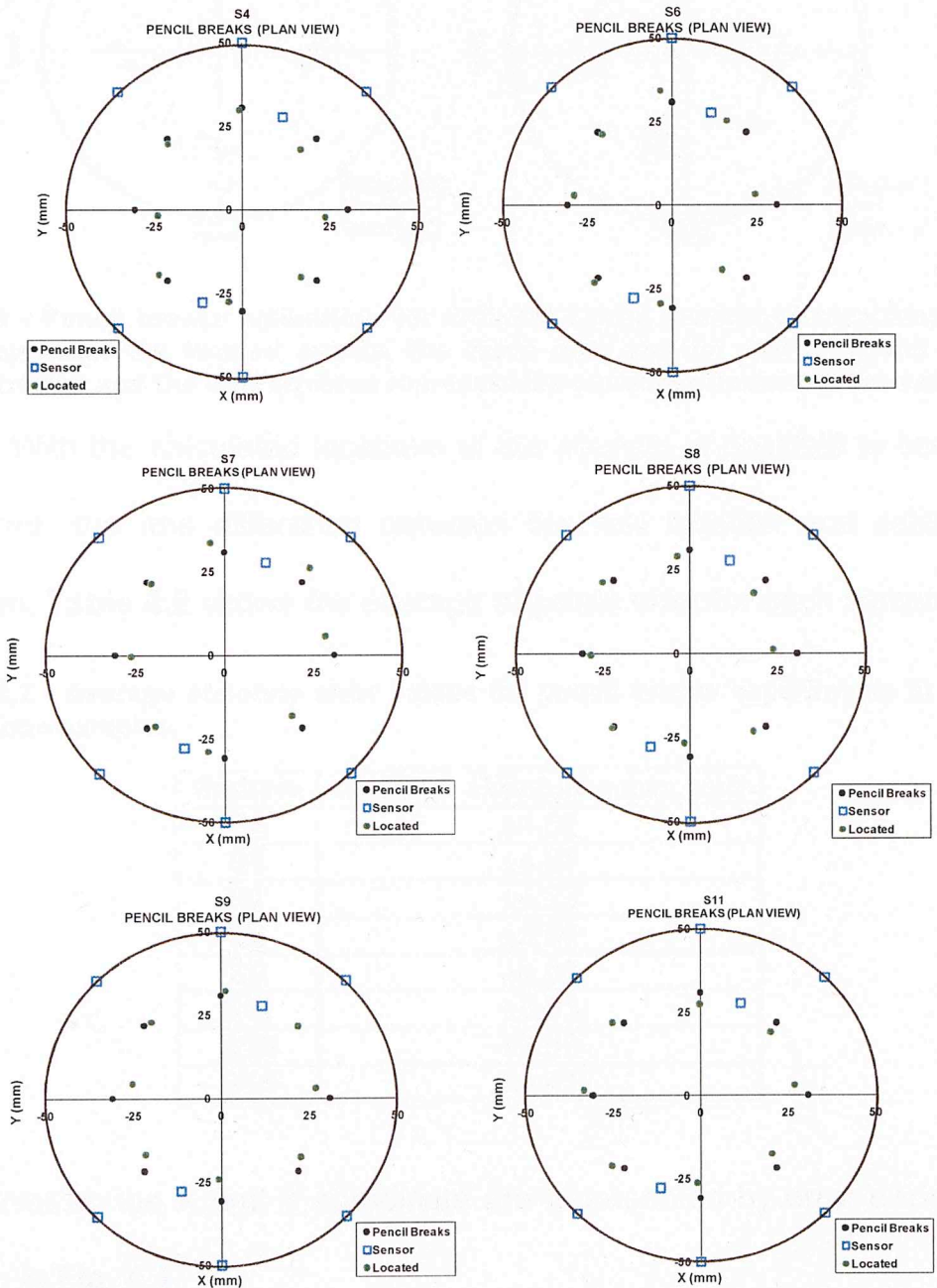


Fig. 4.2 - Pencil breaks calibration for different Indiana Limestone samples C14 (upper left), C15 (upper right) and C16 (bottom), showing the error in the X- and Y-axis with error ellipses (red lines)

4.1.2 Lyons sandstone

Eight different Lyons sandstone samples were analyzed; S4, S6, S7, S8, S9, S11, S13 and S14. **Fig. 4.3** shows calibration results for all eight samples. The figures show a plan view of the samples where the blue

squares represent the sensors, the green dots are the located events and the black dots are the actual locations of the pencil breaks.



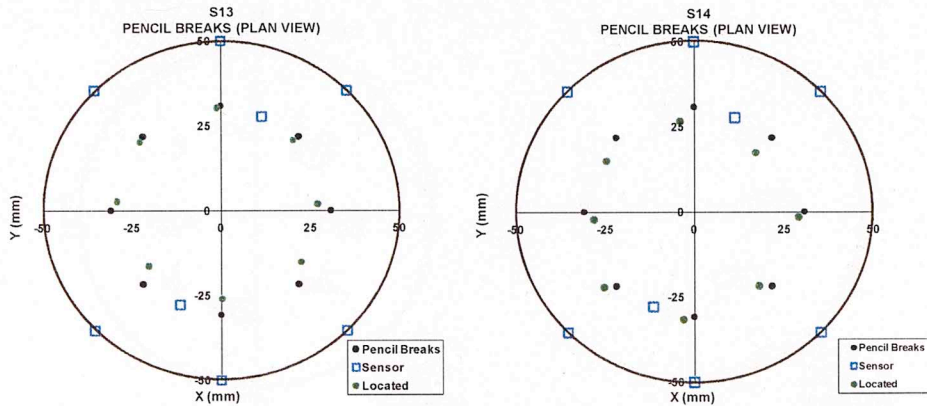


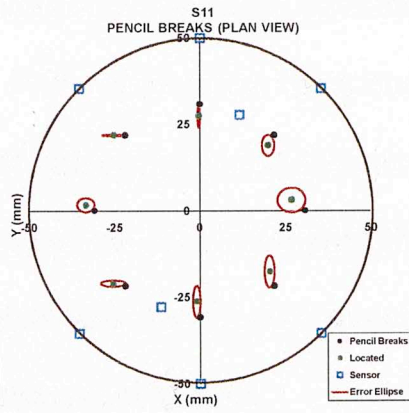
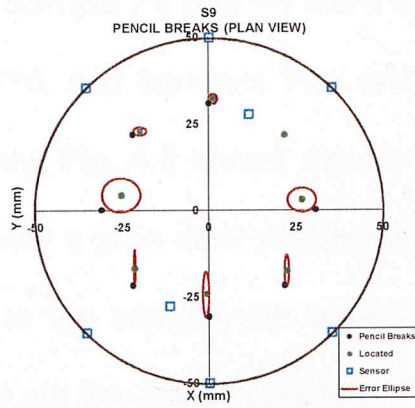
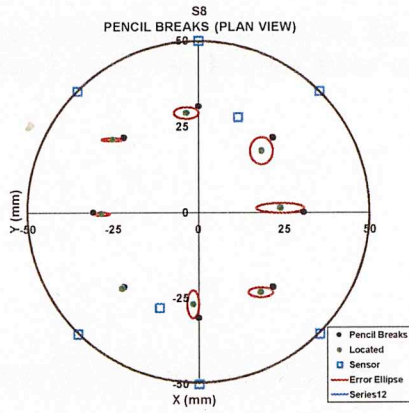
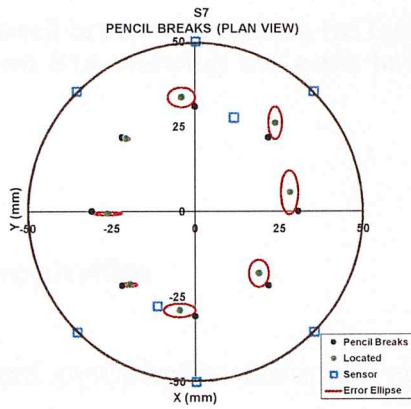
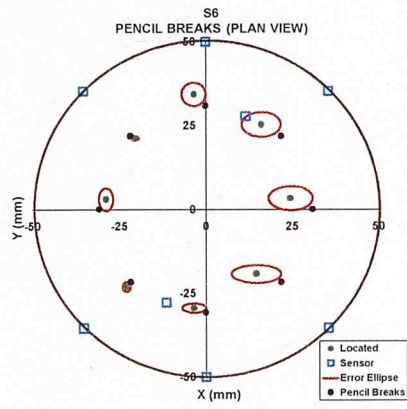
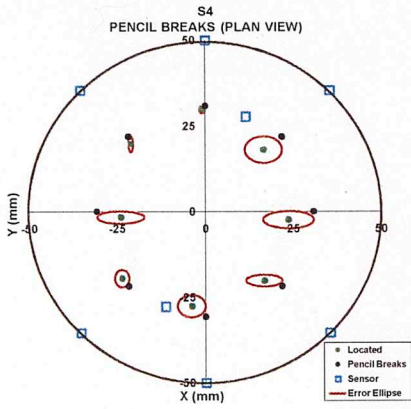
Fig. 4.3 - Pencil breaks calibration for different Lyons sandstone samples; green dots represent the located events, the black dots are the real locations of the pencil breaks and the blue squares represent the sensors attached to the sample

With the calculated locations of the sources is possible to compute the error, the rms difference between the real location and calculated location. **Table 4.2** shows the average absolute error for each sample.

Table 4.2 - Average absolute error values for pencil breaks experiments in Lyons sandstone samples.

Sample	Average absolute error, mm
S4	±4.32
S6	±4.61
S7	±4.23
S8	±3.86
S9	±4.06
S11	±3.91
S13	±3.67
S14	±4.41

The error en the X and Y coordinate are represented by error ellipses as shown in **Fig. 4.4**.



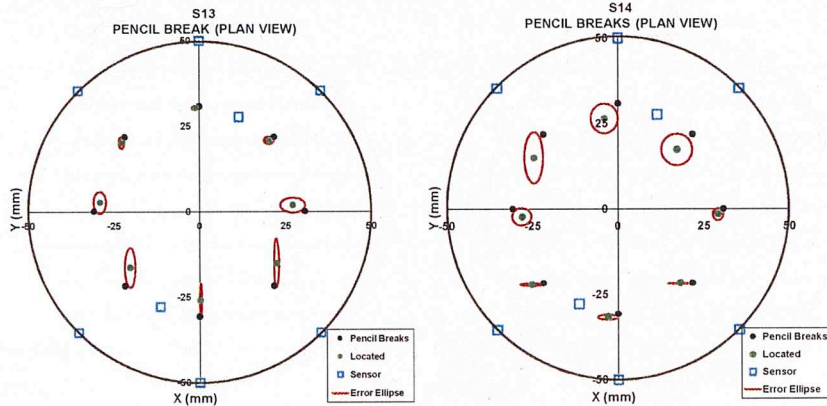


Fig. 4.4 - Pencil break calibrations for Lyons Sandstone samples S4, S6, S7, S8, S9, S11, S13 and S14 showing the error in the X- and Y-axis with error ellipses (red lines)

4.1.3 Pyrophyllite

Six different pyrophyllite samples were analyzed; P5, P6, P9, P10, P12 and P16. Sample P5 and P6 were taken from the same cylinder, samples P9 and P10, and samples P11 and P12, were taken from one cylinder, respectively. **Fig. 4.5** shows results of calibration for all six samples. The figures show a plan view where the cyan squares represent the sensors attached to the sample, the green dots are the located events and the black dots are the actual locations of the pencil breaks.

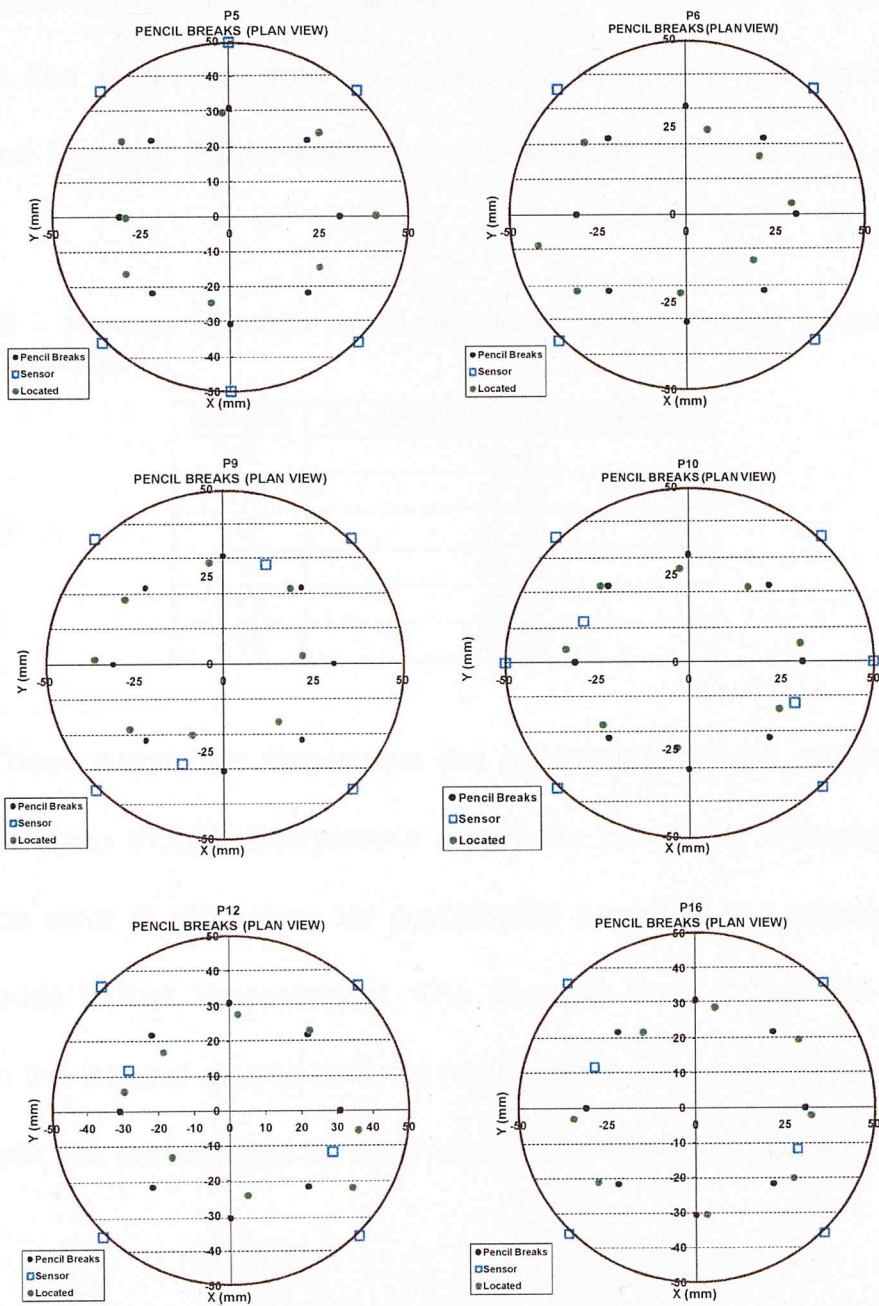


Fig. 4.5 - Pencil break calibrations for different pyrophyllite samples; green dots represent the located events, the black dots are the real locations of the pencil breaks and the blue squares represent the sensors attached to the sample. The dashed lines represent the fabric direction in the sample.

With the calculated locations of the sources it is possible to compute the error, the rms difference between the real location and calculated location. **Table 4.3** shows the average absolute error for each sample.

Table 4.3 - Average absolute error values for pencil breaks experiments in pyrophyllite samples.

Sample	Average absolute error, mm
P5	±6.47
P6	±7.94
P9	±7.10
P10	±5.33
P12	±6.83
P16	±5.25

These errors are larger due the anisotropic nature of pyrophyllite samples. Even though Berryman's equations for strong anisotropy were used, the error is still larger for pyrophyllite samples; the velocity model used needs further improvement. The absolute error is just the distance between the located source and the real location. The error in the X and Y coordinate are represented by error ellipses as shown in **Fig. 4.6**.

Fig. 4.5 - Pencil break calibrations for pyrophyllite samples P5, P6, P9, P12 and P16 showing the error in the X- and Y-axis with error ellipses (red lines)

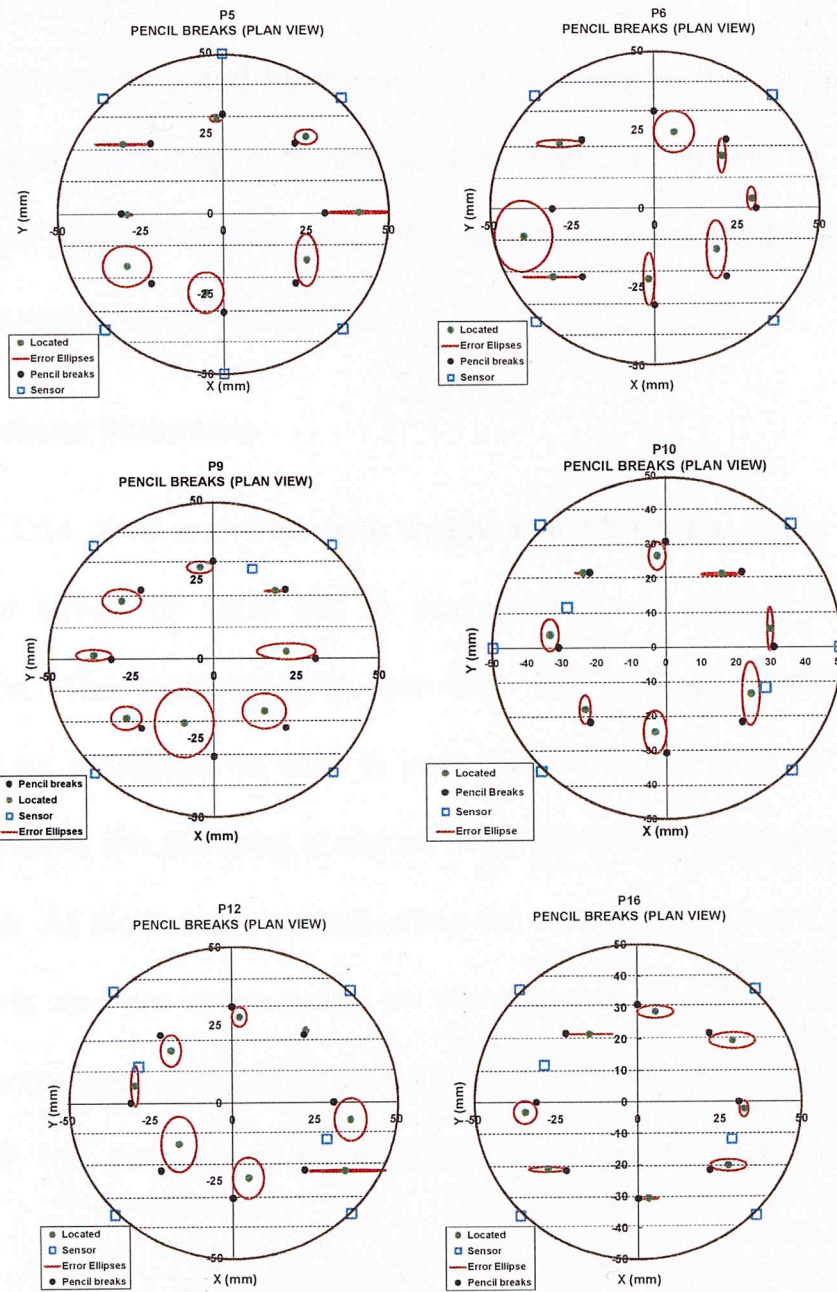


Fig. 4.6 - Pencil break calibrations for pyrophyllite samples P5, P6, P9, P12 and P16 showing the error in the X- and Y-axis with error ellipses (red lines)

4.2 Microseismic event location

The waveforms recorded by the sensors attached to the samples during the hydraulic fracturing experiments are used, along with a previously established velocity model, to locate the hypocenter of the microseismic events as explained in section 2.4.

4.2.1 Indiana limestone

Samples C14, C15 and C16 were hydraulically fractured while applying a horizontal stress of 1000 psi to each sample to control the fracture orientation. The pumping pressure and the acoustic emissions were recorded as a function of time in each experiment (**Fig. 4.7**). The black lines represent the pumping pressure while the red circles are the acoustic emissions. All the events located within the sample have been divided into three parts and are represented as early time (green dots), intermediate time (orange dots) and late time (purple dots) events. Such color coding is used with the purpose of highlighting the propagation of the hydraulic fracture.

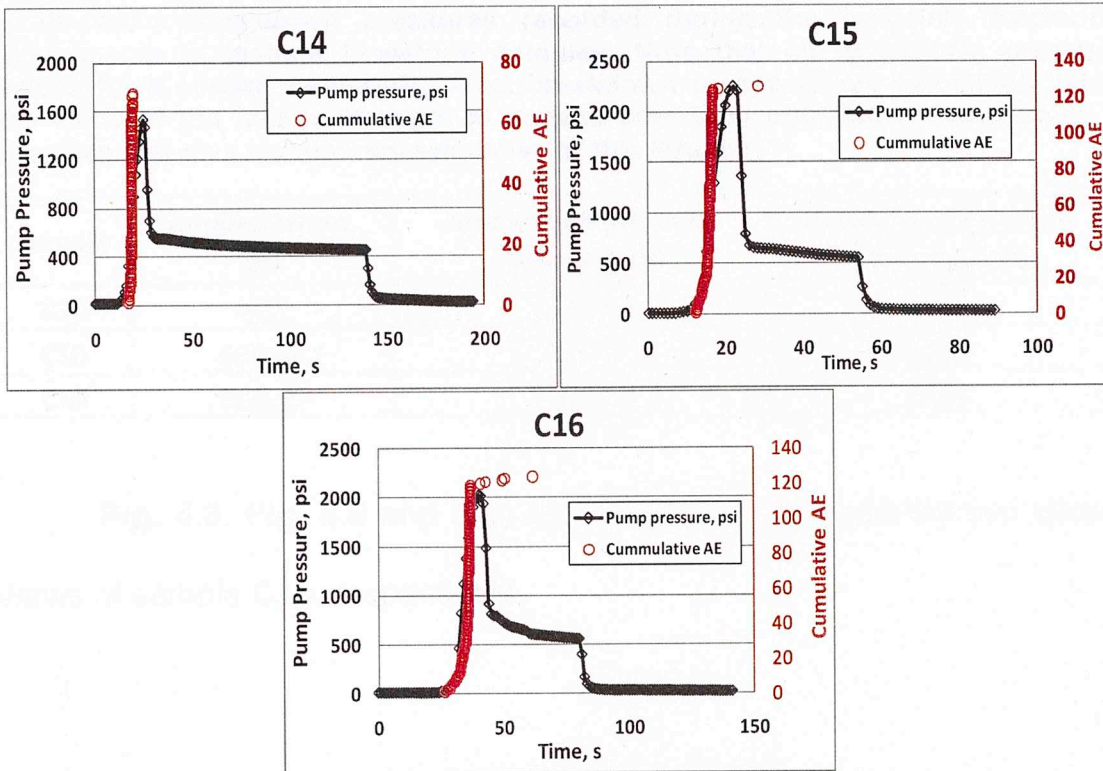


Fig. 4.7- Pump pressure (black) and cumulative AE (red) as a function of time. Note that in all experiments that the majority of AE activity occurs prior to the actual breakdown pressure.

Table 4.4 shows a summary of breakdown pressures recorded during each of the hydraulic fracturing experiments in Indiana limestone samples. Also, the tensile strength of Indiana limestone was measured by performing a Brazilian test on a representative sample. The tensile strength of Indiana limestone is 841 psi. This value was used to calculate the breakdown pressures for each sample (Table 4.4). The average absolute difference between the recorded and calculated breakdown pressures is 359 psi for Indiana limestone samples.

Table 4.4 - Breakdown pressures recorded during the hydraulic fracturing experiments in Indiana limestone samples. Note that all breakdown pressure values have similar magnitude. Also, breakdown pressures are calculated using the value of the tensile strength of Indiana limestone obtained by performing a Brazilian test on a sample representative of this lithology.

Sample	Applied stress, psi	Breakdown pressure recorded, psi	Breakdown pressure calculated, psi
C14	833	1528	1674
C15	839.98	2246	1681
C16	809.55	2017	1651

Fig. 4.8, Fig. 4.9 and Fig. 4.10 show the plan and the two lateral views of sample C14, respectively.

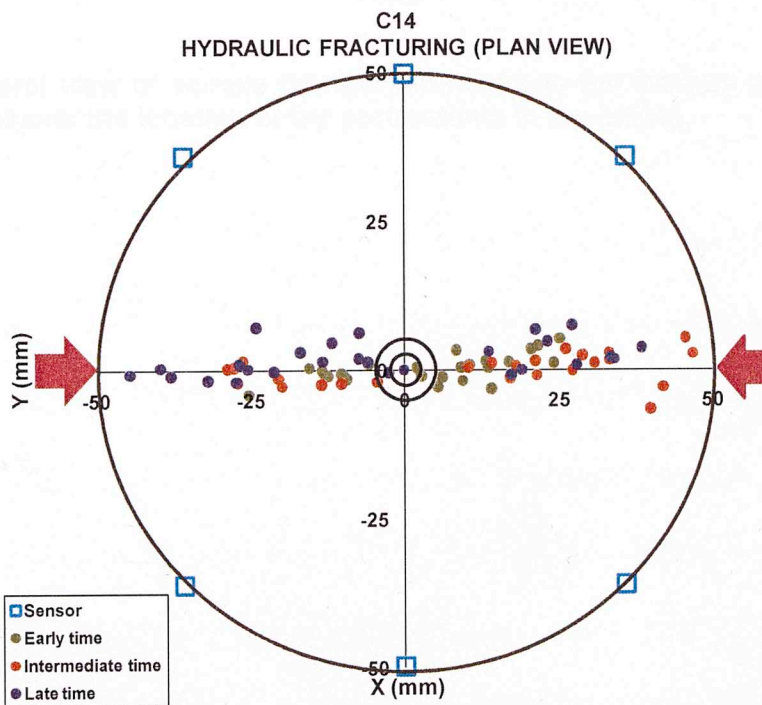


Fig. 4.8 - Plan view of sample C14 (Indiana limestone) showing the spatial and temporal evolution of the hydraulic fracture. The green dots represent the early time events, while the orange and purple represent the intermediate and late time events, respectively. The cyan squares represent sensors attached to the sample.

The red arrows represent the direction of the stress applied with a magnitude of 833 psi. The two circles in the center of the plot represent the counter borehole and the borehole. 77 MS events were locatable within the sample.

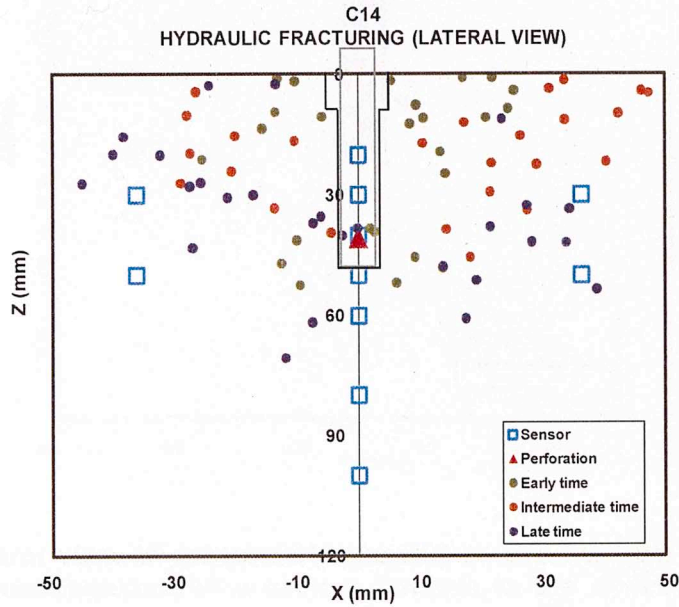


Fig. 4.9 - Lateral view of sample C14 perpendicular to the fracture plane. The red triangle represents the location of the perforations in the tubing.

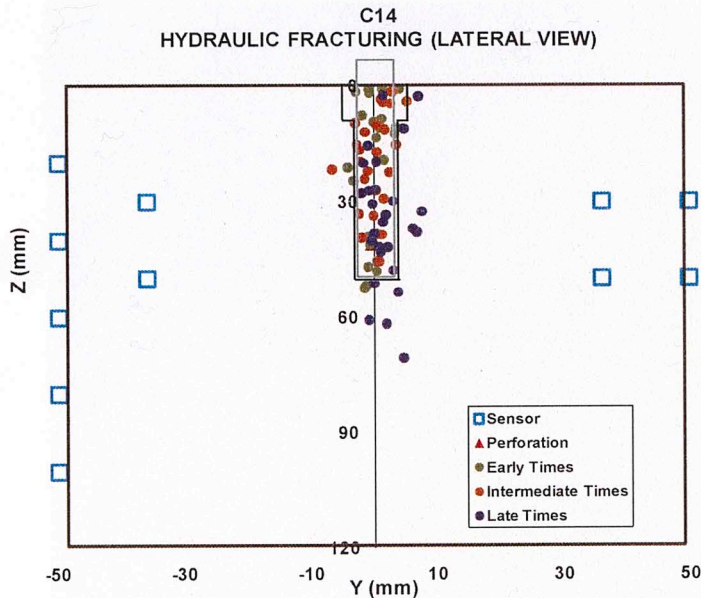


Fig. 4.10 - Lateral view of sample C14 parallel to the fracture. This view allows observing the development of a narrow fracture in the direction of the applied stress.

From **Fig. 4.7** (top left) it can be observed that the majority of the microseismic events are recorded before reaching the breakdown pressure (1528 psi) which is represented by the peak in the pressure plot. As expected for isotropic samples, the fracture grows in the direction of the stress applied (**Fig. 4.8**). Time progression shows the development of the fracture as it moves away from the injection source. There are, however, late stage events recorded in zones previously fractured. The majority of the events are confined to the upper half of the sample. Physical observation of the sample (**Fig. 4.11**) shows a fracture that agrees with the locations of the microseismic events on the sample surface.

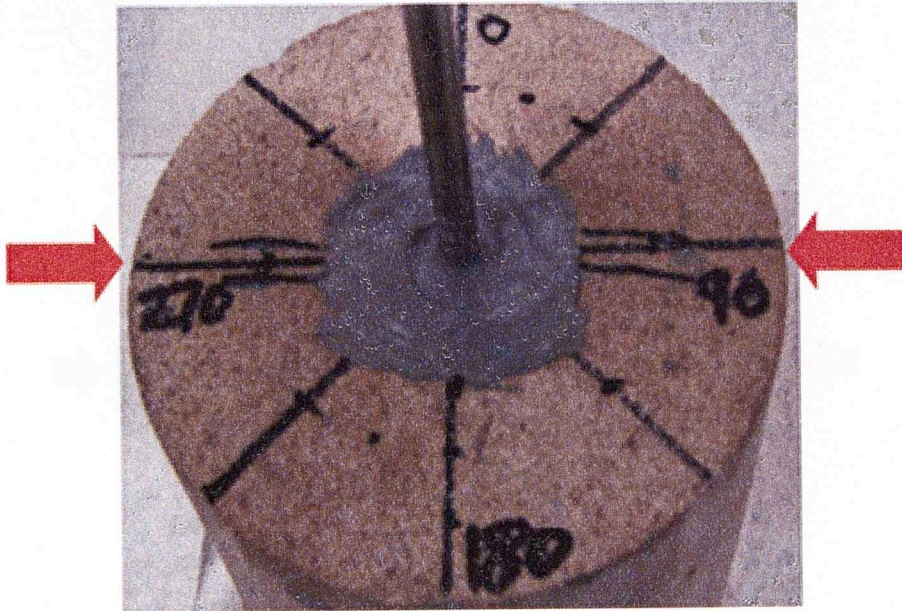


Fig. 4.11 - Surface of sample C14 showing a fracture enclosed by the dark blue lines in the direction of the stress applied (red arrows)

Fig. 4.12, Fig. 4.13 and Fig. 4.14 represent different views of sample C15 (Indiana limestone) which show the locations of the microseismic events.

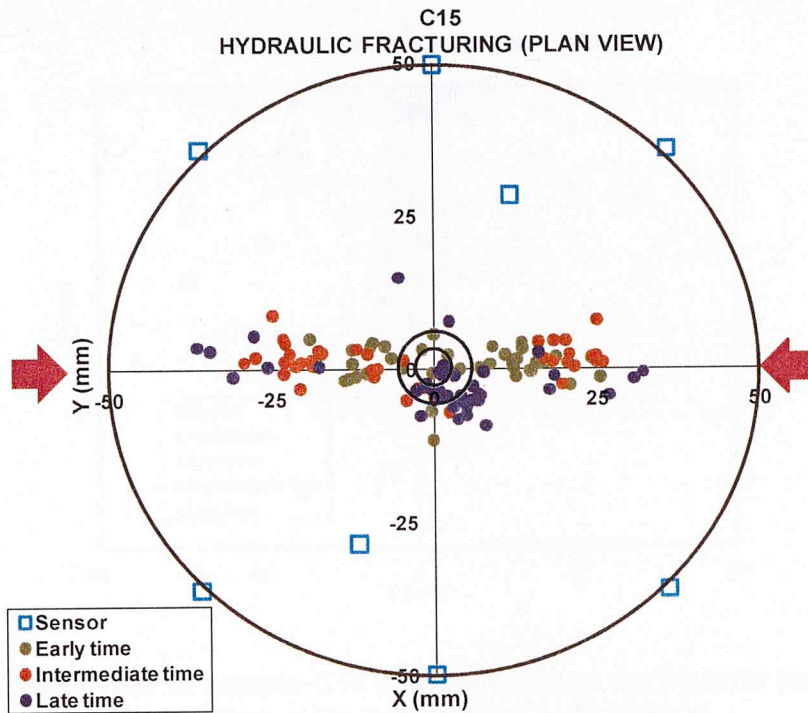


Fig. 4.12 - Plan view of sample C15 showing the spatial and temporal evolution of the hydraulic fracture. The green dots represent the early time events, while the orange and purple represent the intermediate and late time events, respectively. The cyan squares represent sensors attached to the sample. The red arrows represent the direction of the stress applied with a magnitude of 840 psi. The two circles in the center of the plot represent the counter borehole and the borehole. 124 MS events were locatable within the sample.

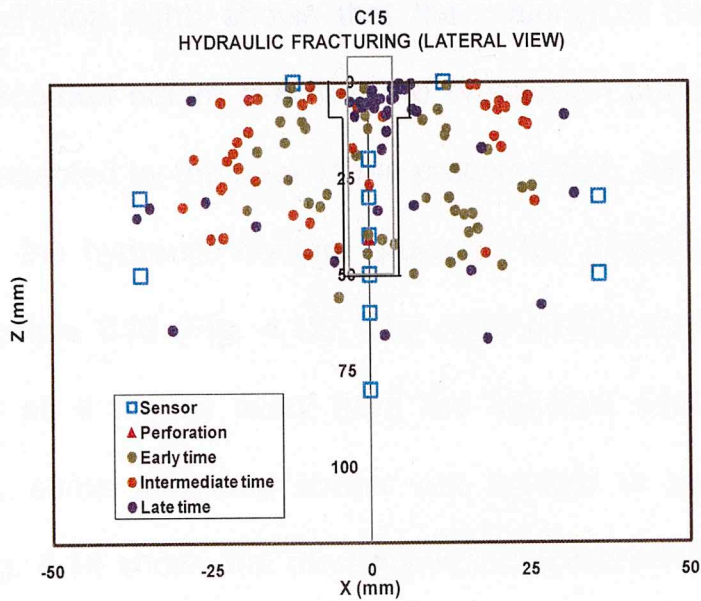


Fig. 4.13 - Lateral view of sample C15 perpendicular to the fracture plane. The red triangle represents the location of the perforations in the tubing.

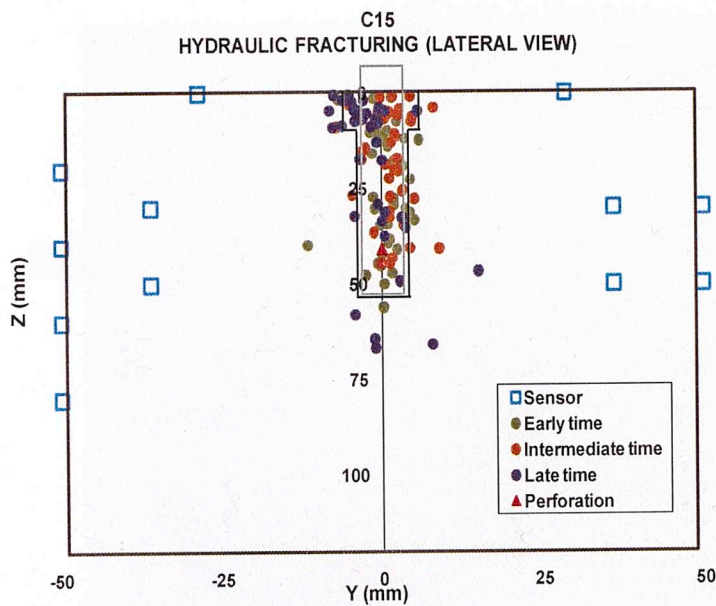


Fig. 4.14 - Lateral view of sample C15 parallel to the fracture. This view allows observing the development of a narrow fracture in the direction of the applied stress.

Fig. 4.7 (top right) shows that the majority of the microseismic events are recorded before reaching the breakdown pressure (2246 psi) which is represented by the peak in the pressure plot. Just as observed in sample C14, the hydraulic fracture grows in the direction of the stress applied in sample C15 (**Fig. 4.12**). The color coding shows the fracture development as it moves away from the injection source. Just as in sample C14, some late time events are located in zones previously fractured. **Fig. 4.14** shows the development of a narrow fracture fairway. **Fig. 4.15** shows physical evidence of the fracture on the upper sample surface which agrees with location of microseismic events.

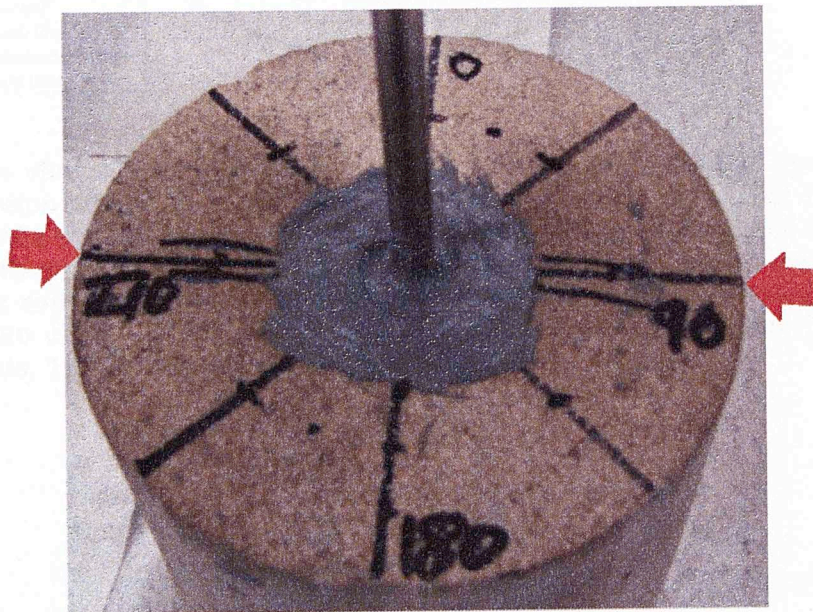


Fig. 4.15 - Surface view of sample C15 showing a fracture growing in the direction of the stress applied (red arrows). The fracture is enclosed by the dark blue lines.

Fig. 4.16, Fig. 4.17 and Fig. 4.18 show the plan, and lateral views of sample C16 (Indiana limestone).

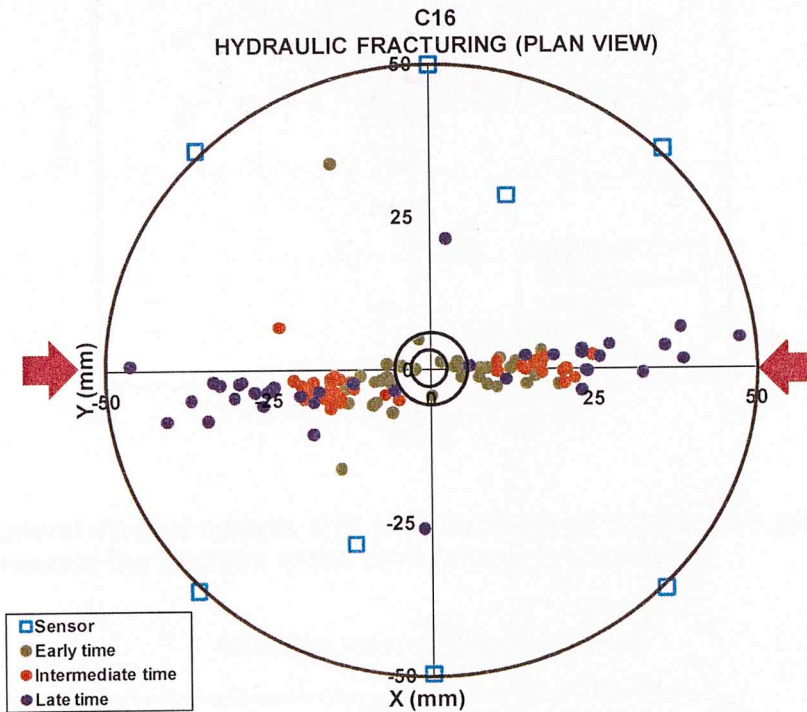


Fig. 4.16 - Plan view of sample C16 (Indiana limestone) showing the spatial and temporal evolution of the hydraulic fracture. The green dots represent the early time events, while the orange and purple represent the intermediate and late time events, respectively. The cyan squares represent sensors attached to the sample. The red arrows represent the direction of the stress applied with a magnitude of 809 psi. The two circles in the center of the plot represent the counter borehole and the borehole. 118 MS events were locatable within the sample.

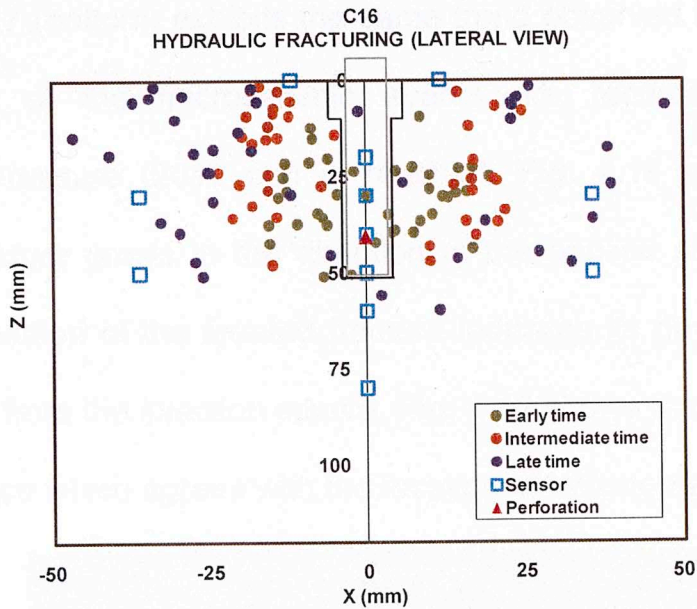


Fig. 4.17 - Lateral view of sample C16 perpendicular to the fracture plane. The red triangle represents the location of the perforations in the tubing.

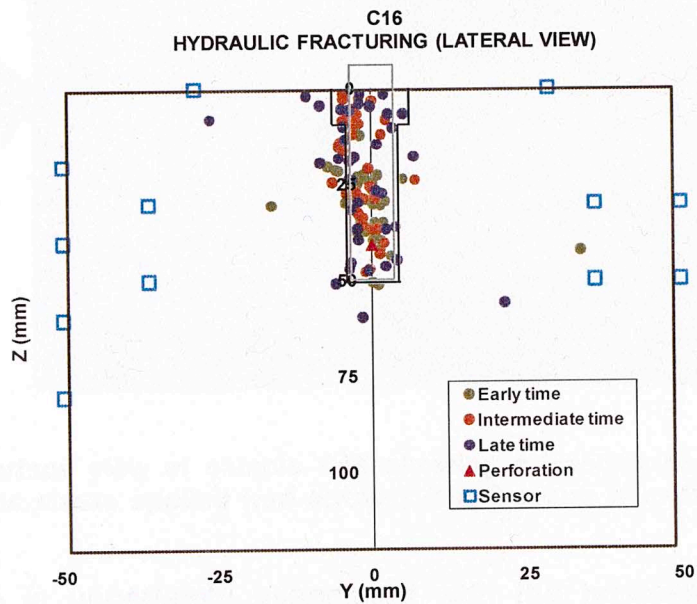


Fig. 4.18 - Lateral view of sample C16 parallel to the fracture. This view allows observing the development of a narrow fracture in the direction of the stress applied.

Fig. 4.7 (bottom) exhibits the same trend observed in sample C16; the majority of the microseismic events are recorded before the breakdown pressure (2017 psi) is reached. **Fig. 4.16** shows how the hydraulic fracture grows in the direction of the applied stress. Also, the temporal evolution of the created fracture indicates its development as it moves away from the injection source. **Fig. 4.19** shows the fracture on the sample surface which agrees with the location of hypocenters.



Fig. 4.19 - Surface view of sample C16 showing a fracture development in the direction of the stress applied (red arrows). The fracture is enclosed by the dark blue lines.

There is uncertainty associated with the process of hypocenter location due to errors in selecting the arrival time and the velocity model used. **Table 4.5** shows the values of average uncertainty for the three spatial coordinates in each sample.

Table 4.5 - Average uncertainty values for each coordinate in all three Indiana limestone samples.

Sample	Uncertainty x, mm	Uncertainty y, mm	Uncertainty z, mm
C14	0.20	0.10	0.37
C15	0.35	0.19	0.49
C16	0.26	0.14	0.39

In all samples the uncertainty in the Z-direction is the greatest, while the uncertainty in the Y-direction is the least. In two out of the three samples (C15 and C16) there are two sensors placed on the top surface of the sample to constraint the Z-direction. There are 14 sensors attached around the circumference of the sample. Also, sensors were not placed on the bottom surface of the sample which contributes to uncertainty in the Z-direction. **Fig. 4.20** and **Fig. 4.21** represent a plan and a lateral view perpendicular to the applied stress for sample C14. Both plots represent the distribution of the error ellipses which represent the uncertainties in the different spatial coordinates.

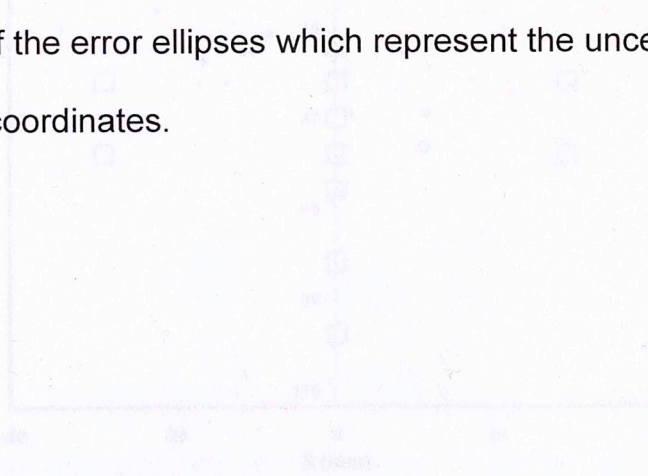


Fig. 4.21 - Lateral view perpendicular to the fracture plane for sample C14 showing uncertainties of MS events in the X-Z plane; higher uncertainties are in the Z-direction. No surface sensors are used in this sample.

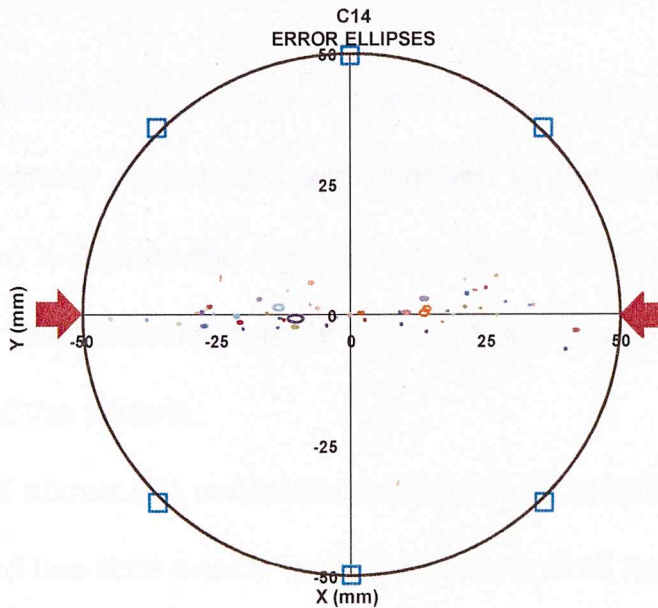


Fig. 4.20 – Plan view of sample C14 showing the uncertainties of the MS events as error ellipses; it can be observed the highest uncertainties in the X-Y plane are in the X-direction where there are no sensors attached to the sample.

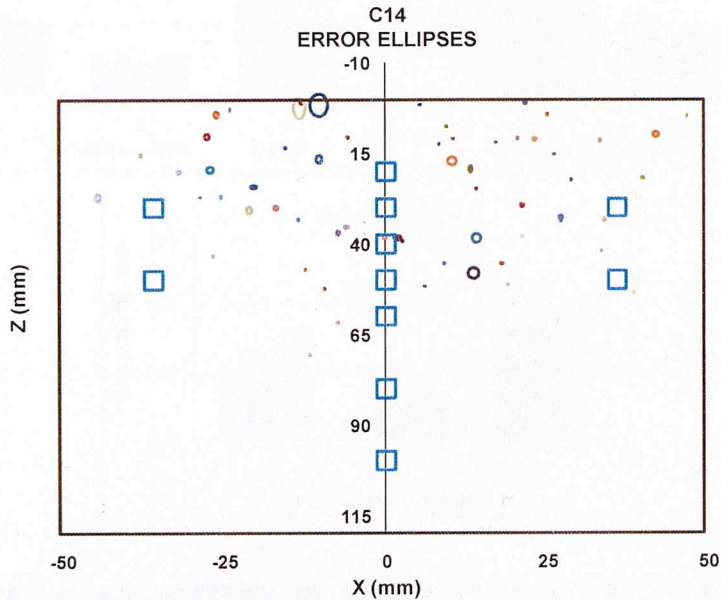


Fig. 4.21 – Lateral view perpendicular to the fracture plane for sample C14 showing uncertainties of MS events in the X-Z plane; higher uncertainties are in the Z-direction. No surface sensors are used in this sample.

Fig. 4.20 shows that in the X-Y plane the higher uncertainties are in the x-direction where no sensors are attached to the sample. Fig. 4.21 shows that in the X-Z plane the highest uncertainties are found to be in the Z-direction. For this particular sample there are no sensors attached to the upper surface of the sample.

Fig. 4.22 shows the uncertainty values in all coordinates for early, intermediate and late time events for samples C14, C15 and C16.

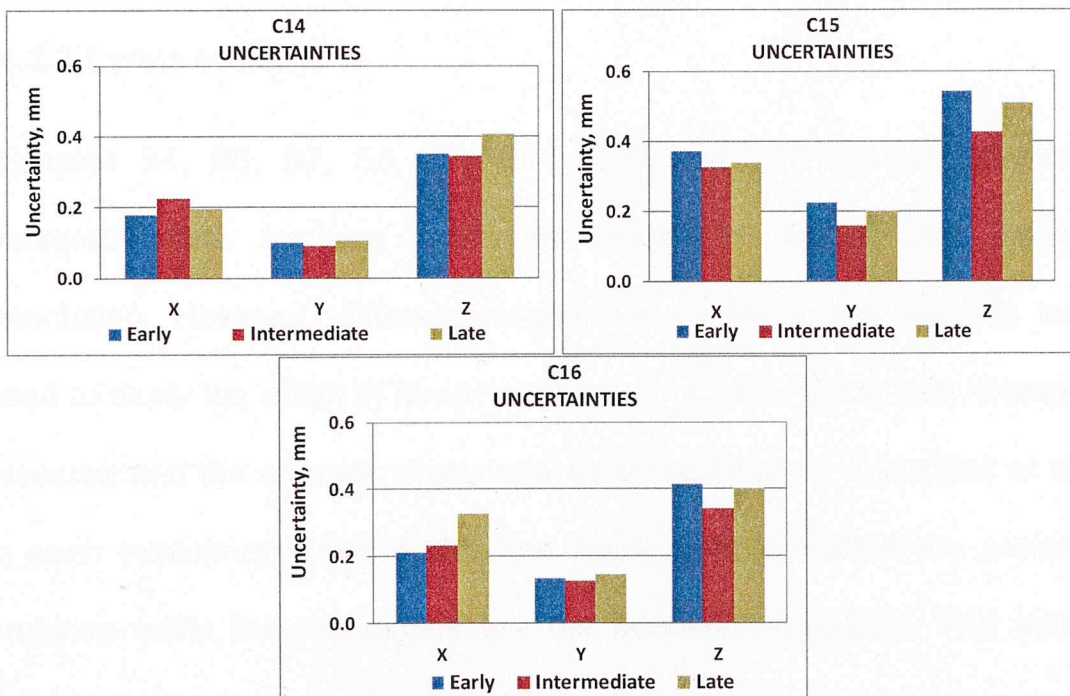


Fig. 4.22 - Average uncertainties of hypocenter locations in each coordinate indicating values for early, intermediate and late time events for samples C14, C15 and C16

From Fig. 4.22 it is clear that the highest uncertainty occurs in the Z-direction. However, uncertainties by time of occurrence do not show a

clear pattern. This indicates that while crack density increases with time its effect on attenuation has minimal effect on our ability to pick first arrivals.

Table 4.6 shows the values of the root mean square (rms) error for each Indiana Limestone sample.

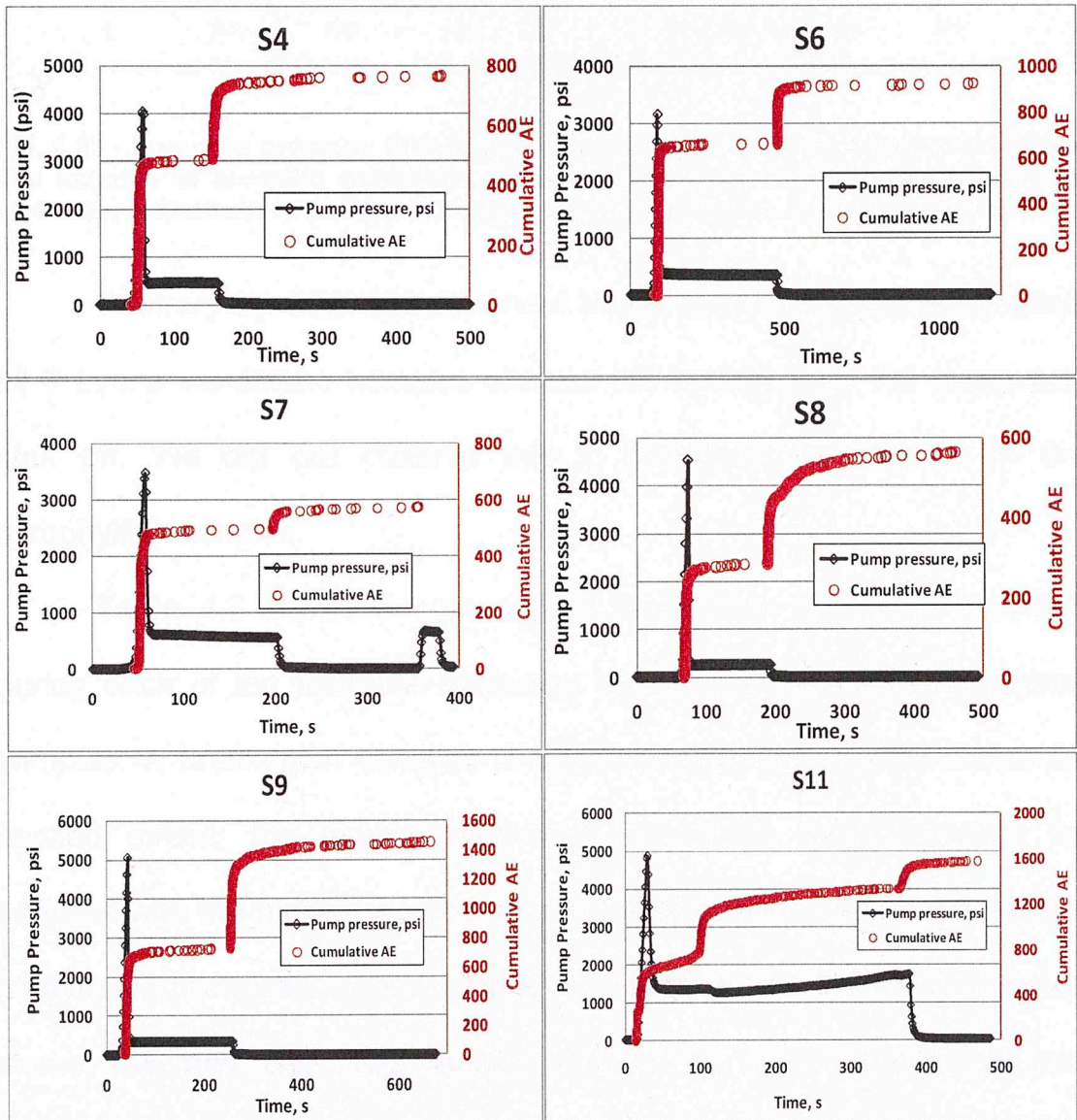
Table 4.6 - Root mean square error for each Indiana limestone sample.

Sample	rms error, mm
C14	0.44
C15	0.67
C16	0.50

4.2.2 Lyons sandstone

Samples S4, S6, S7, S8, S9, S11, S13 and S14 were hydraulically fractured while applying horizontal stress to control the fracture orientation. However, different magnitudes of horizontal stresses were used to study the effect of stress on fracture growth (**Table 3.5**). Pumping pressure and the acoustic emissions were recorded as a function of time in each experiment (**Fig. 4.23**). The black lines represent the pumping pressure while the red circles are the acoustic emissions. The events located within the sample have been divided into three parts and are represented as early time (green dots), intermediate time (orange dots) and late time (purple dots) events. Such color coding is used with the purpose of highlighting the propagation of the hydraulic fracture.

The permeability of the Lyons sandstone is 20 μD , which is three orders of magnitude lower than the permeability of the Indiana limestone, therefore a change in the distribution of microseismic events due to fluid diffusion is expected in these samples.



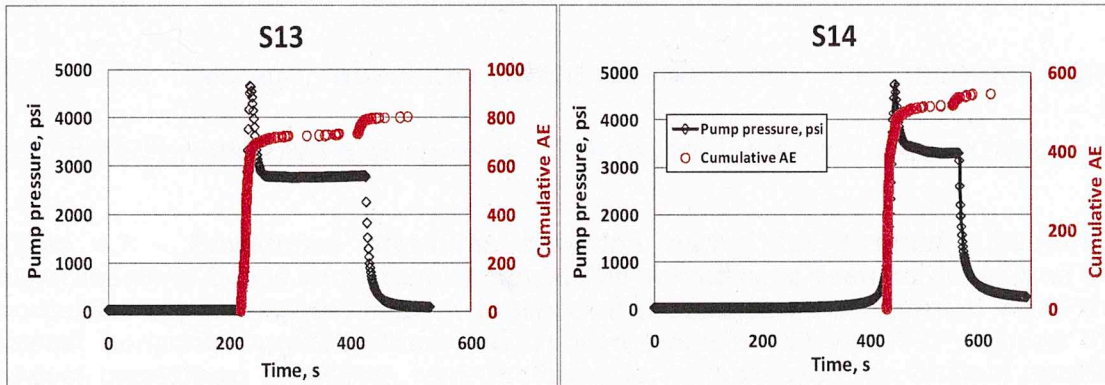


Fig. 4.23 - Pumping pressure (black) and cumulative AE (red) as a function of time. The majority of acoustic emissions are recorded before reaching the breakdown pressure. A secondary activity is noticeable in all samples once the pump is shut off.

Contrary to what was observed in the Indiana limestone samples, all 8 Lyons sandstone samples showed AE activity after the pump was shut off. We did not observe this in limestone samples or in the pyrophyllite samples.

Table 4.7 shows a summary of breakdown pressures recorded during each of the hydraulic fracturing experiments in Lyons sandstone samples. A breakdown variation is observed according to the horizontal applied stress; the lowest breakdown pressures were recorded for samples with the highest applied stress (S4, S6, S7), whereas the highest breakdown pressures were recorded for samples with the lowest applied stress (S8 and S9). The tensile strength of Lyons sandstone was measured by performing a Brazilian test on a sample representative of this lithology. The tensile strength of Lyons sandstone is 1734 psi. This value

was used to calculate the breakdown pressures for each sample (**Table 4.7**). The average absolute difference between the recorded and calculated breakdown pressures is 1919 psi for Lyons sandstone samples.

Table 4.7 - Breakdown pressures recorded during the hydraulic fracturing experiments in Lyons sandstone samples. The breakdowns seem to depend on the horizontal applied stress; highest breakdown pressures were recorded when the lowest horizontal applied stress was applied (samples S8 and S9) whereas the lowest breakdown pressures were recorded for sample with the highest applied stress (S4, S6 and S7). Breakdown pressures were calculated for each sample using the tensile strength of Lyons sandstone obtained by performing a Brazilian test on a sample representative of this lithology.

Sample	Applied stress, psi	Breakdown pressure recorded, psi	Breakdown pressure calculated, psi
S4	1040	4038	2774
S6	1080	3154	2814
S7	1160	3475	2894
S8	150	4527	1884
S9	150	5061	1884
S11	580	4873	2314
S13	580	4639	2314
S14	550	4748	2284

Fig. 4.24, Fig. 4.25 and Fig 4.26 show the plan and two lateral views of sample S4, respectively.

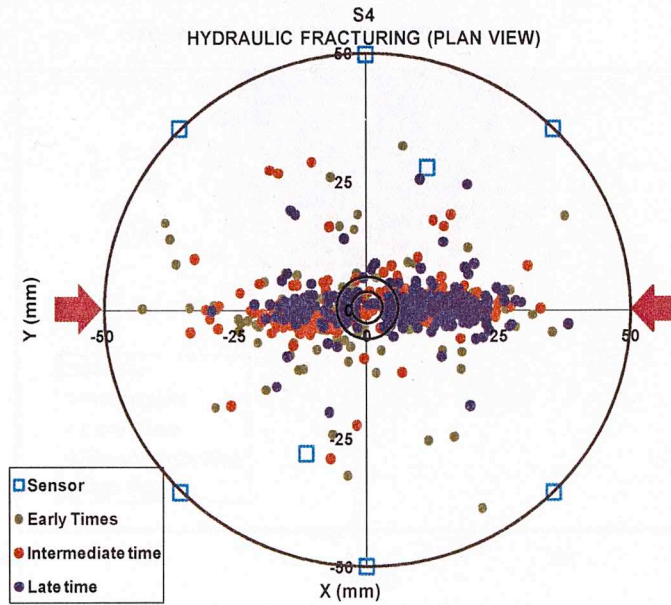


Fig. 4.24 - Plan view of sample S4 (Lyons sandstone) showing the spatial and temporal evolution of the hydraulic fracture. The green dots represent the early time events, while the orange and purple represent the intermediate and late time events, respectively. The cyan squares represent sensors attached to the sample. The red arrows represent the direction of the stress applied with a magnitude of 1040 psi. The two circles in the center of the plot represent the counter borehole and the borehole. 765 MS events were locatable within the sample.

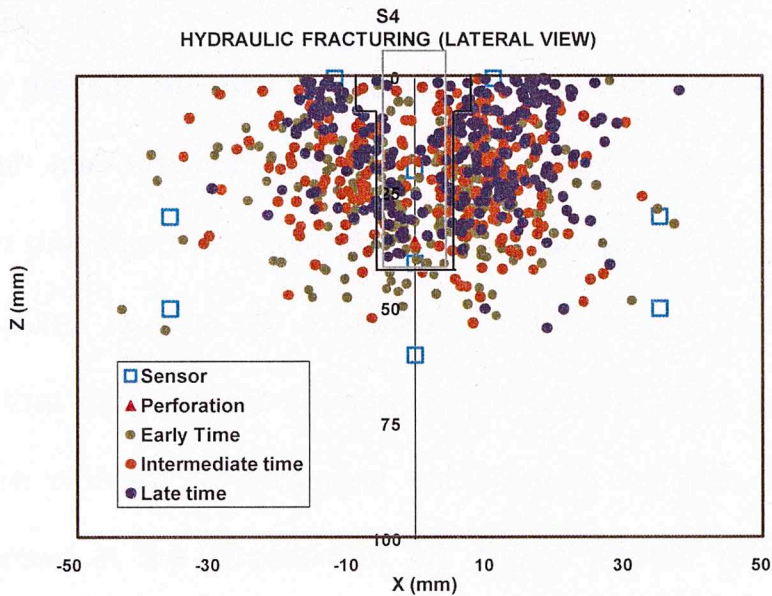


Fig. 4.25 - Lateral view of sample S4 perpendicular to the fracture plane. The red triangle represents the location of the perforations in the tubing.

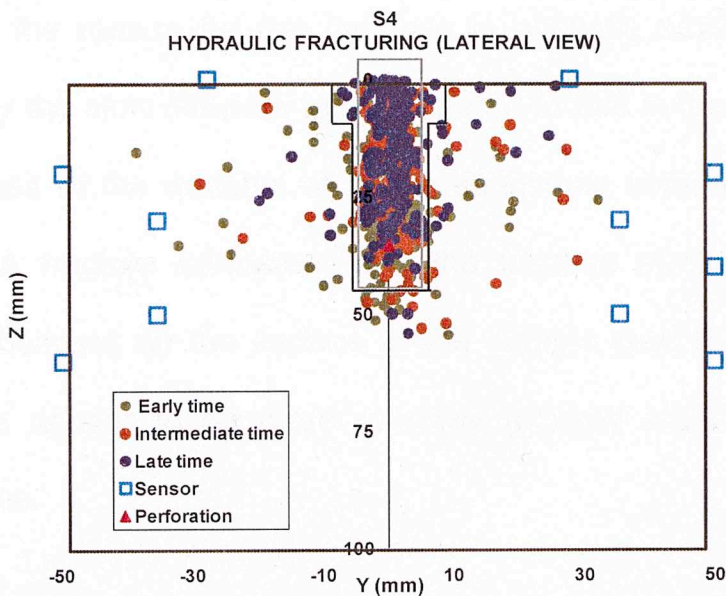


Fig. 4.26 - Lateral view of sample S4 parallel to the fracture. This view shows the development of a fracture in the direction of the stress applied with some events

out of plane. Later events , purple, are more concentrated about the hydraulic fracture plane.

The pressure/AE plot for sample S4 from **Fig. 4.23** shows that the majority of microseismic events are recorded before reaching the breakdown pressure (4038 psi). Also, secondary activity can be observed once the pump is shut off; a possible reason for this is the failure of asperities that were created during the hydraulic fracturing process during the fracture closure. As expected for isotropic samples, the hydraulic fracture grows in the direction of the stress applied (**Fig. 4.24**). The temporal evolution of the fracture shows growth away from the injection source. The fracture propagation is very similar to that on the Indiana limestone except that the number of events recorded for this lithology is far greater; the reason for this increase in acoustic emission events is explained by the slow diffusion rate compared to that in the limestone and the brittleness of the material of Lyons sandstone compared to Indiana limestone. A fracture consistent with the location of the microseismic events is observed on the surface of the sample (see **Fig. 4.27**). Later hypocenters appear to be more narrowly focused about the hydraulic fracture plane.

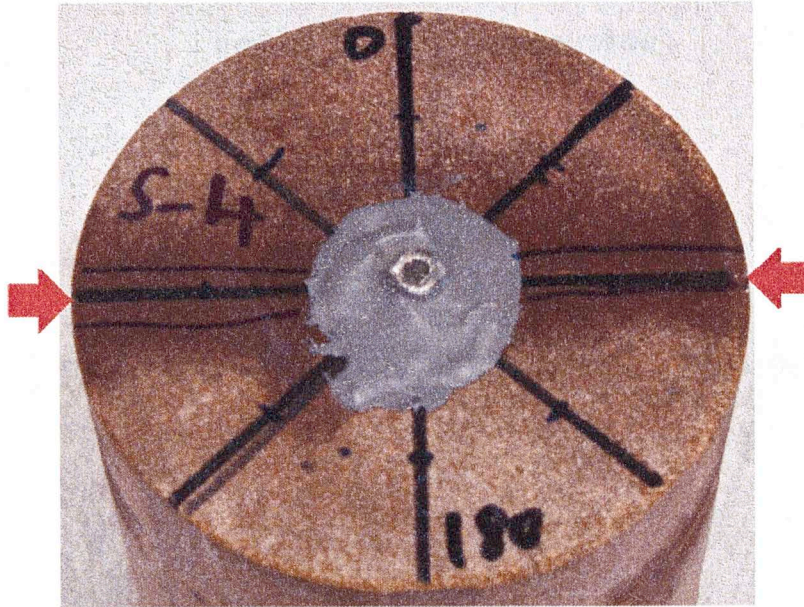


Fig. 4.27 - Surface view of sample S4 indicating the fracture growing in the direction of stress applied (red arrows). The fracture is enclosed by the dark blue lines.

Fig. 4.28, Fig. 4.29 and Fig 4.30 show the plan and two lateral views of sample S6, respectively.

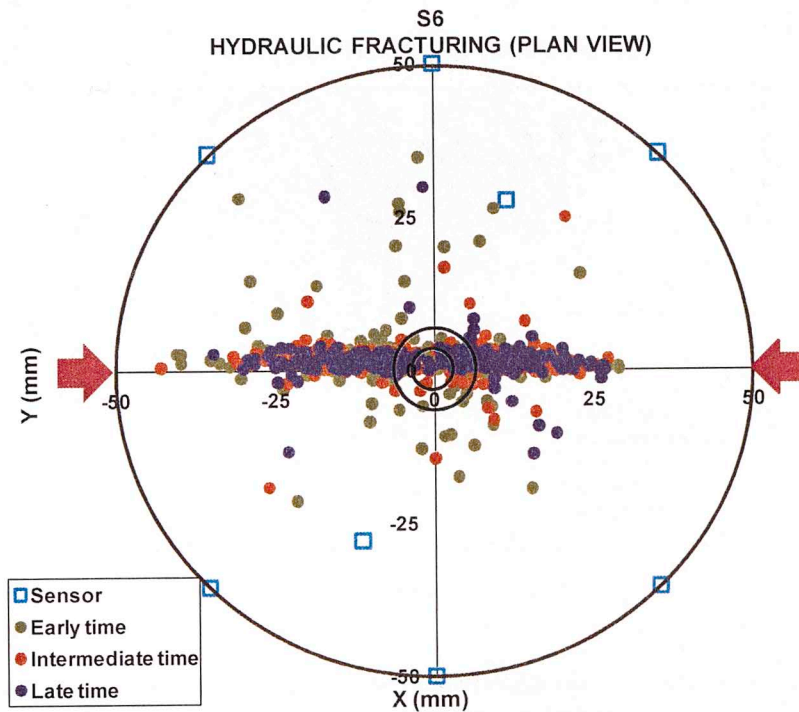


Fig. 4.28 - Plan view of sample S6 (Lyons sandstone) showing the spatial and temporal evolution of the hydraulic fracture. The green dots represent the early time events, while the orange and purple represent the intermediate and late time events, respectively. The cyan squares represent sensors attached to the sample. The red arrows represent the direction of the stress applied with a magnitude of 1080 psi. The two circles in the center of the plot represent the counter borehole and the borehole. 861 MS events were located within the sample. Note narrower purple distribution.

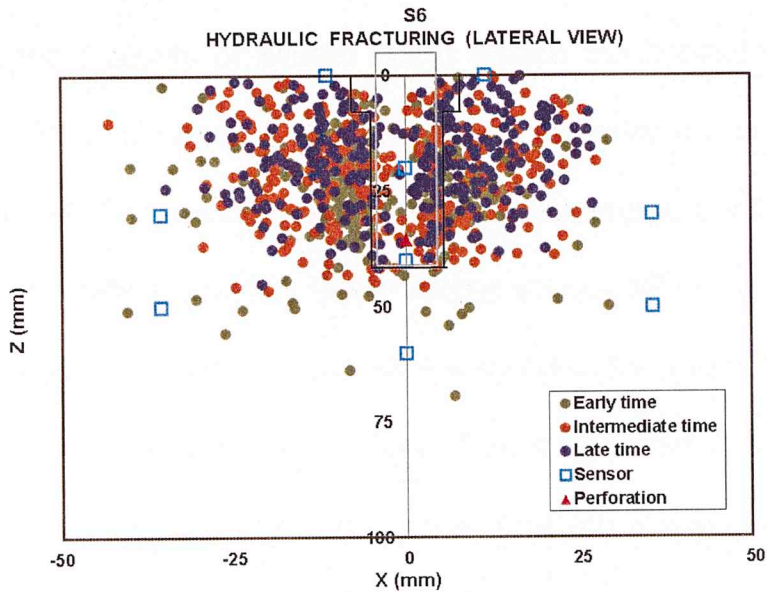


Fig. 4.29 - Lateral view of sample S6 perpendicular to the fracture plane. The red triangle represents the location of the perforations in tubing.

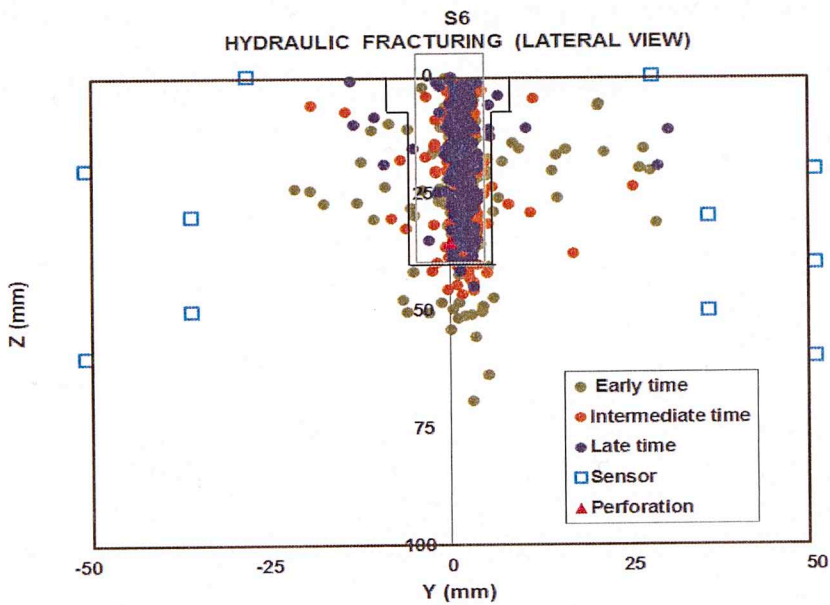


Fig. 4.30 - Lateral view of sample S6 parallel to the fracture plane. The red triangle represents the location of the perforations in tubing. Note narrowly focused late time events (purple).

Similar to sample S4, the pressure-AE plot (**Fig. 4.23**) of sample S6 shows that the majority of events occur before the breakdown pressure (3154 psi). Also, a secondary activity is observed once the pump is turned off. From **Fig. 4.28** it can be observed the development of a fracture in the direction of the stress applied. Color coding shows the occurrence of late time events (purple) in zones that were previously fractured; this late time events are confined to a narrower zone. **Fig. 4.30** shows the creation of a vertical narrow fracture with some out-of-plane events due the fluid diffusion. As for sample S4, a higher number of events were recorded for this sample compared to Indiana limestone samples (Factor of 8). When observing the surface of the sample (**Fig. 4.31**) a fracture that agrees with the location of the microseismic events is noticeable.

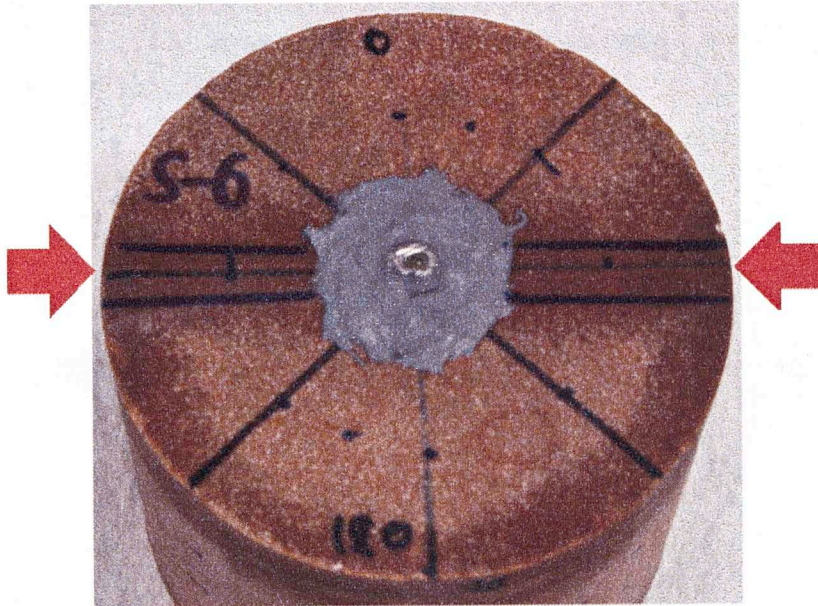


Fig. 4.31 - Surface view of sample S6 indicating the fracture growing in the direction of stress applied (red arrows). The fracture is enclosed by the dark blue lines

Fig. 4.32, Fig. 4.33 and Fig. 4.34 represent the plan, and two lateral views of sample S7, respectively.

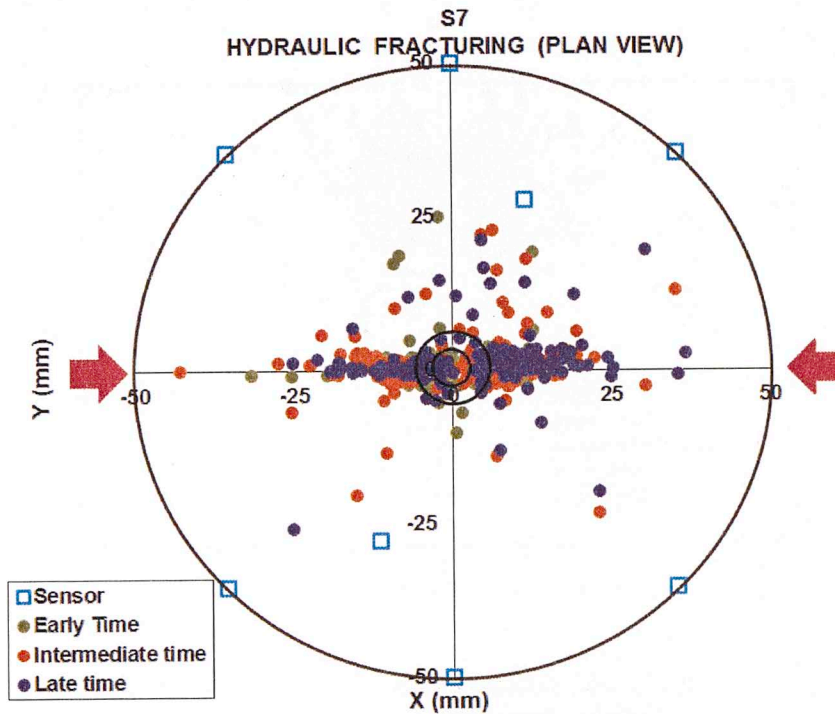


Fig. 4.32 - Plan view of sample S7 (Lyons sandstone) showing the spatial and temporal evolution of the hydraulic fracture. The green dots represent the early time events, while the orange and purple represent the intermediate and late time events, respectively. The cyan squares represent sensors attached to the sample. The red arrows represent the direction of the stress applied with a magnitude of 1160 psi. The two circles in the center of the plot represent the counter borehole and the borehole. 531 events were located within the sample.

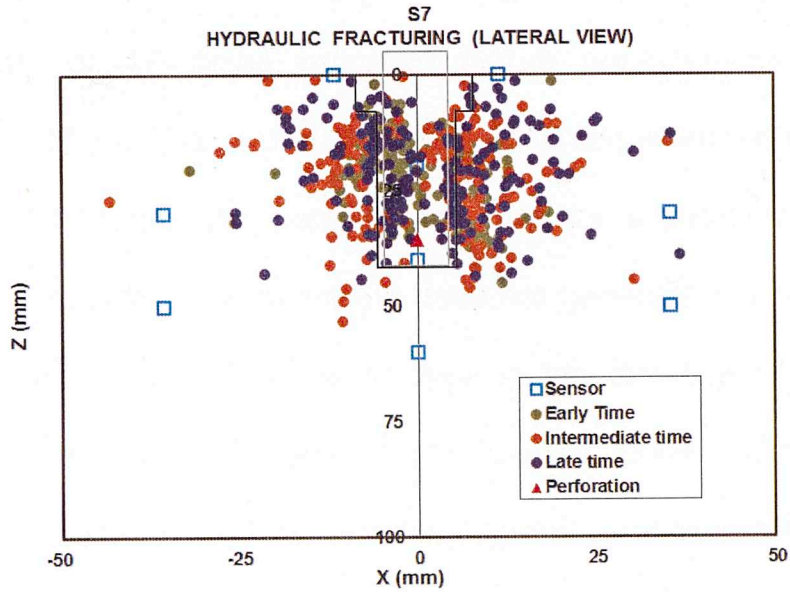


Fig. 4.33 - Lateral view of sample S7 perpendicular to the fracture plane. The red triangle represents the location of the perforations in tubing.

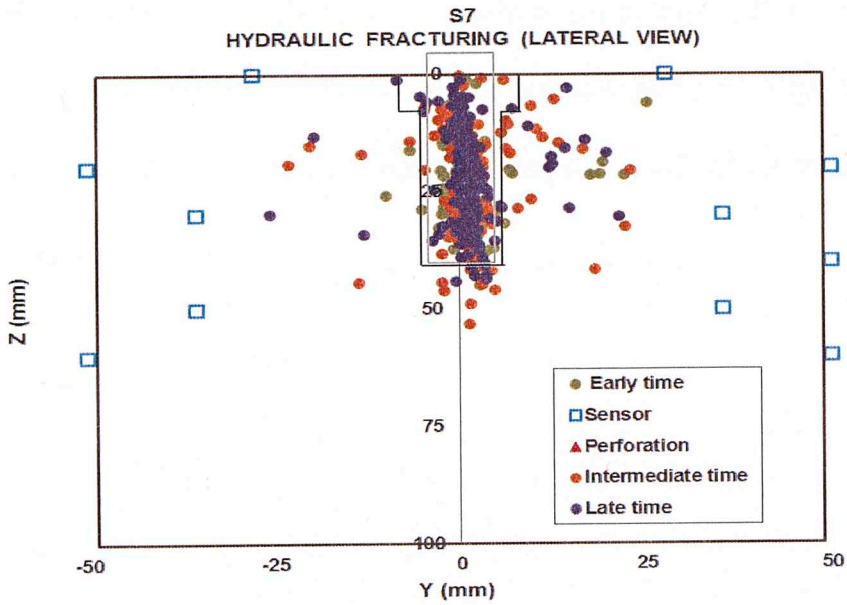


Fig. 4.34 - Lateral view of sample S7 parallel to the fracture plane. The red triangle represents the location of the perforations in tubing. Notice the narrower distribution of purple events.

Again, the pressure-AE plot for sample S7 from **Fig. 4.23** shows the majority of AE being recorded before reaching the breakdown pressure (3475 psi). Secondary activity is observed when the pump is shut off (**Fig. 4.23**). Later, the pumping resumes for a short period of time causing an increase in pressure but does not generate any AE. **Fig. 4.32** shows the development of the fracture in the direction of the applied stress. The temporal evolution of the fracture (color coding) shows it grows as it gets away from the injection source. However, some late time events occurred in zones previously fractured. **Fig. 4.34** shows a narrow fracture with some events out-of-plane due to the diffusion of the fracturing fluid. Also, the locations of the events show an inclination at the bottom of the fracture. Physical observation of the sample surface (**Fig. 4.35**) shows an agreement between the actual fracture and the location of the microseismic events.

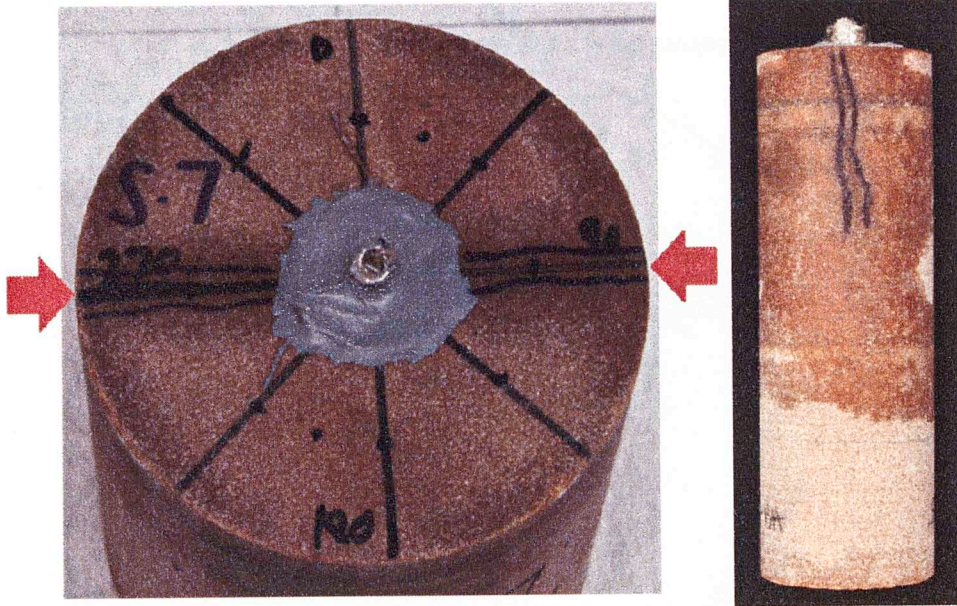


Fig. 4.35 – Left) Surface view of sample S7 indicating the fracture growing in the direction of stress applied (red arrows). The fracture is enclosed by the dark blue lines. Right) One inch diameter plug taken at the borehole position (Y-Z view) showing the induced fracture enclosed by the black lines.

Fig. 4.36, Fig. 4.37 and Fig. 4.38 show the plan and two lateral views for sample S8, respectively. However, the horizontal stress applied on this sample is only 150 psi.

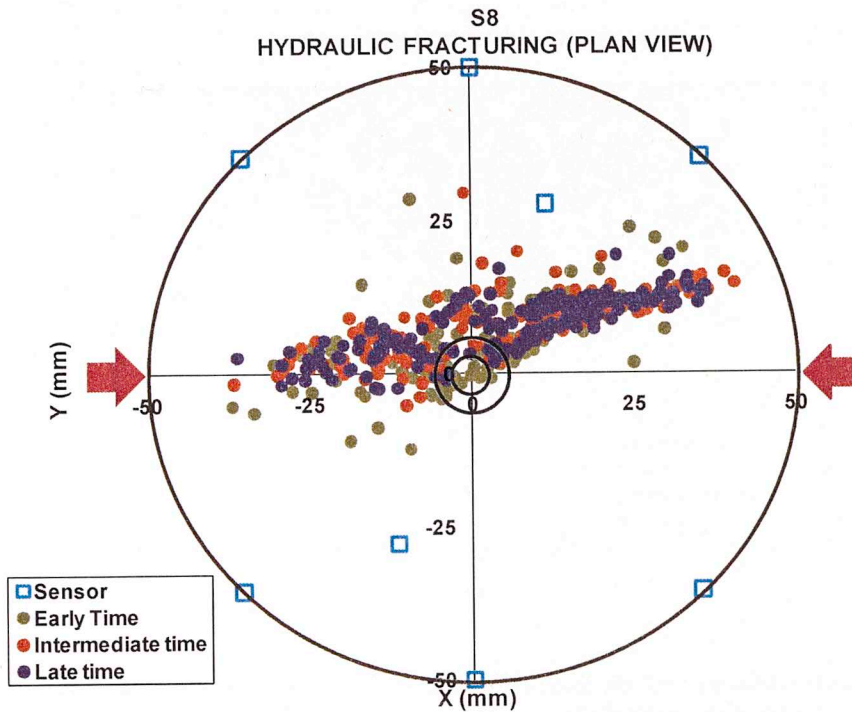


Fig. 4.36 - Plan view of sample S8 (Lyons sandstone) showing the spatial and temporal evolution of the hydraulic fracture. The green dots represent the early time events, while the orange and purple represent the intermediate and late time events, respectively. The cyan squares represent sensors attached to the sample. The red arrows represent the direction of the stress applied with a magnitude of 150 psi. The two circles in the center of the plot represent the counter borehole and the borehole. Note the orientation of the fracture is at an angle to the applied stress.

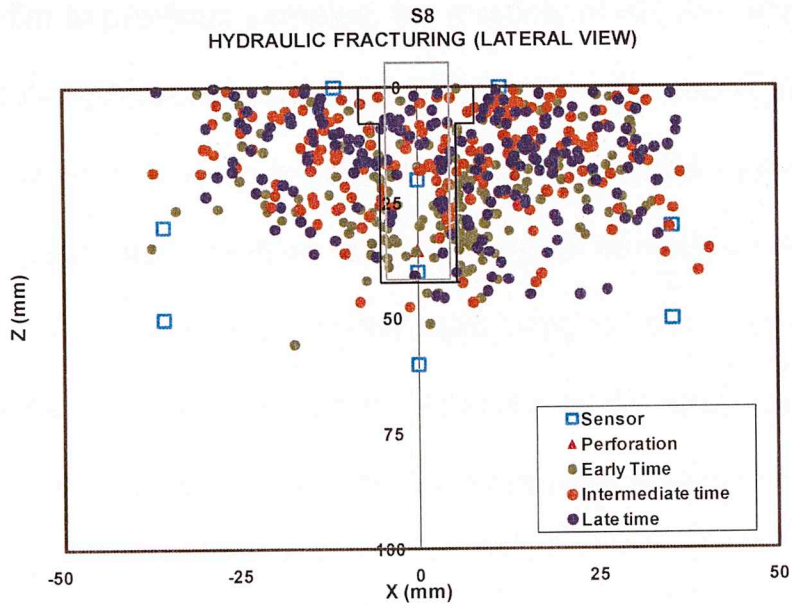


Fig. 4.37 - Lateral view of sample S8 perpendicular to the applied stress direction. The red triangle represents the location of the perforations in tubing.

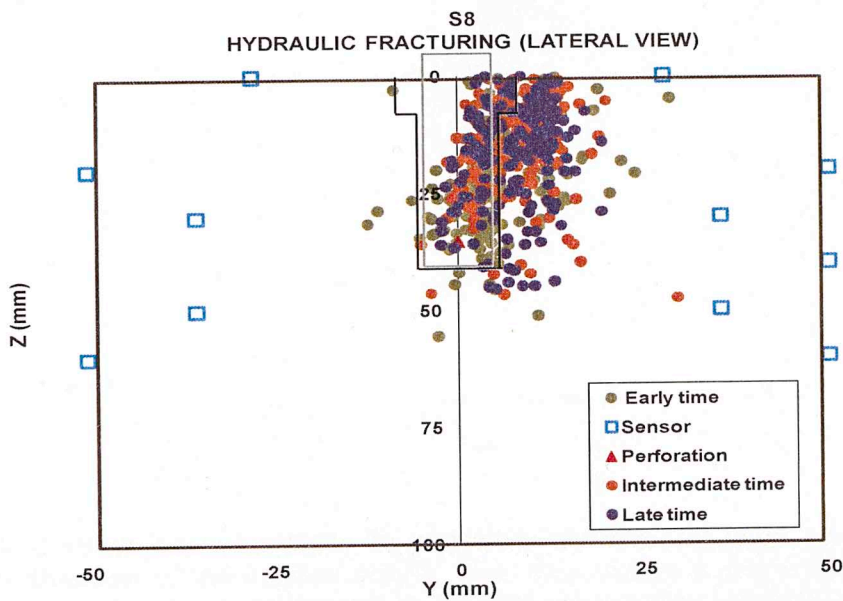


Fig. 4.38 - Lateral view of sample S8 parallel to the applied stress direction. The red triangle represents the location of the perforations in tubing. An apparent wider zone is evident due the out of plane growth of the fracture.

Similar to previous samples, the majority of AE are recorded before the breakdown pressure is reached (4527 psi) and a secondary activity is noticeable when the pump is shut off. From **Fig. 4.36** it can be observed that the hydraulic fracture does not follow a path completely parallel to the direction of the stress applied; the right wing of the created hydraulic fracture deviates about 25° from the direction of the stress applied. From **Fig. 4.38** we can observe the hydraulic fracture is inclined with respect to the vertical axis.

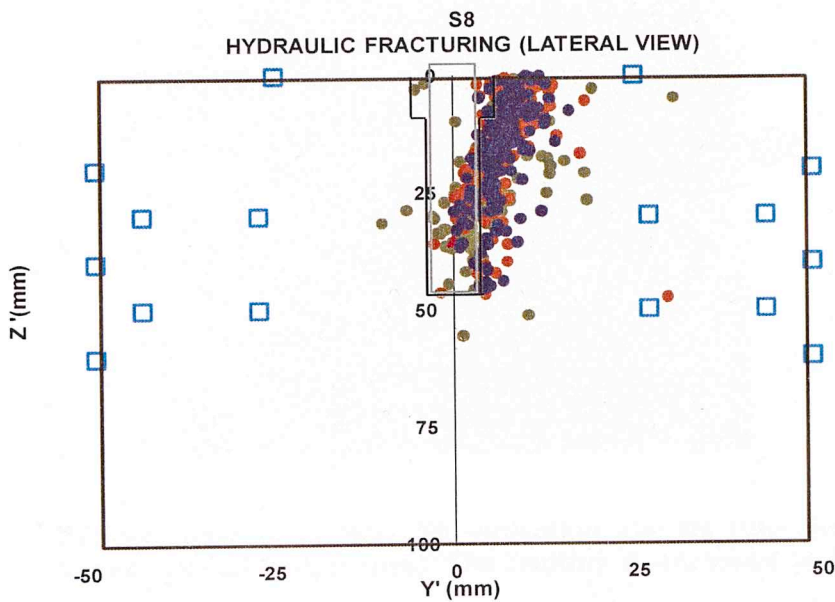


Fig. 4.39 - Lateral view of sample S8 parallel to the fracture plane which is 10° off from the direction of the applied stress. This view shows a much thinner width of the microseismic cloud compared to the apparent width observed in the view parallel to the applied stress. It also shows a growth of a fracture that is inclined with respect to the vertical axis.

Fig. 4.39 shows a view parallel to the fracture plane showing the real width of the microseismic cloud which is thinner than the width

observed in **Fig. 4.38** which is a “false” zone due to the out of plane growth of the fracture. The low differential stress on the sample appears to be insufficient to control the orientation of the hydraulic fracture. The stimulated reservoir volume (SRV) also appears greater than SRV for high applied stress tests. Observation of the surface sample (**Fig. 4.40**) shows an agreement with the location of the microseismic events.

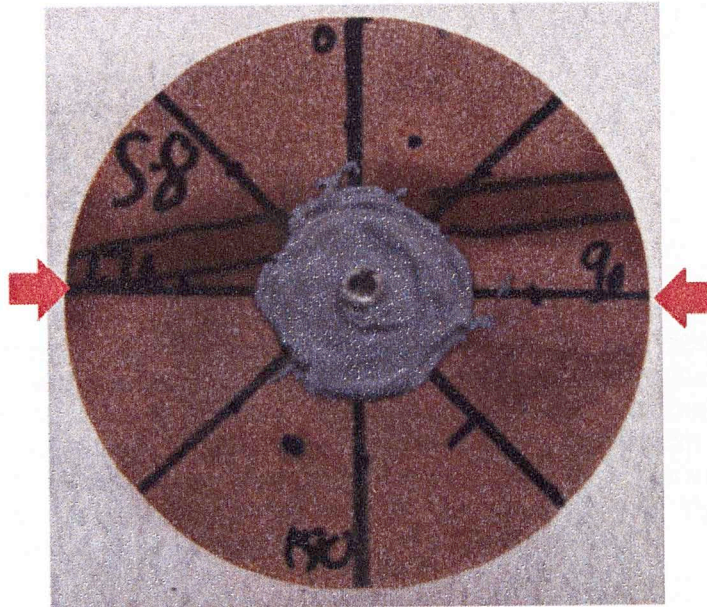


Fig. 4.40 - Surface view of sample S8 indicating the fracture growing in the direction of stress applied (red arrows). The fracture is enclosed by the dark blue lines

Fig. 4.41, Fig. 4.42 and Fig. 4.43 show the plan and two lateral views for sample S9, respectively. However, the horizontal stress applied on this sample is 150 psi.

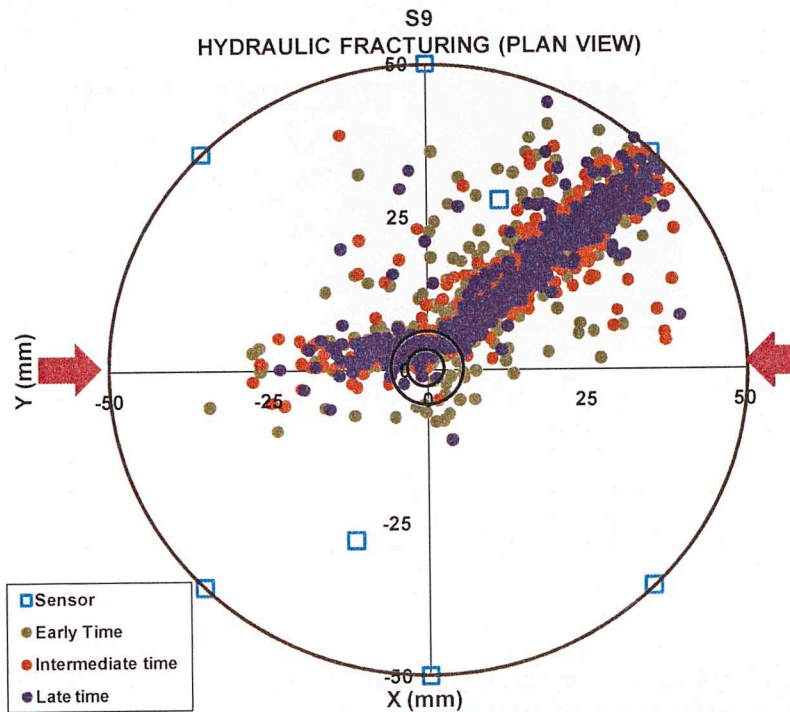


Fig. 4.41 - Plan view of sample S9 (Lyons sandstone) showing the spatial and temporal evolution of the hydraulic fracture. The green dots represent the early time events, while the orange and purple represent the intermediate and late time events, respectively. The cyan squares represent sensors attached to the sample. The red arrows represent the direction of the stress applied with a magnitude of 150 psi. The two circles in the center of the plot represent the counter borehole and the borehole. Asymmetrical wing development and note right wing is not parallel to the applied stress direction.

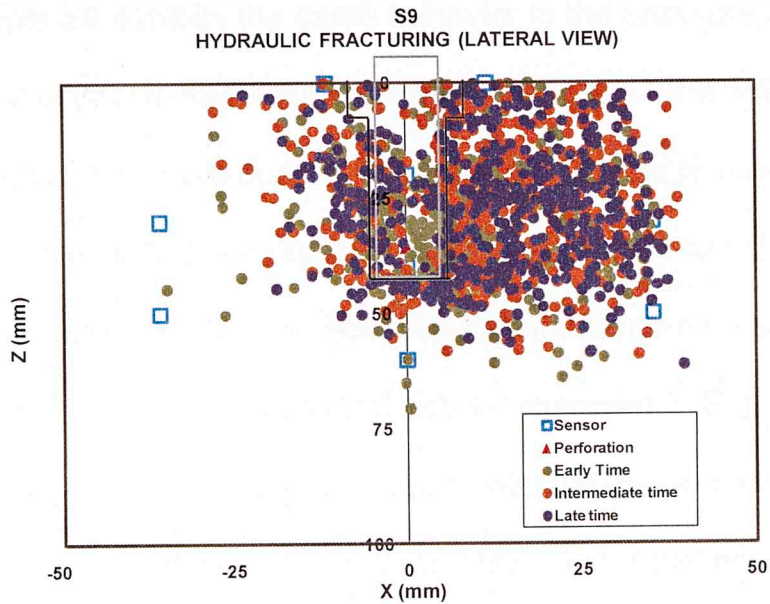


Fig. 4.42 - Lateral view of sample S9 perpendicular to the applied stress. The red triangle represents the location of the perforations in the tubing. It is evident that the left wing of the hydraulic fracture is underdeveloped in comparison to the right wing.

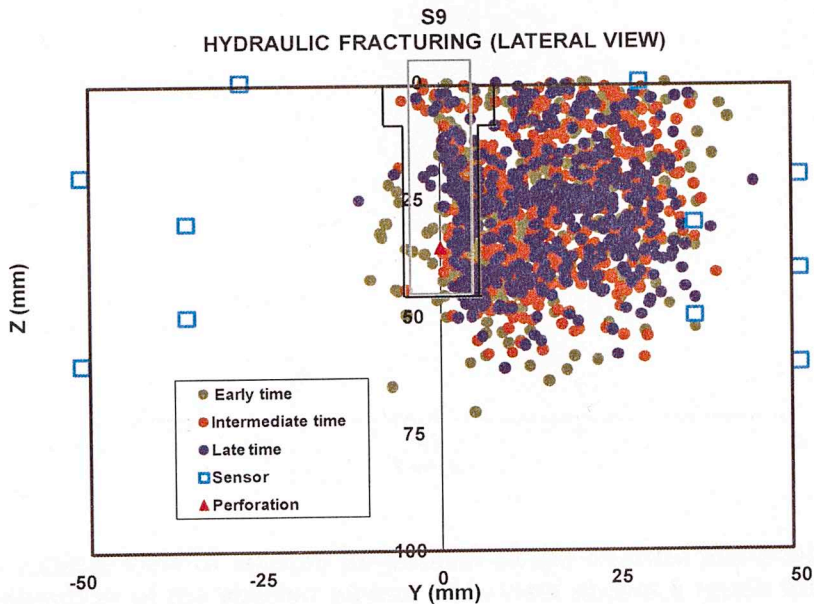


Fig. 4.43 - Lateral view of sample S9 parallel to the applied stress. The red triangle represents the location of the perforations in the tubing. Out of plane growth of the sample give this apparent wider process zone.

Sample S9 exhibits the same behavior in the pressure-AE plot (Fig. 4.23) as the previous sandstone samples; almost all the MS events are recorded before the breakdown pressure (5061 psi) is reached. Also, the secondary burst of MS events is observed when the pump is shut off. Samples S8 and S9 do not have hydraulic fractures parallel to the orientation of the stress applied (150 psi) as observed in Fig. 4.41; the left side of the hydraulic fracture coincides with the direction of the stress applied whereas the right wing deviates about 45°. Also, the length of the right side wing is considerable greater than that of the left side wing.

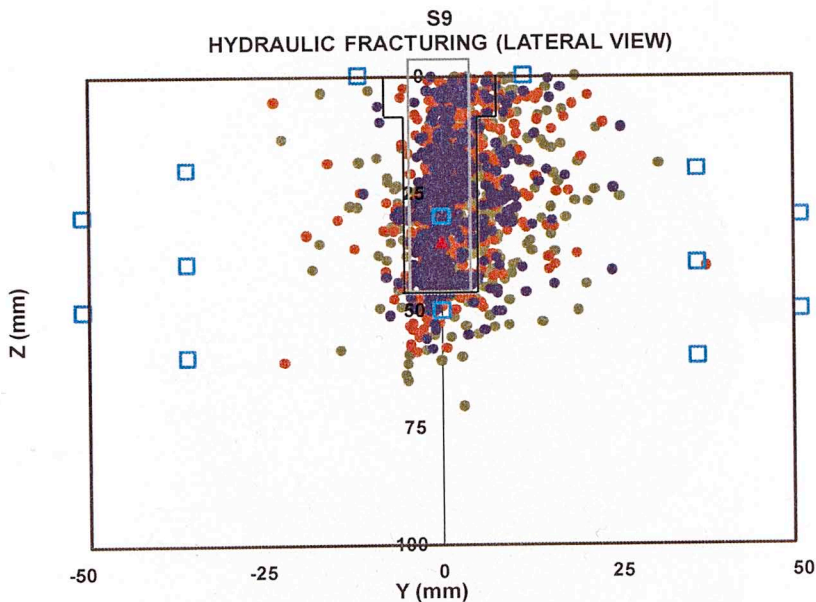


Fig. 4.44 - Lateral view of sample S9 parallel to the fracture plane which is 45° off from the direction of the applied stress. This view shows a much thinner width of the process zone compared to the apparent width observed in the view parallel to the applied stress. However, the width of the process zone is biased since the left wing is not aligned with the right wing which leads to observation of a wider zone.

Fig. 4.44 shows a view parallel to the right wing orientation of the fracture, which is 45° from the direction of applied stress. This view shows a real width of the process zone which is smaller if compared to the zone width observed in **Fig. 4.43**. However, the width of the process zone is biased since the right wing is not aligned with the left wing. The low value of applied stress on the sample seems to be insufficient to control the orientation of the hydraulic fracture and leads to a greater SRV. **Fig. 4.45** shows the surface of the sample indicating an agreement between the fracture and the location of the microseismic events.

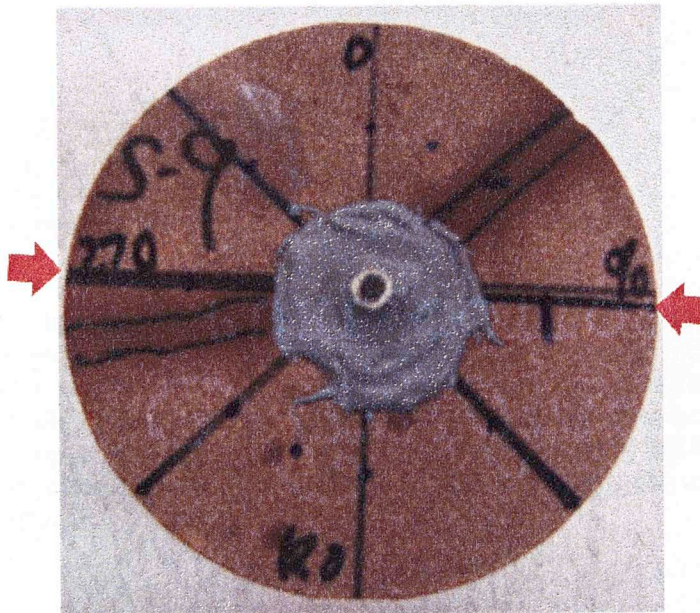


Fig. 4.45 - Surface view of sample S9 indicating the fracture growing in the direction of stress applied (red arrows). The fracture is enclosed by the dark blue lines

Fig. 4.46, Fig. 4.47 and Fig. 4.48 show the plan and two lateral views for sample S11, respectively. However, the horizontal applied stress on this sample is 580 psi.

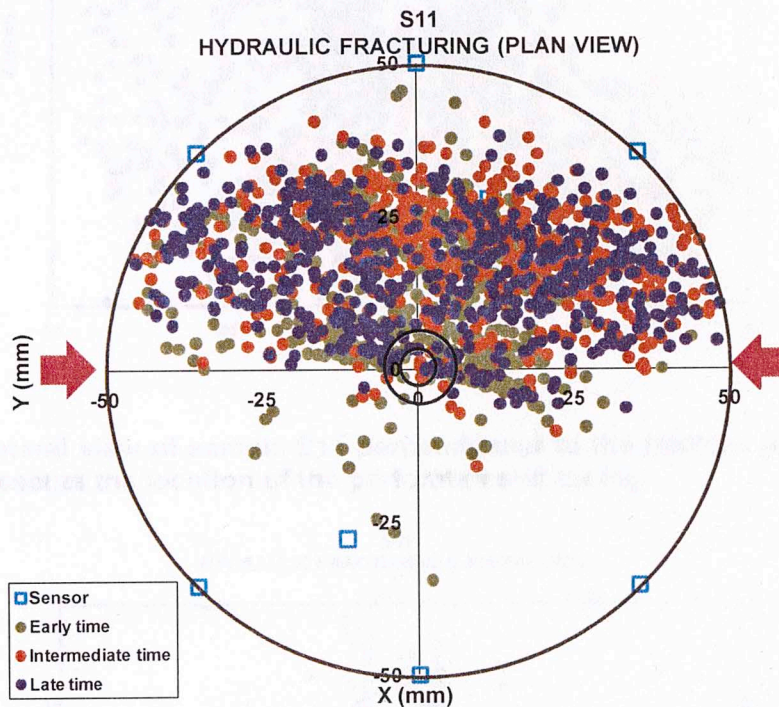


Fig. 4.46 - Plan view of sample S11 (Lyons sandstone) showing the spatial and temporal evolution of the hydraulic fracture. The green dots represent the early time events, while the orange and purple represent the intermediate and late time events, respectively. The cyan squares represent sensors attached to the sample. The red arrows represent the direction of the stress applied with a magnitude of 580 psi. The two circles in the center of the plot represent the counter borehole and the borehole.

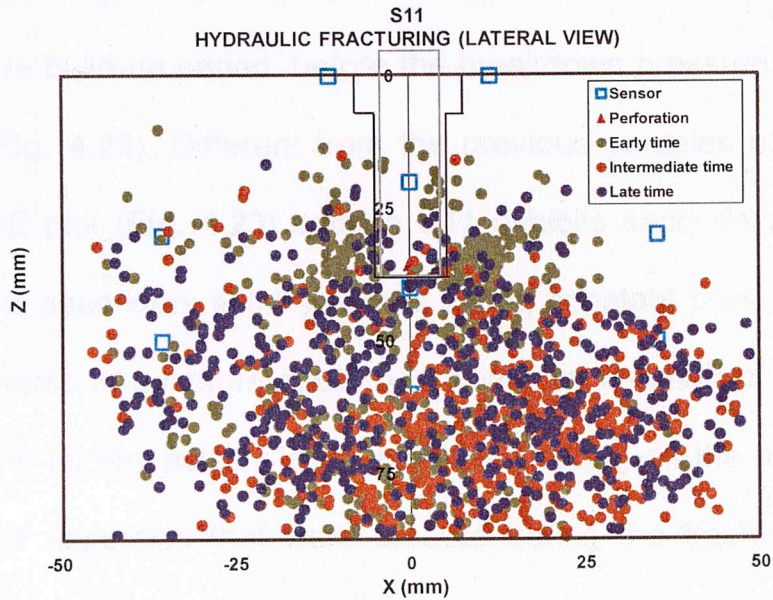


Fig. 4.47 - Lateral view of sample S11 perpendicular to the fracture plane. The red triangle represents the location of the perforations in tubing.

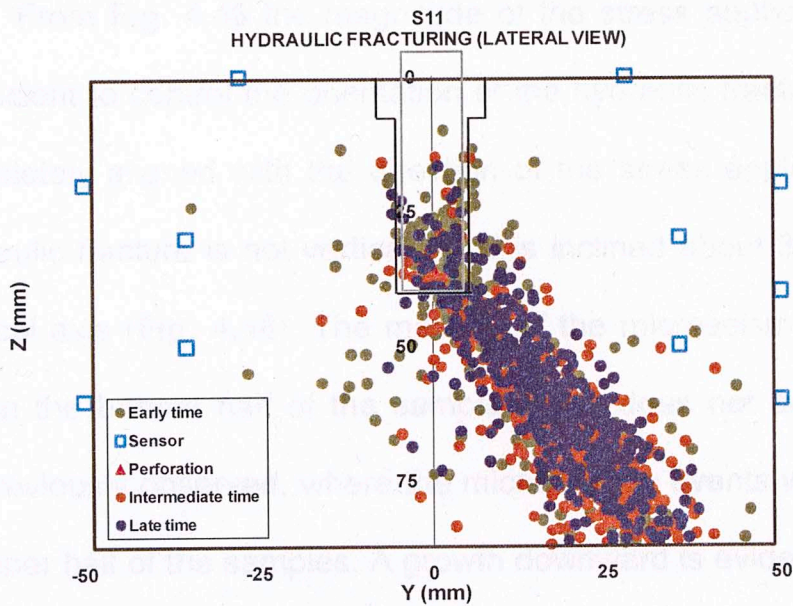


Fig. 4.48 - Lateral view of sample S11 parallel to the fracture plane. The red triangle represents the location of the perforations in the tubing. Note the downward growth.

Similar to previous sandstone samples, the MS events occur during the pressure build-up period, before the breakdown pressure (4873 psi) is reached (**Fig. 4.23**). Different from the previous samples examined, the pressure/AE plot (**Fig. 4.23**) sample S11 exhibits secondary and tertiary activity. The secondary activity occurs during constant pressure period; a small decrease in pressure could be caused by creation of new fracture volume. The tertiary activity is the result of shutting off the pump, leading to failure of asperities that were created during the fracturing process. Sample S11 was loaded with an intermediate value of horizontal stress, 580 psi compared to the 150 and 1100 psi used on the other sandstone samples. From **Fig. 4.46** the magnitude of the stress applied appears to be insufficient to control the orientation of the hydraulic fracture since it is not completely aligned with the direction of the stress applied. However the hydraulic fracture is not vertical but it is inclined about 30° respect to the vertical axis (**Fig. 4.48**). The majority of the microseismic events are located in the bottom half of the sample which does not agree with the trends previously observed, where the microseismic events were confined to the upper half of the samples. A growth downward is evident which may be caused by preexisting flaws in the sample. **Fig. 4.49** shows a lateral view (Y-Z view) showing an agreement between the hydraulic fracture and

the location of the MS events. Also it can be observed the fracture developed downwards, toward the lower permeable band (Fig. 4.49).

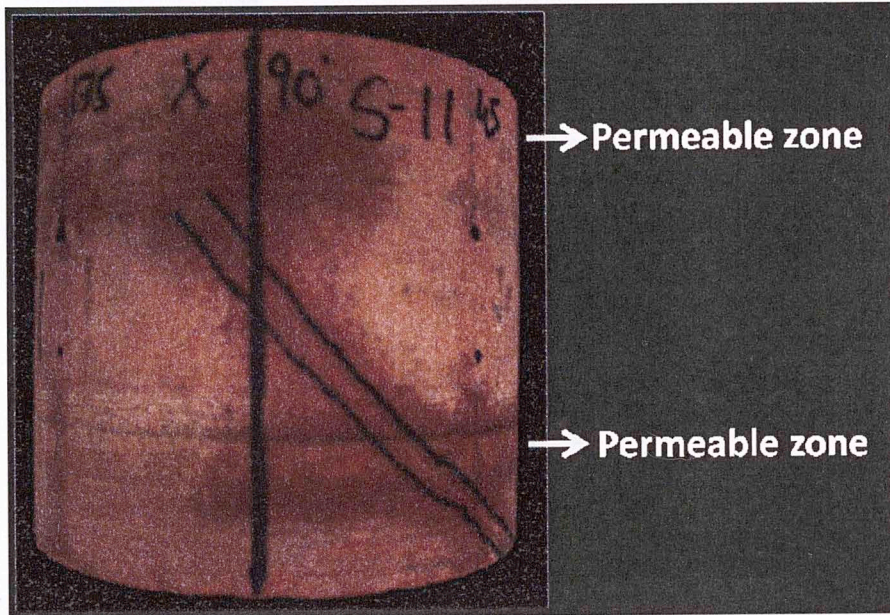


Fig. 4.49 - Lateral view of sample S11 showing the induced hydraulic fracture enclosed by the two black lines. Good agreement with physical fracture and microseisms locations.

Fig. 4.50, Fig. 4.51 and Fig. 4.52 show the plan and two lateral views for sample S13, respectively. However, the horizontal applied stress on this sample is 580 psi.

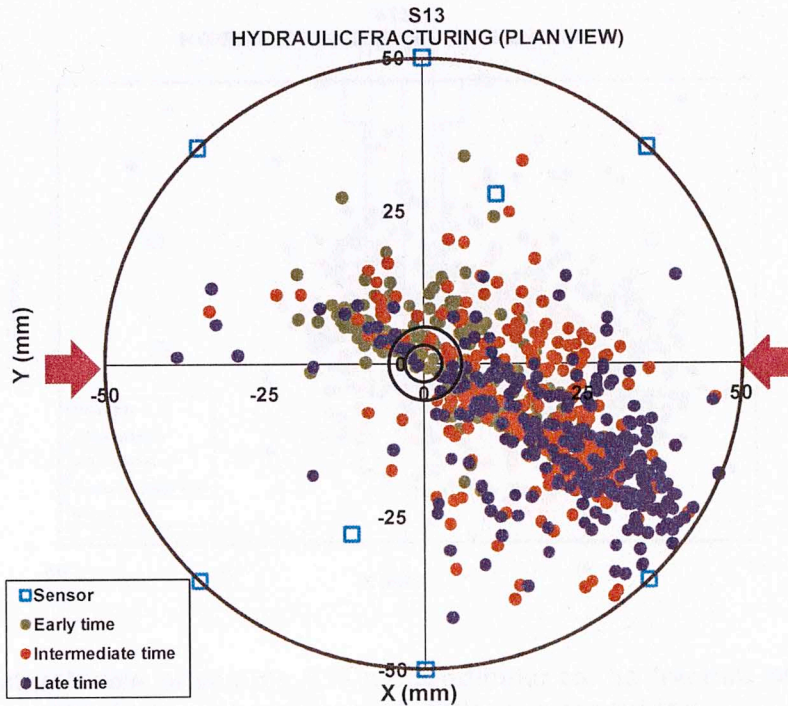


Fig. 4.50 - Plan view of sample S13 (Lyons sandstone) showing the spatial and temporal evolution of the hydraulic fracture. The green dots represent the early time events, while the orange and purple represent the intermediate and late time events, respectively. The cyan squares represent sensors attached to the sample. The red arrows represent the direction of the stress applied with a magnitude of 580 psi. The two circles in the center of the plot represent the counter borehole and the borehole. Note the departure of the fracture direction from the applied stress and the asymmetric wing development.

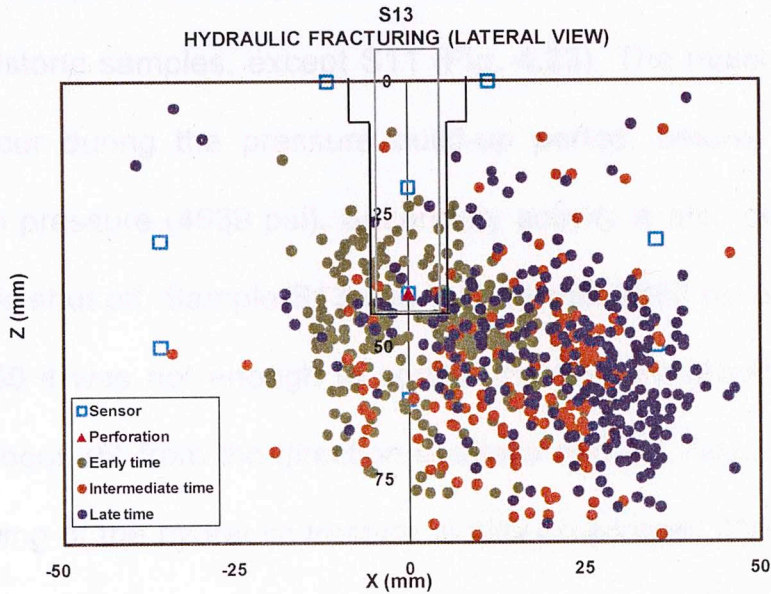


Fig. 4.51 - Lateral view of sample S13 perpendicular to the fracture plane. The red triangle represents the location of the perforations in the tubing.

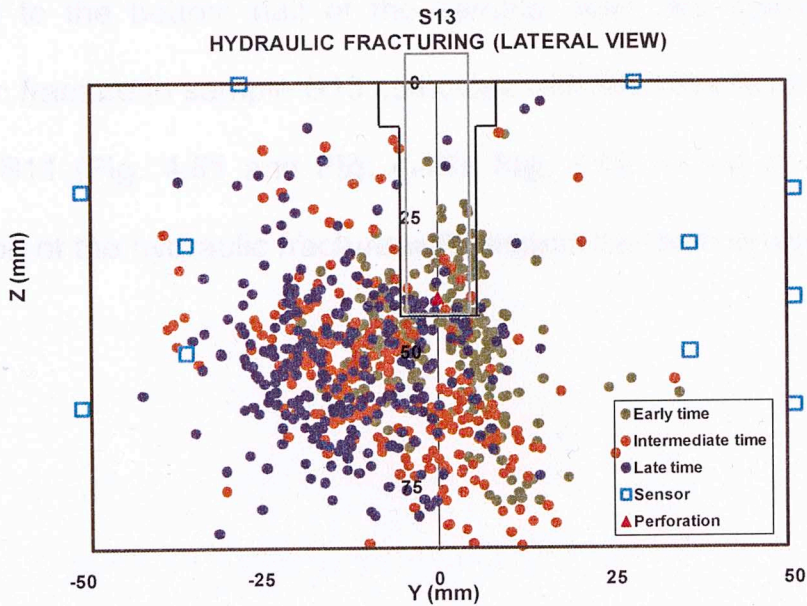


Fig. 4.52 - Lateral view of sample S13 parallel to the fracture plane. The red triangle represents the location of the perforations in the tubing. Note the downward growth and because of the projection a false width of the fractured zone is observed.

For sample S13, the pressure-AE plot behaves very similar to the other sandstone samples, except S11 (**Fig. 4.23**). The majority of the MS events occur during the pressure build-up period, before reaching the breakdown pressure (4639 psi). Secondary activity is also observed once the pump is shut off. Sample S13 was loaded with 2000 psi and according to **Fig. 4.50** it was not enough to control the fracture orientation since it deviates about 35° from the direction of stress applied. Also, it seems only the right wing of the hydraulic fracture is fully developed. The color coding indicates the temporal evolution of the fracture; it grows away from the injection source. Just like in sample S11, the majority of the events are confined to the bottom half of the sample. Also, the orientation of the hydraulic fracture in sample S13 coincides with the orientation observed in sample S11 (**Fig. 4.51** and **Fig. 4.46**). **Fig. 4.52** shows an indication of inclination of the hydraulic fracture with respect the vertical axis.

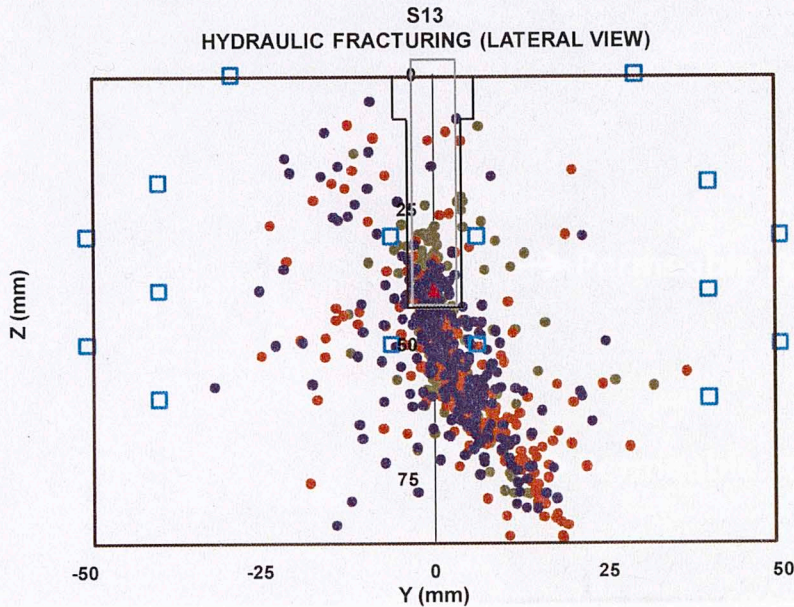


Fig. 4.53 - Lateral view of sample S13 parallel to the fracture plane. The red triangle represents the location of the perforations in the tubing. Note the downward growth and because of the projection a false width of the fractured zone is observed.

Fig. 4.53 shows a view parallel to the fracture plane, which is 35° from the direction of applied stress. This view shows a real width of the process zone which is smaller if compared to the zone width observed in **Fig. 4.52**. Physical observation of the sample surface supports this; **Fig. 4.54** shows a lateral view of sample S13 (Y-Z plane) where an inclined and concave fracture is enclosed by the black lines.

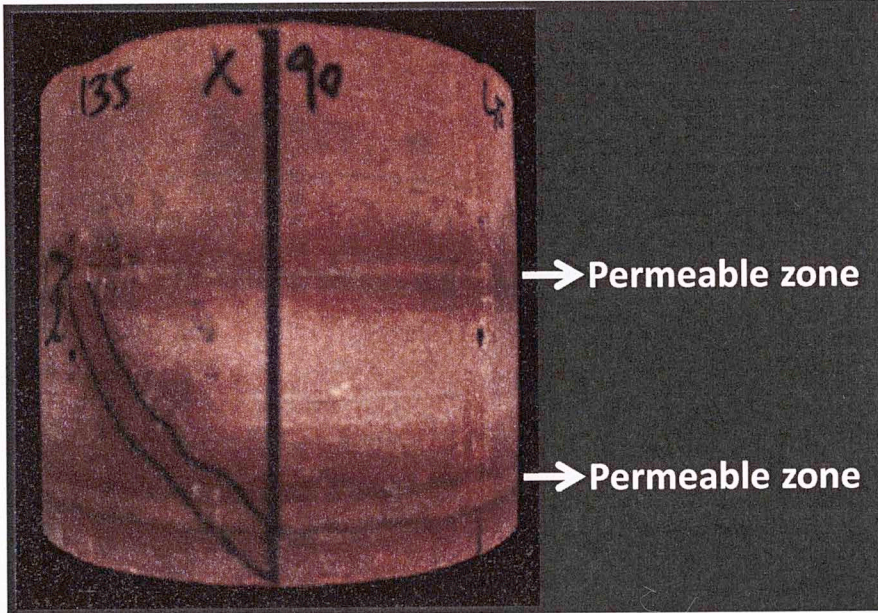


Fig. 4.54 - Lateral view (Y-Z plane) of sample S13 showing an inclined and concave fracture. Microseisms locations agree with the observed visual fracture orientation and location.

Fig. 4.55, Fig. 4.56 and Fig. 4.57 represent the plan and two lateral views of sample S14 which was loaded with 550 psi.

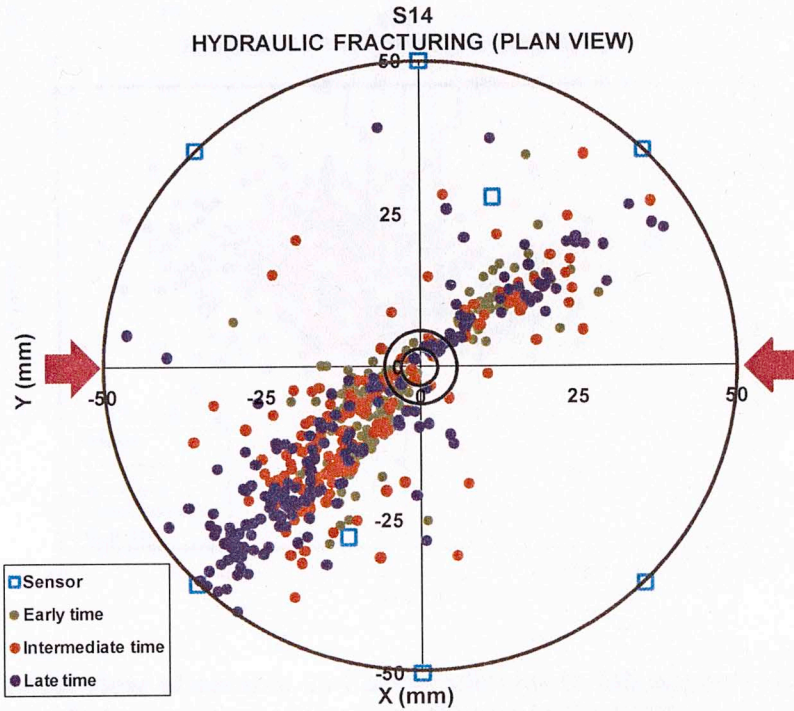


Fig. 4.55 - Plan view of sample S14 (Lyons sandstone) showing the spatial and temporal evolution of the hydraulic fracture. The green dots represent the early time events, while the orange and purple represent the intermediate and late time events, respectively. The cyan squares represent sensors attached to the sample. The red arrows represent the direction of the stress applied with a magnitude of 550 psi. The two circles in the center of the plot represent the counter borehole and the borehole. Again, asymmetric wing development and deviation of fracture direction from the applied stress direction is observed.

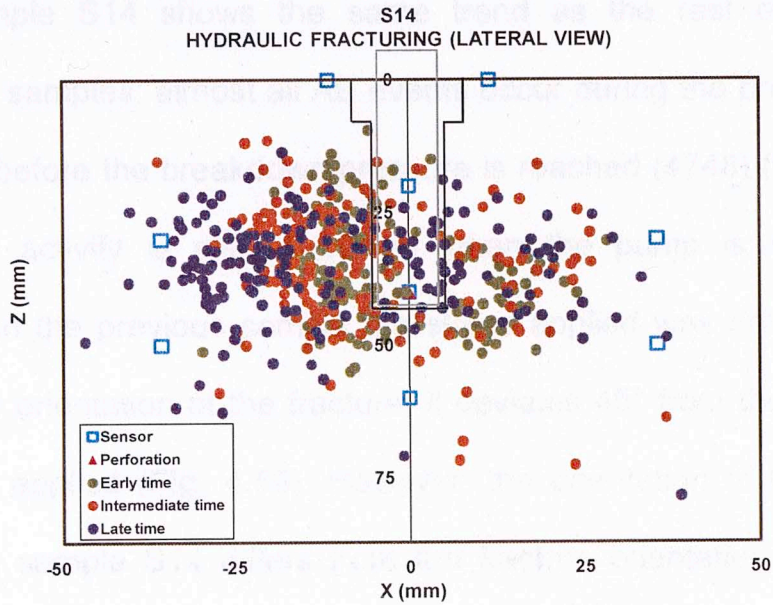


Fig. 4.56 - Lateral view of sample S14 perpendicular to the applied stress. The red triangle represents the location of the perforations in the tubing.

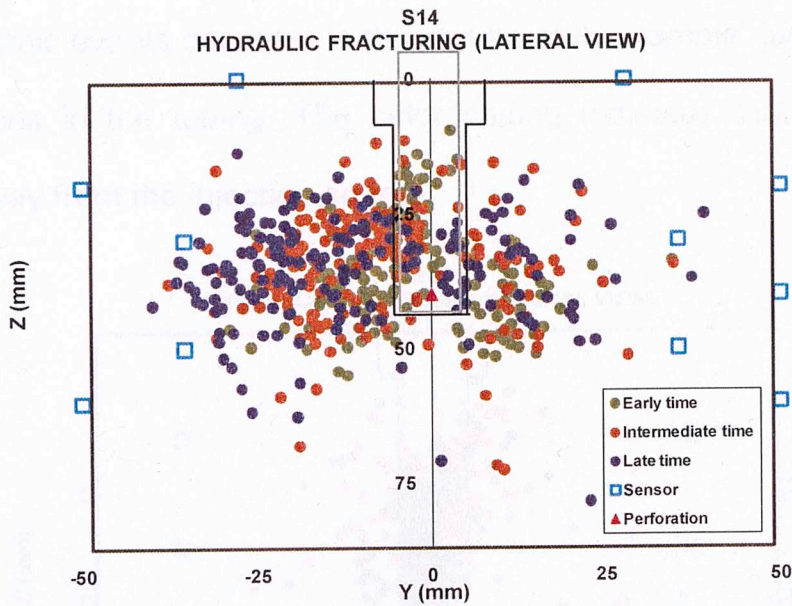


Fig. 4.57 - Lateral view of sample S14 parallel to the applied stress. The red triangle represents the location of the perforations in the tubing. Out of plane projection gives a false representation of process zone.

Sample S14 shows the same trend as the rest of the Lyons sandstone samples; almost all AE events occur during the pressure build-up period before the breakdown pressure is reached (4748) (Fig. 4.23). A secondary activity is also observed when the pump is shut off. As observed in the previous sample the stress applied was not sufficient to control the orientation of the fracture, it deviates 45° from the direction of the stress applied (Fig. 4.55). However, the orientation of the hydraulic fracture in sample S14 differs from the fracture orientation observed in both S11 and S13 which can be caused by the presence of preexisting flaws in this sample. From Fig. 4.56 and Fig. 4.57 it is evident that the microseismic events occurred in the middle of the sample, just around the perforations in the tubing. The color coding indicates that the fracture grows away from the injection source.

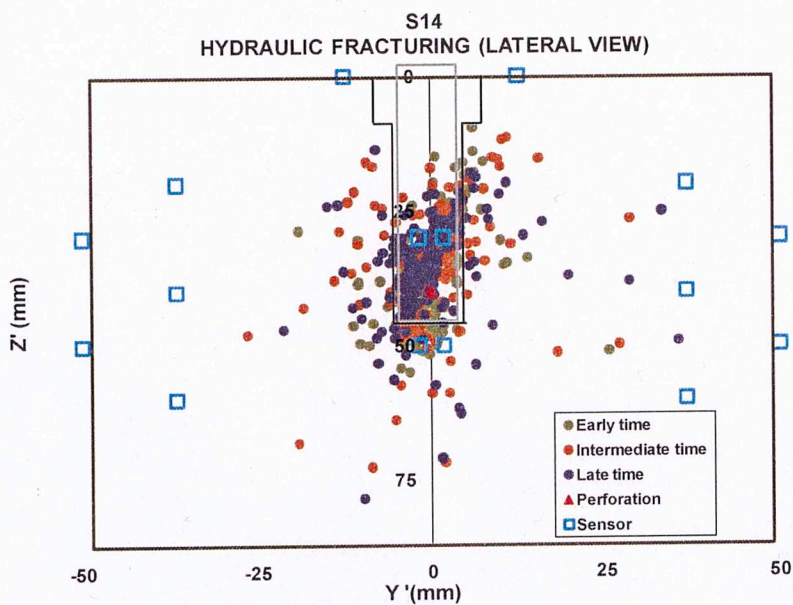


Fig. 4.58 - Lateral view of sample S14 parallel to the applied stress. The red triangle represents the location of the perforations. Out of plane projection gives a false representation of process zone.

Fig. 4.58 shows a view parallel to the fracture plane, which is 43° from the direction of applied stress. This view shows a real width of the process zone which is smaller if compared to the zone width observed in **Fig. 4.57**. **Fig. 4.58** shows the fracture is inclined with respect to the vertical axis. Physical examination of the sample shows indication of fracture on the circumference of the sample; **Fig. 4.59-Left** shows the Y-Z plane where the fracture is enclosed by the black lines. The fracture is not aligned with the direction of stress applied; but, deviated 45 degrees which agrees with location of MS events. **Fig. 4.59- Right** is a plug that was taken of the sample at 45 degrees from the direction of the stress applied. This supports the location of the MS events.

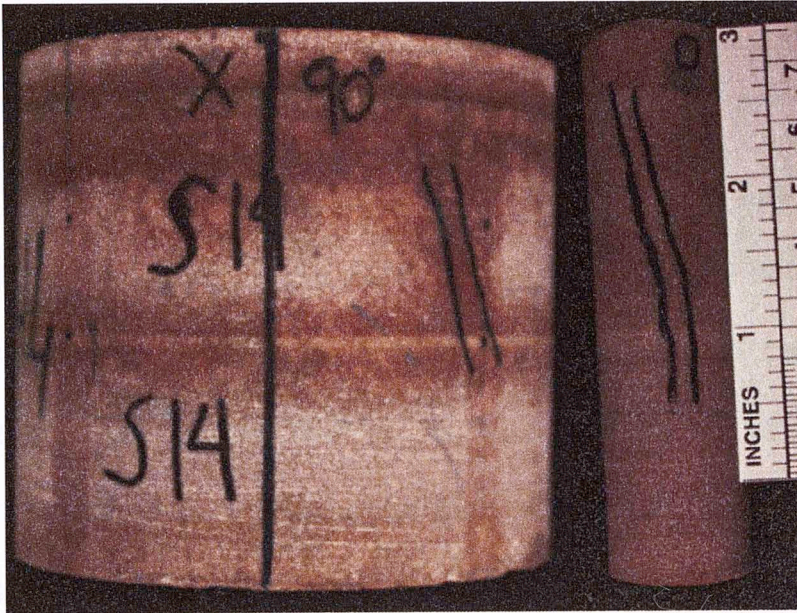


Fig. 4.59 - Left) Lateral view of sample S14 (Y-Z plane) showing a fracture that is not aligned with the direction of the stress applied but it is deviated 45 degrees. Right) One inch diameter plug taken out of the sample at 45 degrees from the direction of the stress applied indicating the existence of a fracture (enclosed by black lines)

Locations of hypocenters have uncertainty produced by the selection of the arrival time and the velocity model used. **Table 4.8** shows the values of average uncertainty for the three spatial coordinates for each sample.

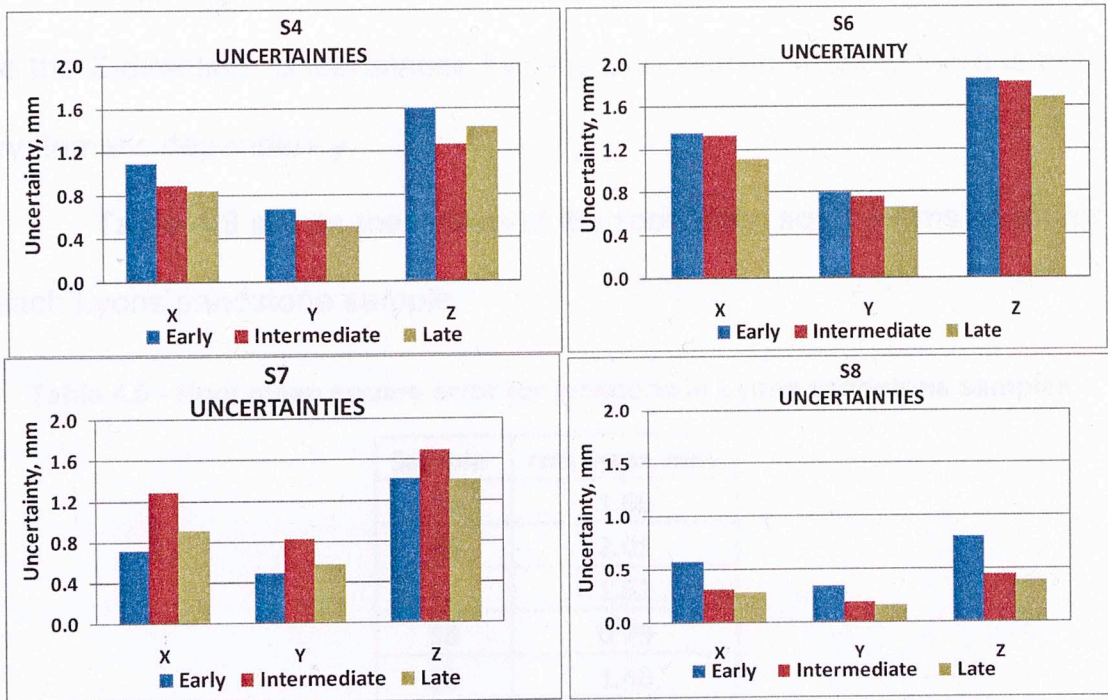
Table 4.8 - Average uncertainty values for each coordinate in all Lyons sandstone samples.

Sample	Uncertainty x, mm	Uncertainty y, mm	Uncertainty z, mm
S4	0.94	0.58	1.40
S6	1.24	0.72	1.73
S7	0.97	0.63	1.51
S8	0.39	0.23	0.55
S9	0.87	0.56	1.09
S11	0.81	0.58	1.47

S13	1.05	0.61	1.67
S14	1.24	0.87	1.61

In all samples uncertainty in the Z-direction is the greatest, while the uncertainty in the Y-direction is the lowest. All eight samples have two sensors placed on the top surface of the sample to constraint the Z-direction; however, this number is small compared to the number of sensors attached to the circumference of the sample (fourteen sensors). Also, sensors were not placed on the bottom surface of the sample which contributes to a greater uncertainty in the Z-direction.

Fig. 4.60 shows the uncertainty values in all spatial coordinates for early, intermediate and late time events for all sandstone samples.



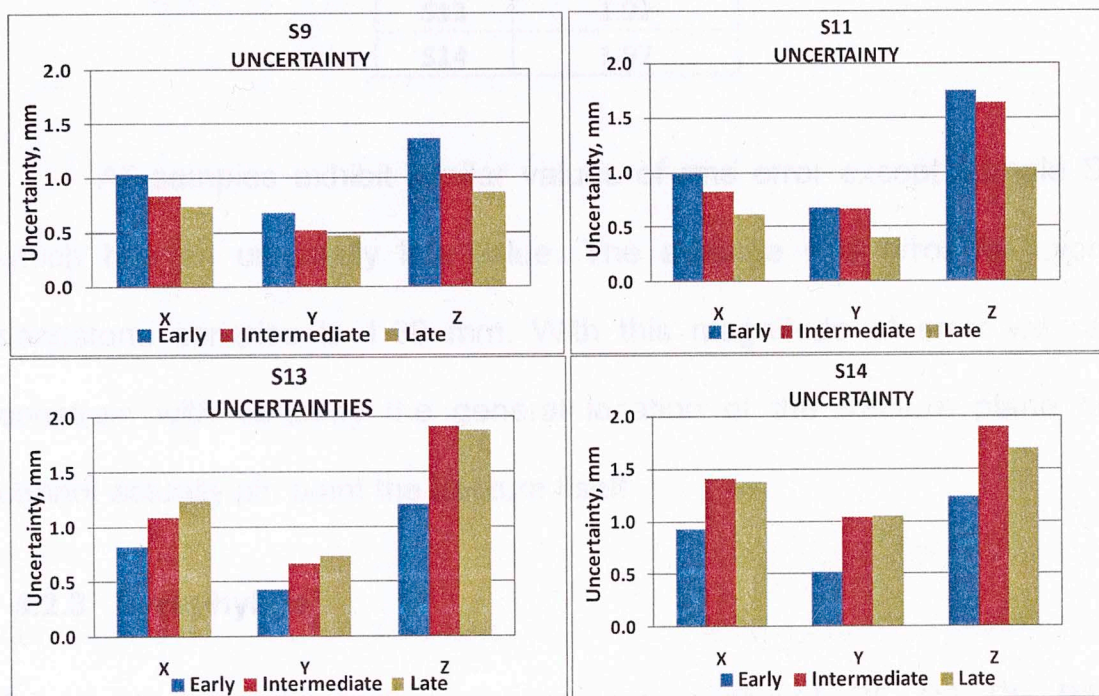


Fig. 4.60 - Average uncertainties of hypocenter locations in each coordinate for early, intermediate and late time events for Lyons sandstone samples.

From **Fig. 4.60** it is clear that the greatest uncertainty corresponds to the Z-direction. Uncertainties by time of occurrence show there is not a systematic dependency.

Table 4.9 shows the values of the root mean square (rms) error for each Lyons sandstone sample.

Table 4.9 - Root mean square error for locations in Lyons sandstone samples.

Sample	rms error, mm
S4	1.66
S6	2.05
S7	1.62
S8	0.79
S9	1.46
S11	1.97

S13	1.92
S14	1.97

All samples exhibit similar values of rms error except sample S8 which has an unusually low value. The average rms error for Lyons sandstone samples is 1.69 mm. With this magnitude of error we can constrain with certainty the general location of the fracture plane but cannot actually pin point the fracture itself.

4.2.3 Pyrophyllite

Seven different pyrophyllite samples were analyzed; P5, P6, P9, P10, P11, P12 and P16. Samples P5 and P6, P9 and P10, P11 and P12 are taken from the upper and lower portions of common cylinders. Pyrophyllite is a mineral of variable chemical composition and microstructure and is found as a product of metamorphic processes in homogeneous very fine grained specimens (Sachse and Ruoff, 1975). Common clays exhibit varying degrees of swelling upon absorption of water; pyrophyllite structure does not change upon exposure to water. Pyrophyllite occurs largely through the hydrothermal alteration of feldspars and is often found in regions of low grade metamorphism in association with dolomitic limestones and ultrabasic rocks (Sondergeld et al., 1980).

Pyrophyllite was chosen to represent anisotropic elastic behavior of shales without their chemical reactivity. Circumferential Velocity Analysis (CVA) confirms this. The permeability of pyrophyllite was measured to be 120 nD (Tinni, 2011), which is three orders of magnitude lower than the permeability of the Lyons sandstone.

Samples P5, P6, P9, P10, P11, P12 and P16 were hydraulically fractured applying different magnitudes of horizontal stress as shown in **Table 3.6**. Also, two different sets of experiments were carried out; the first experiment is with the stress applied parallel to the fabric orientation, while the second is with the stress applied perpendicular to the fabric which simulates a horizontal well.

The pumping pressure and the acoustic emissions were recorded as a function of time in each experiment (**Fig. 4.61**). The black lines represent the pumping pressure while the red circles are the acoustic emissions. Similar to the Indiana limestone and Lyons sandstone experiments the events located within the sample have been divided into three parts and are represented as early time (green dots), intermediate time (orange dots) and late time (purple dots) events. Such color coding is used with the purpose of mapping the propagation of the hydraulic fracture.

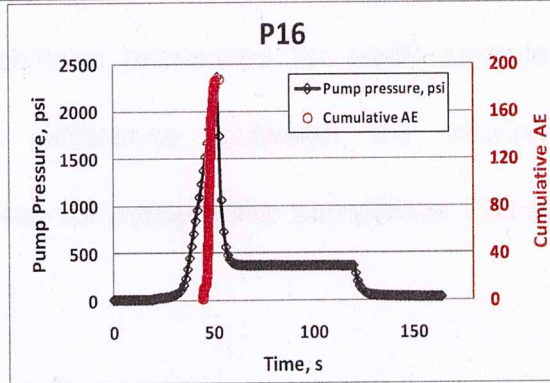
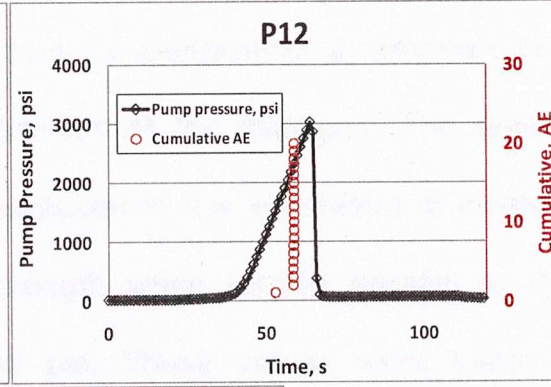
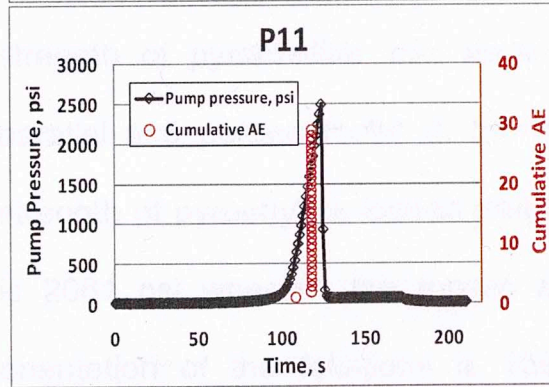
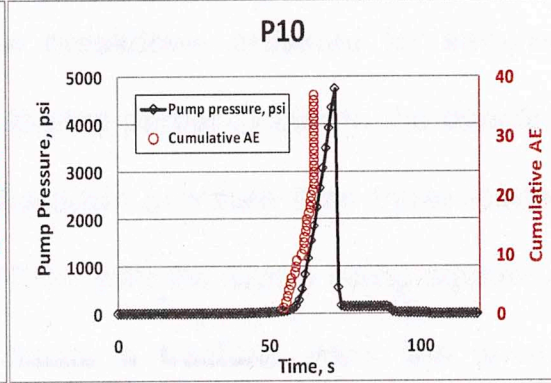
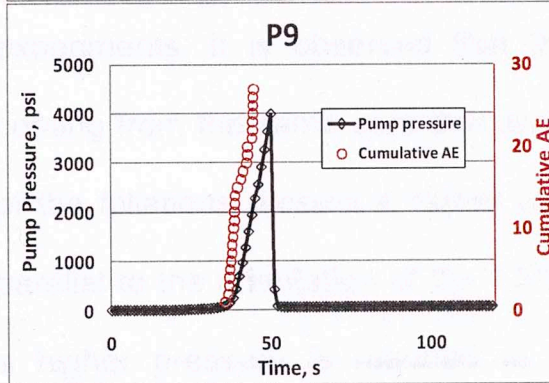
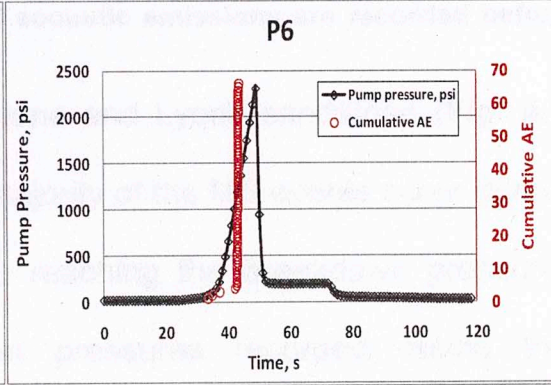
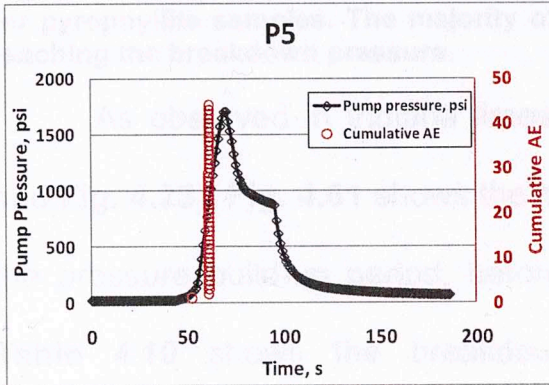


Fig. 4.61 - Pumping pressure (black) and cumulative AE (red) as a function of time for pyrophyllite samples. The majority of acoustic emissions are recorded before reaching the breakdown pressure.

As observed in Indiana limestone and Lyons sandstone (**Fig. 4.7** and **Fig. 4.23**), **Fig. 4.61** shows the majority of the MS events occur during the pressure build-up period, before reaching the breakdown pressure. **Table 4.10** shows the breakdown pressures recorded during the experiments. It is observed that the breakdown pressure for samples coming from the same core that are loaded perpendicular to the direction of the foliations present a higher breakdown pressure than those loaded parallel to the orientation of the foliations; with the layers being squeezed a higher pressure is required to initiate a fracture. Also, the tensile strength of pyrophyllite was measured by performing a Brazilian test parallel and perpendicular to the direction of the foliations. The tensile strength of pyrophyllite loaded perpendicular to the orientation of foliation is 2061 psi whereas the tensile strength when loaded parallel to the orientation of the foliations is 1582 psi. These values were used to calculate the breakdown pressures for each sample (**Table 4.10**). The average absolute difference between the recorded and calculated breakdown pressures for pyrophyllite samples is 724 psi.

Table 4.10 – Recorded breakdown pressures compared to the calculated values. Pressure were calculated using tensile strength of the pyrophyllite obtained from a Brazilian test performed on a representative sample of pyrophyllite.

Sample	Applied stress, psi	Breakdown pressure recorded, psi	Breakdown pressure calculated, psi
P5	970	1700	2552
P6	990	2302	3051
P9	980	3978	2562
P10	960	4747	3021
P11	950	2494	2532
P12	1020	3019	3081
P16	520	2353	2581

Fig. 4.62, Fig. 4.63 and Fig. 4.64 present the plan and two lateral views of sample P5 which was loaded to 970 psi parallel to the fabric orientation (red arrows).

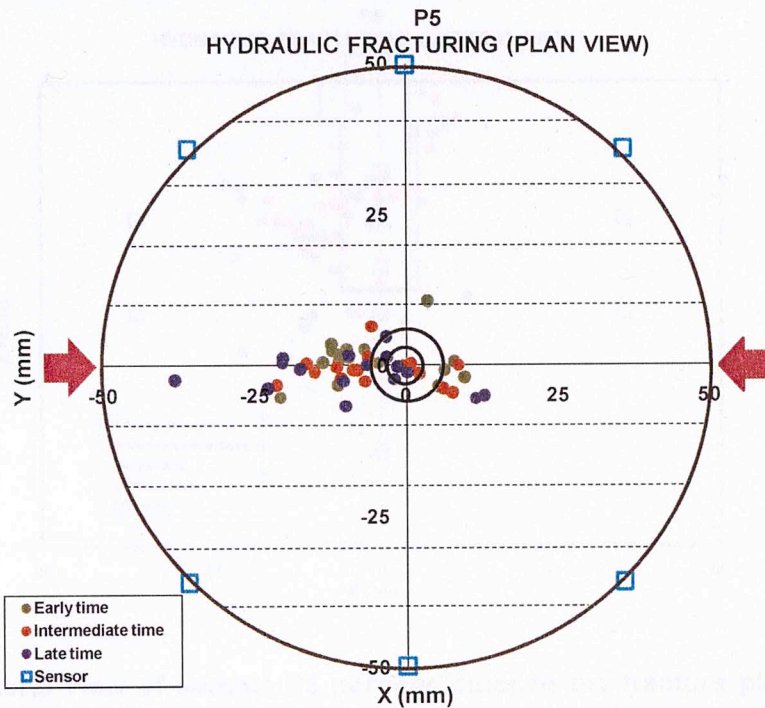


Fig. 4.62 - Plan view of sample P5 showing the spatial and temporal evolution of the hydraulic fracture. The green dots represent the early time events, while the orange and purple represent the intermediate and late time events, respectively. The cyan squares represent sensors attached to the sample. The red arrows represent the direction of the stress applied with a magnitude of 970 psi. The two circles in the center of the plot represent the counter borehole and the borehole. The dotted lines represent the bedding planes. Note the paucity of activity. If representative, the asymmetry wing development.

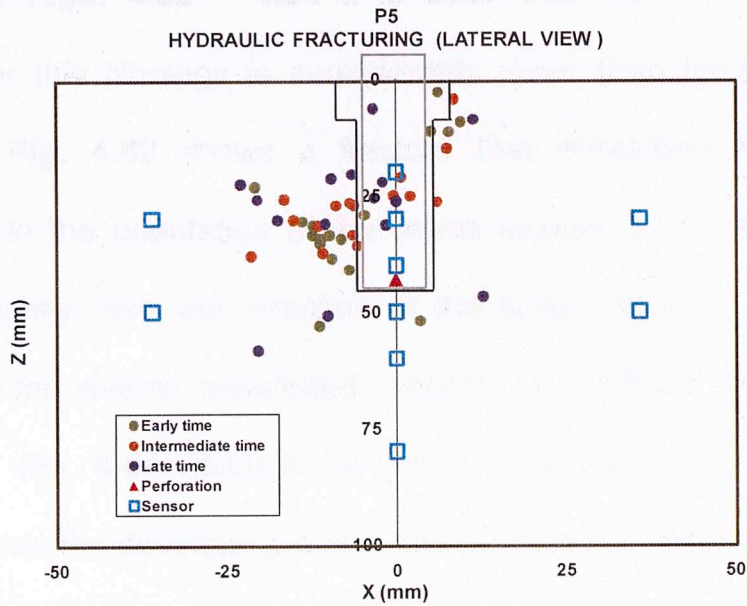


Fig. 4.63 - Lateral view of sample P5 perpendicular to the fracture plane. The red triangle represents the location of the perforations in the tubing.

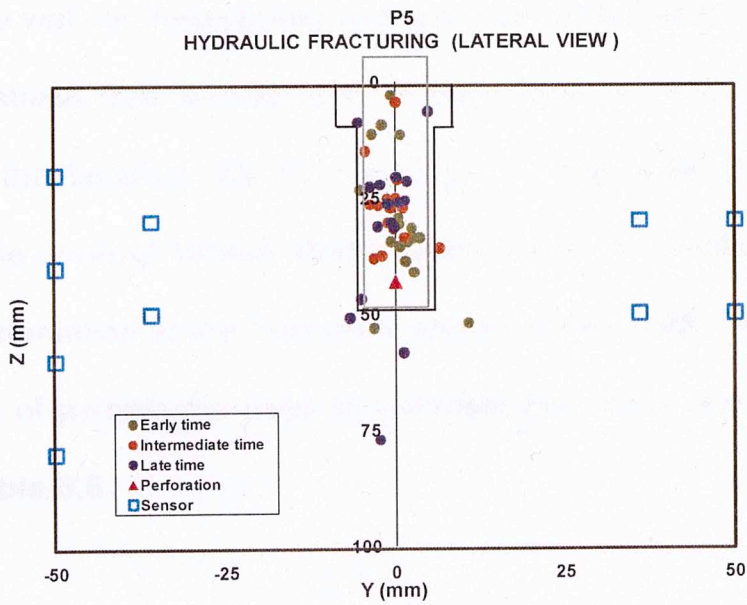


Fig. 4.64 - Lateral view of sample P5 parallel to the fracture plane. The red triangle represents the location of the perforations in the tubing.

From **Figs. 4.62 – 4.64** it is clear that the number of events recorded for this lithology is considerably lower than for the other two lithologies. **Fig. 4.62** shows a fracture that developed in a direction subparallel to the orientation of the stress applied; it shows the fracture deviates slightly from the direction of the stress applied. However, the majority of the events developed around the wellbore and above the perforation. **Fig. 4.64** which is the lateral view parallel to the hydraulic fracture shows the development of a narrow fracture. Physical observation of the sample shows no visible fracture on the surface of the sample.

Analytical solution for the concentration of hoop stresses around the wellbore wall for transversely isotropic materials (Section 2.5), when a horizontal stress (red arrows) with a magnitude of 1000 psi is applied parallel to the bedding direction is shown in **Fig. 4.65**. The red circle indicates the zone of tensile stress state around the wellbore wall. The expected orientation of the fracture is shown in **Fig. 4.65**. The anisotropic parameters of pyrophyllite used to calculate the stress concentration are given in **Table 3.5**.

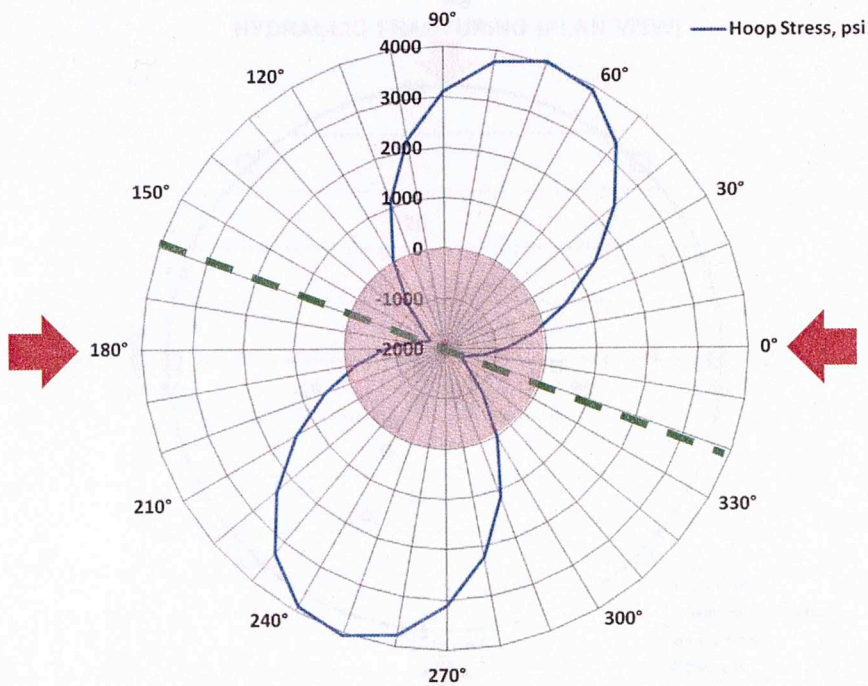


Fig. 4.65 – Analytical solution for hoop stress concentration around wellbore wall (Aadnoy, 1987) when a horizontal stress (red lines) with a magnitude of 1000 psi is applied parallel to the direction of the bedding planes (0° - 180°). The red circle indicates the zone of tensile state in the wellbore wall. The green dashed line is the predicted orientation the fracture should follow. The fracture shows a deviation of 20° from the orientation of the applied stress.

Fig. 4.66, **Fig. 4.67** and **Fig. 4.68** represent the plan and two lateral views of sample P6 which was loaded with 990 psi perpendicular to the fabric orientation (red arrows). This configuration simulates a horizontal wellbore in anisotropic shale.

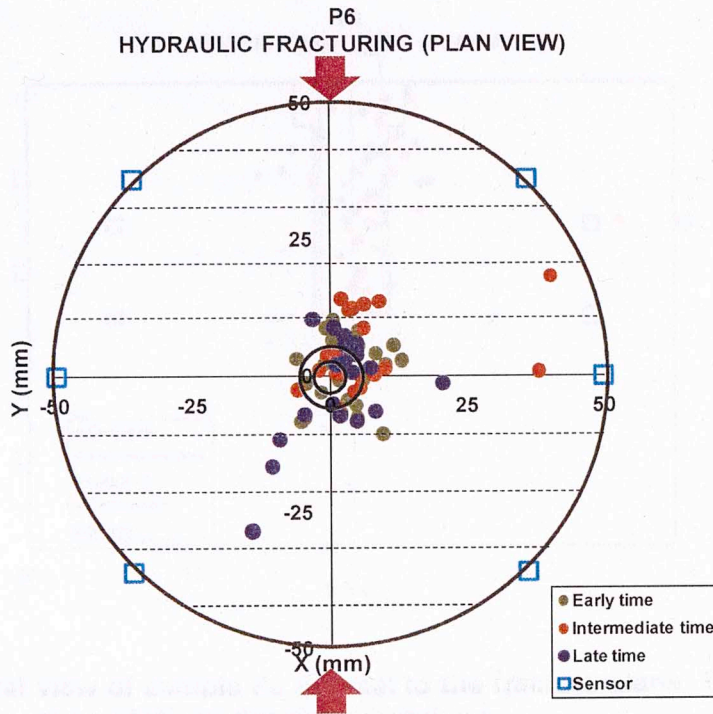


Fig. 4.66 - Plan view of sample P6 showing the spatial and temporal evolution of the hydraulic fracture. The green dots represent the early time events, while the orange and purple represent the intermediate and late time events, respectively. The cyan squares represent sensors attached to the sample. The red arrows represent the direction of the stress applied with a magnitude of 990 psi. The two circles in the center of the plot represent the counter borehole and the borehole. The dotted lines represent the fabric planes.

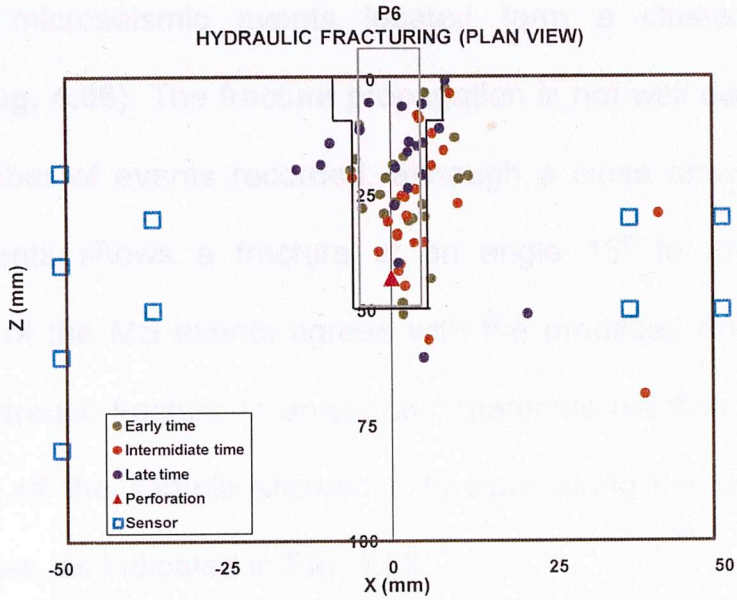


Fig. 4.67 - Lateral view of sample P6 parallel to the fracture plane. The red triangle represents the location of the perforations in tubing.

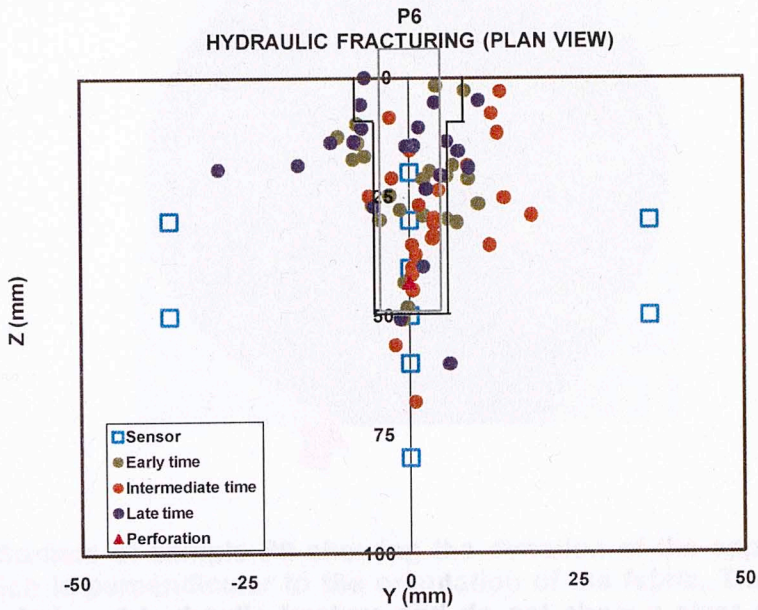


Fig. 4.68 - Lateral view of sample P6 perpendicular to the fracture plane. The red triangle represents the location of the perforations in tubing.

The microseismic events located form a cluster around the borehole (Fig. 4.66). The fracture propagation is not well defined from the limited number of events recorded, although a close observation of the located events shows a fracture at an angle 15° to the East. The distribution of the MS events agrees with the predicted orientation of an induced hydraulic fracture in anisotropic materials (section 2.5). Physical observation of the sample showed a fracture along the direction of the applied stress, as indicated in Fig. 4.69.

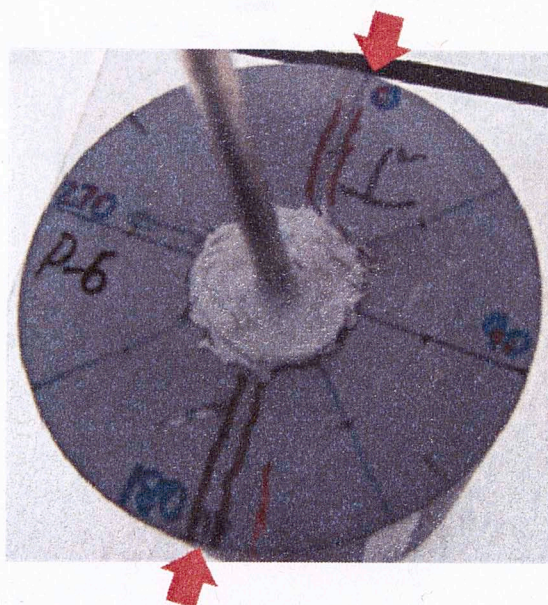


Fig. 4.69 - Surface of sample P6 showing the direction of the applied stress (red arrows) which is perpendicular to the orientation of the fabric. The dark red lines enclose the induced hydraulic fracture and do not show a clear deviation of the fracture from the applied stress.

The concentration of hoop stresses around the wellbore wall for transversely isotropic materials was also solved for a horizontal stress

applied perpendicular to the direction of the bedding planes (Section 2.5). Fig. 4.70 shows the expected orientation of the fracture (green dashed line) when a stress is applied with a magnitude of 1000 psi (red arrows) perpendicular to the direction of the foliation in pyrophyllite samples, where the red circle indicates the zone of tensile stress state around the wellbore wall.

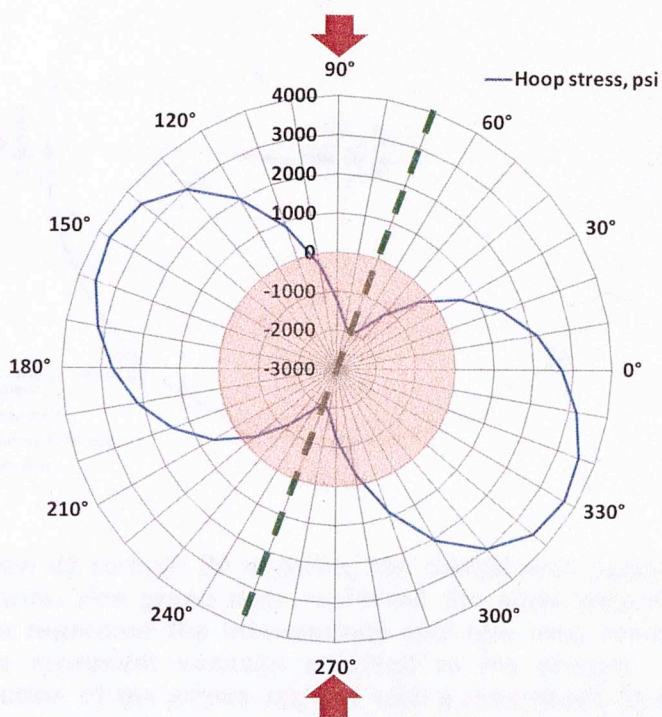


Fig. 4.70 – Analytical solution for hoop stress concentration around wellbore wall (Aadnoy, 1987) when a horizontal stress (red lines) with a magnitude of 1000 psi is applied perpendicular to the direction of the bedding planes (0°-180°). The reddish circle indicates the zone of tensile state in the wellbore wall. The green dashed line is the predicted orientation the fracture should follow. The fracture shows a deviation of 20° from the orientation of the applied stress.

Fig. 4.71, Fig. 4.72 and Fig. 4.73 represent the plan and two lateral views of sample P9 which was loaded with 980 psi parallel to the bedding orientation (red arrows).

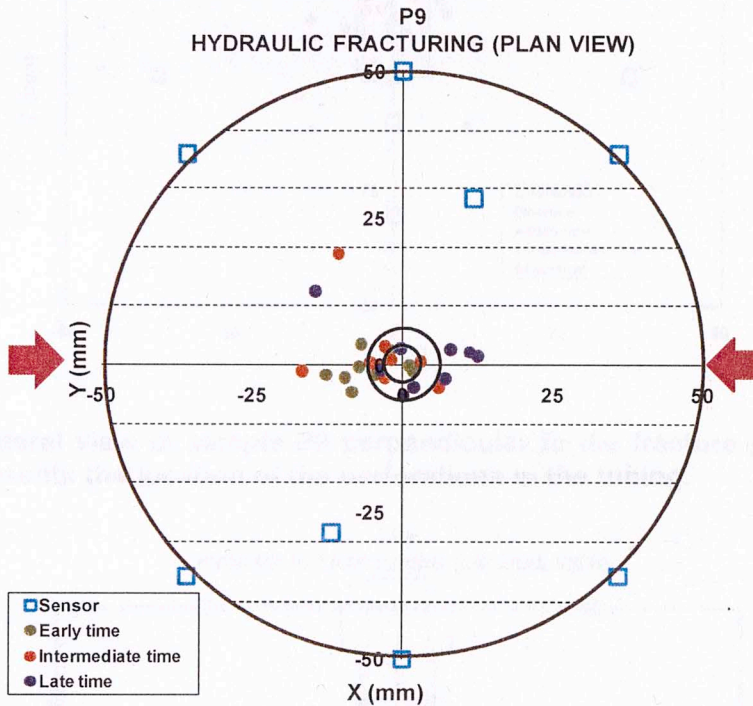


Fig. 4.71 - Plan view of sample P9 showing the spatial and temporal evolution of the hydraulic fracture. The green dots represent the early time events, while the orange and purple represent the intermediate and late time events, respectively. The cyan squares represent sensors attached to the sample. The red arrows represent the direction of the stress applied with a magnitude of 980 psi. The two circles in the center of the plot represent the counter borehole and the borehole. The dotted lines represent the foliation planes.

Fig. 4.72 - Lateral view of sample P9 parallel to the fracture plane. The red triangle represents the location of the perforations in the tubing.

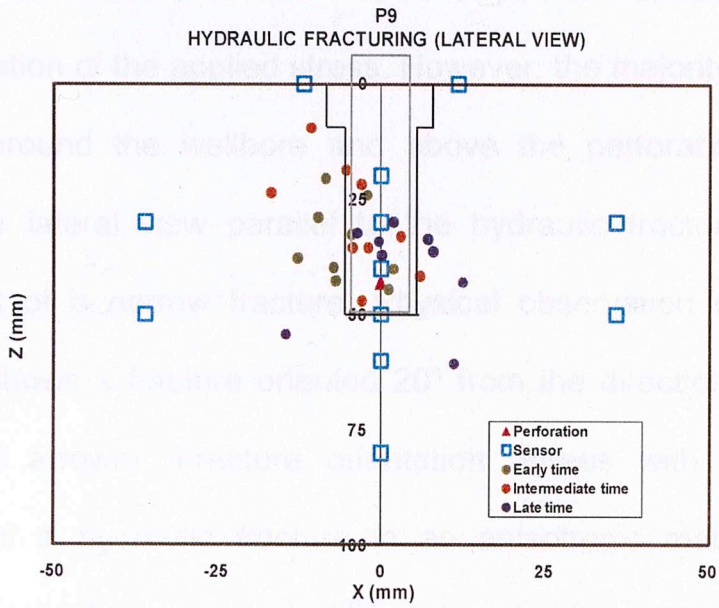


Fig. 4.72 - Lateral view of sample P9 perpendicular to the fracture plane. The red triangle represents the location of the perforations in the tubing.

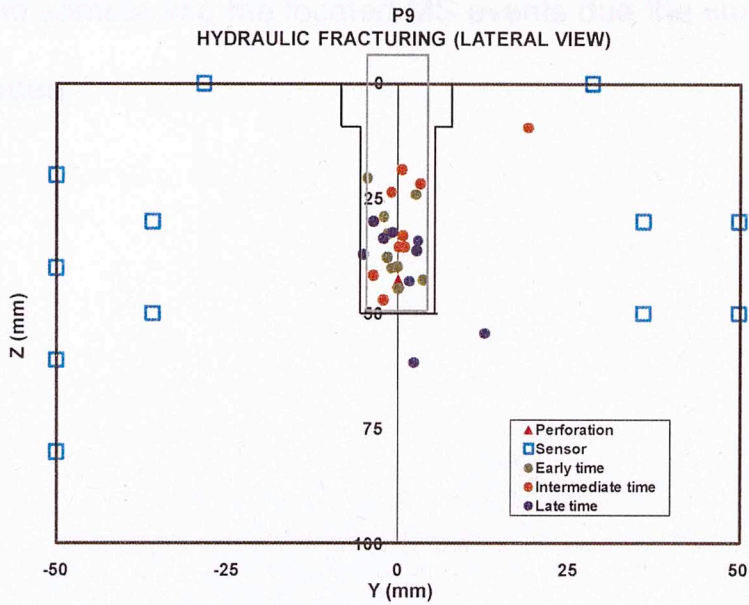


Fig. 4.73 - Lateral view of sample P9 parallel to the fracture plane. The red triangle represents the location of the perforations in the tubing.

Fig. 4.71 shows a fracture that developed in a direction subparallel to the orientation of the applied stress. However, the majority of the events developed around the wellbore and above the perforation. **Fig. 4.73**, which is the lateral view parallel to the hydraulic fracture, shows the development of a narrow fracture. Physical observation of the sample (**Fig. 4.74**) shows a fracture oriented 20° from the direction of the stress applied (red arrows). Fracture orientation agrees with the predicted orientation of a hydraulic fracture in an anisotropic material with the anisotropic properties of pyrophyllite and under the experimental stress conditions (**Fig 4.70**). It is hard to compare the actual fracture on the surface of the sample and the located MS events due the small number of events recorded.

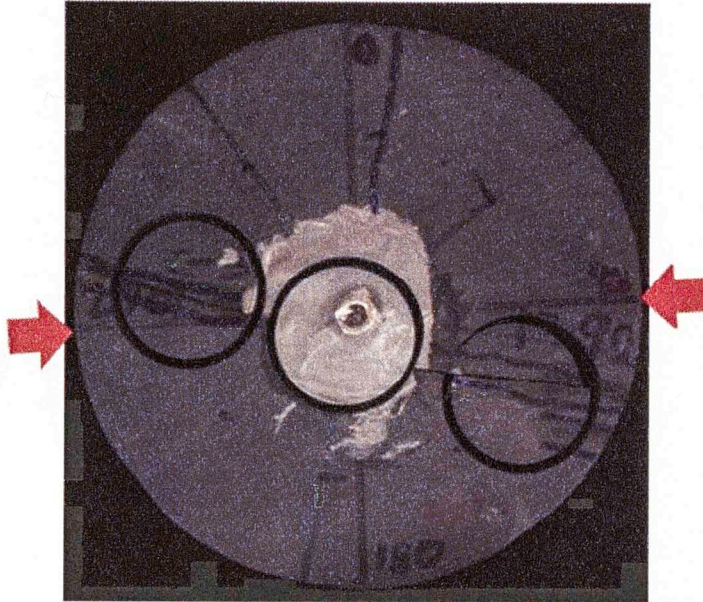


Fig. 4.74 - Plan view of sample P9 showing a fracture deviated 20 degrees from the direction of the stress applied (red arrows).

Fig. 4.75, Fig. 4.76 and Fig. 4.77 represent the plan and two lateral views of sample P10 which was loaded with 960 psi perpendicular to the foliation orientation (red arrows).

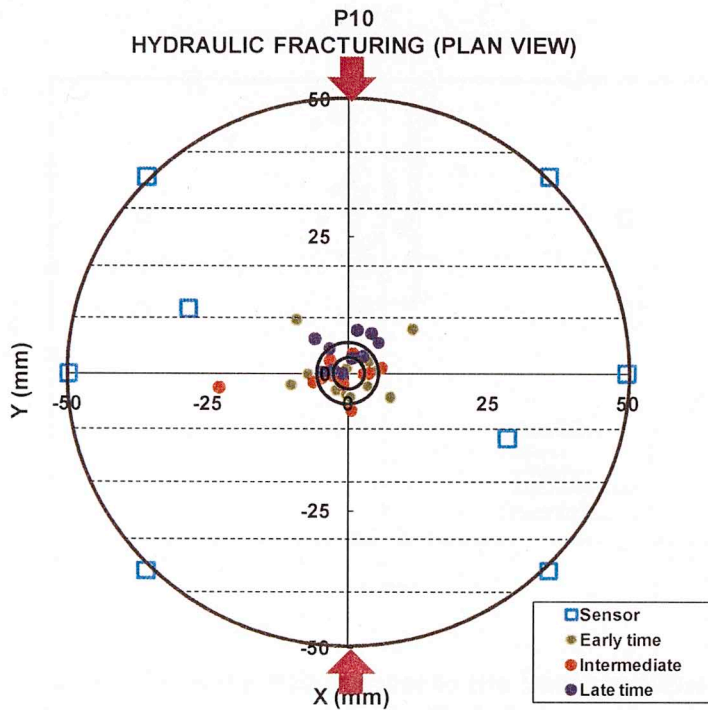


Fig. 4.75 - Plan view of sample P10 showing the spatial and temporal evolution of the hydraulic fracture. The green dots represent the early time events, while the orange and purple represent the intermediate and late time events, respectively. The cyan squares are sensors attached to the sample. The red arrows represent the direction of the stress applied with a magnitude of 960 psi. The two circles in the center of the plot represent the counter borehole and the borehole. The dotted lines represent the foliation planes.

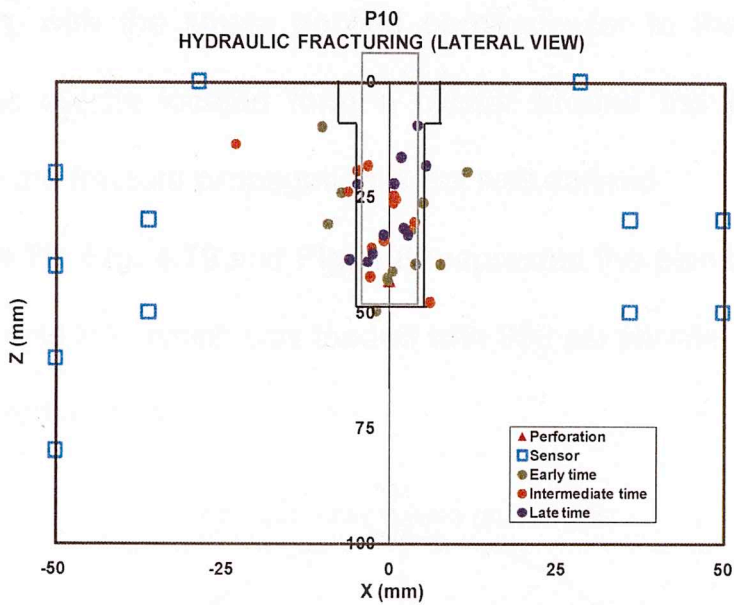


Fig. 4.76 - Lateral view of sample P10 parallel to the fracture plane. The red triangle represents the location of the perforations in the tubing.

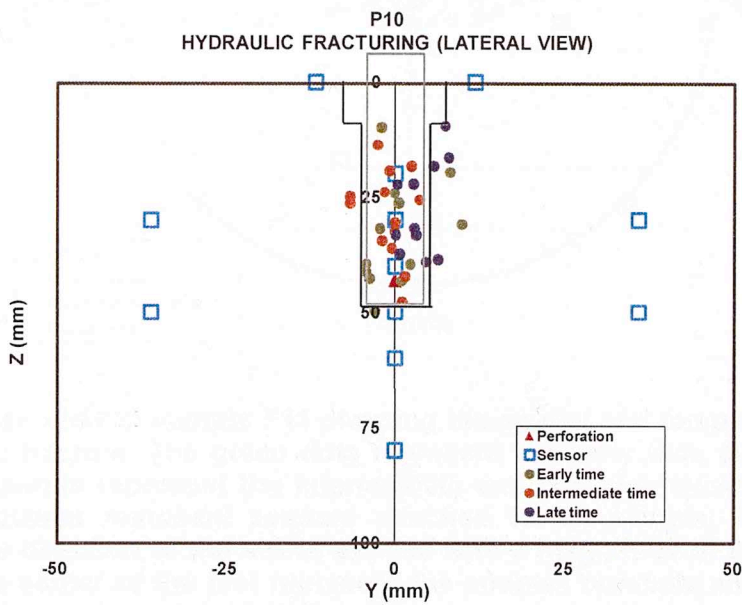


Fig. 4.77 - Lateral view of sample P10 perpendicular to the fracture plane. The red triangle represents the location of the perforations in the tubing.

Again, with the stress applied perpendicular to the foliation, the microseismic events located form a cluster around the borehole (Fig. 4.75) where the fracture propagation is not well defined.

Fig. 4.78, Fig. 4.79 and Fig. 4.80 represent the plan and two lateral views of sample P11 which was loaded with 950 psi parallel to the foliation orientation (red arrows).

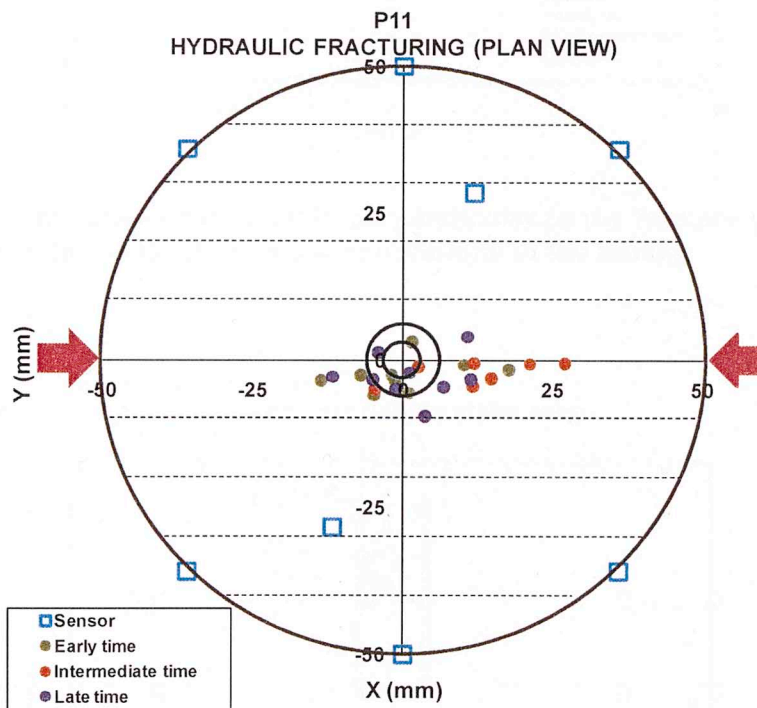


Fig. 4.78 - Plan view of sample P11 showing the spatial and temporal evolution of the hydraulic fracture. The green dots represent the early time events, while the orange and purple represent the intermediate and late time events, respectively. The cyan squares represent sensors attached to the sample. The red arrows represent the direction of the stress applied with a magnitude of 950 psi. The two circles in the center of the plot represent the counter borehole and the borehole. The dotted lines represent the foliation planes.

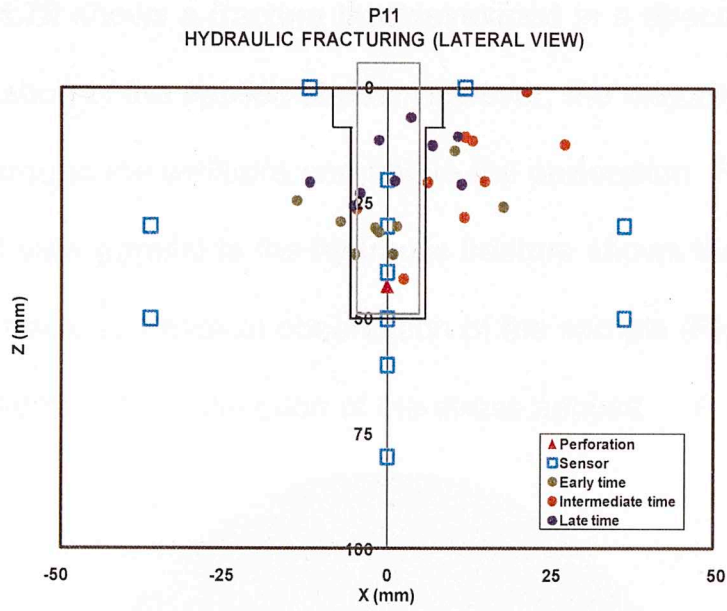


Fig. 4.79 - Lateral view of sample P11 perpendicular to the fracture plane. The red triangle represents the location of the perforations in the tubing.

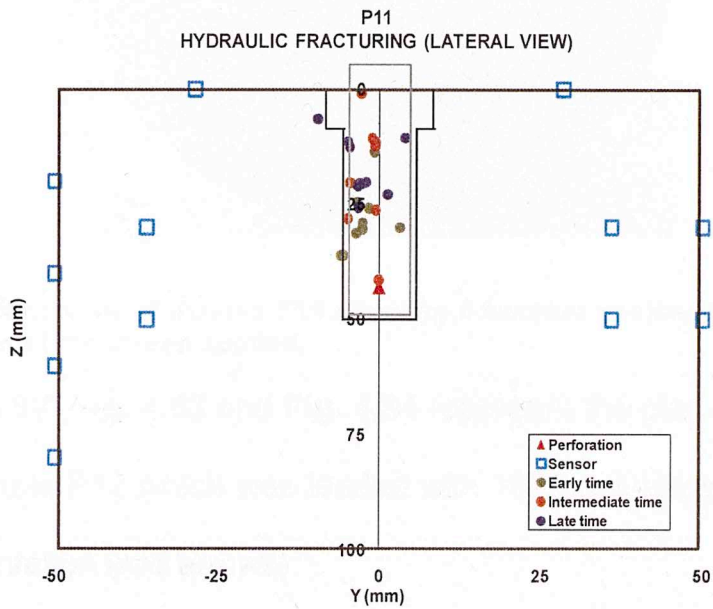


Fig. 4.80 - Lateral view of sample P11 parallel to the fracture plane. The red triangle represents the location of the perforations in the tubing.

Fig. 4.78 shows a fracture that developed in a direction subparallel to the orientation of the applied stress. However, the majority of the events developed around the wellbore and above the perforation. **Fig. 4.80** which is the lateral view parallel to the hydraulic fracture shows the development of a narrow fracture. Physical observation of the sample (**Fig. 4.81**) shows a fracture oriented in the direction of the stress applied.

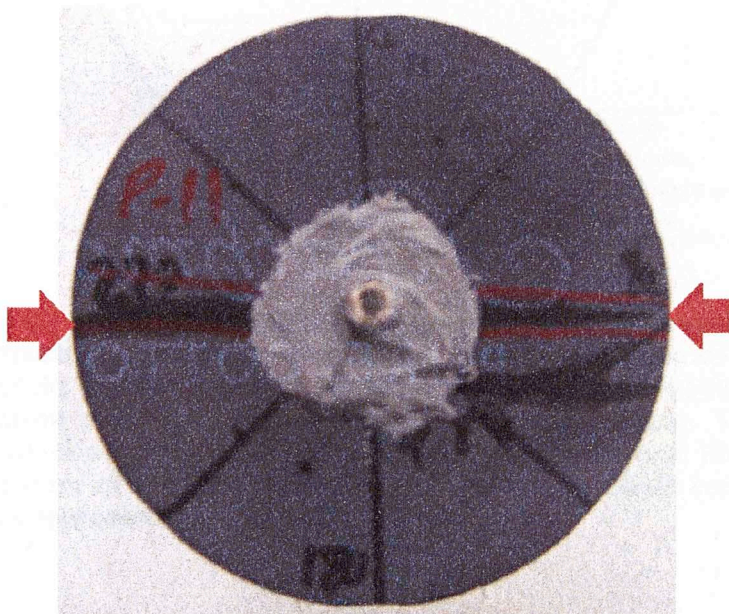


Fig. 4.81 - Surface view of sample P11 showing a fracture enclosed by the red lines in the direction of the stress applied.

Fig. 4.82, **Fig. 4.83** and **Fig. 4.84** represent the plan and two lateral views of sample P12 which was loaded with 1020 psi perpendicular to the foliation orientation (red arrows).

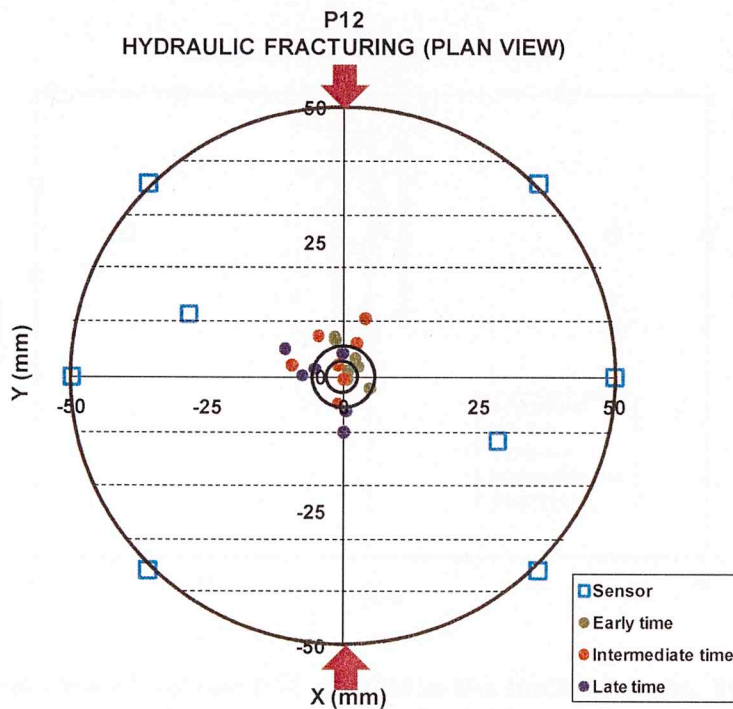


Fig. 4.82 - Plan view of sample P12 showing the spatial and temporal evolution of the hydraulic fracture. The green dots represent the early time events, while the orange and purple represent the intermediate and late time events, respectively. The cyan squares represent sensors attached to the sample. The red arrows represent the direction of the stress applied with a magnitude of 1020 psi. The two circles in the center of the plot represent the counter borehole and the borehole. The dotted lines represent the foliation planes.

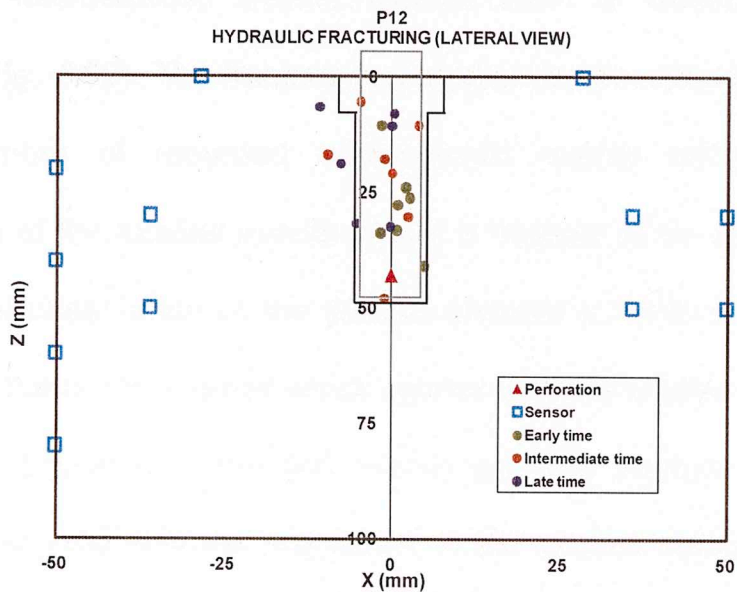


Fig. 4.83 - Lateral view of sample P12 parallel to the fracture plane. The red triangle represents the location of the perforations in the tubing.

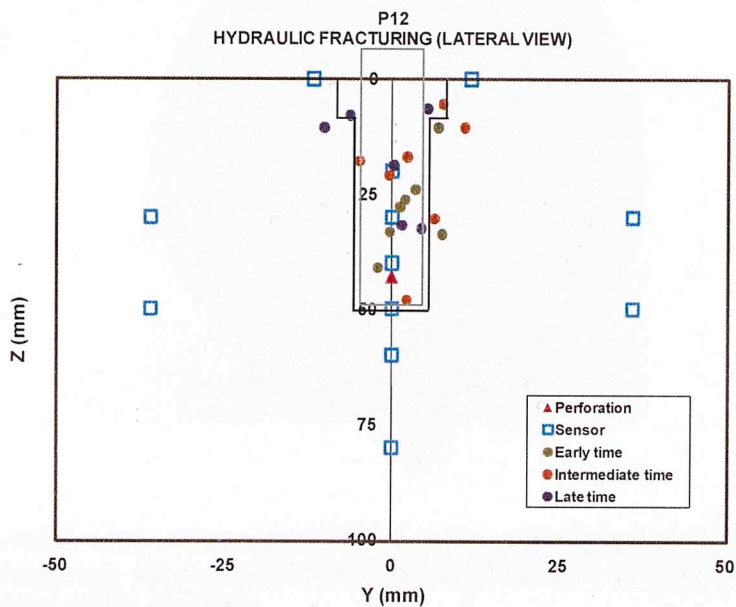


Fig. 4.84 - Lateral view of sample P12 perpendicular to the fracture plane. The red triangle represents the location of the perforations in the tubing.

The microseismic events located form a cluster around the borehole (**Fig. 4.82**). The fracture propagation is not well defined from the limited number of recorded microseismic events although a close observation of the located events shows a fracture at an angle 10° to the East. Visual observation of the sample showed a fracture 10° off of the direction of the applied stress which agrees with the location of MS events (**Fig. 4.85**). Location of the MS events and the fracture itself are not completely aligned with the orientation of the applied stress as predicted for anisotropic materials (**Fig 4.70**).

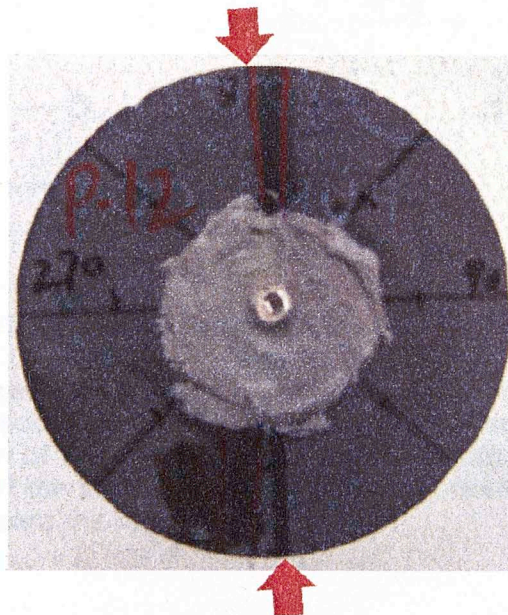


Fig. 4.85 - Surface view of sample P12 showing a fracture (enclosed by red lines) that is not completely aligned with the direction of stress applied (red arrows). The fracture deviates 10° to the East.

Fig. 4.86, Fig. 4.87 and Fig. 4.88 represent the plan and two lateral views of sample P16 which was loaded with 520 psi perpendicular to the foliation orientation (red arrows).

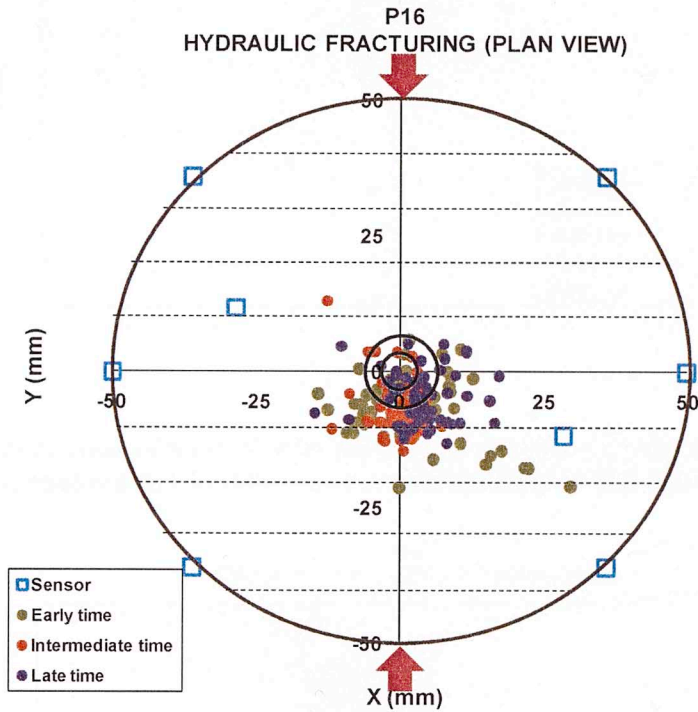


Fig. 4.86 - Plan view of sample P16 showing the spatial and temporal evolution of the hydraulic fracture. The green dots represent the early time events, while the orange and purple represent the intermediate and late time events, respectively. The cyan squares represent sensors attached to the sample. The red arrows represent the direction of the stress applied with a magnitude of 520 psi. The two circles in the center of the plot represent the counter borehole and the borehole. The dotted lines represent the foliation planes.

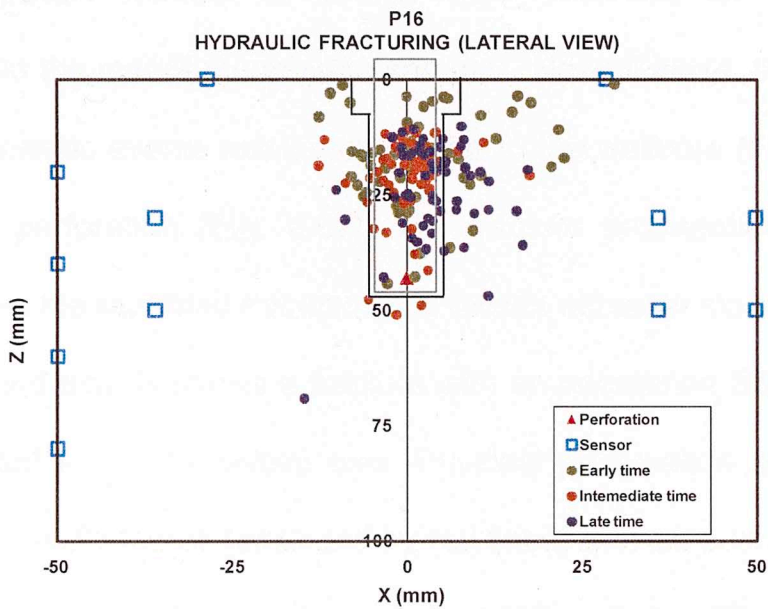


Fig. 4.87 - Lateral view of sample P16 parallel to direction of the stress applied. The red triangle represents the location of the perforations in the tubing.

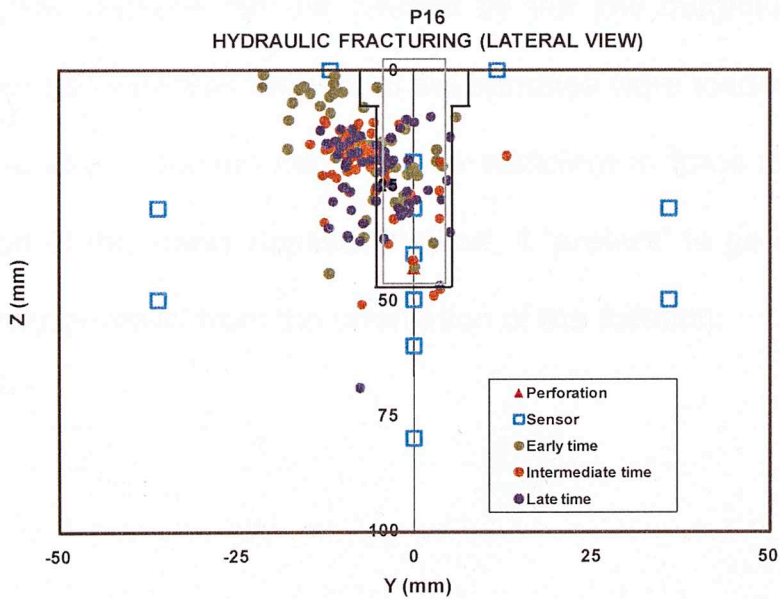


Fig. 4.88 - Lateral view of sample P16 perpendicular to direction of the stress applied. The red triangle represents the location of the perforations in the tubing.

A greater number of events were recorded for sample P16 compared to the rest of pyrophyllite samples. Nevertheless, the majority of the microseismic events are located close to the wellbore (Fig. 4.86) and above the perforation (Fig. 4.87). The fracture propagation is not well defined from the recorded microseismic events although close observation of the located events shows a fracture with an orientation S50°E, with the north located in the Y-positive axis. Physical observation of the sample surface shows a fracture (enclosed by red lines) with an orientation S55°E which agrees with the location of the MS events (Fig. 4.89). The difference in fracture orientation in sample P16 when compared to the rest of pyrophyllite samples can be caused by the low magnitude of stress applied (520 psi) whereas the rest of the samples were loaded with ~1000 psi. The low stress applied might not be sufficient to force the fracture in the direction of the stress applied. Instead, it “prefers” to go in a direction that is slightly deviated from the orientation of the foliation.

Table 4.11 - Average uncertainty values for each coordinate in all pyrophyllite samples

Sample	Uncertainty x, mm	Uncertainty y, mm	Uncertainty z, mm
P5	0.57	0.35	0.82
P6	0.44	0.32	1.46
P9	0.23	0.12	0.32
P10	0.16	0.26	0.63
P11	0.49	0.36	0.78
P12	0.19	0.28	0.54
P16	0.32	0.10	0.79

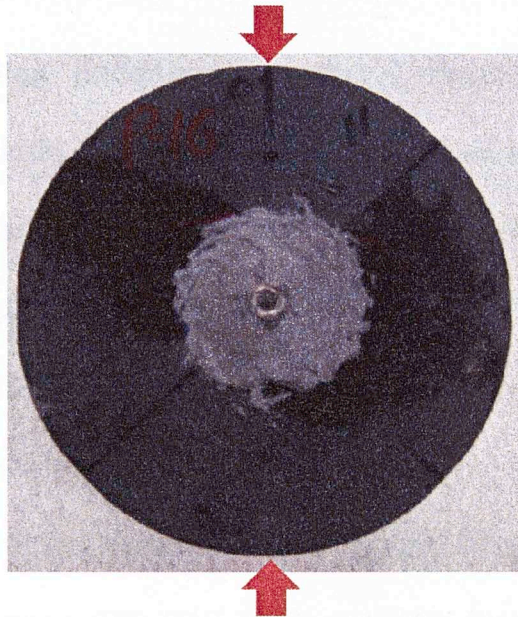


Fig. 4.89 - Surface view of sample P16 showing a fracture (enclosed by red lines) that deviates 55° to the west from the direction of stress applied (red arrows). The induced fracture seems to be more oriented towards the direction of the foliation.

Locations of hypocenters have uncertainty associated with the selection of the arrival time and the velocity model used. **Table 4.11** shows the values of average uncertainty for the spatial coordinates for each sample.

Table 4.11 - Average uncertainty values for each coordinate in all pyrophyllite samples.

Sample	Uncertainty x, mm	Uncertainty y, mm	Uncertainty z, mm
P5	0.57	0.35	0.82
P6	0.44	0.52	1.45
P9	0.23	0.12	0.32
P10	0.16	0.25	0.53
P11	0.49	0.26	0.76
P12	0.19	0.28	0.54
P16	0.32	0.50	0.79

In all samples uncertainty in the Z-direction is the greatest. Samples P5 and P6 did not have sensors placed on the top surface of the sample which explains the larger errors in the Z-direction. In samples where the applied stress was parallel to the planes of foliation (P5, P9 and P11) the vertical sub-array of sensors was located in the Y-axis; it was in this direction where samples P5, P9 and P11 presented the lower uncertainty. On the other hand, when the applied stress was perpendicular to the planes of foliation (P6, P10, P12 and P16) the vertical sub-array of sensors was located in the X-axis; for these samples the smallest errors were found in the X-axis.

Table 4.12 shows the values of the root mean square (rms) error for each pyrophyllite sample.

Table 4.12 - Root mean square error for locations in pyrophyllite samples.

Sample	rms error, mm
P5	1.05
P6	1.42
P9	0.39
P10	0.86
P11	0.60
P12	0.60
P16	1.06

The average rms error for pyrophyllite samples is 0.85 mm. All values are within one standard deviation of the mean values except the rms error of sample P6. With this magnitude of error we can constrain with certainty the general location of the fracture plane but cannot actually pinpoint the fracture itself.

During hydraulic fracturing mapping procedures in shale, the location of MS events strongly depends on an accurate velocity model. In anisotropic formations the P-wave velocity is not constant; the P-wave (and S-wave) velocity varies due to layering, mineralogy and natural fractures (Warpinski et al., 2009). Hence, using a constant velocity model to locate MS event in an anisotropic formation can lead to errors in hypocenter location. **Fig. 4.90** shows plan and lateral views of pyrophyllite samples showing MS events hypocenters using Berryman's equation for strong anisotropy (green dots) (Berryman, 2008) and a constant velocity model (black triangles). The MS events located using a constant velocity model (black triangles) form a cluster around the borehole in all samples except sample P11, where a trend similar to that observed when MS event are located using Berryman's equation for strong anisotropy is evident. Nevertheless, it is hard to make a comparison between both models since the number of MS events recorded is low.

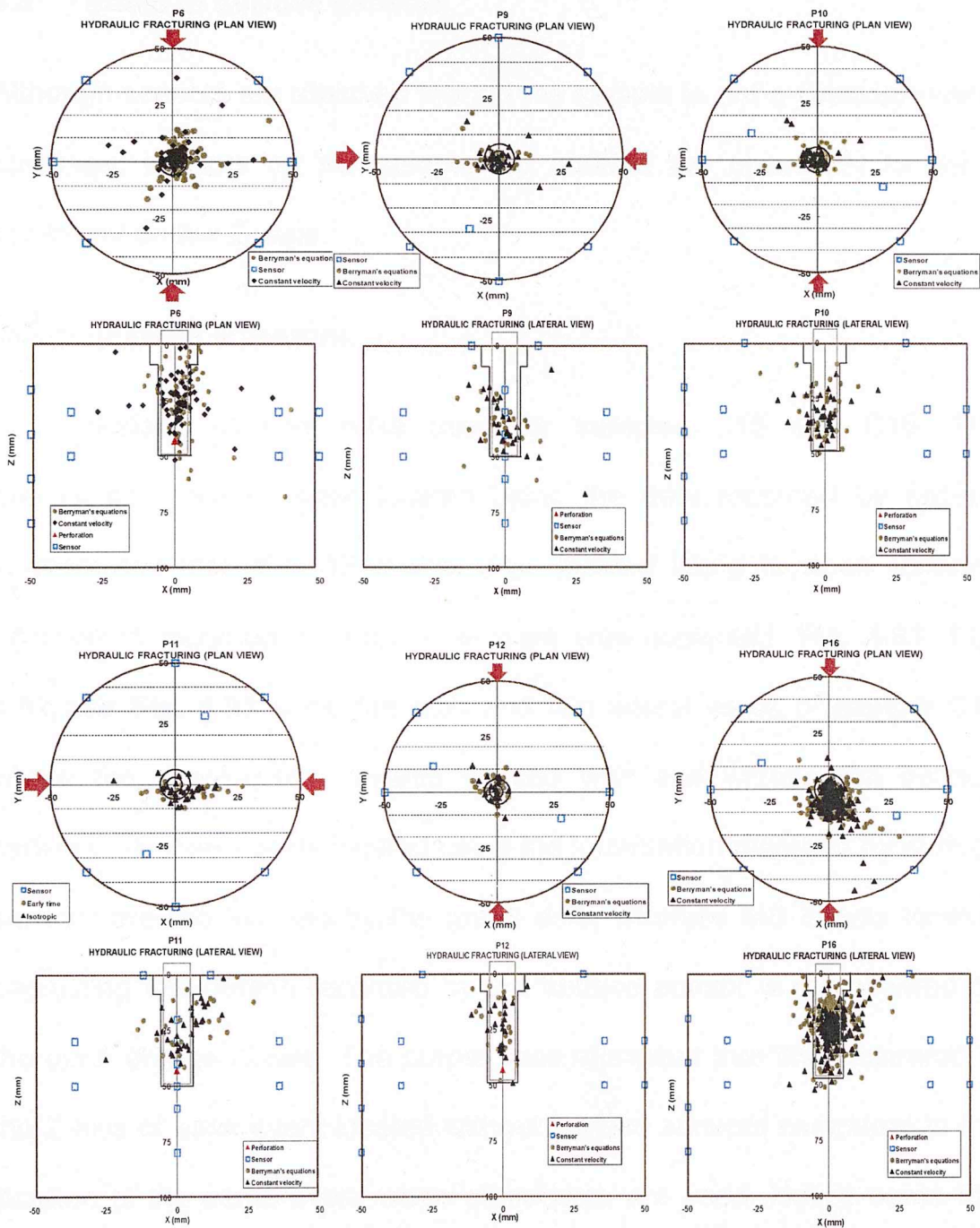


Fig. 4.90 – Plan and lateral views of pyrophyllite samples showing location of MS events using Berryman’s equations for strong anisotropy (Berryman, 2008) (green dots) and a constant velocity model (black triangles). Hypocenters located using a constant velocity model form a cluster around the borehole in most cases.

4.3 Effect of surface sensors

Although sensors are attached around the sample to get a good azimuthal coverage, sensors on the sample top surface are necessary to get a constraint on the Z- axis.

4.3.1 Indiana limestone

Surface sensors were used for samples C15 and C16. The microseismic events were located using the data recorded by sixteen sensors and then the MS events were located using fourteen sensors; information recorded by surface sensors was neglected. **Fig. 4.91**, **Fig. 4.92** and **Fig. 4.93** show the plan and two lateral views of sample C15 where the microseismic events located with and without the surface sensors. The MS events located using the information recorded by surface sensors are represented by the green dots, whereas MS events located neglecting information recorded by the surface sensor is represented by the open orange circles. The purple lines represent the “displacement” in the Z-axis of each event located without surface sensors compared to the location of the same event when all sensors are used. Notice some MS events are located outside the sample when surface sensors are not taken into account (**Fig. 4.92**).

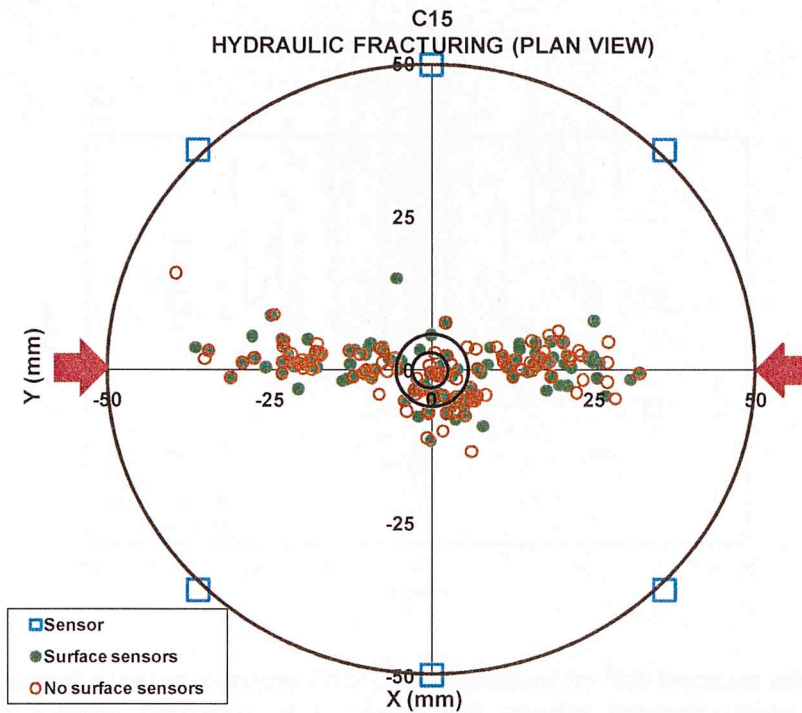


Fig. 4.91 - Plan view of sample C15 showing the different spatial distribution between MS events located using information recorded by the surface sensors (green dots) and the MS events located neglecting the information recorded by the surface sensors (orange open circles). The red arrows represent the orientation of the stress applied with a magnitude of 1000 psi.

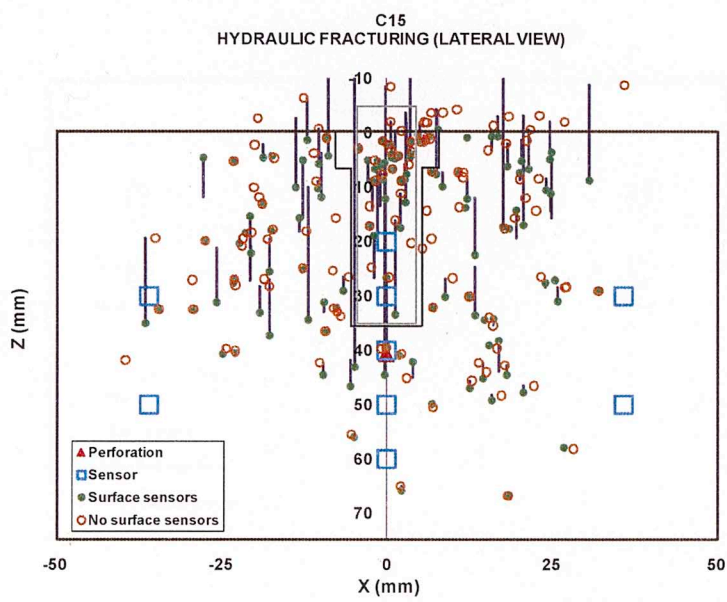


Fig. 4.92 - Lateral view of sample C15 perpendicular to the fracture plane showing the different spatial distribution between MS events located using information recorded by the surface sensors (green dots) and the MS events located neglecting the information recorded by the surface sensors (orange open circles). The purple lines represent the displacement in the Z-axis of each event located ignoring the information recorded by the surface sensors compared to the location of the same event when all sensors are used. The red triangle represents the perforation point in the tubing. Note some events are located outside the sample when surface sensors are not taken into account.

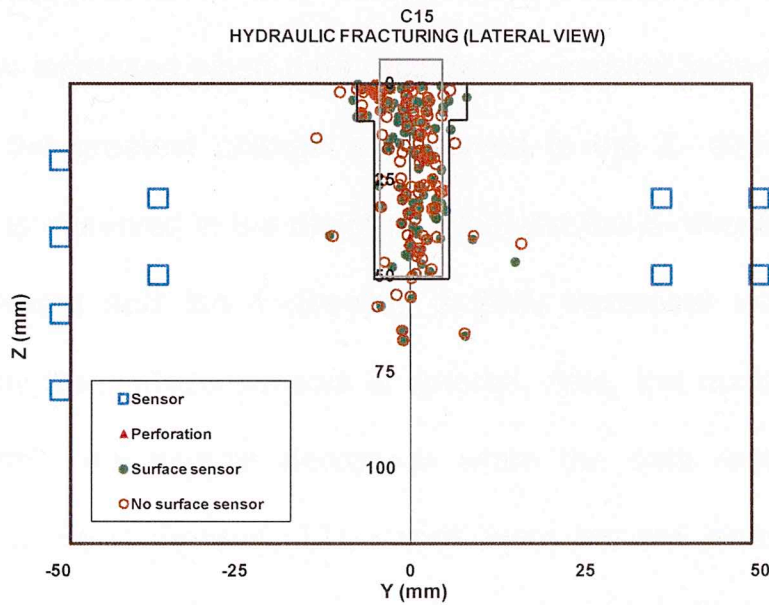


Fig. 4.93 - Lateral view of sample C15 parallel to the fracture plane showing the different spatial distribution between MS events located using information recorded by the surface sensors (green dots) and the MS events located neglecting the information recorded by the surface sensors (orange open circles). The red triangle represents the perforation point in the tubing.

When MS events are located ignoring the information recorded by the surface sensors, an increase in errors is observed in the Z-direction (Table 4.13). Also, when surface sensors are not taken into account fewer MS events are locatable within the sample; some MS events are located outside the sample. Table 4.13 shows the values of average uncertainty in the X, Y and Z coordinates for both cases.

Table 4.13 - Average uncertainty values for X, Y and Z coordinates in sample C15.

	Uncertainty x, mm	Uncertainty y, mm	Uncertainty z, mm
No surface sensors	0.40	0.24	0.85
Surface sensors	0.35	0.19	0.49

From **Table 4.13** it is evident that uncertainties in all spatial coordinates increased when data recorded by surface sensors is ignored. However, the greatest change is observed in the Z- direction; a 73% increment is observed in the direction, whereas the X- direction exhibits a 14% increment and the Y-direction a 26% increment when the data recorded by the surface sensors is ignored. Also, the number of events located within the sample decreases when the data recorded by the surface sensors is ignored; 124 events were located when all sensors were used, whereas 107 events were located when surface sensors were omitted. **Table 4.14** shows the values of average uncertainty in all spatial coordinates for samples C15 and C16 with and without sensors attached on the upper surface of the sample, along with the number of events located for both cases.

Table 4.14 - Average uncertainty values for samples C15 and C16 with and without sensors placed on the upper surface of the sample. Error increased in the Z-direction when no surface sensors were used on the upper surface of the samples.

		Uncert. x, mm	Uncert. y, mm	Uncert. z, mm	Number of events
C15	No surface sensors	0.40	0.24	0.85	107
	Surface sensors	0.35	0.19	0.49	124
C16	No surface sensors	0.32	0.17	0.58	112
	Surface sensors	0.26	0.14	0.39	118

Table 4.14 shows an increase in all spatial coordinates, especially in the Z-direction. Also, it shows that more events are located within the sample when sensors are placed on the upper surface of the sample. **Table 4.15** shows the percentage of increase of error in each spatial coordinate when no surface sensors are attached to the upper surface of the sample.

Table 4.15 - Increase (percentage) of error in spatial coordinates for Indiana limestone samples C15 and C16 when no sensors are attached to the upper surface of the sample.

	X-axis, %	Y-axis, %	Z-axis, %
C15	14	26	73
C16	23	21	49

It is clear that ignoring the data recorded by the top sensors generates higher uncertainty in all spatial coordinates, especially in the Z-direction. **Table 4.16** shows the rms error for samples C15 and C16 when surface sensors are used and when they are ignored.

Table 4.16 - rms error for Indiana limestone C15 and C16 when surface sensors are used and when they are not used.

	rms error, mm	
	C15	C16
Surface sensors	0.67	0.50
No surface sensors	1.01	0.68

From **Table 4.16** it is observed that when information recorded by the surface sensors is not taken into account, the rms error increases as much as 43%.

4.3.2 Lyons sandstone

Fig. 4.94, Fig. 4.95 and Fig. 4.96 show the plan and two lateral views of sample S4 where microseismic events have been located for both cases when the information recorded by the surface sensors has been used and when it has not.

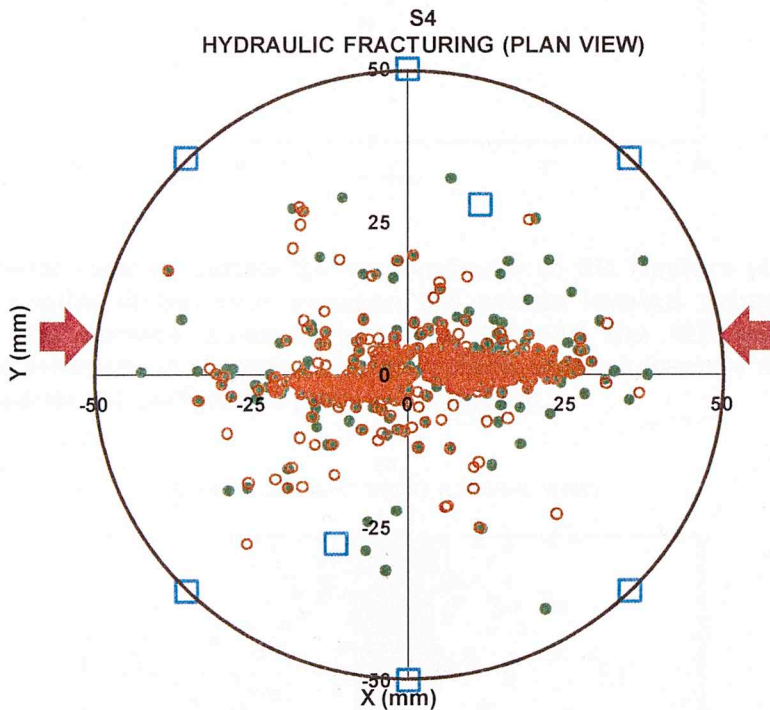


Fig. 4.94 - Plan view of sample S4 showing the different spatial distribution between MS events located using information recorded by the surface sensors (green dots) and the MS events located neglecting the information recorded by the surface sensors (orange open circles). The red arrows represent the orientation of the applied stress with a magnitude of 1040 psi.

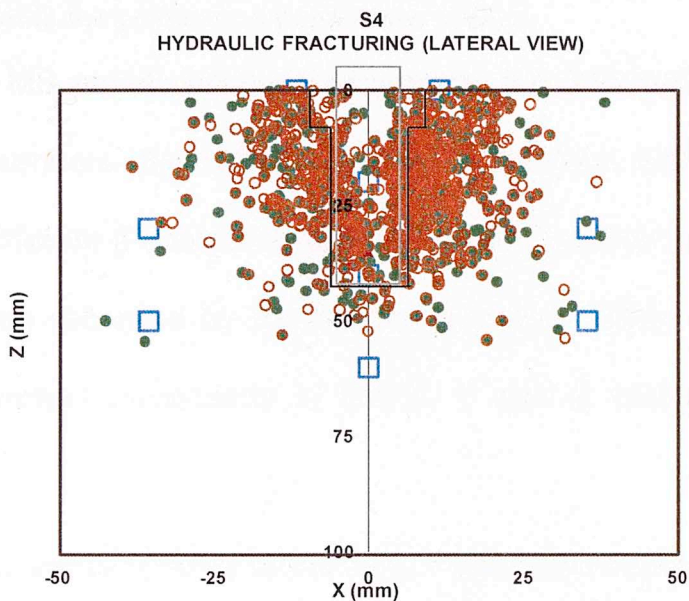


Fig. 4.95 - Lateral view of sample S4 perpendicular to the fracture plane showing the different spatial distribution between MS events located using information recorded by the surface sensors (green dots) and the MS events located neglecting the information recorded by the surface sensors (orange dots). The red triangle represents the perforation point in the tubing.

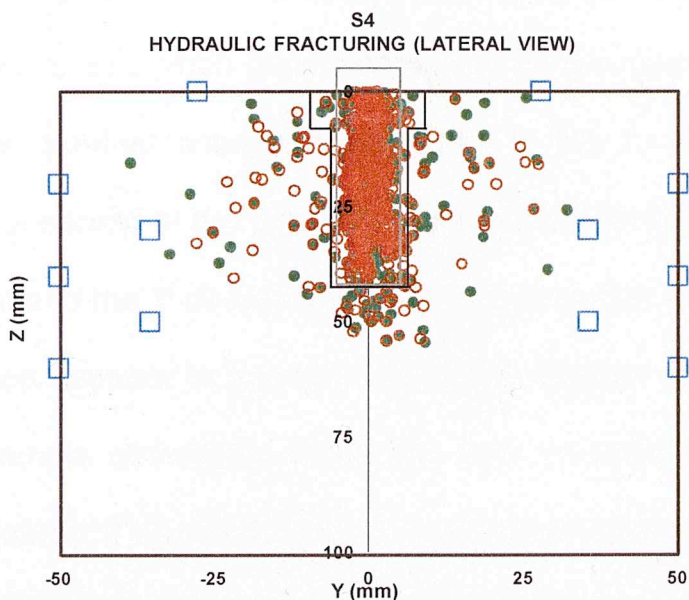


Fig. 4.96 - Lateral view of sample S4 parallel to the fracture plane showing the different spatial distribution between MS events located using information recorded by the surface sensors (green dots) and the MS events located

neglecting the information recorded by the surface sensors (orange dots). The red triangle represents the perforation point in the tubing.

When MS events are located ignoring the information recorded by the surface sensors, the ultimate spatial distribution and the number of events are different if compared to those when the location is done using the information recorded by the surface sensors. **Table 4.17** shows the values of average uncertainty in the X, Y and Z coordinates for both cases.

Table 4.17 - Average uncertainty values for X, Y and Z coordinates in sample S4.

	Uncertainty x, mm	Uncertainty y, mm	Uncertainty z, mm
No surface sensors	0.97	0.61	2.22
Surface sensors	0.94	0.58	1.40

From **Table 4.17** it is evident that uncertainties in all spatial coordinates increased when data recorded by surface sensors is ignored. However, the greatest change is observed in the Z- direction; a 59% increment is observed in the direction, whereas the X- direction exhibits a 3% increment and the Y-direction a 5% increment when the data recorded by the surface sensors is ignored. Also, the number of events located within the sample decreases when the data recorded by the surface sensors is ignored; 712 events were located when all sensors were used, whereas 655 events were located when surface sensors were omitted.

Table 4.18 shows the values of average uncertainty in all spatial coordinates for Lyons sandstone samples with and without sensors attached on the upper surface of the sample, along with the number of events located for both cases.

Table 4.18 - Average uncertainty values for Lyons sandstone samples with and without sensors placed on the upper surface of the sample. Error increased in the Z-direction when no surface sensors were used on the upper surface of the samples.

		Uncert. x, mm	Uncert. y, mm	Uncert. z, mm	Number of events
S4	No surface sensors	0.97	0.61	2.22	655
	Surface sensors	0.94	0.58	1.40	712
S6	No surface sensors	1.29	0.75	2.60	807
	Surface sensors	1.27	0.74	1.79	861
S7	No surface sensors	1.08	0.71	2.61	500
	Surface sensors	0.97	0.63	1.51	530
S8	No surface sensors	0.86	0.69	1.81	473
	Surface sensors	0.39	0.23	0.55	535
S9	No surface sensors	0.86	0.69	1.81	1370
	Surface sensors	0.87	0.56	1.09	1455
S11	No surface sensors	1.69	1.04	3.78	1356
	Surface sensors	0.81	0.58	1.47	1576
S13	No surface sensors	1.43	0.89	2.62	713
	Surface sensors	1.05	0.61	1.67	803
S14	No surface sensors	1.42	0.99	2.56	460
	Surface sensors	1.24	0.87	1.61	545

Table 4.18 shows an increase in all spatial coordinates, especially in the Z-direction. Also, it shows that more events are located within the sample when sensors are placed on the upper surface of the sample.

Table 4.19 shows the percentage of increase of error in each spatial coordinate when no surface sensors are attached to the upper surface of the sample.

Table 4.19 - Increase (percentage) of error in spatial coordinates for Lyons sandstone samples when no sensors are attached to the upper surface of the sample.

	X-axis, %	Y-axis, %	Z-axis, %
S4	3	5	59
S6	2	1	45
S7	11	13	73
S8	120	200	229
S9	1	23	66
S11	108	79	157
S13	36	46	57
S14	14	14	59

Table 4.19 shows the maximum variation in location when sensors are not attached to the upper surface of the samples happens in the Z-direction.

It is clear that ignoring the data recorded by the top sensors generates higher uncertainty in all spatial coordinates, especially in the Z-direction. **Table 4.20** shows the rms error for Lyons sandstone samples when surface sensors are used and when they are ignored.

Table 4.20 - rms error for Lyons sandstone samples when surface sensors are used and when they are not used.

	rms error, mm							
	S4	S6	S7	S8	S9	S11	S13	S14
Surface sensors	1.66	2.13	1.62	0.79	1.46	1.97	1.92	1.97
No surface sensors	2.41	2.75	2.47	1.83	1.96	3.80	2.51	2.55

From **Table 4.20** it is observed that when information recorded by the surface sensors is not taken into account, the rms error increases an average of 45%.

4.3.3 Pyrophyllite

Fig. 4.97, **Fig. 4.98** and **Fig. 4.99** show the plan and two lateral views of sample P11 where microseismic events have been located for both cases when the information recorded by the surface sensors has been used and when it has not.

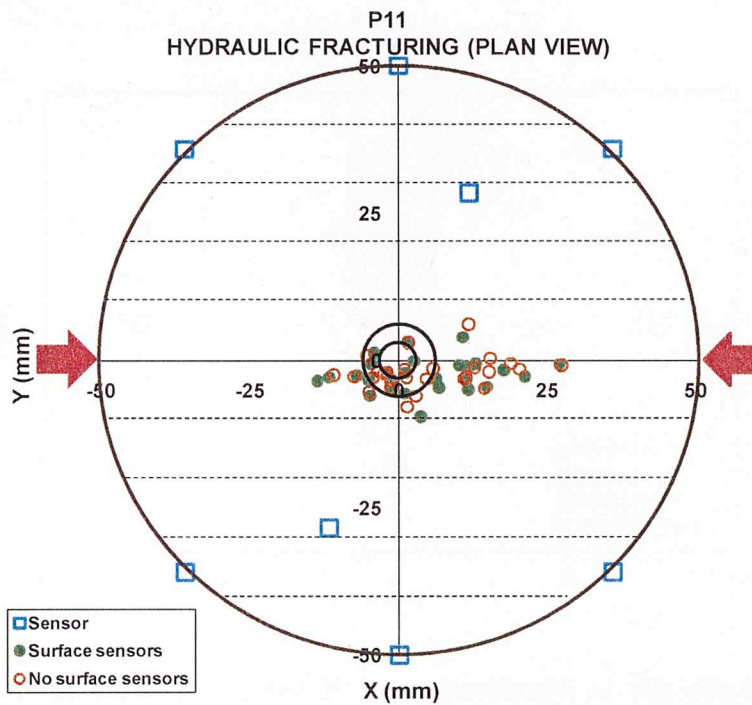


Fig. 4.97 - Plan view of sample P11 showing the different spatial distribution between MS events located using information recorded by the surface sensors (green dots) and the MS events located neglecting the information recorded by the surface sensors (orange dots) . The red arrows represent the orientation of the stress applied with a magnitude of 950 psi. The dashed lines represent the bedding planes.

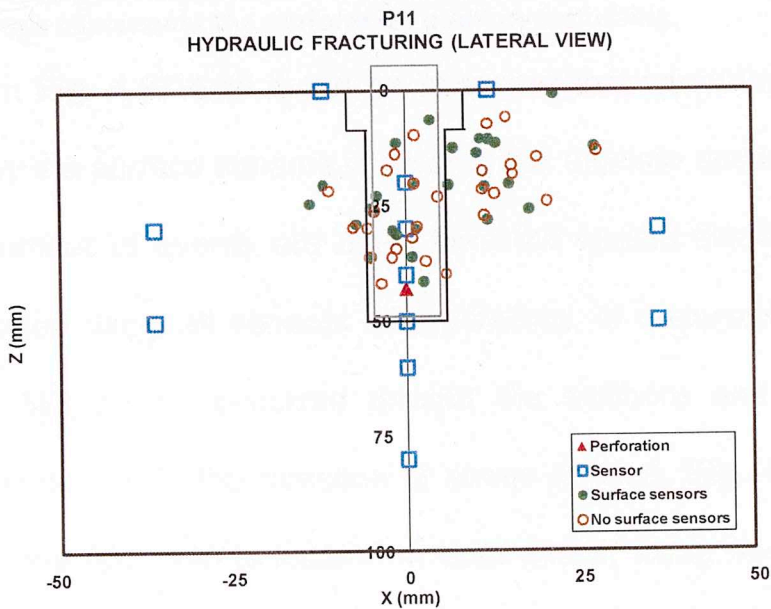


Fig. 4.98 - Lateral view of sample P11 perpendicular to the direction of stress applied showing the different spatial distribution between MS events located using information recorded by the surface sensors (green dots) and the MS events located neglecting the information recorded by the surface sensors (orange dots). The red triangle represents the perforation point in the tubing.

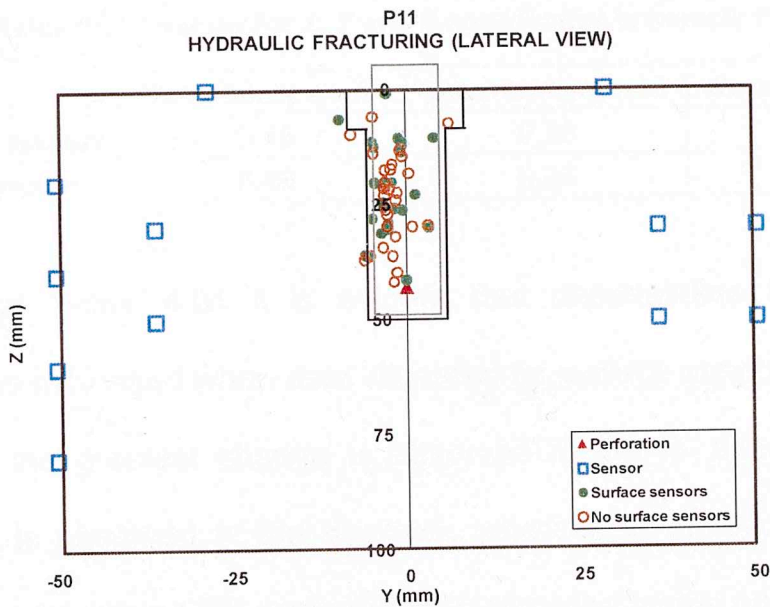


Fig. 4.99 - Lateral view of sample P11 parallel to the direction of stress applied showing the different spatial distribution between MS events located using information recorded by the surface sensors (green dots) and the MS events

located neglecting the information recorded by the surface sensors (orange dots). The red triangle represents the perforation point in the tubing.

From **Fig. 4.97-4.99** it can be observed that when the information recorded by the surface sensors is ignored the ultimate spatial distribution and the number of events are differ from the spatial distribution of MS events located using all sensors. Nevertheless, is observed that in both cases the MS events occurred around the wellbore and the fracture propagation occurs in the direction of stress applied. **Fig. 4.98** and **Fig. 4.99** show that MS events located in both cases, using surface sensors and ignoring them, fall in the same depth range, above the tubing perforation. **Table 4.21** shows the values of average uncertainty in the X, Y and Z coordinates for both cases.

Table 4.21 - values for X, Y and Z coordinates in sample P11.

	Uncertainty x, mm	Uncertainty y, mm	Uncertainty z, mm
No surface sensors	0.46	0.26	1.09
Surface sensors	0.49	0.26	0.76

From **Table 4.21** it is evident that uncertainties in all spatial coordinates increased when data recorded by surface sensors is ignored. However, the greatest change is observed in the Z- direction; a 43% increment is observed in the direction, whereas in the X- direction the uncertainty decreased 6% when the data recorded by the surface sensors

is ignored. The uncertainty in the Y-direction did not change. The number of events located within the sample remained constant for both cases.

Table 4.22 shows the values of average uncertainty in all spatial coordinates for pyrophyllite samples with and without sensors attached on the upper surface of the sample, along with the number of events located for both cases.

Table 4.22 - Average uncertainty values for pyrophyllite samples with and without sensors placed on the upper surface of the sample. Error increased in the Z-direction when no surface sensors were used on the upper surface of the samples.

		Uncertainty x, mm	Uncertainty y, mm	Uncertainty z, mm	Number of events
P9	No surface sensors	0.23	0.15	0.44	26
	Surface sensors	0.23	0.12	0.32	27
P10	No surface sensors	0.18	0.29	0.69	35
	Surface sensors	0.16	0.25	0.53	36
P11	No surface sensors	0.46	0.26	1.09	27
	Surface sensors	0.49	0.26	0.76	27
P12	No surface sensors	0.21	0.20	0.80	20
	Surface sensors	0.19	0.28	0.54	20
P16	No surface sensors	0.37	0.57	1.42	173
	Surface sensors	0.32	0.50	0.79	186

Table 4.22 shows an increase in all spatial coordinates, especially in the Z-direction. Also, it shows that more events are located within the sample when sensors are placed on the upper surface of the sample.

Table 4.23 shows the percentage of increase of error in each spatial

coordinate when no surface sensors are attached to the upper surface of the sample.

Table 4.23 - Increase (percentage) of error in spatial coordinates for pyrophyllite samples when no sensors are attached to the upper surface of the sample.

	X-axis, %	Y-axis, %	Z-axis, %
P9	0	25	38
P10	12	16	30
P11	6	0	43
P12	10	28	48
P16	16	24	80

Table 4.23 shows the maximum variation in location when sensors are not attached to the upper surface of the samples happens in the Z-direction in each case.

Again, it is clear that ignoring the data recorded by the top sensors generates higher uncertainty in all spatial coordinates, especially in the Z-direction. **Table 4.24** shows the rms error for pyrophyllite samples when surface sensors are used and when they are ignored.

Table 4.24 - rms error for pyrophyllite samples when surface sensors are used and when they are not used.

	rms error, mm				
	P9	P10	P11	P12	P16
Surface sensors	0.39	0.86	1.02	0.60	1.06
No surface sensors	0.53	0.90	1.29	0.95	1.59

From **Table 4.24** it is observed that when information recorded by the surface sensors is ignored, the rms error increases an average of 35%. It also shows that sample P10, loaded with 960 psi, has the smallest increase in rms error when surface sensors are not used if compared to other pyrophyllite samples.

Table 4.25 shows the variation of the dimensions of the hydraulic fracture with or without sensors attached to the upper surface of the sample. Results for Indiana limestone, Lyons sandstone and pyrophyllite are shown.

Table 4.25 - Values of process zone length, width and height with or without sensors attached to the upper surface of the sample. The area of the process zone (length*width) is exhibited along with the SRV (Stimulated Reservoir Volume).

	Surface sensors					No surface sensors				
	Length, mm	Height, mm	Width, mm	Area, mm ²	SRV, mm ³	Length, mm	Height mm	Width mm	Area, mm ²	SRV, mm ³
C15	23	68	22	506	34408	20	68	24	480	32640
C16	86	60	16	1376	82560	88	60	17	1496	89760
S4	75	50	25	1875	93750	71	48	26	1846	88608
S6	72	50	17	1224	61200	74	56	14	1036	58016
S7	58	45	16	928	41760	62	42	14	868	36456
S8	76	48	20	1520	72960	82	60	16	1312	78720
S9	71	60	29	2059	123540	75	55	24	1800	99000
S11	95	72	19	1805	129960	63	70	24	1512	105840
S13	75	77	16	1200	92400	54	60	20	1080	64800
S14	87	40	22	1914	76560	73	74	24	1752	129648
P9	33	29	12	396	11484	30	32	10	300	9600
P10	19	30	16	304	9120	19	32	16	304	9728
P11	44	41	14	616	25256	40	39	15	600	23400
P12	25	35	16	400	14000	32	39	19	608	23712

P16	37	50	27	999	49950	41	56	30	1230	68880
-----	----	----	----	-----	-------	----	----	----	------	-------

The variation of the area of the process zone (length*width) is shown in **Table 4.21**. In 10 out of the 15 samples (C15, S4, S6, S7, S8, S9, S11, S14, P9 and P11) studied the area is larger when the surface sensors are attached to the upper surface of the samples, whereas in 4 samples (C16, S13, P12, P16) the area is larger when no surface sensors are used. One sample (P10) showed no variation in the process zone area in both cases.

4.4 Microscopic observations

After samples where hydraulically fractured, 1" diameter by 2" long plugs were taken from each sample along the direction of the hydraulic fracture (**Fig. 4.100**).

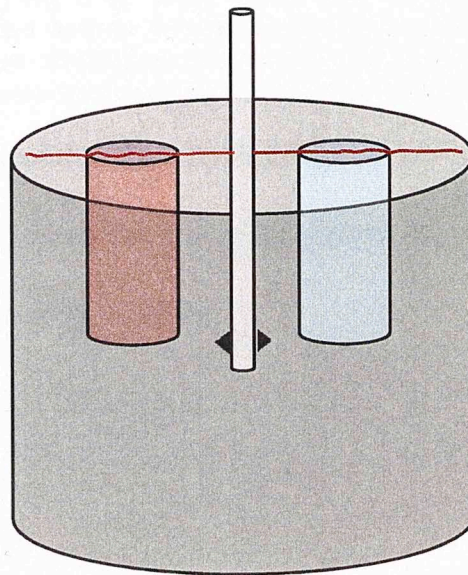


Fig. 4.100 – Two plugs are taken out from the sample along the direction of the fracture after it is fractured. The red and blue cylinders are the 1” diameter by 2” long plugs and the red line represents the fracture on the upper surface of the sample.

4.4.1 Indiana limestone

After the fracture is cored vertical slices are cut and observed under the microscope (Fig. 4.101).

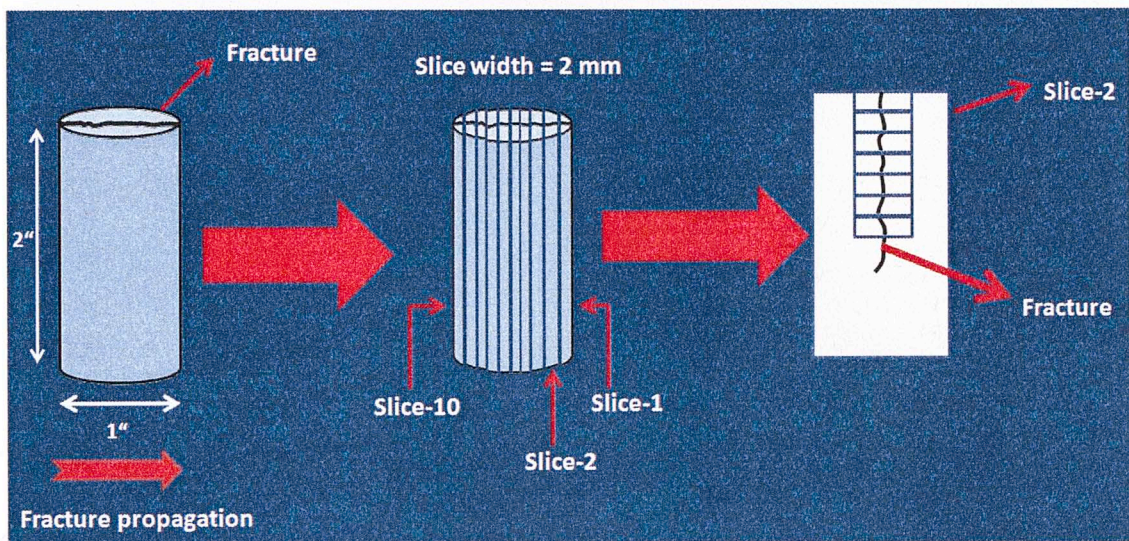
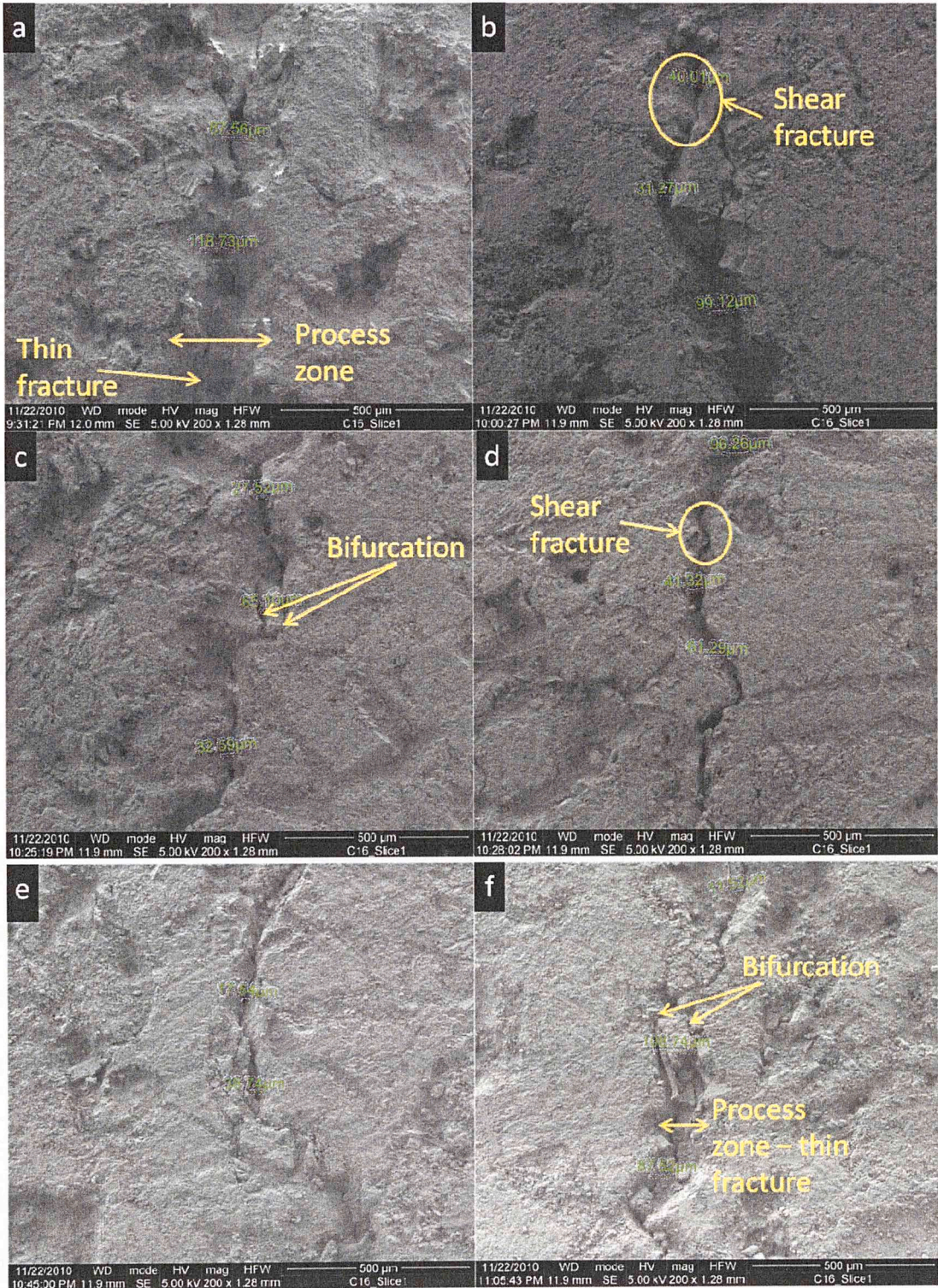


Fig. 4.101 – The right plug (Fig. 4.99) is cut into 10 slices where slice 1 is the farthest from the injection source whereas slice 10 is the closes to the perforation point. Each slice is 2 mm width and 50 mm long. The figure in the far right shows the eight pictures that were taken along the fracture in slice 2.

Slice 1 was observed under the SEM (Scanning-Electron Microscope) FEI Quanta 200™ starting from the top of the slice and moving downward until the end of the fracture (Fig. 4.102).



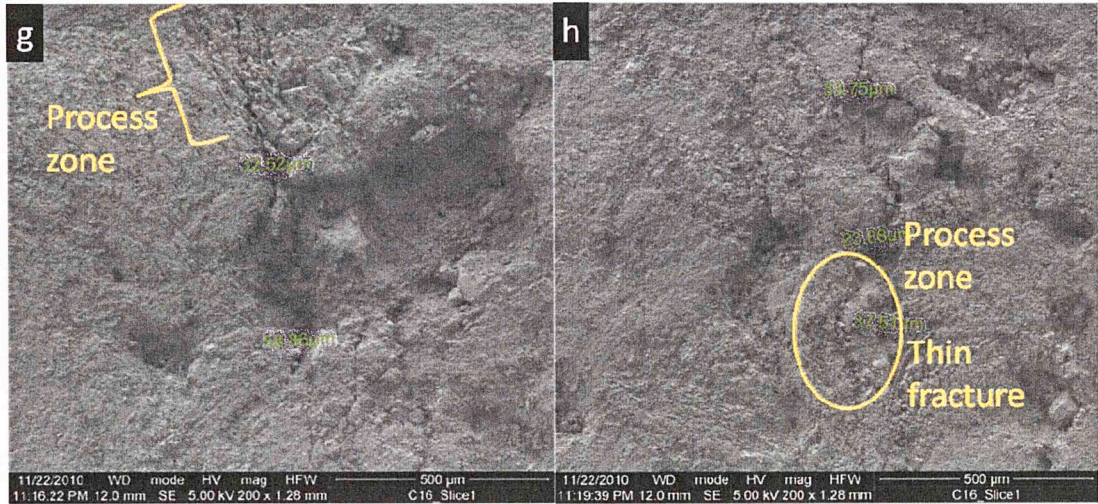


Fig. 4.102 – Fracture morphology observation of slice 1 of sample C16 (Indiana limestone). Pictures were taken starting at the top of the slice moving downwards (From a to h). The induced fracture is observed in the different pictures showing that it is not a planar feature. Bifurcation is observed in some cases (b, c and f).

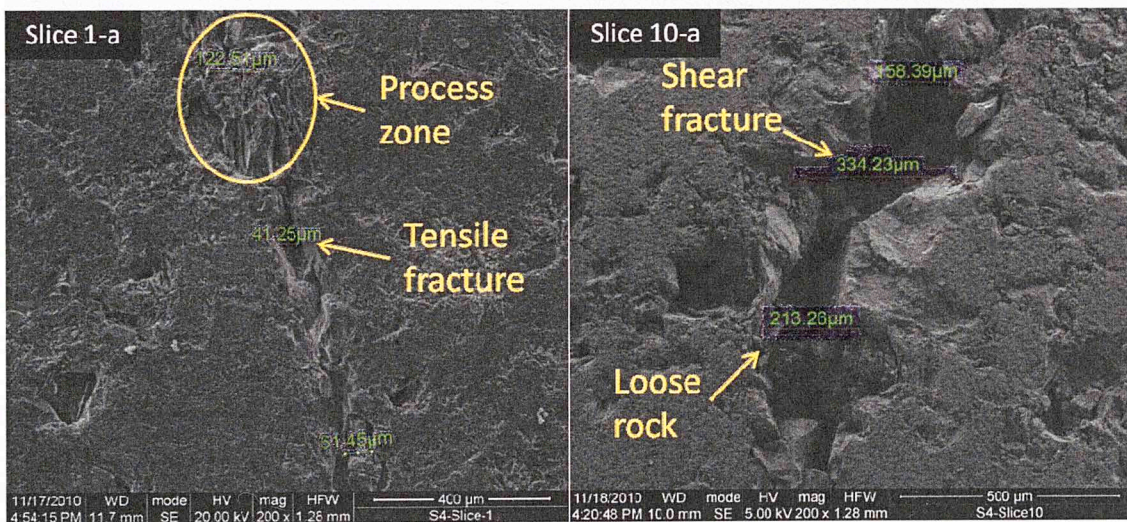
Fig. 4.102 shows SEM observations of slice 1 from sample C16 (Indiana limestone). It can be observed that as we move downward in the slice (a → h) the fracture gets thinner. In all observations is clear that fractures are not planar features; they can deviate by surrounding a grain that comes into the fracture path (**Fig. 4.102d**). Also, bifurcation of the fracture is observed (**Fig. 4.102b,c,f,e**). Observations of the SEM pictures show a large process zone containing a very thin fracture; **Fig. 4.102f** shows a wide process zone (~100 μm) and a thin fracture (~30 μm).

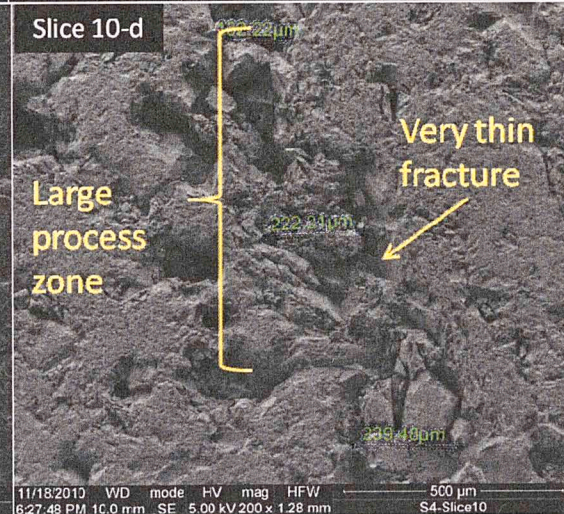
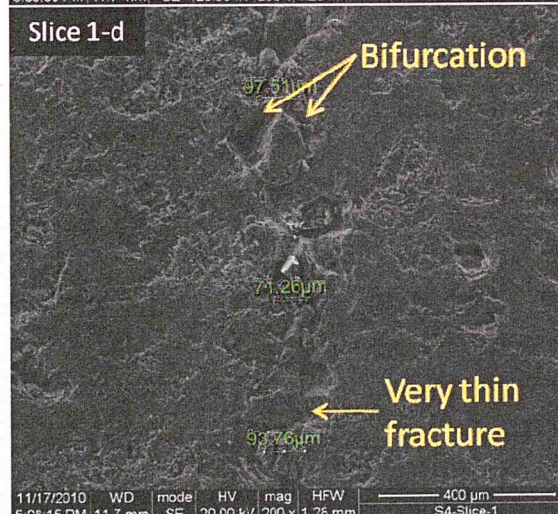
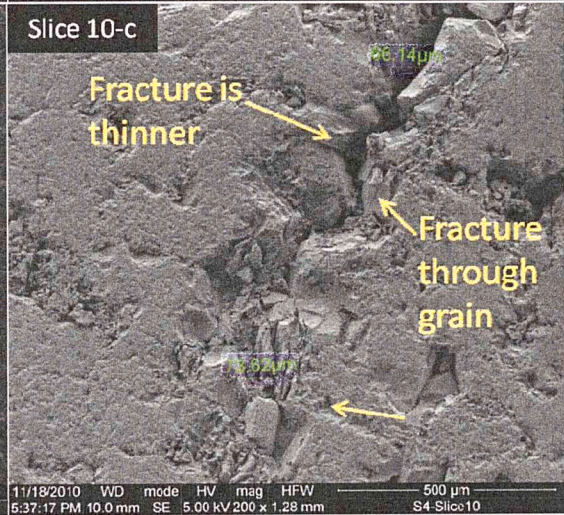
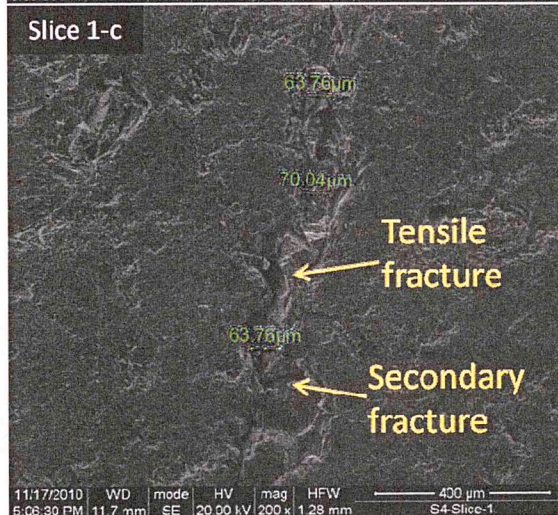
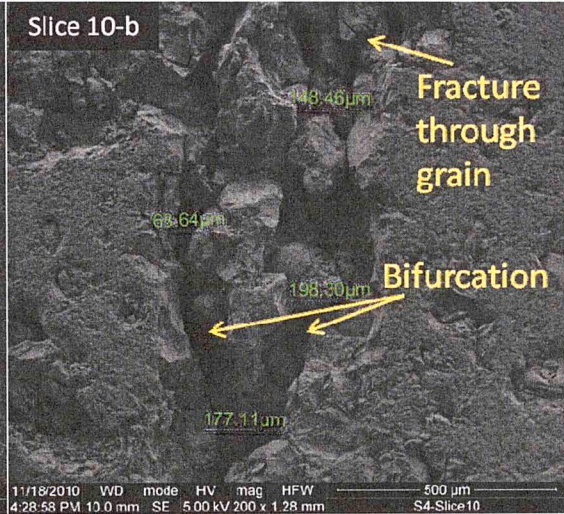
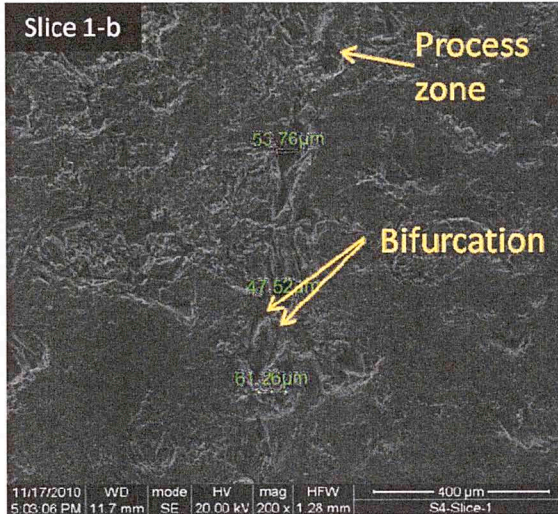
The polarization of the P-wave first arrival motions can be used to study the fracture mechanisms. Focal mechanism analysis of the MS events is a tool to identify the different failure mechanisms that occur during the fracturing process. Fall et al., (1992) classified focal

mechanisms into four different types: tensile, compressive, shear and complex. Chitralla (2011) found that the dominant mechanism of failure for Indiana limestone samples is shear failure. This is supported by observation of shear failure in the SEM pictures (Fig. 4.102b,d).

4.4.2 Lyons sandstone

The same procedure followed for Indiana limestone samples was used for Lyons sandstone samples (Fig. 4.101). Slices 1 and 10 from sample S4 were examined for differences in the fracture as it propagated away from the injection source (Fig. 4.103).





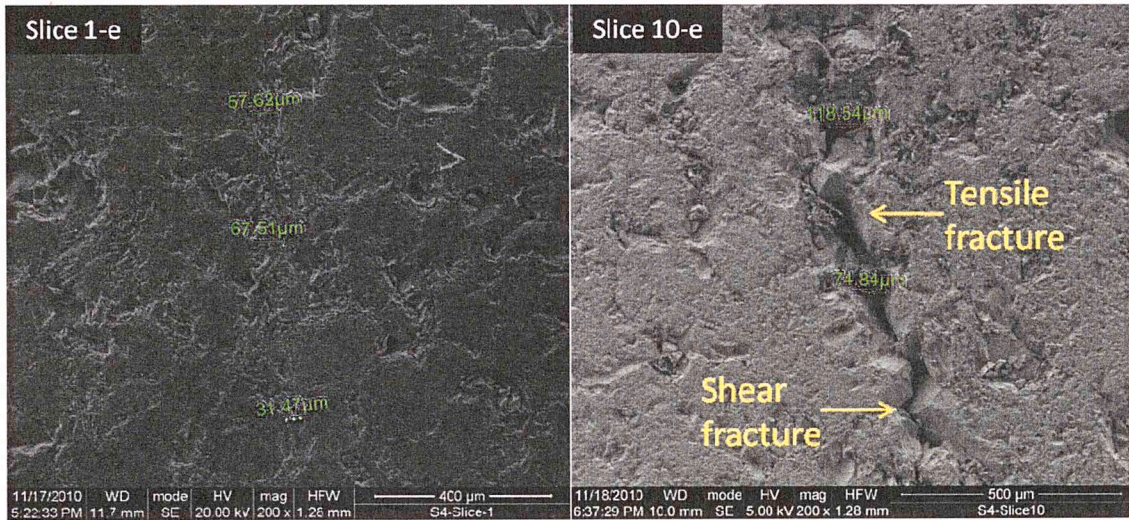


Fig. 4.103 – Fracture morphology observation of slice 1 and 10 of sample S4 (Lyons sandstone). Pictures were taken starting at the top of the slices moving downwards (From a to e). Slice 1 is farthest from the injection source than slice 10. It is clear that the fracture observed in the slice closer to the injection point (slice 10) is wider than the fracture in slice 1.

Fig. 4.103 shows SEM observations for slice 10 and slice 1 in sample S4 (Lyons sandstone). Slice 1 is the farthest from the injection source whereas slice 10 is the closest (**Fig. 4.101**). It is clear that the fracture in slice 10 is wider than in slice 1, suggesting the fracture is thinner as it moves away from the injection point.

As in Indiana limestone, **Fig. 4.103** shows induced fractures are not planar features but they deviate around surrounding grains that come into its path (**Fig. 4.103 - Slice1b,d, Fig. 4.103 – Slice10b**). Nevertheless, there is evidence of fractures that go through the grains (**Fig. 4.103 Slice 10b,c**). **Fig. 4.103** (Slice 10a) shows that during the process of hydraulic fracturing loose fragments can get into the fracture itself acting as a

“natural proppant”. **Fig. 4.103** (Slice 1c) shows the process zone ($\sim 60 \mu\text{m}$) is much wider than the actual fracture ($\sim 10 \mu\text{m}$). **Fig. 4.103** shows the fracture gets thinner as we move downward in both slices; this agrees with **Fig 4.25** which indicates the fracture tapers as it moves away from the injection point.

After Focal mechanisms studies, Chitralla (2011) found that shear failure is the dominant failure mechanism in sandstone samples. However, tensile events also occur during the fracturing process. **Fig. 4.103** shows evidence of both failure mechanisms occurring.

4.4.3 Pyrophyllite

After plugging hydraulic fracture (**Fig 4.100**) discs are cut perpendicular to the Z-axis and observed under the microscope (**Fig. 4.104**).

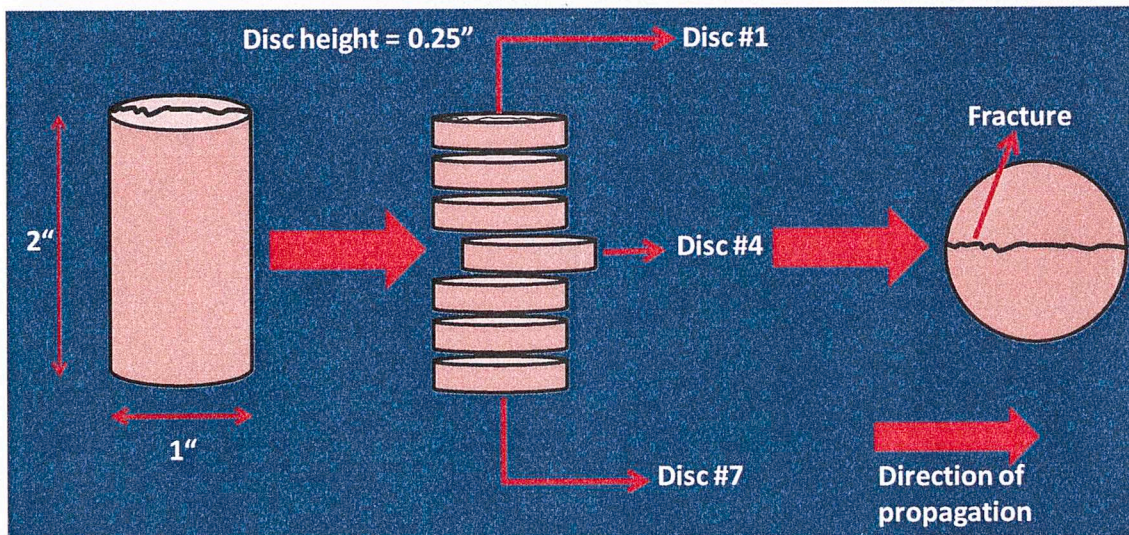
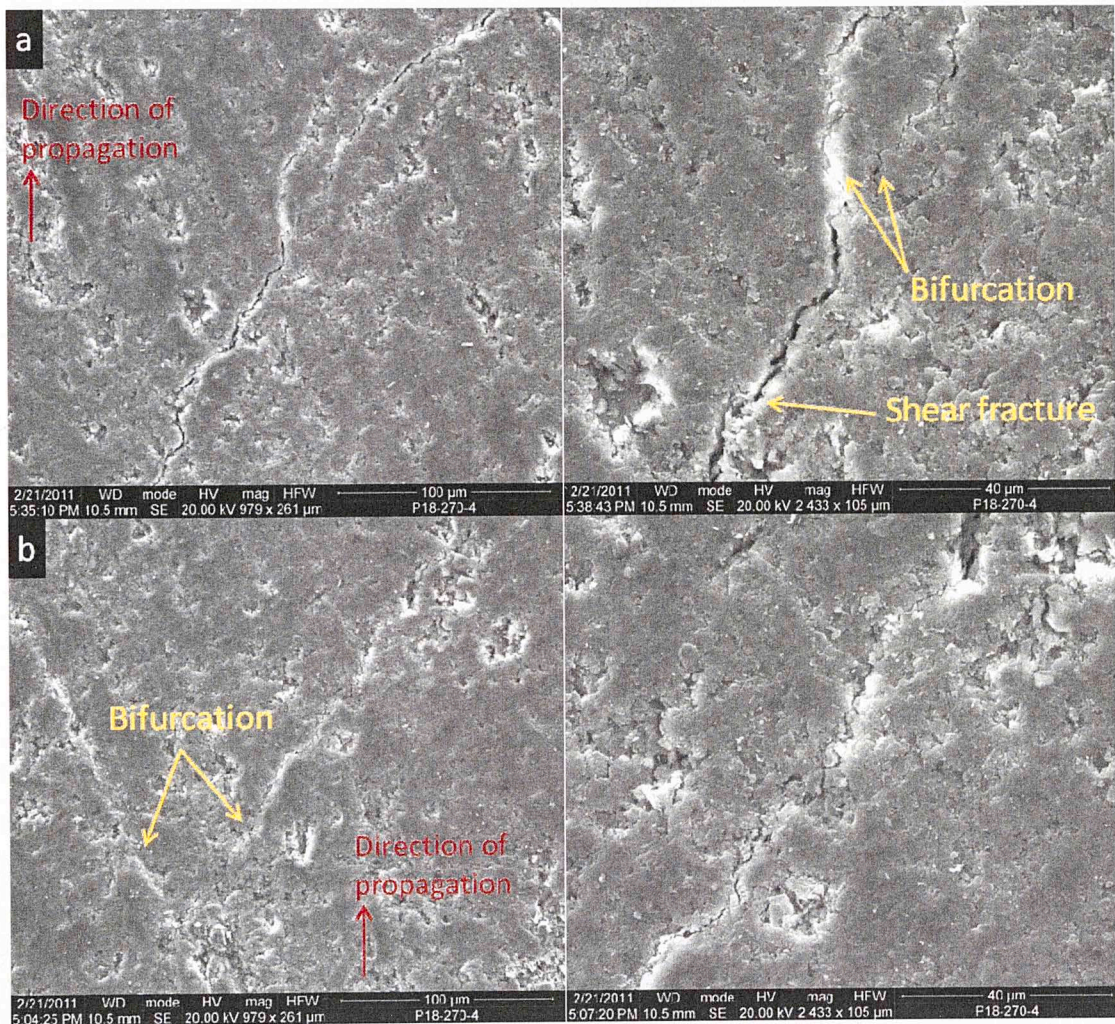


Fig. 4.104 – The left plug (Fig. 4.99) is cut into 7 discs where disc 1 is at the top of the plug whereas disc 7 is at the bottom. Each disc has a height of 5 mm and a diameter of 25 mm.

Fig. 4.105 shows the fracture morphology in sample P18 (pyrophyllite) observed in disc 4; Fig. 4.105a is the closest position the injection source while Fig. 4.105e is the farthest. The figures in the right are a magnification of the figures in the left in order to obtain a more detailed observation of the fracture.



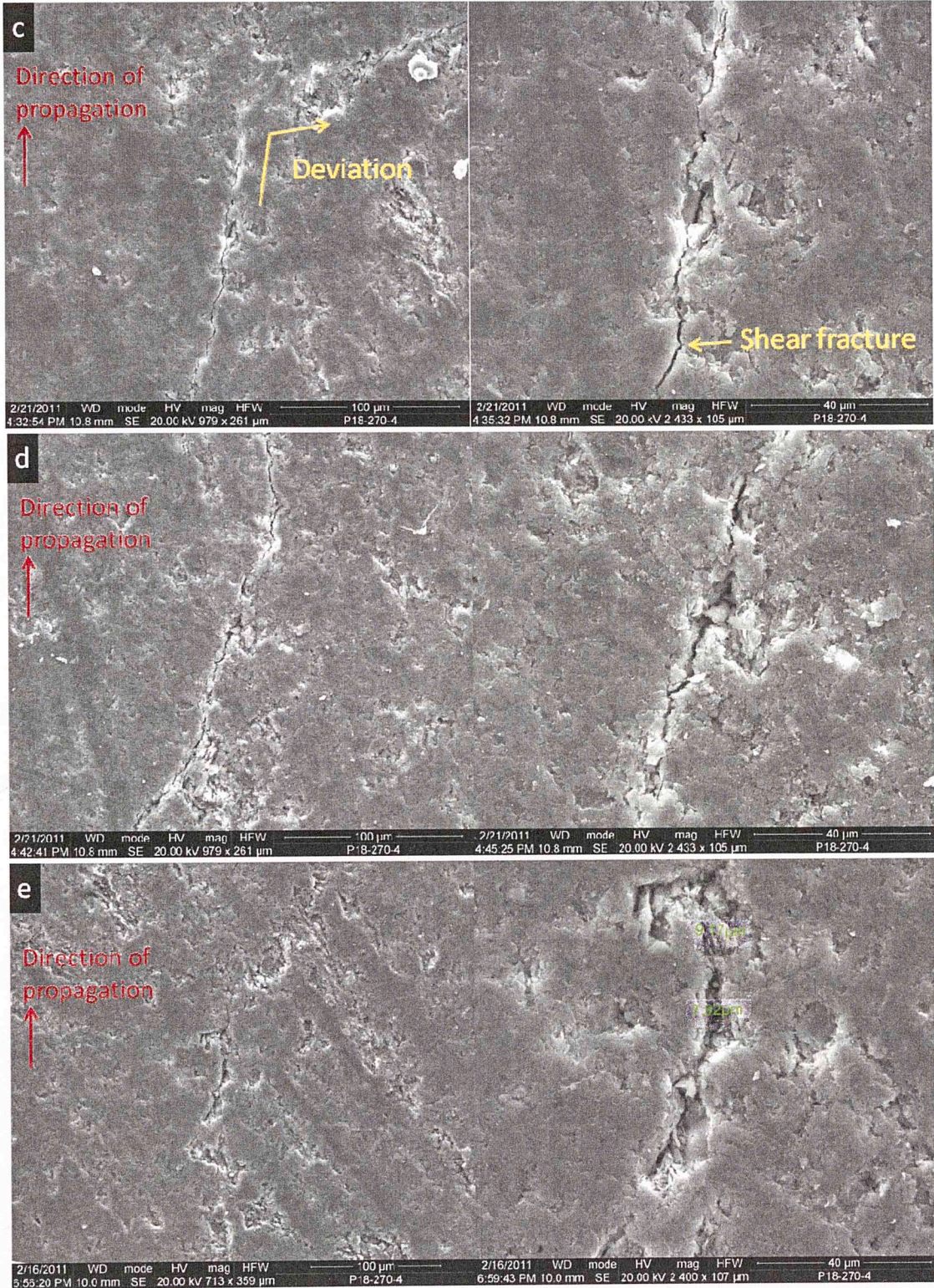


Fig. 4.105 – Fracture morphology observation of disc 4 of sample P18 (pyrophyllite). Pictures of the fracture were taken starting at the closest point from the injection point of the disc moving outwards (From a to e). The figures on the right are magnified images.

Fig. 4.105 shows the induced fracture is not a planar feature. Instead it deviates (**Fig. 4.105c**) and zigzags (**Fig. 4.105b-right**). Also, it is clear that the fracture gets thinner as it moves away from the injection source; in **Fig 4.105e** (left) a fracture is barely visible.

As in Indiana limestone and Lyons sandstone, bifurcation of the fracture is observed (**Fig. 4.105a,b**). Using focal mechanism solutions, Chitrala (2011) found shear failure is the dominant failure mechanism in pyrophyllite sample; **Fig. 4.105a,c** show evidence of shear failure.

Fig 4.106 shows observations of the same positions as shown in **Fig. 4.105** but at higher magnification. **Fig. 4.106a** and **Fig. 4.106b** show evidence of shear failure and zigzagging, respectively.

High magnification of the fracture reveals the small width of the fracture compared to the fractures observed in Indiana limestone and Lyons sandstone (**Fig. 4.106**); fracture width in pyrophyllite ranges from hundreds of nm to few μm , while in Lyons sandstone and Indiana limestone the fracture width is approximately 10 and 30 μm (**Fig. 4.102** and **Fig. 4.103**).

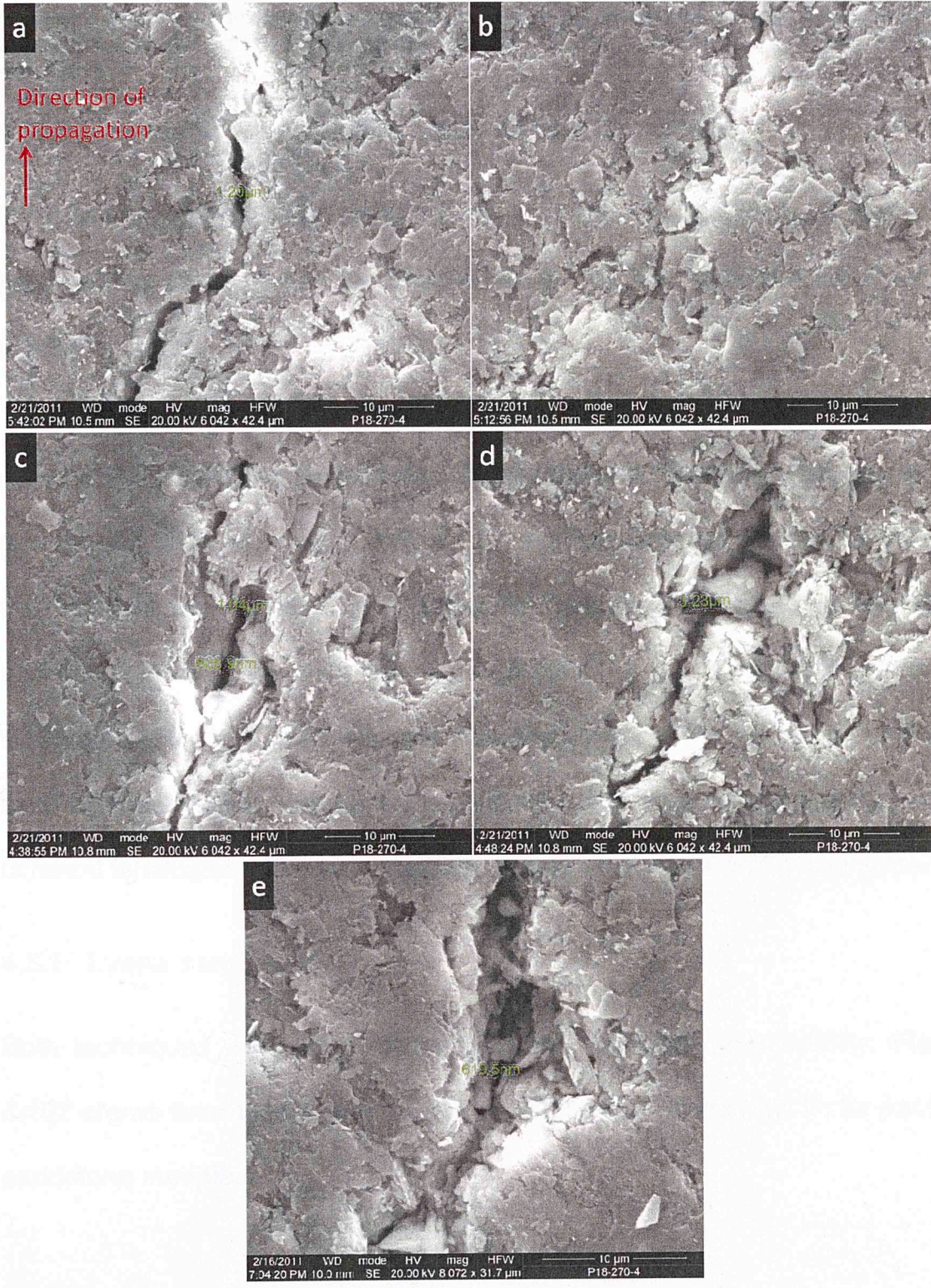


Fig. 4.106 – Fracture morphology observation of disc 4 of sample P18 (pyrophyllite) at higher magnification than Fig. 4.104. Evidence of shear failure and zigzagging is observed. Small widths of the induced fracture are observed (600 nm- 3 μ m).

4.5 Permeability estimation using microseismicity

Microseismic data has been used recently to estimate formation permeability as reported by Shapiro et al., (2006) and Dinske et al., (2010).

They have proposed two different techniques to estimate formation permeability using microseismic data; the r-t method derives the permeability from the rate of growth of a microseismic cloud by measuring the changes in distances, r , between the recorded microseismic events and the fluid injection point with time (Shapiro et al., 2006). The second technique estimates formation permeability by using the geometry of the microseismic cloud. Formation permeability has been calculated for two different lithologies of low permeability: Lyons sandstone and pyrophyllite.

4.5.1 Lyons sandstone

Both techniques were used to calculate the formation permeability. **Fig. 4.107** shows the r-t plots with the values of apparent diffusivity, D , for each sandstone sample.

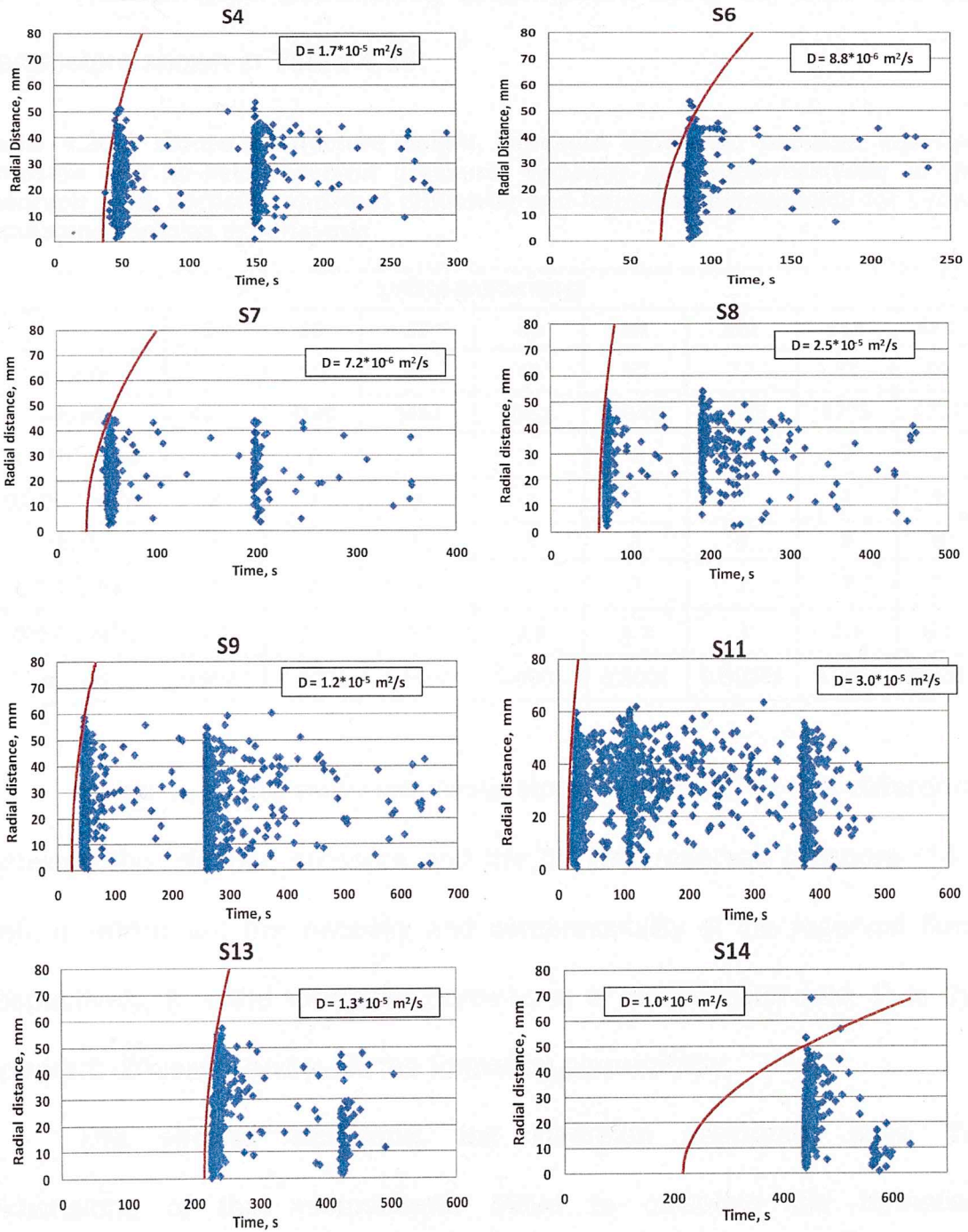


Fig. 4.107 - r-t plots for each Lyons sandstone showing the radial distance of each MS event to the perforation point as a function of time since the start of the injection. The blue diamonds represent the MS events and the red line is the triggering front of microseismicity which is defined by the diffusivity, D.

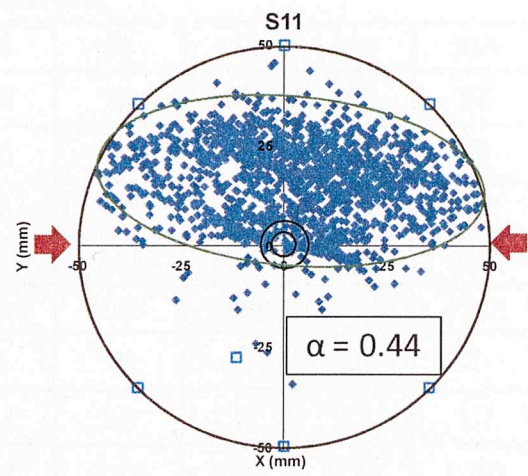
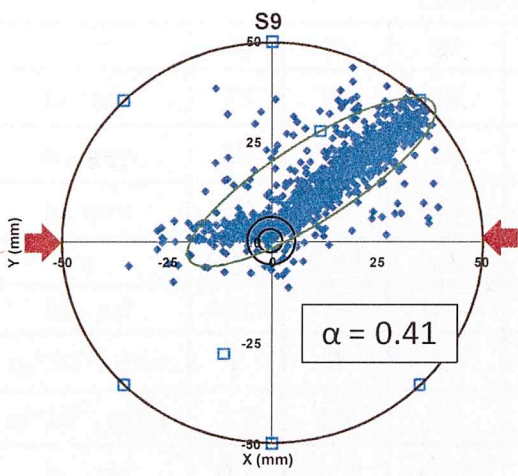
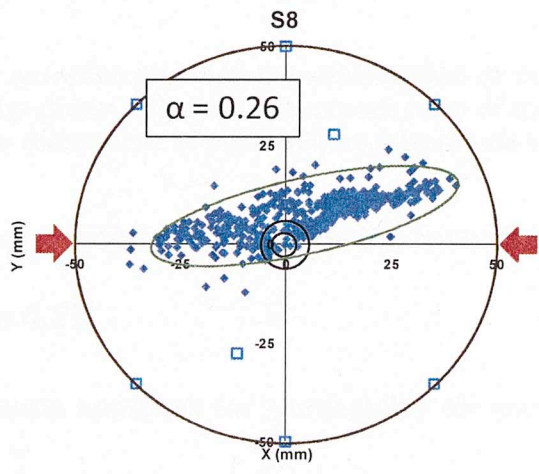
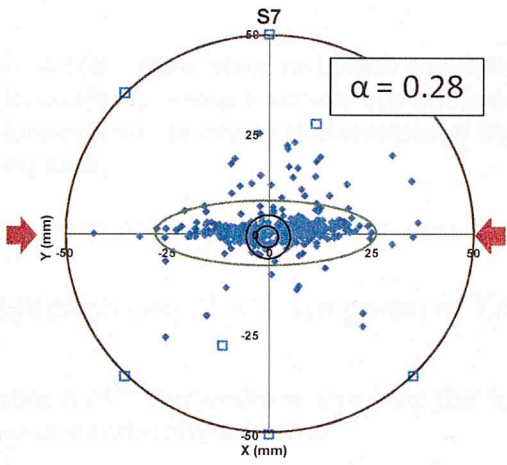
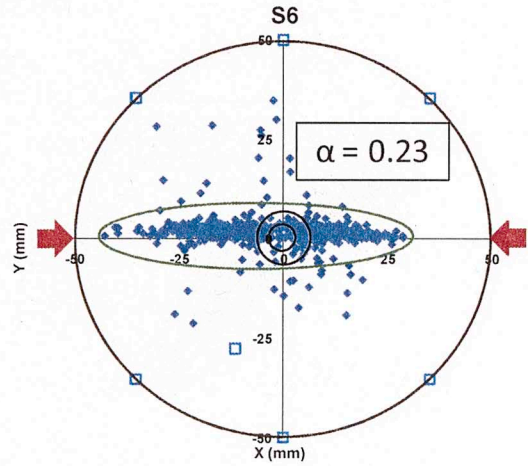
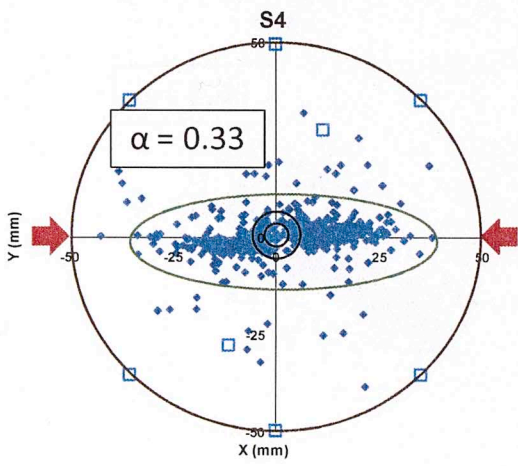
The formation permeability is computed using eq. 2.33 and the parameters shown in **Table 4.26**.

Table 4.26 - Values of fracture height, pressure difference between injection pressure and far-field reservoir pressure, viscosity and compressibility of the reservoir fluid, porosity, apparent diffusivity and formation permeability for Lyons sandstone samples experiments.

LYONS SANDSTONE								
	S4	S6	S7	S8	S9	S11	S13	S14
h_f , mm	50	50	45	48	60	72	77	40
ΔP , psi	4023	3140	3461	4512	5045	4858	2775	4733
$\eta_r * 10^{-5}$, Pa-s	2	2	2	2	2	2	2	2
$Q_i * 10^{-7}$, m ³ /s	2	2	2	2	2	2	2	2
Φ , %	8	8	8	8	8	8	8	8
$c_r * 10^{-6}$, Pa ⁻¹	7	7	7	7	7	7	7	7
$D * 10^{-5}$, m ² /s	1.7	0.9	0.7	2.5	1.2	3	1.3	0.1
k_{r-t} , μ d	0.0002	0.0007	0.0002	0.0001	0.0001	0.00005	0.0003	0.004

where h_f is the microseismicity cloud height, ΔP is the difference between the injection pressure and the far-field reservoir pressure (14.7 psi), η_r and c_r are the viscosity and compressibility of the reservoir fluid, respectively, ϕ is the formation porosity, q_i is the injection rate, D is the apparent diffusivity and k_{r-t} is the formation permeability.

The second technique, the inversion approach, uses the dimensions of the microseismic cloud to calculate the formation permeability. **Fig. 4.108** shows plan views of each sandstone sample where the microseismic cloud can be observed (blue diamonds).



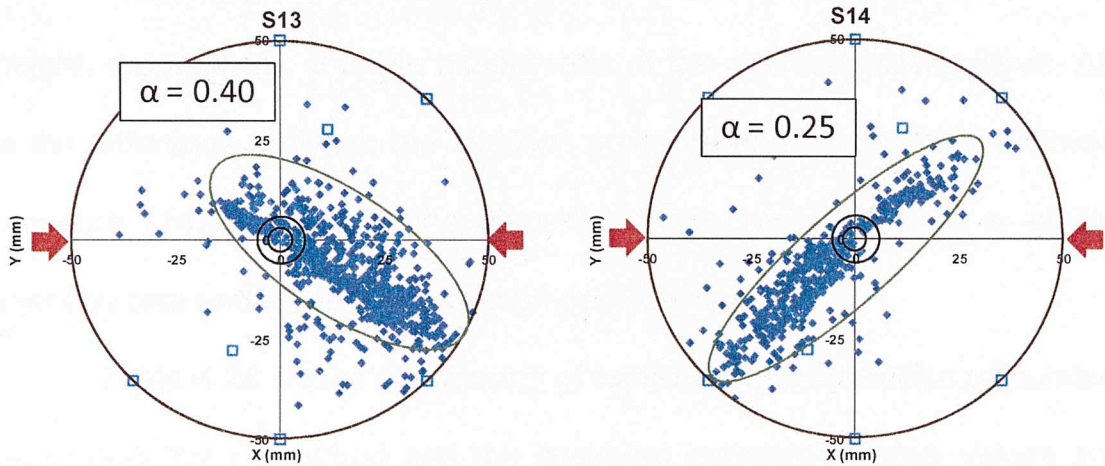


Fig. 4.108 - Plan view of Lyons sandstone samples showing the distribution of the microseismic clouds which are enclosed by green ellipses. The aspect ratio of the microseismicity cloud is determined by the dimension of each ellipse (short axis to long axis)

The formation permeability and the parameters required for the inversion approach (eq. 2.41) are given in Table 4.27.

Table 4.27 - Parameters used by the inversion approach for permeability for each Lyons sandstone sample.

LYONS SANDSTONE								
	S4	S6	S7	S8	S9	S11	S13	S14
L_f , mm	75	72	58	76	71	95	75	87
w_f , mm	25	17	16	20	20	42	30	22
h_f , mm	50	50	45	48	60	72	77	40
α	0.33	0.23	0.28	0.26	0.28	0.44	0.40	0.25
ΔP , psi	4023	3140	3461	4512	5045	4858	2775	4733
$\eta_r \cdot 10^{-5}$, Pa-s	2	2	2	2	2	2	2	2
$q_i \cdot 10^{-7}$, m ³ /s	1.7	1.7	1.7	1.7	1.7	1.7	1.7	1.7
k_{inv} , μd	0.2	0.18	0.22	0.15	0.11	0.15	0.23	0.16

where L_f , w_f and h_f are the microseismicity cloud length, width and height, respectively, α is the aspect ratio of the microseismicity cloud, ΔP is the difference between the injection pressure and the far-field reservoir pressure (14.7 psi), η_r is the viscosity of the reservoir fluid, q_i is the injection rate and k_{inv} is the formation permeability.

Table 4.28 shows a summary of formation permeabilities calculated using both the r-t method and the inversion approach. Those values are compared to values measured on a core plug recovered from a representative Lyons sandstone sample, which yielded a permeability of 20 μD .

Table 4.28 - Formation permeability values for Lyons sandstone samples obtained using the inversion approach, r-t method and measured using the AP608.

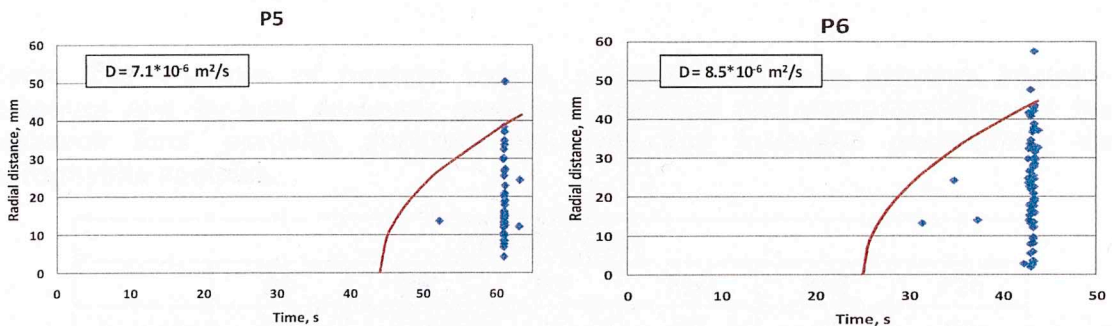
	S4	S6	S7	S8	S9	S11	S13	S14
$k_{inv}, \mu d$	0.2	0.18	0.22	0.15	0.17	0.15	0.23	0.16
$k_{r-t}, \mu d$	0.0002	0.0007	0.0002	0.0001	0.0001	0.00005	0.0003	0.004
$K_{AP-608}, \mu d$	20±4							

The inconsistency observed between values of permeability obtained using the r-t method and those obtained experimentally can be attributed to erroneous value of diffusivity used to calculate the triggering front envelope in the former. According to Shapiro et al., (2006), one signature of the r-t plot occurs during the first 10 minutes of fracturing; during this period, a quasi linear growth of the microseismic cloud is

observed, new fracture volume creation is dominant. The events occurring in this period are omitted during the process of calculating the diffusivity value. For the hydraulic fracturing experiments performed, the events were recorded within the first 5 minutes, falling into the quasi linear fracture growth behavior. Therefore, using this technique yields inaccurate values of the formation permeability. Formation permeability obtained through the inversion approach is principally affected by the uncertainties in the location since these affect the aspect ratio, which is always less than 1 and as low as 0.23 in sandstone samples.

4.5.2 Pyrophyllite

Both techniques were used to calculate the formation permeability. **Fig. 4.109** shows the r-t plots with the values of apparent diffusivity, D , for each pyrophyllite sample.



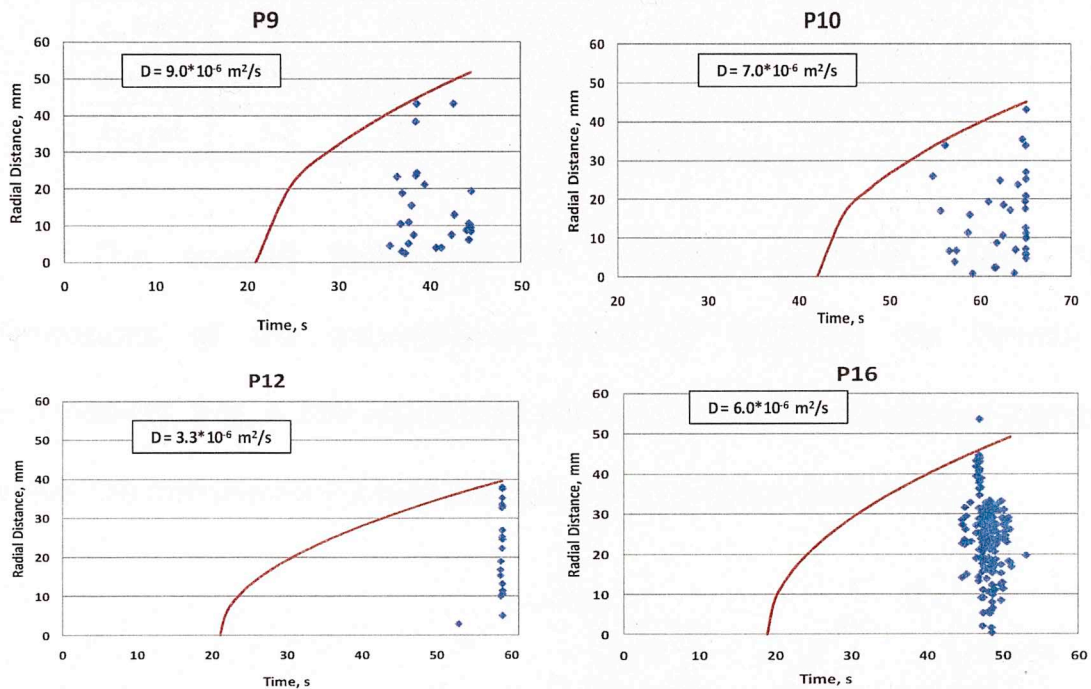


Fig. 4.109 - r-t plots for each pyrophyllite sample showing the radial distance of each MS event to the perforation point as a function of time since the start of the injection. The blue diamonds represent the MS events and the red line is the triggering front of microseismicity which is defined by the diffusivity, D

With the values of apparent diffusivity obtained from the r-t plots the formation permeability is computed using eqn. 2.33 and the parameters shown in Table 4.29.

Table 4.29 - Values of fracture height, pressure difference between injection pressure and far-field reservoir pressure, viscosity and compressibility of the reservoir fluid, porosity, apparent diffusivity and formation permeability for pyrophyllite samples.

PYROPHYLLITE						
	P5	P6	P9	P10	P12	P16
h_f , mm	50	50	29	30	42	50
ΔP , psi	1700	2288	3964	4732	3004	2338
η_r , Pa-s	$2 \cdot 10^{-5}$					
q_i , m ³ /s	$8 \cdot 10^{-8}$					
Φ , %	8	8	8	8	8	8

c_r, Pa^{-1}	$7 \cdot 10^{-6}$					
$D, \text{m}^2/\text{s}$	$1.7 \cdot 10^{-5}$	$8.5 \cdot 10^{-6}$	$7.2 \cdot 10^{-6}$	$2.5 \cdot 10^{-5}$	$1.2 \cdot 10^{-5}$	$3.0 \cdot 10^{-5}$
k_{r-t}, nd	1.2	0.6	0.6	0.5	1.3	0.8

The second technique, the inversion approach, uses the dimensions of the microseismic cloud to calculate the formation permeability. **Fig. 4.110** represents plan views of each sandstone sample where the microseismic cloud can be observed (blue diamonds).

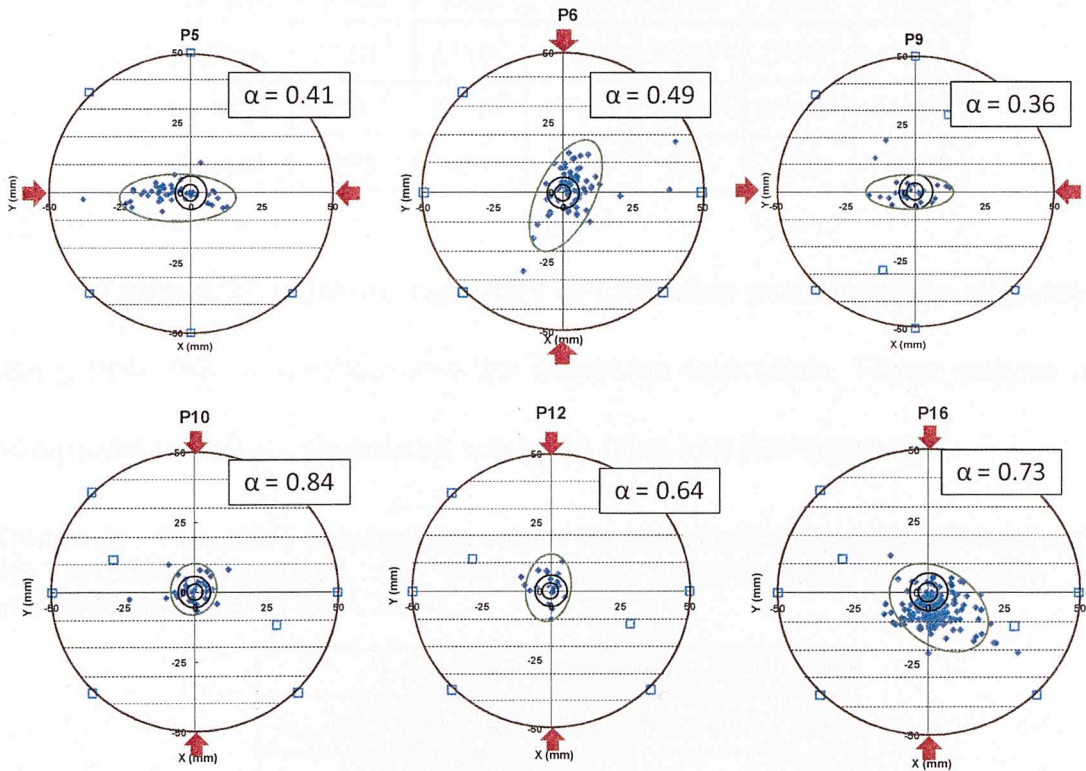


Fig. 4.110 - Plan view of pyrophyllite samples showing the distribution of the microseismic clouds which are enclosed by green ellipses. The aspect ratio of the microseismicity cloud is determined by the dimension of each ellipse (short axis to long axis)

The formation permeability and the parameters required based on the inversion approach (eqn. 2.41) are shown in **Table 4.30**.

Table 4.30 - Parameters used by the inversion approach for permeability samples.

PYROPHYLLITE						
	P5	P6	P9	P10	P12	P16
L_f , mm	41	43	29	19	25	37
w_f , mm	17	21	12	16	16	27
h_f , mm	50	50	35	30	42	50
α	0.41	0.49	0.36	0.84	0.64	0.73
ΔP , psi	1700	2288	3964	4732	3004	2338
η_r , Pa-s	$2 \cdot 10^{-5}$					
q_i , m ³ /s	$8 \cdot 10^{-8}$					
k_{inv} , μd	299	261	194	363	310	382

Table 4.31 shows a summary of formation permeabilities calculated using both the r-t method and the inversion approach. Those values are compared to values measured using an ultra-low permeameter.

Table 4.31 - Formation permeability values for pyrophyllite samples obtained using the inversion approach, r-t method and experimentally using ultra low permeameters (ULP) (Tinni, 2011).

	P5	P6	P9	P10	P12	P16
k_{inv} , nd	299	261	148	363	373	382
k_{r-t} , nd	1.2	0.6	0.3	0.5	1.8	0.8
K_{ULP} , nd	120	120	120	120	120	120

As observed in Lyons sandstone samples, there is an inconsistency between measured values of permeability and those obtained using the r-t method and those obtained experimentally which can be attributed to erroneous value of diffusivity used to calculate the triggering front envelope in the former. Formation permeability obtained through the inversion approach is principally affected by the aspect ratio of the microseismic cloud; since the number of events recorded and located for each pyrophyllite sample was small the length of the hydraulic fracture was underestimated leading to the calculation of high aspect ratios and estimation of higher permeability values than actually measured. However, all things considered they are right order of magnitude.

Table 4.32 shows a summary of formation permeabilities calculated using both the r-t method and the inversion approach for Lyons sandstone and pyrophyllite samples.

Table 4.32 - Formation permeability values for Lyons sandstone and pyrophyllite samples obtained using the inversion approach and r-t method.

	k_{inv} , nD	k_{r-t} , nD
P5	299	1.2
P6	261	0.6
P9	148	0.3
P10	363	0.5
P12	373	1.8
P16	382	0.8
	k_{inv} , μ D	k_{r-t} , μ D

S4	0.2	0.0002
S6	0.18	0.0007
S7	0.22	0.0002
S8	0.15	0.0001
S9	0.17	0.0001
S11	0.15	0.00005
S13	0.23	0.0003
S14	0.16	0.004

5. CONCLUSIONS

Hydraulic fracture mapping is a technique that works and yields important constraints on the geometry and orientation of the induced hydraulic fracture.

For isotropic materials such as Indiana limestone and Lyons sandstone, the spatial and temporal propagation of the fracture follows the applied stress direction as predicted by the theory when applied stress is sufficiently high. However, in the anisotropic case, pyrophyllite, the fracture direction depends on the direction and magnitude of stress applied with respect to foliation planes and the magnitude of anisotropy.

The majority of AE activity occurs in the pressure build-up period, before reaching the breakdown pressure. This trend is observed in all samples studied. During the pressure build-up period microfracturing takes place. Once the breakdown pressure is reached, these microfractures coalesce to form the “main” fracture. Pressure plots of Lyons sandstone samples show lower recorded breakdown pressures with higher horizontal applied stress, except for sample S8 (150 psi horizontal stress applied) where a breakdown pressure of 4527 psi was recorded. This value is very similar to the values recorded for samples loaded with ~550 psi (S11, S13, S14). In pyrophyllite samples, comparing samples coming from the same core (P15 and P6; P9 and P10; P11 and P12)

show that the breakdown pressures recorded in samples loaded perpendicular to the orientation of the foliation is always higher than the pressure recorded for sample loaded parallel to the fabric.

Calibration shows the absolute error in the acoustic emission events of anisotropic samples is almost twice that of isotropic samples even with a measured velocity model. Accurate velocity models and full anisotropic considerations are critical in controlling location accuracy.

The rms error of the location of the MS events allows constraining with certainty the general location of the fracture plane but cannot actually pin point the fracture itself.

Location of MS events can be improved by adding surface sensors to the sensors already distributed around the circumference of the sample; when sensors were not attached to the upper surface of each studied sample an increase in spatial uncertainties was reported. However, the greatest increase was observed in the Z-direction in all samples. Also, rms error for each rock studied showed an increase when the surface sensors were not taken into account; the rms error in Indiana limestone increased an average of 43%, in Lyons sandstone a 35% and in pyrophyllite a 35%.

SEM observations of hydraulic fractures show the induced fractures are not planar features as assumed by most models. The fractures deviate, bifurcate and are discontinuous like in natural systems. SEM

observations of the fractures indicate the existence of thin fractures that do not agree with the width of microseismic clouds observed. This is of great importance since the SRV (Stimulated Reservoir Volume) is a parameter used to estimate production in field applications; overestimating the real geometry of the fracture can lead to overestimation of production.

Process zone width in Lyons sandstone samples is found to decrease with higher applied stress. The length of the microseismic cloud reached its lower values with high applied stresses (S4, S6, S7). However, the greater values of the microseismic cloud are obtained with intermediate applied stresses (S11, S13, S14). Variation of SRV (Stimulated Reservoir Volume) with applied stress shows SRV decreases with high applied stresses (S4, S6, S7) and it is fairly constant for intermediate and low values of applied stress (S8, S9, S11, S13, S14).

Permeability influences the distribution of AE events. Ultra low permeability rocks, such as pyrophyllite, exhibit tightly clustered distributions of AE events, whereas more permeable rocks, such as Lyons sandstone, present a more diffuse distribution. Rocks with even higher permeability, such as Indiana limestone, the high leak-off rates limit the AE event distributions. Estimation of in-situ formation permeability using the r-t method leads to erroneous results due to short time duration of the

experiments. Results obtained using the inversion approach are in good agreement with the results obtained experimentally.

1. Kinsler, L. E., 1959, "Acoustic Emission from Fracturing in Dimensionally Anisotropic Rocks," *SPE* 17119.
2. King, J. R. and Pearson, C. F., 1982, "Acoustic Emission as a Tool for Hydraulic Fracture Location Experiments at High-Pressure Hot Dry Rock Sites," *SPE Journal*, V. 22 (4), 523-530.
3. Open, 1977, Annual Report, 1977, Hot Dry Rock Exploration Study, Department of Energy, Los Alamos Scientific Laboratory, Progress Report LA-7109-2K, Los Alamos, New Mexico, February 1978.
4. Ewing, R., 1982, "The Behavior of Brittle Rocks Around Micro Fractures," *Journal of Geophysical Research*, 87, 6073-6078.
5. King, J. R., 1982, "Acoustic Emission Monitoring of Rock Specimens Under Uniaxial Compression," *Journal of Geophysical Research*, 87, 6079-6084.
6. King, J. R., 1982, "Acoustic Emission Monitoring of Rock Specimens Under Uniaxial Compression," *International Journal of Rock Mechanics and Mining Sciences*, V. 19, 65-76.
7. Kinsler, L. E., Freese, W. C., and Kenny, J., 1982, "Improving the Performance of a Geophone Through Capacitive Position Sensing and Feedback," *ASME Dynamic Systems and Control Division*, V. 84, 529-539.
8. Brinlyman, J. G., 2006, "Fast Seismic Velocities for Transversely Isotropic Media and Extended Thomsen Formulas for Strongly Anisotropic Geophysics," *Geophysics*, V. 73 (1), D1-D10.
9. Oyler, J. D. and Lockner, D., 1977, "Acoustic Emission During Fluid Injection," *Proceedings First Conference on Acoustic*

REFERENCES

1. Aadnoy, B.S., 1987, Stresses around boreholes drilled in sedimentary rocks, SPE17119.
2. Albright, J.N. and Pearson, C.F., 1982, Acoustic Emissions as a Tool for Hydraulic Fracture Location: Experience at the Fenton Hill Hot Dry Rock Site, SPE Journal, V. 22 (4): 523-530.
3. Anon., 1978, Annual Report – 1977, Hot Dry Rock Geothermal Energy Development Project, Los Alamos Scientific Laboratory Progress Report LA-7109-PR, Los Alamos, New Mexico, February 1978.
4. Barron, K., 1969, The Fracture of Brittle Rocks Around Mine Excavations, Internal Report MR 69/25 LD, Mining Research Center, Department of Energy, Mines and Resources, Ottawa.
5. Barron, K., 1970, Detection of Fracture Initiation in Rock Specimens by the Use of a Simple Ultrasonic Listening Device, International Journal of Rock Mechanics and Mining Sciences, V. 8: 55-59.
6. Barzilai, A., VanZandt, T. and Kenny, T., 1998, Improving the Performance of a Geophone Through Capacitive Position Sensing and Feedback, ASME Dynamic Systems and Control Division, V. 64: 629-636.
7. Berryman, J.G., 2008, Exact Seismic Velocities for Transversely Isotropic Media and Extended Thomsen Formulas for Stronger Anisotropies, Geophysics, V. 73 (1): D1-D10.
8. Byerlee, J.D. and Lockner, D., 1977, Acoustic Emission During Fluid Injection, Proceedings First Conference on Acoustic

- Emission/Microseismic Activity in Geologic Structures and Materials, Pennsylvania State University, June 1975, Trans Tech Publications, Clausthal, Germany.
9. Castano, A.F., 2010, Estimation of Uncertainty in Microseismic Event Location Associated with Hydraulic Fracturing, Master's Thesis, University of Oklahoma.
 10. Cipolla, C.L., Lolon, E.P., Mayerhofer, M.J. and Warpinski, N.R., 2009, Fracture Design Considerations in Horizontal Wells Drilled in Unconventional Gas Reservoirs, SPE Hydraulic Fracturing Technology Conference, 19-21 January, The Woodlands, Texas, USA.
 11. Cipolla, C.L., Warpinski, N.R., Mayerhofer, M.J. and Lolon, E.P., 2010, The Relationship Between Fracture Complexity, Reservoir Properties, and Fracture-Treatment Design, SPE Productions and Operations, V. 25 (4): 438-452.
 12. Cheung, L.S. and Haimson, B., 1989, Hydrofracturing Stress Measurements in Fractured Rock: A Laboratory Study, The 30th U.S. Symposium on Rock Mechanics, June 19-22, 1989, Morgantown, WV.
 13. Chitrala, Y., Moreno, C., Sondergeld, C.H. and Rai, C., 2010, Microseismic Mapping of Laboratory Induced Hydraulic Fractures in

- Anisotropic Reservoirs, SPE Tight Gas Conference, 2-3 November 2010, San Antonio, Texas, USA.
14. Chitrala, Y., 2011, Microseismic Analysis of Laboratory Induced Fractures, Master's Thesis, University of Oklahoma.
 15. Clark, J.B., 1949, A Hydraulic Process for Increasing the Productivity of wells, 1949, Journal of Petroleum Technology – Transactions, V. 1 (3): 1-6.
 16. de Pater, C.J. and Dong, Y., 2007, Experimental Study of Hydraulic Fracturing in Sands as a Function of Stress and Fluid Rheology, SPE-Hydraulic Fracturing Technology Conference 2007, V. 2007: 87-96.
 17. Detournay, E. and Cheng, A.H., 1992, Influence of pressurization rate on the magnitude of the breakdown pressure, Proceedings of the 33rd U.S. Symposium on Rock Mechanics, Santa Fe, eds. J.R. Tillerson and W.R. Wawersik, Balkema, pp. 325-333, June 8-10, 1992.
 18. Dinske, C., Shapiro, S.A. and Rutledge, J.T., 2010, Interpretation of Microseismicity Resulting from Gel and Water Fracturing of Tight Gas Reservoirs, Pure Applied Geophysics, V. 167 (1-2): 169-182.
 19. Dozier, G., Elbel, J., Fielder, E., Hoover, R., Lemp, S., Reeves, S., Siebrits, E., Wisler, D. and Wolhart, S., Refracturing Works, Schlumberger Oilfield Review Article, Autumn 2003.

20. Economides, M.J. and Nolte, K.G., 2003, Reservoir Stimulation, John Wiley.
21. Energy Information Administration, EIA Annual Energy Outlook, 2011, http://www.eia.gov/energy_in_brief/about_shale_gas.cfm.
22. Faber, K. and Maxwell, P.W., 1996, Geophone Spurious Frequency: What is it and how does it affect seismic data quality?, SEG International Exposition & 66th Annual Meeting, November 10-15 1996, Denver, Colorado.
23. Fall, S.D., Young, R.P., Carlson, S.R. and Chow, T., 1992, Ultrasonic Tomography and Acoustic Emission of Hydraulically Fractured Lac du Bonnet Grey Granite, Journal of Geophysical Research, V. 97 (B5): 6867-6884.
24. Fisher, M.K., Wright, C.A., Davidson, B.M., Goodwin, A.K., Fielder, E.O., Buckler, W.S. and Steinsberger, N.P., 2002, Integrating Fracture Mapping Technologies to Optimize Stimulations in the Barnett Shale, SPE Production & Facilities, V. 20 (2): 85-93.
25. Gidley, J.L., Holditch, S.A., Nierode, D.E. and Veatch Jr., W., 1989, Recent Advances in Hydraulic Fracturing, SPE Monograph Series, V. 12.
26. Goodman, R.E., 1963, Subaudible Noise During Compression of Rocks, Geological Society of America Bulletin, V. 74: 487-490.

27. Grechka, V., Mazumdar, P. and Shapiro, S.A., 2010, Predicting Permeability and Gas Production of Hydraulically Fractured Tight Sands from Microseismic Data, *Geophysics*, V. 75 (1): B1-B10.
28. Groenenboom, J., van Dam, D.B. and de Pater, C.J., 1999, Time Lapse Ultrasonic Measurements of Laboratory Hydraulic Fracture Growth: Width Profile and Tip Behaviour, SPE Annual Technical Conference and Exhibition, 3-6 October 1999, Houston, Texas USA.
29. Ground Water Protection Council, 2009, Modern Shale Gas – Development in the United States: A Premier, Prepared for U.S Department of Energy, Office of Fossil Energy and National Technology Laboratory.
30. Haimson, B. and Fairhurst, C., 1969, Hydraulic Fracturing in Porous-Permeable Materials, *Journal of Petroleum Technology*, V. 21 (7): 811-817
31. Haimson, B.C. and Kim, K., 1977, Acoustic Emission and Fatigue Mechanisms in Rock, Proceedings First Conference on Acoustic Emission/Microseismic Activity in Geologic Structures and Materials, Pennsylvania State University, June 1975, Trans Tech Publications, Clausthal, Germany.
32. Haimson, B.C. and Zhao, Z., 1991, Effect of Borehole Size and Pressurization rate on Hydraulic Fracturing Breakdown Pressure, The 32th U.S. Symposium on Rock Mechanics, July 10-12 1991, Norman, OK

33. Hassebroek, W.E. and Waters, A.B., 1964, Advancements Through 15 Years of Fracturing, *Journal of Petroleum Technology*, V. 16 (7): 760-764.
34. Heydarabadi, F.R., Moghadasi, J., Safian, G. and Ashena, R., 2010, Criteria for Selecting a Candidate Well for Hydraulic Fracturing, 34th Annual SPE International Conference and Exhibition, 31 July-7 August 2010, Tinapa-Calabar, Nigeria.
35. Holcomb, D.J., 1993, General Theory of the Kaiser Effect, *International Journal of Rock Mechanics and Mining Science & Geomechanics Abstracts*, V.30 (7): 929-935.
36. Hornby, B.E., Howie, J.M. and Ince, D.W., 1999, Anisotropy Correction for Deviated Well Sonic Logs: Application to Seismic Well Tie, *Extended Abstracts, SEG 69th Annual Meeting*: 112-115.
37. Hsu, N. N. and Breckenridge, F. R., 1981, Characterization and calibration of acoustic emission sensors, *Materials Evaluation*, V. 39 (1): 60-68.
38. Isaac, J.H. and Lawton, D.C., 1999, Image Mispositioning Due to Dipping TI Media: a Physical Seismic Modeling Study, *Geophysics*, V. 64 (4): 1230-1238.
39. Karastathis, A., 2007, Petrophysical Measurements on Tight Gas Shale, M.S. Thesis, University of Oklahoma.

40. Khair, A.W., 1977, A Study of Acoustic Emission During Laboratory Fatigue Tests on Tennessee Sandstone, Proceedings First Conference on Acoustic Emission/Microseismic Activity in Geologic Structures and Materials, Pennsylvania State University, June 1975, Trans Tech Publications, Clausthal, Germany.
41. Kranz, R.L., Satoh, T., Nishizawa, O., Kusunose, K., Takahashi, M., Masuda, K. and Hirata, A., 1990, Laboratory Study of Fluid Pressure Diffusion in Rock Using Acoustic Emissions, Journal of Geophysical Research, V. 95 (B13): 21,593-21,607.
42. Lhomme, T.P., de Pater, C.J. and Helfferich, P.H., 2002, Experimental Study of Hydraulic Fracture Initiation in Colton Sandstone, SPE/ISRM Rock Mechanics Conference, 20-23 October 2002, Irving, Texas.
43. Lockner, D. and Byerlee, J.D., 1977(a), Hydrofracture in Weber Sandstone at High Confining Pressure and Differential Stress, Journal of Geophysical Research, V. 82 (14): 2018-2026
44. Lockner, D. and Byerlee, J.D., 1977(b), Acoustic Emission and Fault Location in Rocks, Proceedings First Conference on Acoustic Emission/Microseismic Activity in Geologic Structures and Materials, Pennsylvania State University, June 1977, Trans Tech Publications, Clausthal, Germany: 99-107.
45. Lockner, D., 1993, The Role of Acoustic Emission in the Study of Rock Fracture, 1993, International Journal of Rock Mechanics and Mining Sciences & Geomechanics Abstracts, V. 30 (7): 883-899.

46. Mae, I. and Nakao, K., 1968, Characteristics in the Generation of Microseismic Noises Under Under Uniaxial Compressive Load, *Journal of the Society of Materials Science*, V. 17 (181): 62-67.
47. Majer, E.L. and Doe, T.W., 1986, Studying Hydrofractures by High Frequency Seismic Monitorin, *International Journal of Rock Mechanics and Mining Sciences & Geomechanics Abstracts*, V. 23 (3): 185-199
48. Margesson, R.W. and Sondergeld, C.H., 1998, Anisotropy And AVO: A Case History from West of Shetlands, *Petroleum Geology of Northwest Europe*, Proceedings of the 5th Conference, Ed. By Fleet and Boldy.
49. Masuda, K., Nishizawa, O., Kusunose, K. and Satoh, t., 1993, Laboratory Study of Effects of In Situ Stress State and Strength on Fluid-induced Seismicity, *International Journal of Rock Mechanics and Mining Sciences & Geomechanics Abstracts*, V. 30 (1): 1- 10.
50. Matsunaga, I., Kobayashi, H., Sasaki, S. and Ishida, T., 1993, Studying Hydraulic Fracturing Mechanism by Laboratory Experiments with Acoustic Emission Monitoring, *The 34th U.S. Symposium on Rock Mechanics*, June 28-30 1993, Madison, WI
51. Matthews, H.L., Schein, G. and Malone, M., 2007, Stimulation og Gas Shales: They're All the Same – Right?, *SPE Hydraulic*

Fracturing Technology Conference, 29-31 January 2007, College Station, Texas USA.

52. Mavko, G., Mukerji, T. and Dvorkin, J., 2003, The Rock Physics Handbook, Cambridge University Press, Cambridge, UK.
53. Mayerhofer, M.J., Lolon, E.P., Youngblood, J.E. and Heinze, J.R., 2006, Integrations of Microseismic Fracture Mapping Results with Numerical Fracture Network Production Modeling in the Barnett Shale, 2006 SPE Annual Technical Conference and Exhibition, 24-27 September, San Antonio, Texas, USA.
54. Medlin, W.L. and Masse, L., 1979, Laboratory Investigation of Fracture Initiation Pressure and Orientation, Society of Petroleum Engineers of AIME Journal, V. 19 (2): 129-144.
55. Medlin, W.L. and Masse, L., 1984, Laboratory Experiments in Fracture Propagation, SPE Journal, V. 24 (3): 256-268.
56. Mogi, K., 1962, Study of the Elastic Shocks Caused by the Fracture of Heterogeneous Materials and its Relation to Earthquake Phenomena, Bulletin of Earthquake Research Institute, V. 40: 125-173.
57. Nordgren, R.P., 1972, Propagation of a Vertical Hydraulic Fracture, SPE Journal, V. 12 (4): 306-314.
58. Obert, L. and Duvall, W.I., 1942, Use of Subaudible Noise for Prediction of Rock Bursts, Part II, U.S. Bureau of Mines, RI 3654.

59. Obert, L. and Duvall, W.I., 1945(a), Microseismic Method of Predicting Rock Failure in Underground Mining, Part I. General Method, U.S. Bureau of Mines, RI 3797.
60. Obert, L. and Duvall, W.I., 1945(b), Microseismic Method of Predicting Rock Failure in Underground Mining, Part II. Laboratory Experiments, U.S. Bureau of Mines, RI 3803.
61. Obert, L., 1975, The Microseismic Method: Discovery and Early History, Proceedings First Conference on Acoustic Emission/Microseismic Activity in Geologic Structures and Materials.
62. Parker, M.A., Vitthal, S., Rahimi, A., McGowen, J.M. and Martch Jr., W.E., 1994, Hydraulic Fracturing of High-Permeability Formations to Overcome Damage, SPE International Symposium on Formation Damage Control, 7-10 February 1994, Lafayette, Louisiana, USA.
63. Patterson Jr., B.F., 1957, Hydraulic Fracturing in the Caddo-Pine Island Field, Journal of Petroleum Technology, V. 9 (1): 11-16.
64. Perkins, T.K. and Kern, L.R., 1961, Widths of Hydraulic Fractures, Journal of Petroleum Technology, V. 13 (9): 937-949.
65. Rutledge, J. and Phillips, W.S., 2001, Hydraulic Stimulation of Natural Fractures as Revealed by Induced Microearthquakes, Carthage Cotton Valley Gas Field, East Texas, Los Alamos National Laboratory.

66. Sachse, W. and Ruoff, A.L., 1975, Elastic Moduli of Precompressed Pyrophyllite used in Ultralight-pressure Research, *Journal of Applied Physics*, V. 46 (9): 3725-3730.
67. Scholz, C.H., 1968(a), Experimental Study of the Fracturing Process in Brittle rock, *Journal of Geophysical Research*, V. 73 (4): 1447-1454.
68. Scholz, C.H., 1968(b), Microfracturing and the Inelastic Deformation of Rock in Compression, *Journal of Geophysical Research*, V. 73 (4): 1417-1432.
69. Shapiro, S.A., Dinske, C. and Rothert, E., 2006, Hydraulic-fracturing Controlled Dynamics of Microseismic Clouds, *Geophysical Research Letters*, V. 33 (14): L14312.
70. Sleefe, G.E., Warpinski, N.R. and Engler, B.P., 1995, The Use of Broadband Microseisms for Hydraulic-Fracture Mapping, *SPE Formation Evaluation*, V. 10 (4): 233-240.
71. Solberg, P., Lockner, D. and Byerlee, J., 1977, Shear and Tension Hydraulic Fractures in Low Permeability Rocks, *Pure and Applied Geophysics*, V. 115 (1-2): 191-198.
72. Sondergeld, C.H., Getting, I.C., Spetzler, H.A. and Sobolev, G.A., 1980, Velocity Changes Associated with Generalized Triaxial

- Deformation of Pyrophyllite, *Pure and Applied Geophysics*, V. 118 (4): 975-989.
73. Sondergeld, C.H. and Estey, L.H., 1982, Source Mechanisms and Microfracturing during Uniaxial Cycling of Rock, *Pure Applied Geophysics*, V. 120 (1): 151-166.
74. Sondergeld, C.H. and Rai, C.S., 1992, Laboratory Observations of Shear Wave Propagation in Anisotropic Media, *The Leading Edge*, V. 11: 38-43.
75. Sondergeld, C.H. and Rai, C.S., 2011, Elastic Anisotropy of Shales, *The Leading Edge*, V. 30 (3): 324-331.
76. Song, I. and Haimson, B.C., 2001, Effect of Pressurization Rate and Initial Pore Pressure on the Magnitude of Hydrofracturing Breakdown Pressure in Tablerock Sandstone, *The 38th U.S. Symposium on Rock Mechanics*, July 7-10 2001, Washington D.C.
77. Song, I., Suh, M., Won, K.S. and Haimson, B., 2001, A Laboratory Study of Hydraulic Fracturing Breakdown Pressure in Table-Rock Sandstone, *Geosciences Journal*, V.5 (3): 263-271.
78. Stein, S. and Wysession, M., 2003, *An Introduction to Seismology, Earthquakes, and Earth Structure*, Blackwell Publishing Ltd., Malden, MA, USA.

79. Surdi, A.A., Ekart, D.D., Duran, P. and Suarez-Rivera, R., 2010, Possible Sources of Acoustic Emission Events During Hydraulic Fracturing, 44th U.S. Rock Mechanics Symposium and 5th U.S.-Canada Rock Mechanics Symposium, Salt Lake City, Utah, June 27-30, 2010.
80. Suzuki, T., Sasaki, K. and Hirota, T., 1964, A New Approach to the Prediction of Failure by Rock Noise, Proceedings Fourth International Conference on Strata Control and Rock Mechanics, Columbia University, New York: 1-9.
81. Talebi, S. and Boone, T., 1998, Source parameters of injection-induced microseismicity, *Pure Applied Geophysics*, 153, 113-130.
82. Thomsen, L., 1986, Weak Elastic Anisotropy, *Geophysics*, V. 51 (10): 1954-1966.
83. Tinni, A., 2011, Personal Communication.
84. Urbancic, T.I. and Maxwell, S.C., 2002, Source Parameters of Hydraulic Fracture Induced Microseismicity, SPE Annual Technical Conference and Exhibition, 29 September-2 October 2002, San Antonio, Texas USA.
85. van Dam, D.B., de Pater, C.J. and Romijn, R., 1998, Analysis of Hydraulic Fracture Closure in Laboratory Experiments, Proceedings of the SPE/ISRM Rock Mechanics in Petroleum Engineering Conference, V. 2: 365-374.

86. Veatch Jr., R.W., 1983, Overview of Current Hydraulic Fracturing Design and Treatment Technology-Part 1, Journal of Petroleum Technology, V. 35 (4): 677-687.
87. Verdon, J., Kendall, J.M. and Maxwell, S.C., 2010, A Comparison of Passive Seismic Monitoring of Fracture Stimulation from Water and CO₂ Injection, Geophysics, V. 75 (3): MA1-MA7.
88. Vestrum, R.W., Lawton, D.C. and Schmid R., 1999, Imaging Structures Below Dipping TI Media, Geophysics, V. 64 (4): 1239-1246.
89. Vinegar, H.J., Wills, P.B. and Shlyapobersky, J., 1992, Active and Passive Seismic Imaging of a Hydraulic Fracture in a Diatomite, Journal of Petroleum Technology, V. 44 (1): 28-34, 88-90.
90. Walker, R.N., Hunter, J.L., Brake, A.C., Fagin, P.A. and Steinsberger, N., 1998, Proppants, We Still don't Need no Proppants – A Perspective of Several Operators, SPE Annual Technical Conference and Exhibition, 27-30 September 1998, New Orleans, Louisiana USA.
91. Walter, W.R. and Brune, J.N., 1993, Spectra of Seismic Radiation from a Tensile Crack, Journal of Geophysical Research, V. 98 (B3): 4449-4459.
92. Wang, Z., 2002, Seismic Anisotropy in Sedimentary Rocks, Part 2: Laboratory Data, Geophysics, V. 67 (5): 1423-1440.

93. Warpinski, N.R., Uhl, J.E. and Engler, B.P., 1997, Review of Hydraulic Fracture Mapping Using Advanced Accelerometer-Based Receiver Systems, Sandia National Laboratories.
94. Warpinski, N.R., Branagan, P.T., Peterson, R.E., Wolhart, S.L. and Uhl, J.E., 1998, Mapping Hydraulic Fracture Growth and Geometry Using Microseismic Events Detected by Wireline Retrievable Accelerometer Array, SPE Gas Technology Symposium, 15-18 March 1998, Calgary, Alberta, Canada.
95. Warpinski, N.R., 2000, Analytic Crack Solutions for Tilt Fields Around Hydraulic Fractures, Journal of Geophysical Research, V. 105 (23): 23,463 – 23,478.
96. Warpinski, N.R., Waltman, C.K., Du, J. and Ma, Q., 2009, Anisotropy Effects on Microseismic Mapping, SPE Annual Technical Conference and Exhibition, 4-7 October 2009, New Orleans, Louisiana, USA.
97. Wyss, M. and Brune, J.N., 1968, Seismic Moment, Stress and Source Dimensions for Earthquakes in the California-Nevada Region, Journal of Geophysical Research, V. 73 (14): 4681-4694.
98. Zoback, M.D., Rummel, F., Jung, R. and Raleigh, C.B., 1977, Laboratory Hydraulic Fracturing Experiments in Intact and Pre-Fractured Rock, International Journal of Rock Mechanics and Mining Sciences & Geomechanics Abstracts, V. 14 (2): 49-58.

APPENDIX A: TRANSVERSE ISOTROPY

(After Wang, 2002)

A transverse isotropic material has a hexagonal symmetry. TI rocks have five independent elastic constants. The stress-strain relationship is given by:

$$\sigma_i = C_{ij} \varepsilon_j = \begin{bmatrix} \sigma_1 \\ \sigma_2 \\ \sigma_3 \\ \sigma_4 \\ \sigma_5 \\ \sigma_6 \end{bmatrix} = \begin{bmatrix} C_{11} & C_{12} & C_{13} & & & \\ C_{12} & C_{11} & C_{13} & & & \\ C_{13} & C_{13} & C_{33} & & & \\ & & & C_{44} & & \\ & & & & C_{44} & \\ & & & & & C_{66} \end{bmatrix} \begin{bmatrix} \varepsilon_1 \\ \varepsilon_2 \\ \varepsilon_3 \\ \varepsilon_4 \\ \varepsilon_5 \\ \varepsilon_6 \end{bmatrix} \quad (\text{A-1})$$

Where where σ_i and ε_j are the stress and strain components and where C_{ij} is the elastic constant tensor. Although equation (A-1) shows six elastic constants, only five are independent because $C_{66} = 1/2 (C_{11}-C_{12})$. The corresponding elastic velocities are:

$$V_p = \sqrt{\frac{A+B}{2\rho}} \quad (\text{A-2})$$

$$V_{s1} = \sqrt{\frac{A-B}{2\rho}} \quad (\text{A-3})$$

$$V_{s2} = \sqrt{\frac{C_{66}\sin^2\theta - C_{44}\cos^2\theta}{\rho}} \quad (\text{A-4})$$

Where ρ is the bulk density, θ is the angle between the symmetry axis and the direction of wave propagation, and:

$$A = C_{11}\sin^2\theta + C_{44} + C_{33}\cos^2\theta \quad (\text{A-5})$$

$$B = \sqrt{[(C_{11} - C_{44})\sin^2\theta - (C_{33} - C_{44})\cos^2\theta]^2 + 4(C_{13} + C_{44})^2\sin^2\theta\cos^2\theta} \quad (\text{A-6})$$

When $\theta = 0^\circ$, the waves are propagating parallel to the symmetry axis (perpendicular to lamination or bedding), and the velocities are:

$$V_{p,0} = \sqrt{\frac{C_{33}}{\rho}} \quad (\text{A-7})$$

$$V_{s,0} = V_{s1,0} = V_{s2,0} = \sqrt{\frac{C_{44}}{\rho}} \quad (\text{A-8})$$

When $\theta = 90^\circ$, the waves are propagating perpendicular to the symmetry axis (parallel to the lamination or bedding), in which the velocities are:

$$V_{p,90} = \sqrt{\frac{C_{11}}{\rho}} \quad (\text{A-9})$$

$$V_{s1,90} = \sqrt{\frac{C_{44}}{\rho}} \quad (\text{A-10})$$

$$V_{s2,90} = \sqrt{\frac{C_{66}}{\rho}} \quad (\text{A-11})$$

To calculate the three (one P and two S) velocities at any angle of wave propagation, all five elastic constants and the bulk density must be known. Inversely, the elastic constants can be calculated from five velocities (three compressional and two shear) measured at three different angles and bulk density. Usually, velocities at $\theta = 0^\circ$, $\theta = 90^\circ$, and $\theta = 45^\circ$ are measured so that equations (A-2)-(A-6) have the simplest mathematical

form. Those velocities are measured using the three-plug technique indicated in **Fig. A-1**.

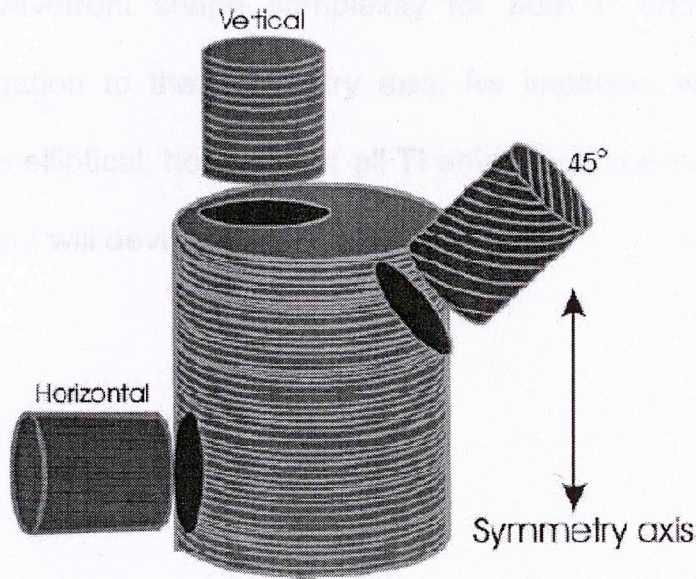


Fig. A-1 – Three-plug technique schematics used to measure 5 different velocities. Three adjacent core plugs (one parallel, one perpendicular and one 45° to symmetry axis) are used (Wang, 2002).

The elastic constants are used to calculate the anisotropy parameters (ϵ , δ and γ) as:

$$\epsilon = \frac{C_{11} - C_{33}}{2C_{33}} \tag{A-12}$$

$$\gamma = \frac{C_{66} - C_{44}}{2C_{44}} \tag{A-13}$$

$$\delta = \frac{(C_{13} - C_{44})^2 - (C_{33} - C_{44})^2}{2C_{33}(C_{33} - C_{44})} \tag{A-14}$$

Parameter ϵ describes the difference of the P-wave velocities in the vertical and horizontal directions. γ describes the fractional difference of the SH-wave velocities between vertical and horizontal directions, which is

equivalent to the difference between the vertical and horizontal polarizations of the horizontally propagating S-wave. δ is a parameter that controls the wavefront shape complexity for both P and S waves at oblique propagation to the symmetry axis; for instance, when $\delta=\epsilon$, the wave fronts are elliptical; however for all TI anisotropic systems having $\delta-\epsilon \neq 0$, the wavefront will deviated from being elliptical.

This volume is the property of the University of Oklahoma, but the literary rights of the author are a separate property and must be respected. Passages must not be copied or closely paraphrased without the previous written consent of the author. If the reader obtains any assistance from this volume, he must give proper credit in his own work.

I grant the University of Oklahoma Libraries permission to make a copy of my thesis upon the request of individuals or libraries. This permission is granted with the understanding that a copy will be provided for research purposes only and that requestors will be informed of these restrictions.

NAME _____

DATE _____

A library which borrows this thesis for use by its patrons is expected to secure the signature of each user.

This thesis _____ CAMILO MORENO _____ has been used by the following persons, whose signatures attest their acceptance of the above restrictions.

NAME AND ADDRESS

DATE

A THESIS
SUBMITTED TO THE GRADUATE COLLEGE
in partial fulfillment of the requirements for the
Degree of
MASTER OF SCIENCE